Synthesis and Characterization of Hard Cr_2O_3 and Superhard Cr-Zr-O PVD Coatings

A Thesis Submitted to the College of Graduate and Postdoctoral Studies
In Partial Fulfillment of the Requirements
For the Degree of Doctor of Philosophy
In the Department of Mechanical Engineering
University of Saskatchewan
Saskatoon

By
Masoud Mohammad Taheri

PERMISSION TO USE

In presenting this thesis in partial fulfillment of the requirements for a postgraduate degree from the University of Saskatchewan, I agree that the Libraries of this University may make it freely available for inspection. I further agree that permission for copying of this thesis in any manner, in whole or in part, for scholarly purposes, may be granted by professor Qiaoqin Yang who supervised my thesis work or, in her absence, by the College of Graduate and Postdoctoral Studies (CGPS), the Head of the Department or the Dean of the College in which my thesis work was done. It is understood that any copying or publication or use of this thesis or parts thereof for financial gain shall not be allowed without my written permission. It is also understood that due recognition shall be given to me and to the University of Saskatchewan in any scholarly use which may be made of any material in my thesis.

Requests for permission to copy or to make other use of the material in this thesis in whole or part should be addressed to:

Head of the Department of Mechanical Engineering
57 Campus Drive, University of Saskatchewan
Saskatoon, Saskatchewan, S7N 5A9 Canada
OR
Dean of College of Graduate and Postdoctoral Studies
University of Saskatchewan
116 Thorvaldson Building, 110 Science Place
Saskatoon, Saskatchewan, S7N 5C9 Canada

ABSTRACT

Reactive radio-frequency magnetron sputter technique (RF-MS) was used to deposit Cr-O and Cr-Zr-O coatings on silicon, SS316L, WC-Co, and HSS M42 substrates. The effects of deposition temperature, chemical composition, and subsequent heat treatment on microstructural, thermal stability, and mechanical properties of both Cr-O and Cr-Zr-O coatings were investigated. The deposited coatings were characterized using scanning electron microscopy, X-ray diffraction, Raman spectroscopy, X-ray photoelectron spectroscopy, Energy dispersive spectroscopy, nanoindentation, Rockwell "C" indentation, optical profilometer, reciprocating wear testing, electrochemical testing, and inductively coupled plasma analysis.

The results showed that appropriate deposition conditions were required in order to obtain hard Cr_2O_3 coating. A Cr_2O_3/Cr duplex interlayer was found to be suitable for nucleation of diamond coatings on WC-Co substrates as it restricted graphite formation before diamond nucleation, thus, continuous diamond coatings with good adhesion were successfully deposited on Cr_2O_3/Cr interlayered WC-Co substrates. Furthermore, hard Cr_2O_3 coatings were shown to be a potential candidate to improve the mechanical properties and to reduce the toxic ion release rate of orthopedic implants. The coated SS316L substrates illustrated better wear and corrosion resistance and lower friction coefficient compared to bare 316L substrates under a reciprocating sliding condition in saline solution. Furthermore, many fewer Cr ions were released from coated SS316L substrates after immersion tests.

Adding zirconium to Cr_2O_3 coating shifted the onset of crystallization for the Cr_2O_3 coating to higher temperatures and superhard Cr-Zr-O coatings with a hardness value over 40 GPa could be obtained at a zirconium concentration of around 9.5 at. % and a substrate temperature of 300°C. The obtained superhardness could be attributed to the formation of a nanocomposite structure.

ACKNOWLEDGMENTS

First and foremost, I would like to express my deepest gratitude and thanks to my supervisor, Professor Qiaoqin Yang for her continuous motivation and support during the whole study and research period. Second, I would like to thank my advisory committee members Professors Jerzy A. Szpunar, Ike N. Oguocha, W.J. Zhang, and Michael P. Bradley, for their critical guidance and valuable advice.

I would like to thank the entire faculty and staff in the Department of Mechanical Engineering, especially Mr. Zhao Nan Fang and Mr. Robert Peace, for providing an excellent research environment and technical support.

I should also thank the staff at Saskatchewan Structural Science Center (SSSC), especially Jason Maley for Raman spectroscopy training, Dr. George Belev and Dr. Danielle Covelli for performing XPS analysis, and Dr. Jianfeng Zhu for the grazing incidence XRD training. Furthermore, I am grateful to my group members for their support and advice.

I also highly appreciate the financial support from the University of Saskatchewan, the Canada Research Chair Program, the Natural Sciences and Engineering Research Council of Canada, and the Canada Foundation for Innovation.

Finally, I would like to give my deepest thanks to my wife, parents, and all other family members for their love and support.

DEDICATION

To

My Wife:
Sheyda Shahsavari

My Son:
Saman

And
My Parents

TABLE OF CONTENTS

LIST OF TABLES

LIST OF FIGURES

ABBREVIATIONS

Acronyms	Unit	Definition
A_p	mm^2	Projected contact surface
d_{hkl}	nm	Distance of the lattice planes hkl
E_i	GPa	Young's modulus of the indenter
E_{IT}	GPa	Indentation modulus
E_s	GPa	Young's modulus of the substrate
F_{max}	N	Maximum force under load
h_c	mm	Contact depth of the indenter at F_{max}
h_{max}	mm	Maximum penetration depth
h_p	mm	Permanent penetration depth
H_{IT}	GPa	Indentation hardness
ν_s		Poisson number of the substrate
ν_i		Poisson number of the indenter
h_s	µm	Thicknesss of substarte
h_f	µm	Thicknesss of coating
C	µm/N	The contact stiffness
P	Pa	Pressure
P’	W	Power
R_a	µm	Arithmetic Roughness
P/A	W/m^2	Power density

Acronyms	Unit	Definition
FWHM	Rad	Full Width at Half Maximum
θ	°	Diffraction angle
β	°	Angle between crystal plans
T	°C	Temperature
t	s	Time
T_N	°K	Néel Temperature
a	nm	Lattice parameter
b	nm	Lattice parameter
c	nm	Lattice parameter
CVD		Chemical Vapor deposition
PVD		Physical Vapor deposition
RF-MS		Radio-Frequency Magnetron Sputtering
XPS		X-ray Photoelectron Spectroscopy
XRD		X-ray Diffraction
SEM		Scanning Electron Microscopy
TEM		Transmission Electron Microscopy
ICP		Inductively Coupled Plasma
EDS		Energy Dispersive Spectroscopy
HSS		High Speed Steel
UBM		Unbalance Magnetron Sputtering
DCMS		DC Magnetron Sputtering
ZTA		Zirconia Toughened Alumina
PSZ		Partially Stabilised Zirconia
DZC		Disperced Zircona Ceramics

CHAPTER 1

INTRODUCTION

1.1 Research Motivation

Surface coating is an important technology for improving the durability and performance of materials. It reduces operating costs, energy consumption, and environmental degradation, and leads to the development of new products. In addition to the bulk properties of the substrates, coated materials can be enhanced to have a range of specific surface properties, such as a low friction coefficient, high resistance to wear, corrosion, and oxidation, high thermal conductivity, and excellent biocompatibility. Surface coatings are being used, for example, in electronics for memory chips and processors, in optics for lenses and mirrors or in automobile construction for tappets and rolling bearings. Wear-resistant protective coatings have been widely adopted for wear protection on tools for cutting, forming and stamping. Typical wear-resistant protective coatings already used in industry are TiN, TiAlN, TiC, CrN, DLC (Diamond Like Carbon) or Al_2O_3. The application of coatings has already achieved considerable economic benefits in today market. The industries listed above give an idea of the enormous economic potential of the research and development of such materials.

Chemical vapor deposition (CVD[1]) and physical vapor deposition (PVD[2]) are the advanced techniques being used for creating surface coatings. In CVD processes, the layer is formed by chemical reactions of the gas phases on a heated substrate, whereas, in PVD processes, the desire

---

[1] CVD: Chemical Vapor Deposition

[2] PVD: Physical Vapor Deposition

solid materials gasified by different methods (such as high power electricity, laser, high energy ions, and etc.) are condensed on the substrate to form a layer. Compared to CVD processes, PVD processes do not require high surface temperatures or special gas compounds, and thus allow a wider choice of starting materials and substrates, as well as low deposition temperature.

The high quenching rates of PVD processes, compared to powder or melt metallurgy processes, also allow the deposition of metastable phases at room temperture. In these processes, the structure of the deposited coatings can be adjusted by altering the deposition parameters e.g. pressure, reactive gases, temperature, etc. and thus a variety of coating properties can be achieved through coating design to meet specific application requirements. Therefore, it is of great importance to select the appropriate processing methode and parameters as well as the right materials.

Ceramic materials are generally characterized by their high hardness and high chemical and thermal resistance. Oxides are a subcategory of ceramic materials and possess good mechanical, thermal and optical properties, and thus have been used as corrosion and wear protection coatings or transparent layers. α-Cr_2O_3 (eskolaite), isostructural to α-Al_2O_3 (corundum), has a high bulk hardness and holds great potential to be used as wear and corrosion protection coatings. Nevertheless, it is hard to obtain Cr_2O_3 coatings with corundum structure. Although many methods, including plasma-spray, sputtering, chemical vapor deposition, and pulsed laser deposition, have already been employed to deposit Cr_2O_3 coatings [1–7], most of the chromium oxide coatings obtained were of weak mechanical properties due to inappropriate deposition parameters selected during the coating processing. Chromium can form different oxides including CrO_3, $CrO_{2.906}$, Cr_8O_{21}, Cr_5O_{12}, CrO_2, Cr_2O_3, Cr_3O_4, CrO, and Cr_3O, due to its different valence states. The formation of various forms of chromium oxides with different microstructures and chemical compositions could be the main reason for the wide range of mechanical properties observed in chromium oxide coatings. Hence, in the present Ph.D. research, a reactive RF-magnetron sputtering technique was employed to prepare chromium oxide coatings and the effect of deposition parameters on microstructural and mechanical properties of coatings was investigated systematically to establish a correlation between the processing, structure, and mechanical properties of the RF-MS chromium oxide coatings. An appropriate deposition conditions were then found to obtain hard Cr_2O_3 coating on strategic important substrates to evaluate its properties for potential protective applications.

ZrO_2 is a classic engineering ceramic whose martensitic phase transformation can be used to increase the toughness of materials and is therefore of particular interest for applications with mechanical stress. So, it can be used to tailor and improve the mechanical properties of Cr_2O_3 coatings as a result of the phase mixtures formation in addition to single-phase solid solutions. For instance, a higher hardness can be achieved by solid solution hardening, compared to the materials of the binary systems with comparable structure or the stabilization of the ZrO_2 high-temperature phases at room temperature are favored by the incorporation of Cr. This can happen during the coating formation by combining the elements of the ternary Cr-Zr-O system. Thus, the mechanical properties of Cr_2O_3 coatings are expected to be improved if they are doped with zirconium and form a nanocomposite structure similar to the well-studied Ti-Si-N superhard nanocomposite coatings. However, ceramists previously paid little attention to the Cr_2O_3-ZrO_2 system due to poor densification ability of these mixtures in the sintering process. This is due to the fact that volatilization of Cr_2O_3 at high temperature results in materials with low density which have poor mechanical properties. But, nowadays various type of coatings can be deposited at room temperature by employing physical vapor deposition (PVD) techniques. Hence, these techniques provide new ways for the researchers to produce the temperature sensitive compounds at low temperature. Therefore, in the current research, the potential of the ternary Cr-Zr-O system for improving properties of Cr_2O_3 coatings and creation of novel oxide-based superhard coatings is also investigated.

1.2 Research Objectives

Oxide-based hard coatings have already been of great interest for many applications such as cutting tools, electronics, optics, and automobile constructions. However, they might have the potential to be used for many other applications if we can have a deep understanding of the relationships of processing, structure, and properties. Hence, the overal objective of the present research is to achieve the sysnthesis of superhard ternary Cr-Zr-O coatings based on the deposition of hard Cr_2O_3 coating using reactive magnetron sputtering and to obtain the relationships of processing, structure, and properties of the coatings. It has the following specific objectives:

1. Synthesis of hard Cr_2O_3 coating and establishment of a correlation between process parameters, microstructure, phase composition, and mechanical properties of binary Cr-O coatings;

2. Determination of the tribo-corrosion properties and ion release rate of the hard Cr_2O_3 coating as potential candidate for orthopedic implants;

3. Enhancement of diamond coating nucleation and adhesion on WC-Co substrates. by employing Cr_2O_3 coating as an interlayer;

4. Synthesis of superhard oxidation resistant Cr-Zr-O coatings by addition of Zr into hard Cr_2O_3 coatings.

1.3 Research Contributions

1. Adherent hard Cr_2O_3 coatingswere deposited on SS316L with improved tribo-corrosive properties and reduced toxic ion release rate suitable for orthopedic applications.

2. Cr_2O_3/Cr coating was successfully used as a buffer layer to deposite diamond on WC-Co substrate with enhanced nuclation and adhesion.

3. Superhard Cr-Zr-O coatings were sucessfully synthesized for the first time by doping Zr into hard Cr_2O_3 coatings. The superhard ternary coatings show an interesting composite structure of t-ZrO_2 + m-ZrO_2 + h-Cr_2O_3 at elevated temperatures, which opens new investigation and applications of these oxide coatings.

The aforementioned findings from this research would also help scientist in understanding the effect of deposition parameters on phase, strcuture, and properties of reactively magnetron sputtered chromium oxide coatings and hold great potential for orthopedic applications as Cr_2O_3 coated SS316L samples show much improved tribo-corrosive and reduced toxic ion release rate.

1.4 Thesis Organization

The present thesis is organized into 8 chapters. Chapter 1 covers a brief introduction, motivation, and objectives along with major contributions of this Ph.D. thesis. Chapter 2 deals with literature review as well as background and existing state of knowledge of binary Cr-O, Zr-O and ternary Cr-Zr-O materials. The experimental methods used in this research including deposition method and its parameters and characterization techniques are discribed in Chapter 3. Chapters 4 to 7 report the results for both binary Cr-O and ternary Cr-Zr-O coatings, which were already published in peer reviewed journals. Finally, summary, conclusions, and future work for the present research are presented in Chapter 8.

CHAPTER 2

LITERATURE REVIEW

Generally, ceramic materials compared to metals illustrate better structural and thermal stabilities at high temperatures. They generally also show better resistance to creep, oxidation, corrosion, and perform better in tribological situations. However, they have a significant disadvantage which is their brittleness due to their high ionic bonding fraction. In these materials, dislocation movements, which are the main deformation mechanism, in the horizontal and vertical planes are difficult due to the repulsion of the cations with each other and the anions with each other. This chapter first reviews the state of the literature on the phase formation and properties of materials in binary Cr-O and Zr-O systems in sections 2.1.1 and 2.1.2, respectively. Subsequently, the composition, phases and solubility limits of materials in the Cr-Zr-O system is reviewed in section 2.1.3.

2.1 Chromium and Zirconium Based Oxides

This section introduces the Cr-O and Zr-O binary systems. The phase formations in the thermodynamic equilibrium will be explained with reference to the corresponding phase diagrams. Subsections 2.1.1 and 2.1.2 deal with the structure and essential properties of Cr_2O_3 and ZrO_2, respectively, since these oxidation states of the cations are preferentially formed. ZrO_2 has interesting structural and mechanical properties due to its three modifications. These modifications will be also discussed here. The section then provides an overview of the essential literature with a focus on the resulting phases in PVD coatings.

2.1.1 Chromium Oxide and Chromium Oxide Coatings

Metallic chromium can form an extraordinary number of oxide compounds with oxygen. This is due to the fact that metallic chromium can behave as 2-, 3-, 4-, 5-, 6-, and in some cases as 8-valent element [8,9]. However, the only stable phase in the Cr-O system under standard conditions (i.e. a temperature below 1600°C and oxygen pressures below 1 atm) is rhombohedral (r)[3]-Cr_2O_3 [9]. Equilibrium phase diagram for Cr-O system is shown in Figure 2-1. According to the Cr-O phase diagram r-Cr_2O_3 exactly contains 60 at.% Oxygen and 40 at.% Cr, and no solubility of oxygen in metallic chromium is observed. The incongruent melting point of r-Cr_2O_3 lies between 2265 to 2340°C. This variation in melting point is possibly due to a partial reduction of Cr^{+3} to Cr^{+2}, happens in the heating process, which changes the melting point [9]. Single-phase Cr_3O_4 is formed at 57 at.% Oxygen and 43 at.% Cr. However, compared to r-Cr_2O_3 the transition temperatures or melting points of this phase is up to 700 ° C lower. In addition to the oxidation state 3+ for Cr ions in r- Cr_2O_3 and 2+ and 3+ for Cr_3O_4, there are further oxidation states of Cr, such as 4+ in tetragonal CrO_2, 5+ in monoclinic Cr_2O_5, 6+ in orthorhombic CrO_3, and +2 in CrO which are formed at higher O contents or special condition as described in literature[8,9]. Hence, the absence of these phases in the phase diagram has yet to be confirmed, however, crystal structures of these oxides have been reported in the ICDD (International Center for Diffraction Data) database.

Bulk chromium oxide in the form of Cr_2O_3 is known for its high hardness of 29.5 GPa [9–12]. It is e.g. used as a material additive for increasing the chemical and thermal resistance of ceramic materials [13], in powder form as a green color pigment [14], and as a coating, due to its wear protective, refractory, and anti-reflective properties, for various applications, such as advanced heat engines[15], digital magnetic recording units[16], gas bearing applications[17], electronics[18], and optics[19,20].

---

[3] The eskolaitic structure is often represented as α-Cr_2O_3

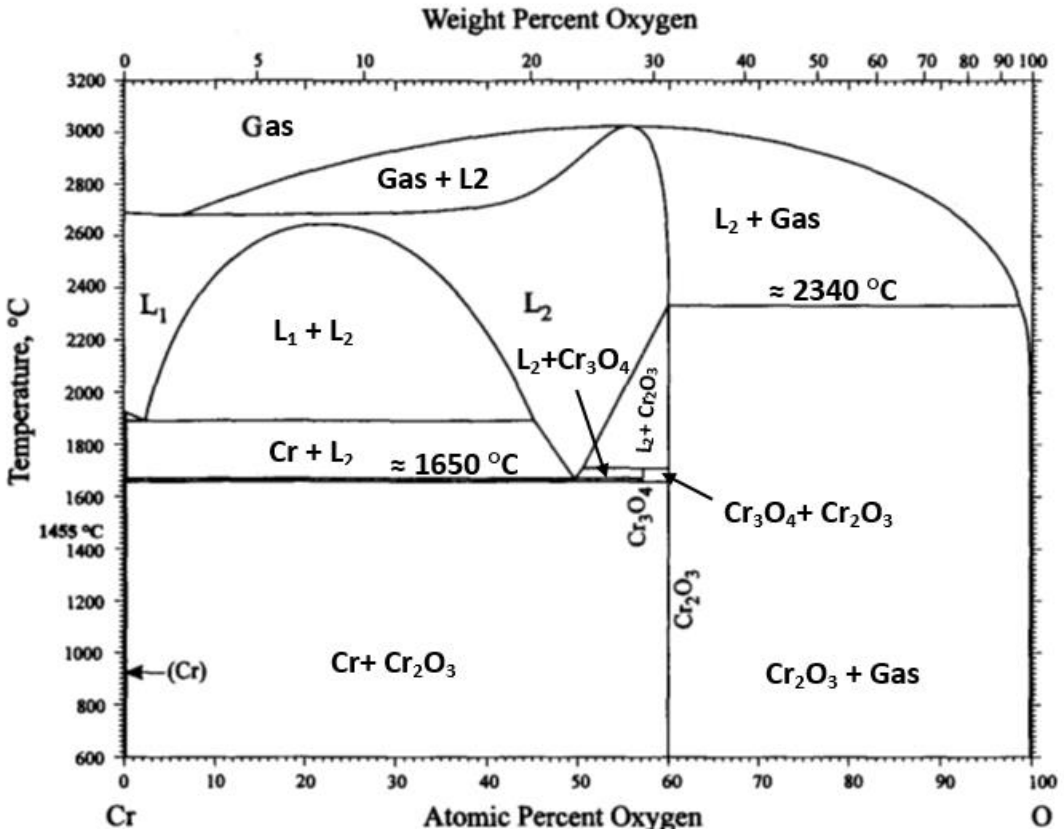

Figure 2-1: Cr-O phase diagram [21,22]. L1 and L2 stand for melts with different compositions. r-Cr_2O_3 is formed at exactly 60 at. % Oxygen and 40 at. % Cr and has no solubility range. Among all occurring solid phase areas, it has the highest melting temperature.

From a magnetic behavior perspective, Cr_2O_3 is antiferromagnetic with a Néel temperature (T_N) of 307°K [23]; however, this behavior can be changed to weak ferromagnetism and even superparamagnetism in chromia nanoparticles [24]. Cr_2O_3 has a rhombohedral or hexagonal unit cell symmetry, being isostructural to sapphire (Corundum type structure Figure 2-2) [10,24,25]. r-Cr_2O_3 has a specific heat of 28.38 Cal/mol. °C at 25°C, and a coefficient of linear expansion of 9.6 $\times 10^{-6}$ $°C^{-1}$ between 20-1400°C [9]. The Poisson ratio number between 0.25 and 0.265, the density of 5.23 g/cm^3, and the mean refraction index of 2.5 has been reported for r-Cr_2O_3 [9,15]. The effective ionic radius of Cr^{3+} in r-Cr_2O_3 is 61.5 pm [25].

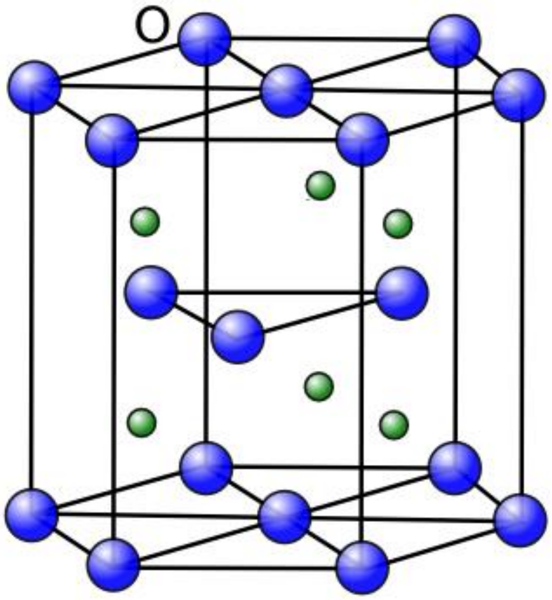

Figure 2-2: Structure of r-Cr_2O_3 in the hexagonal representation (after [26]). The blue spheres symbolize doubly negatively charged O ions, red spheres symbolize triply positively charged Cr ions.

The total optical modes in the r-Cr_2O_3 crystal are represented in Equation 1.

$$\Gamma_{opt} = 2A_{1g} + 2A_{1u} + 3A_{2g} + 2A_{2u} + 5E_g + 4E_u \qquad (1)$$

Nevertheless, due to the inversion symmetry of the Cr_2O_3 unit cell, only the symmetric A_{1g} and E_g modes are Raman active (i.e. in total 7 vibrations are Raman active) [27]. The two A_{1g} modes are observed in the Raman spectrum at wave numbers 266.0 cm^{-1} and 551.3 cm^{-1} and the 5 Eg-modes at 235 cm^{-1}, 298.3 cm^{-1}, 352.0 cm^{-1}, 527.7 cm^{-1} and 615.0 cm^{-1}. However, the appearance of all 7 Raman modes in Raman spectrum are temperature dependent and usually, the two lowest frequency bands at 235 and 266 cm^{-1} are only observed at a much lower temperature than Néel temperature of Cr_2O_3 [28–33].

Cr_2O_3 coatings can be obtained by different techniques such as plasma-spray [1–3], sputtering [4,5], chemical vapor deposition (CVD) [6], and pulsed laser deposition [7]. These coatings have been studied for applications such as wear-resistant protective coatings in gas bearings [17,34] and magnetic media [16] as well as template films for nucleation of Al_2O_3 coatings with corundum structure [35,36].

Dense single phase Cr_2O_3 coatings with a hardness value up to 32 GPa have also been reported in the literature [11,37,38]. A comprehensive overview of the current literature (Please see Table 2-1) on PVD Cr_2O_3 coatings with information on manufacturing, test methods, and the obtained phases has shown that creating the 2/3-stoichiometry as well as increasing the hardness of Cr_2O_3 coatings are the essential intention of the coating and process development.

Table 2-1: Overview of Cr_2O_3 coatings deposited by PVD methods.

Technique	**Target**	**Gases**	**Deposition Parameters**	**Substrate**	**Substrate Temperature (°C)**	**Charact. Meth.**	**Coating**	**Year**	**Ref.**
RF-MS[4]	Cr_2O_3	Ar	P’[5]=200- 400 W P= 5-30 mTorr Spacing: 43.1-63.5 mm Bias= 0-100W	Inconel X-750 foil, Glass, Carbon	Not Heated	EPMA[6], SEM[7], XRD[8], AES[9], Adhesion	CrO_X	1979	[39]
RF-MS	Cr_2O_3	Ar	P’=200- 400 W P= 5-30 mTorr Spacing: 43.1-63.5 mm Bias= 0-100W	Inconel X-750 foil	a) Not Heated b) Post-heat treated 750°C	AES, XRD	AS[10]-CrO_X HT[11]-Cr_2O_3	1980	[40]
RF-MS	Cr_2O_3	Ar	P’=200- 400 W P= 5-30 mTorr Spacing: 43.1-63.5 mm Bias= 0-100W	Inconel X-750 foil	a) Not Heated b) Post-heat treated 750°C	Friction, Wear	Cr_2O_3	1981	[34]
RF-MS	Cr_2O_3+Ni-Cr	Ar	P’=200- 400 W P= 5-30 mTorr Spacing: 43.1-63.5 mm Bias= 0-100W	Inconel X-750 foil	a) Not Heated b) Post-heat treated 750°C	SEM, AES, XRD	Ni-Cr+ Cr_2O_3	1981	[17]
RF-MS	Cr_2O_3	Ar, O_2	P’ = 0.4 – 1.2 KW P = 0,4 - 2,7 Pa P_{O2} = 0 - 0,08 Pa	Si Wafers	25-150°C	Stress, Hardness, Wear, RBS[12], XRD, SEM	XRD-Unknown RBS-nonstoichiometric Cr_2O_3	1989	[41]

---

[4] Radio Frequency Magnetron Sputtering

[5] P’: Target power (W)

[6] Electron Prob Microanalysis

[7] Scanning Electron Microscope

[8] X-ray Diffraction

[9] Auger Electron Spectroscopy

[10] As-deposited

[11] Heat treated

[12] Rutherford Backscatter Spectroscopy

DC-MS[13]	Cr	Ar, O_2	P' = 0.2 –1KW P= 5-10 mTorr O_2= 3-50%	Si Wafers	Not heated	Transmittance, Density, Refractive Index, Stress, AES, XPS, AFM[14]	Unknown -Cr_xO_y	1993	[19]
RF-MS	Cr	Ar, O_2	P'= 250 W $P_{O2} = 10^{-4}$-10^{-5} mbar	AL_2O_3	T < 200 °C	XPS[15], AES	CrO, Cr_2O_3	1993	[42]
DC-MS	Cr	Ar, O_2	P'= Unknown Ar= 0.034 Pa $m^{-3} s^{-1}$ O_2=0-0.035 Pa $m^{-3} s^{-1}$	Stainless Steel	T= 200 -500 °C	XPS, XRD, Density	Various Cr-O and Cr_2O_3	1997	[4]
RF-MS	Cr	Ar, O_2	Unknown	Al_2O_3–TiC	Unknown	Wear, Scratch, Friction, Hardness, Young's modulus, STM[16], AFM, TEM[17], AES, XPS	CrO_x	1997	[16]
UBM[18]	Unknown	Ar, O_2	Unknown	M2 Steel	Unknown	XRD, SEM, XPS, Hardness, Adhesion	Cr+Cr_2O_3	1998	[43]
RF-MS	Cr	Ar, O_2	P'= 66.3 kWm^{-2} P= 0.1 Pa P_{O2} = 5-30%	Si, Glass, HSS	89-317 °C	EPMA, XRD, AFM, Hardness, Density, Stress,	Cr_2O_3	1999	[11]
UBM	unknown	Ar, O_2	Unknown	M2 Steel	150°C	XRD, SEM, Scratch, Wear, Adhesion	CrN/Cr_2O_3 Duplex coatings	2001	[44]
RF-MS	Cr	Ar, O_2	P: 0.1 Pa P': 350W Ar: 20 Sccm O_2: 3.2 Sccm	Steel	200 °C	SEM, TEM	Cr_2O_3	2007	[45]
RF-MS	Cr	Ar, O_2	P: 0.1 Pa P': 350W Ar: 20 Sccm O_2: 2-3.2 Sccm	Steel	200 °C	XRD, XPS, TEM, Hardness, Modulus, Wear, Adhesion	Cr_2O_3	2007	[46]
RF-MS	Cr	Ar, O_2	P: 0.1 Pa P': 250-450W Ar: 20 Sccm O_2: 2-3.2 Sccm	Steel	200 °C	XRD, Hardness, Modulus, Wear, Scratch	Cr_2O_3	2007	[47]

---

[13] Direct Current Magnetron Sputtering

[14] Atomic Force Microscopy

[15] X-ray Photoelectron Spectroscopy

[16] Scanning Tunneling Microscope

[17] Transmission Electron Microscope

[18] Unbalance Magnetron Sputtering

RF-MS	Cr	Ar, O_2	P: 0.1 Pa P’: 350W Ar: 20 Sccm O_2: 2.3 Sccm	Steel	Heat treated in the air up to 800 °C in Air and Ar	XRD, Hardness, Modulus, Wear, Scratch	Cr_2O_3	2008	[48]
RF-MS	Cr	Ar, O_2	P: 0.1 Pa P’: 250-450W Ar: 20 Sccm O_2: 2-3.2 Sccm	Steel	Heat treated in the air up to 800 °C in Air and Ar	XRD, XPS, Hardness, Modulus, Wear, Scratch	Cr_2O_3	2008	[5]
PDCMS[19]	Cr	Ar, O_2	P: 0.4 Pa P’: 6.79 W/cm^2 Ar: 15 Sccm O_2: 7-15 Sccm	Si, Steel	60°C	XRD, XPS, Raman Spectroscopy, Hardness, AFM, Corrosion	Cr_2O_3	2008	[49]
PDCMS	Cr	Ar, O_2	P: 1.33 Pa P’: 1200 W OEM[20]: 25-50%	Si	90°C	XRD, SEM, Hardness	Cr_2O_3	2008	[50]
RFMS	Cr_2O_3	Ar	P: 0.67 Pa P’: 50 W O_2: 0-30%	Al_2O_3	Not heated	XRD, XPS, HRXRD[21],AFM	Cr_2O_3	2010	[51]
DCMS	Cr	Ar, O_2	P: 0.8 Pa P’: Unknown Ar: 0.7 Pa O_2: 0.05-0.1 Pa	Si	300-450°C	XRD, SEM, RBS, Hardness	Cr_2O_3	2010	[52]
DCMS PDCMS DOMS[22]	Cr	Ar, O_2	P: 0.27 Pa P’: 1.5 KW Ar: 60 Sccm O_2: 40 Sccm Bias: -60 V	Si, Steel	Not heated	XRD, EDS[23], TEM, Hardness, Wear	Cr_2O_3	2015	[38]

Bhushan [39] was the first researcher who tried to deposit Cr_2O_3 coatings by RF diode sputtering method from a r-Cr_2O_3 target in pure Ar atmosphere on Inconel X. 750 films, glass slides and carbon substrates (planchets). In his research, the effect of target-to-substrate distance (4.1 cm to 6.4 cm), the target power (200 W, 400 W), the total gas pressure (0.67 Pa to 4.00 Pa) and the substrate bias (0V, 100V) on stoichiometry and adhesion of chromium oxide layers was investigated. He showed that, regardless of process parameters, all layers were substoichiometric with an average O/Cr ratio of 0.67 and the deposited layers were amorphous. Bhushan [40] in his next research indicated that the amorphous substoichiometric chromium oxides layers can

---

[19] Pulsed DC Magnetron Sputtering

[20] Optical Emission Monitoring

[21] High Resolution XRD

[22] Deep Oscillation Magnetron Sputtering

[23] Energy Dispersive Spectroscopy

crystallize into a r-Cr_2O_3 structure by post-heat treatment at 704 °C for 20 h. He never mentioned the mechanical properties of his deposited chromium oxides coatings. Nevertheless, he used them as wear resistant coatings for journal foil air bearings in gas turbine engines [34]. He showed that the journal foil air bearings coated with chromium oxide layers could withstand 9000 start-stops and high-speed rubs which are desirable for gas turbine engines. Bhushan [17] also investigated the incorporation of Ni-Cr binders into chromium oxide coatings in the hope to improve the ductility of chromium oxide coatings for gas bearing applications. However, he did not mention the effect of Ni-Cr binder on other mechanical properties of chromium oxide coatings, he successfully improved the ductility of coatings in his research by optimizing the process parameters to incorporate Ni-Cr binders into chromium oxide coatings.

Kao et al.[41] investigated the deposition of r-Cr_2O_3 films by means of high-performance cathode sputtering and a r-Cr_2O_3 target. The authors considered the target power (400 W and 1200 W), the total gas pressure (p = 0.4 Pa - 2.7 Pa), the oxygen partial pressure (P_{O2} = 0 Pa - 0.08 Pa) and the substrate temperature (25 °C and 150 °C) as the variables. All the deposited films were amorphous and non-stoichiometric with hardness values up to 21 GPa. According to the authors, the X-ray diffractograms indicated that heat treatment at 300 ° C for 10 h makes the layers semicrystalline and produced a r-Cr_2O_3 phase. They illustrated that grain growth is affected by oxygen partial pressure, substrate temperature and O/Cr ratio. The highest hardness of up to 25 GPa was obtained when only stoichiometric films were deposited in a pure Ar atmosphere and a substrate temperature of 150 °C.

Trube et al. [19] considered chromium oxide layers for X-ray masking applications and they used DC magnetron sputtering technique to deposit chromium oxide layers from a pure metallic Cr target in the presence of Ar and oxygen plasma. The effect of Cr-target power, deposition pressure, and oxygen concentration in the plasma on optical properties, density, and stress of coatings were investigated. Highly transparent, stress-free, and smooth chromium oxide coatings obtained by optimizing the deposition parameters. However, the authors could not confirm that the coatings were Cr_2O_3, as they were amorphous with O/Cr ratio about 1.

Rothhaar and Oechsner [42] studied the chromium oxide coatings deposited by RF-magnetron sputtering technique with metallic Cr-target in Ar+ O_2 plasma on Al_2O_3 substrates. The aim of their research was to realize the appropriate conditions for producing chromium oxide coatings with Cr_2O_3 stoichiometry. The chromium oxide coatings were deposited at 250W target power where Ar partial pressure was 2× 10^{-2} mbar and oxygen flow rate changed between 0-0.35 sccm. They showed that the stoichiometry of oxide coatings can be derived from simple model calculations if a constant Cr flux is assumed to be sputtered from the target on the substrates. The model calculation proposed by Rothhaard and Oechnser was a correlation between the film growth rate and the individual layer density. However, they showed that their proposed model worked very well for coatings with Cr_2O_3 stoichiometry, the model could not be justified for non-stoichiometry or substoichiometry coatings due to the unknown density and lake of fundamental studies on those oxides.

Contoux et al.[4] precisely evaluated a DC-magnetron sputtering deposition process during deposition of chromium oxide coatings to realize the optimal operation point for deposition of coatings with 2/3-stoichiometry. In their study, a metallic Cr was used as a sputtering target and oxygen flow rate changed between 0-0.035 Pa m^{-3} s^{-1} where a constant Ar flow rate of 0.034 Pa m^{-3} s^{-1} had been selected for the deposition process. Unfortunately, the detail deposition parameters during deposition of coatings have not been mention ((i.e. deposition power is unknown) in Contoux et al. work. The poisoning mechanism of Cr target was explained by evaluating the effect of oxygen flow rate on oxygen partial pressure, cathodic voltage, and the light emitted by excited atomic chromium. They showed that well-crystallized Cr_2O_3 coatings are only obtained at temperatures above 300 °C, confirmed by XRD and XPS analysis. However, they did not measure the mechanical properties of deposited Cr_2O_3 coatings and could not identify chromium oxide coatings deposited under other deposition parameters.

After 18 years of the first research on PVD chromium oxide coating by Bhushan [39], in a recent publication, Bhushan et al.[16] investigated the tribological properties of chromium oxide coatings used for magnetic recording applications. The coatings were non-stoichiometric and have a r-Cr_2O_3 structure. Depending on the coating thickness, a hardness of up to 30 GPa and a modulus of elasticity of up to 210 GPa were measured for the deposited coatings. However, this time Bhushan et al. did not disclose the deposition parameters used for achieving chromium oxide coatings with high hardness and the reasons for observing such hard chromium oxide coatings were unknown.

Hones et al. [11] deposited r-Cr_2O_3 coatings by reactive cathode sputtering (in radio frequency (RF) mode) from a Cr target with a power density of P/A = 66.3 kWm^{-2}. The influence of both the oxygen partial pressure and the substrate temperature (between 87 °C and 317 °C) at a constant pressure of 0.1 Pa on the composition, phase formation, mechanical and optical properties of deposited coatings was investigated. They concluded that at a low oxygen partial pressure of <10% of total gas pressure a Cr phase in which oxygen is dissolved was created. This led to high residual compressive stresses of 2 GPa and a hardness of 20 GPa for coatings. Increasing the oxygen partial pressure to more than 10% results in a single-phase r-Cr_2O_3 coatings with a density close to the compact material (maximum 0.5 g /cm^3). The hardness can be increased to 31 GPa at this condition with low compressive stresses (0.9 GPa). At the highest oxygen partial pressure of 30%, the hardness drops to 2.5 GPa and the density to 2.8 g /cm^3. According to the authors, these coatings have a higher oxygen content, which they attributed to the formation of higher oxides in addition to the formation of r-Cr_2O_3. The low density was correlated to a higher porosity, which is created by agglomeration in the gas phase and causes pores in the growing films (no microstructural images were provided in the paper to support this hypothesis). By varying the substrate temperature, the grain size can be influenced, which according to the authors increased linearly with the substrate temperature. From a substrate temperature of 227 °C, the films became crystalline. In one area from 247 ° C to 317 ° C and an oxygen partial pressure of 15% - 25% coatings showed a maximum hardness of 32 GPa due to the formation of stoichiometric, single-phase r-Cr_2O_3 phases. Thanks to Hones et al.[11] who reveal their detail deposition parameters to obtain hard chromium oxide coatings, however, in their research the influence of deposition pressure and Cr target power on properties of chromium oxide coatings was not investigated. Moreover, the supporting data provided in Hones et al.[11] paper, to justify observation of hard chromium oxide coatings, looks to have high uncertainty. For instance, the density of coatings was calculated from thickness, surface area, and weight of substrates before and after deposition which results in high experimental errors in coatings.

Wang et al. [43,44] considered CrN/Cr_2O_3 duplex coatings for injection molding applications. They managed to deposit well-adherent chromium oxide coatings with hardness value about 20 GPa on CrN coated steels by unbalanced magnetron sputtering technique. In their research the deposition parameters for the chromium oxide coatings were unknown and they showed that quality of top Cr_2O_3 coatings can determine the final properties of CrN/Cr_2O_3 duplex coatings such as wear resistance, oxidation resistance, and mold releasing capability.

Pang et al.[5,45–48] obtained r-Cr_2O_3 films by reactive unbalanced high-performance cathode sputtering at 350 W RF Cr target power, 300 ° C substrate temperature and an oxygen flow rate of 2-3.2 sccm at Ar flow rate of 20 sccm. They showed that at low oxygen flux of <2.6 sccm, amorphous films were formed. Increasing the oxygen flux to more than 2.6 sccm produced crystalline r-Cr_2O_3 films, which according to the authors, the hardness of 11 GPa can be increased to 21 GPa and the reduced modulus of elasticity of 170 GPa to 234 GPa. At the maximum oxygen flux of 3.2 sccm, a strong (300) texturing of the Cr_2O_3 films occurred whose calculated residual stresses were 2 GPa. By a subsequent heat treatment of amorphous films, which were deposited at an oxygen flux of 2.3 sccm, at 500 ° C for a post-heat treatment time of 1 h in air (described in a subsequent work of the authors[48]), the hardness of 12.3 GPa in the untreated state could be increased to 26 GPa. Below 470 ° C, the films consist of an amorphous and r-Cr_2O_3 phases. A higher post-treatment temperature resulted in a single-phase crystalline Cr_2O_3 films. A longer duration of heat post-treatment caused grain growth, according to the authors, the hardness decreased slightly. Unfortunately, Pang et al did not evaluate the effect of deposition pressure on properties of chromium oxide coatings. Hence, the effect of this process parameter on the properties of chromium oxide coatings still remained unknown so far.

Barshilia et al.[49] deposited Cr_2O_3 layers using pulsed UBM in the DC mode of two Cr targets (P/A = 6.79 W / cm^2, frequency 100 kHz, pulse duration 2976 ns (30%)) on Si and mild steel substrates. The substrate temperature was constant at 60 °C. In addition, a DC substrate bias of -50V was applied. The Ar gas flow was kept constant at 15 sccm and the oxygen gas flow varied from 7 sccm to 15 sccm. According to the authors (with reference to the X-ray diffractograms), r-Cr_2O_3 crystals formed in an amorphous chromium oxide matrix up to an oxygen flux of 10 sccm. At 13 sccm completely amorphous layers were formed. At 7 sccm, Raman spectroscopy shows r-Cr_2O_3 modes at 544 cm^{-1} (A1g) and 302 cm^{-1}, 349 cm^{-1} and 605 cm^{-1} (Eg). If the oxygen flux increases to more than 11 sccm, the intensity of the Eg-modes drops significantly, which, according to the authors, indicates inclusions of an amorphous phase into the crystalline matrix. This result contradicted with Pang et al [46,48] observations where amorphous chromium oxide phases transferred to crystalline Cr_2O_3 by increasing oxygen flow rate. However, chromium oxide coatings prepared by Barshilia and Rajam reached a maximum hardness of 22 GPa, the coatings were composed of crystalline Cr_2O_3 and amorphous phases which shows the deposition conditions need still to be optimized for the creation of single crystalline Cr_2O_3 coatings.

Audronis et al. [50] used a pulsed-dc sputter deposition in a dual-frequency (2F) mode to deposit chromium oxide coatings. The target and substrate were biased by DC pulse at frequencies of 130 kHz and 250 kHz, respectively. However, they did not disclose the detail of the deposition parameters, the OEM Cr signal intensities were at 25 and 50% during depositions. They showed that crystalline Cr_2O_3 coatings could be deposited at low temperature in an optimal ion bombardment conditions. This result was not in agreement with previous researches indicated that the deposition parameters have a substantial effect on final properties of chromium oxide coatings, the crystalline Cr_2O_3 coatings obtained by this method had a hardness value of 23-27 GPa, which remained almost constant over the investigated range of deposition conditions. Jeong et al. [51] deposited epitaxial Cr_2O_3 layers by high-performance RF sputtering at a power of 50 W from a 5.1 cm diameter r-Cr_2O_3 target on Al_2O_3 (0001) substrates. The total gas pressure was constant at 0.67 Pa, and the Ar/O_2 ratio was varied from a pure Ar atmosphere to 7/3. No additional substrate temperature was applied. The Layers deposited in a pure Ar atmosphere had a r-Cr_2O_3 phase with (0001) orientation. An Ar/O_2 atmosphere produced an O rich orthorhombic CrO_3 phase with (112) orientation. By post-heat treatment of the r-Cr_2O_3 layers at 300 °C-900 °C further reflections were shown in the X-ray diffraction pattern and the crystallinity increased. For CrO_3 layers, a r-Cr_2O_3 phase is formed starting at a post-heat treatment temperature of 300°C. At 900 °C, the CrO_3 phase had been completely converted to r-Cr_2O_3. These layers had strong texturing, with only the layer deposited at an Ar/O_2 ratio of 9/1 having complete (0001) orientation.

Pedersen et al. [52] deposited r-Cr_2O_3 layers by means of DC high-performance cathode sputtering at a power of 40 W with a Cr target (2.5 cm diameter) on Si substrates. The total pressure varied between 0.75 Pa and 0.80 Pa, with an Ar partial pressure of 0.70 Pa and an O_2 partial pressure between 0.05 Pa and 0.10 Pa. The substrate temperature was between 300 ° C and 450 ° C. In addition, an RF substrate bias was varied between 0 V and -200 V (DC equivalent). Oxygen fluxes of <0.5 sccm led to metallic Cr or substoichiometric CrO_x layers(or combination of them). In the following experiments, the oxygen flux was kept constant at 0.5

sccm and 2/3 Cr/O ratio were obtained. Depending on the selected temperature, substrate bias and strength of a superimposed magnetic field in the plasma chamber, crystalline Cr_2O_3 layers with varying degrees of texturing and defects arised. Defects in the layer can serve, according to the authors, as crystallization precursor for the growth of α-Al_2O_3 layers. An additional substrate bias produces a r-Cr_2O_3 layer with small grain size and relatively random orientation. Lin and Sproul[38] produced Cr_2O_3 layers using DC high-performance cathode sputtering, pulsed DC high-performance cathode sputtering, and high-power pulse sputtering at a power of 1.5 kW from a Cr target (10.2 cm x 29.2 cm) deposited on Si and AISI304 Stainless steel substrates. The pressure was kept constant at 0.27 Pa with an O_2/Ar ratio of 40/60 and a DC substrate bias of -60V was applied. All deposited layers were slightly more than stoichiometric with O/Cr ratios of 1.51 to 1.60. The layer deposited by DC high-performance cathode sputtering is amorphous and exhibits the highest deviation from stoichiometry. Here, in comparison to the other methods, the absolute minimum residual compressive stress of 1.2 GPa and hardness of 12 GPa was determined. A fully crystalline r-Cr_2O_3 layer with the least deviation from stoichiometry is formed by high power impulse sputtering due to the high current density at the substrate (65 $mAcm^{-2}$ compared to a maximum of 3.89 $mAcm^{-2}$ in the DC processes). This layer has the highest absolute compressive stress of 3.5 GPa and the highest hardness of 35 GPa.

Besides PVD techniques, other methods, including plasma-spray [1–3], chemical vapor deposition (CVD) [6], and pulsed laser deposition [7], have also been used to produce Cr_2O_3 coatings. Nevertheless, only sputtering techniques have so far been successful in producing Cr_2O_3 coatings with a hardness value close to that of bulk Cr_2O_3. However, the literature review on PVD Cr_2O_3 coatings showed that coatings deposited by sputtering methods can also possess weak mechanical properties if appropriate deposition parameters are not selected during the deposition process. Hence, in the first experiments in this Ph.D. research, chromium oxide coatings were deposited using the same deposition parameters reported by those researchers who successfully obtained hard Cr_2O_3 coatings using the reactive magnetron sputtering technique [5,11,16,38,47]. but unfortunately, the hardness of deposited coatings was as low as 4 GPa. This repeatability problem could be associated with the lack of comprehensive research on the relationships between the processing, structure, and mechanical properties of chromium oxide coatings deposited by reactive magnetron sputtering.

Literature review showed that most researchers, who obtained hard Cr_2O_3 coatings, did not disclose their detail deposition parameters and the reasons for obtaining hard Cr_2O_3 coatings by PVD methods are still unknown. Furthermore, the hardness value reported in the majority of the literature seems to have high uncertainty due to the lack of using international standards. According to the literature review, no previous research exists with an appropriate design of experiment which considers all principal deposition parameters together to show the importance of each deposition parameter in achieving chromium oxide coatings with a hardness value close to the bulk counterpart. Therefore, in the first part of this research, reactive RF magnetron sputtering was used to deposit chromium oxide coatings, considering the effect of principal deposition parameters, including deposition pressure, temperature, Cr-target voltage, and Ar/O_2 ratio on structure, phase composition, and hardness of the chromium oxide coatings. Finally, the reasons for obtaining hard Cr_2O_3 coatings were pointed out by establishing a correlation between the microstructure, phase composition, and mechanical properties of coatings.

2.1.2 Zirconium Dioxide and Zirconium Dioxide Coatings

Zirconia which is referred to ZrO_2 is the stable oxide of zirconium in the Zr-O system [53]. Zirconia-based ceramics can be used in harsh environments especially under various loading conditions as they possess a unique combination of high hardness, toughness, and corrosion resistance. They have already been used for hard to cut materials like magnetic tapes, plastic films, or paper items. It has been approved that hot-extrusion dies made or coated by zirconia perform much better than their conventional counterparts. Zirconia itself has been used for nuclear applications due to its inert characterization which allows it to be a good host material for the destruction of excess plutonium. Zirconia also has been used as sealing material for valves, chemical and slurry pumps, thread guides, and bearings. Other industrial fields that zirconia has been used include, but not limited to, biological implantation materials, solid electrolytes, oxygen sensors, thermal barrier coatings, and materials for fuel cells. Zirconia crystallizes in three well-expressed polymorphic forms, namely monoclinic, tetragonal, and cubic. However, the existence of the orthorhombic form has also been reported at high pressure [54]. According to the Zr-O phase diagrams (Figure 2-3), the monoclinic (α) ZrO_2 phase occurs at 66.7 at. % O up to a temperature of 1205 ° C and then transforms over a 100°C temperature range to the tetragonal (β) ZrO_2 phase which remains stable up to 2330 °C. In this transformation of zirconia, the phenomenon of temperature hysteresis is observed, i.e. the monoclinic phase converts above 1205 ° C into the tetragonal (β) phase whereas upon cooling, the monoclinic phase is formed only at about 950 °C [53]. The phase β-ZrO_2 transforms into the cubic modification γ-ZrO_2 above 2330 °C. This conversion has a minimum temperature hysteresis of ~30°C. At low O contents of <35 at. %, different Zr-based phases (or two-phase areas thereof) are formed up to 2130° C in which O is dissolved. The β-Zr phase has a cubic body-centered lattice in which a maximum of 10.5 at. % O is dissolved. The α-Zr phase has a hexagonal structure, in which octahedral gaps can accommodate up to 35 at% O. In the α phase, the oxygen is randomly distributed while the α' phase is partially ordered and the α'' phases are fully ordered (in terms of stacking order and occupancy of the O intermediate planes). The regions between the Zr-based phases (with hexagonal structure) and the ZrO_2-based phases consist of the corresponding two-phase mixtures. The monoclinic ZrO_2, which is the room temperature stable phase, will transfer into two orthorhombic phases upon increasing the pressure [55].

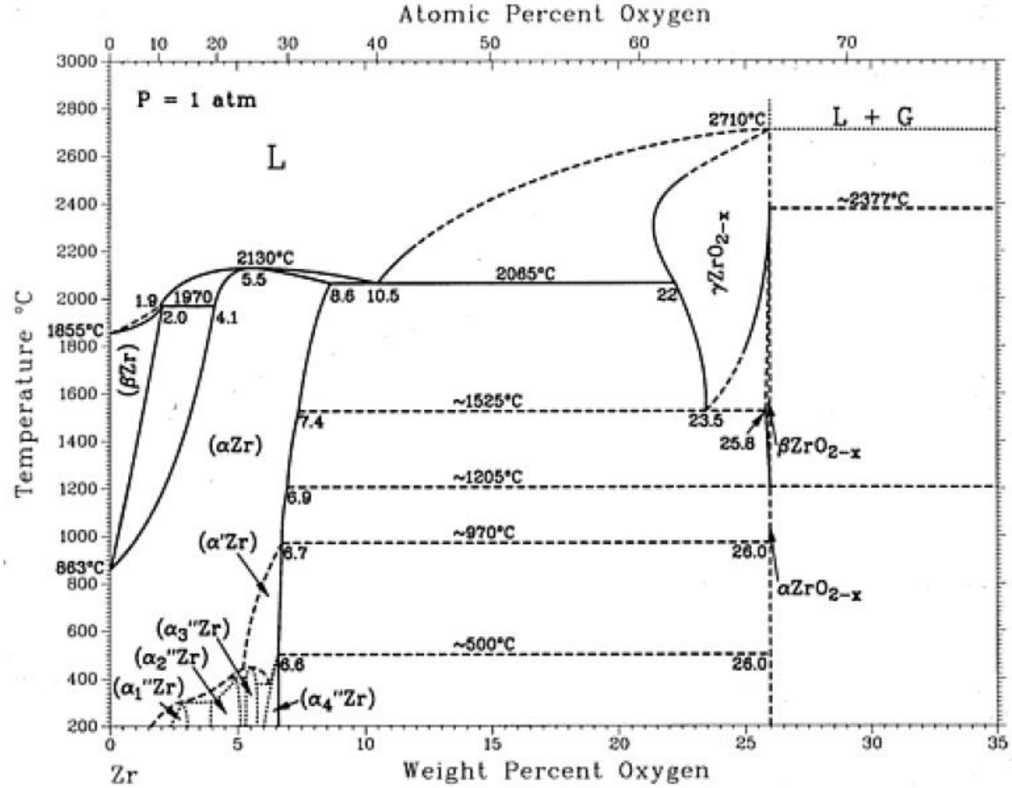

Figure 2-3: Zr-O phase diagram according to [22]: The α-Zr phases have a hexagonal structure, whereas in α 'and α'' the oxygen is partially or completely ordered. The β-Zr phase has a cubic-body-centered structure in which oxygen is also dissolved.

Table 2-2 summarizes selected structural, physical, and mechanical properties for the three modifications of ZrO_2. For illustration, Figure 2-4 shows the unit cells of these three structures of ZrO_2. Fig. 2-4 a) shows the monoclinic, Fig. 2-4 b) the tetragonal, and Fig. 2-4 c) the cubic ZrO_2 structure. The Zr 4 + ions (light yellow spheres) form the sublattice in which the O_2 ions (blue spheres) can occupy the tetrahedral interstitial positions. Monoclinic zirconia consists of a sevenfold coordinated Zr4+ cation, such that the oxygen ions with O_{11} coordination are almost tetrahedral, but with one angle in the structure differing significantly from the tetrahedral value (Figure 2-4-a). Tetragonal zirconia contains the eightfold-coordinated Zr4+ cation with four oxygen ions placed at a distance of 2.065 Å in the form of a flattened tetrahedron, and four at 2.455 Å in an elongated tetrahedron rotated through 90 ° (Figure 2-4-b). The high temperature cubic polymorph has a face-centered CaF_2 structure with an eightfold coordinated Zr4+ atom with oxygen ions arranged in two equal tetrahedra (Figure 2-4-c).

Table 2-2: Selected structural, physical and mechanical properties of the three allotropes of ZrO_2.

Properties	**m-ZrO_2**	**t-ZrO_2**	**c-ZrO_2**
Space group	$P2_1/a$	$P4_2/nmc$	$Fm\bar{3}m$

Lattice parameters	a = 5.1505 Å;
	b = 5.2031 Å;
	c = 5.3154 Å
	β = 99.194° at room temp.[56]
		a = 0,364 nm
		b = 0,527 nm
			a = 5.07 Å [10]

Volume of the unit cell in nm^3	0,141	0,070	0,132
Density in g/cm3	5.56[10]	-	6.27[10]
Hardness in GPa	11.76[56]	10-11[56] (Partially stabilized)	10-15[56] (Fully Stabilized)
Tensile Strength (psi)[24]	$17.9–20 \times 10^3$	-	21×10^6 (MgO stabilized)
Young's modulus in GPa	185[10]	204[56]	206.84[56]
Poisson's ratio	0.32-0.34[56]	0.23[56]	0.23-0.32[56]

---

[24] Tensile strength at room temperature

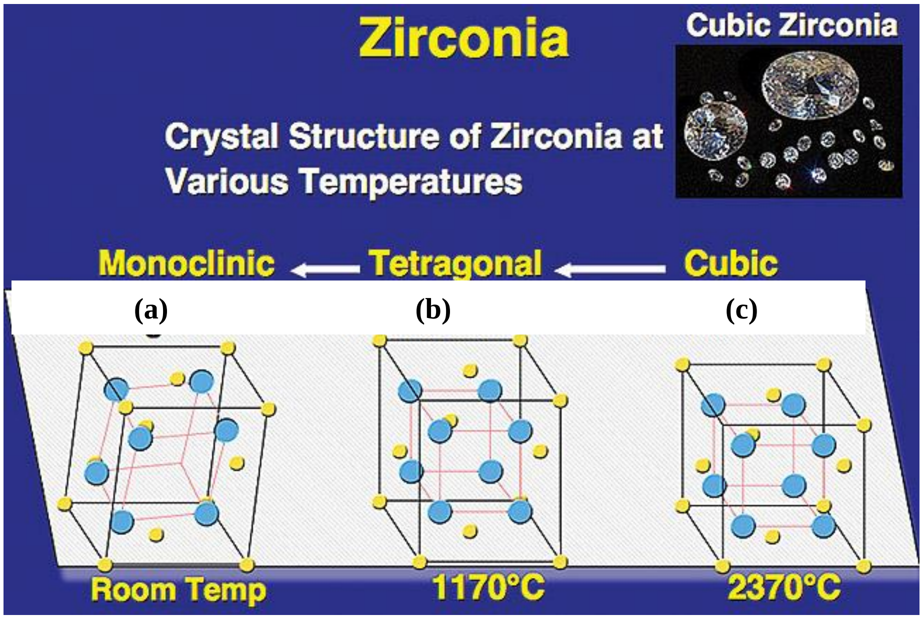

Figure 2-4: Crystal structures of the three modifications of ZrO_2 according to [57]: a) Monoclinic, b) tetragonal and c) cubic crystal structure. The structure is formed by Zr^{4+} ions (yellow) with O^{-2} ions (blue) occupying the tetrahedral positions.

Raman active modes of ZrO_2 polymorphs have been predicted by factor-group analysis. According to this analysis, all the optical modes of the three modifications of ZrO_2 are presented as follows:

- Monoclinic ZrO_2 : $\Gamma_{opt} = 9A_g + 9B_g + 8A_u + 7B_u$, of which just ($9A_g + 9B_g$) i.e. 18 modes are Raman active [58–60].
- Tetragonal ZrO_2: $\Gamma_{opt} = 1A_{1g} + 2B_{1g} + 3E_g + 2A_{2u} + 2E_u$, of which just 6 modes ($1A_{1g} + 2B_{1g} + 3E_g$) are Raman active [58–61].
- Cubic ZrO_2: $\Gamma_{opt} = T_{2g} + T_{1u}$, of which only T_{2g} mode (i.e. 1 mode) is Raman active [58–60].

Metastable high temperature tetragonal and cubic ZrO_2 phases are able to be stabilized at room temperature if they are dopped with Y_2O_3 or CaO. In this case, these phases show additional peaks in the Raman spectrum.

The corresponding Raman wavenumbers of these three ZrO_2 polymorphs are listed in Table 2-3.

Table 2-3: Raman shifts for the three ZrO_2 allotropes (monoclinic, tetragonal and cubic).

Monoclinic ZrO2	**Metastable Tetragonal ZrO_2**	**Metastable Cubic ZrO_2**
Raman Shifts[25] (cm^{-1})	Raman Shifts (cm^{-1})	Raman Shifts (cm^{-1})
37[58]	148[58,61–63]	490[62]
103[58,62]	263[58,61–63]	
158[63]	315[61,63]	
180[58,62,63]	456[61,63]	
192[58,62,63]	607[61,63]	
224[58,62,63]	640[61–63]	
308[58,62,63]		
335[58,62,63]		
349[58,62,63]		
383[58,62,63]		
476[58,62,63]		
503[58,62,63]		
539[58,62,63]		
561[58,62,63]		
617[58,62,63]		
638[58,62,63]		
755[58]		

The transformation from tetragonal to monoclinic ZrO_2 is associated with 3-5% volume increase which has major technological importance. This semi-thermoelastic transformation with high volume increase has been used in enhancing the mechanical properties of ceramics such as Zirconia-Toughened Alumina (ZTA). For this application, the phase transformation can be induced by the stress field at the tip of the propagating crack. The opening of the crack will be hindered by the volume change and shear stress associated with the transformation which results in increasing the resistance of ceramics to crack propagation, thus toughness [54]. However, this

---

[25] Raman shifts with ±5 cm^{-1} error.

stress-induced transformation is related to the size of zirconia particles, where at less than a critical size they will not transform and at larger than the critical size they will transform spontaneously. There is also another toughening mechanism which uses the spontaneous transformation of overcritical zirconia particles known as "microcracking" leads to a branching of the crack. These branched cracks have a higher surface area, which requires more energy as the crack propagates. Therefore, the fracture resistance is increased by the deviation of a propagating crack into the transformed particles.

To be able to use these toughening mechanisms technically, the tetragonal phase must remain stable even under standard conditions. Two methods are mainly used: alloying with a rare earth oxide or the stabilization of the tetragonal phase within a ceramic matrix. In the former case, the stabilization of the tetragonal phase by solid solution formation can be carried out by ions with different valences, provided that the ionic radius is within 40% of the ionic radius of $Zr4^+$. Nevertheless, the exact mechanism of stabilization by solid solution mechanism has not been understood yet, however, researchers suggested that alloying increases the ionic character of bonding resulted in stabilizing the tetragonal/cubic structures at room temperature.
The tetragonal phase can also be stabilized in a ceramic matrix under standard conditions. In this case, the grains of the tetragonal phase can be held under tension by the matrix with a high elastic modulus, so that the conversion to the monoclinic phase is hindered. The matrix usually has a lower thermal expansion coefficient than the tetragonal phase. In this mechanism, there is a critical grain size for stabilized tetragonal phase over which a spontaneous transformation to the monoclinic phase occurs.

Depending on the structure, ZrO_2-containing ceramics can be divided into three categories namely, fully stabilized zirconia (FSZ, fully stabilized cubic phase), partially stabilized Zirconia (PSZ, tetragonal phase dispersed in a cubic/monoclinic matrix) and Tetragonal Zirconia Polycrystals (TZP, fully stabilized tetragonal phase). In addition, there are Dispersed Zirconia Ceramics (DZC), such as the zirconia-reinforced alumina ceramic (ZTA) which already mentioned above. These systems differ mainly in the volume fraction of the tetragonal phase (e.g., 0% in FSZ and 100% in TZP) and the way it is distributed. Further information, such as the amount and type of foreign atoms used to stabilize the tetragonal phase (but also the cubic phase) under standard conditions and commercial applications can be found in various literature. In the field of surface engineering, there are a variety of applications for ZrO_2-based coatings. They have been used as thermal barrier coatings due to their high thermal shock resistance and low thermal conductivity or in optics because of their high refractive index and low absorption in a wide spectral range. Zirconia-based coatings have also been employed in biomedical applications due to their excellent biocompatibility and resistance to crack propagation which solves the problem of brittle alumina coatings. The good chemical resistance of ZrO_2 also allows its applications as corrosion protection coatings against moisture and oxidation [54]. An overview of ZrO_2 coatings deposited using different PVD techniques can be found in Table 2-4. In the next paragraphs a summary of important literature on ZrO_2 PVD coating will be presented.

Table 2-4: Overview of ZrO_2 coatings deposited by PVD methods.

Technique	**Target**	**Gases**	**Deposition Parameters**	**Substrate**	**Substrate Temperature (°C)**	**Charact. Meth.**	**Coating**	**Year**	**Ref.**
DCMS	Zr	Ar, O_2	P’: 400-450W P_{O2}:3×10^{-5} Torr P: 3×10^{-2} Torr	Fused quartz	25-450	XRD, Transmittance, Refractive Index	m-, t-ZrO_2	1992	[64]
RF-MS	Zr	Ar, O_2	P: 5×10^{-3} mbar P’: 1000 W O_2: 1-30 %	Glass	25	XRD, SEM, EDS, Optical Constants	m-, t-ZrO_2	2000	[65]
RF-MS	Zr	Ar, O_2	P’: 600-1000 W P: 5×10^{-3} mbar O_2: 5 % Spacing: 60-100 mm	Glass	25	XRD, SEM, Optical Constants	m-, t-ZrO_2	2000	[66]
RF-MS	Zr	Ar, O_2	P: 1×10^{-3}-1×10^{-2} mbar P’: 1000 W O_2: 5 %	Glass	25	XRD, SEM, EDS,	m-, t-ZrO_2	2001	[67]

RF-MS	ZrO_2	Ar	P: 0.5 Pa P’: 100 W O_2: 20 % Bias: 0-300 V	Si (100) Wafer	550	FT-IR, XRD, AFM, HRTEM, Transmittance	Orthor-ZrO_2	2005	[68]
RF-MS	Zr	Ar, O_2	P: 3.2 Pa O_2: 7-100 % P’: Unknown	Si (100) Wafer	Not heated	HRTEM, AFM, dielectric characteristics	m-, t-ZrO_2	2007	[69]
RF-MS	Zr	Ar, O_2	P: 500 mTorr P’: 200-480 W O_2: 2.5-10 %	Si Wafer	300	SEM, XRD	m-ZrO_2	2007	[70]
RF-MS	Zr	Ar, O_2	P: 1.5 Pa P’: 180 W Bias: 0-150 V Ar: unknown O_2: unknown	Si (100) Wafer, Glass, Fused quartz	25-300	XRD, Optical Constants	m-, t-ZrO_2	2008	[71]
RF-MS	ZrO_2	Ar, O_2	P: 1.5 Pa P’: 100 W Ar: 30 Sccm O_2: 1-10 Sccm	Si	Not heated, HT: 500, 700	XRD, AFM, Electrical properties	m-, t-ZrO_2	2008	[72]
RF-MS	Zr	Ar, O_2	P: 0.5 Pa V: 100 V Ar: 20 Sccm O_2: 8.6 Sccm	Si (100) Wafer, Glass	270	XRD, Raman Spectroscopy, XPS, Optical Properties, Stress	m-, t-ZrO_2	2008	[73]

GFS[26]	Zr	Ar, O_2	P: 25 Pa P’: 50-800 W Ar: 200 Sccm O_2: 0.003-1 Sccm	Unknown	280-350	XRD, SEM, Hardness	m-, t-ZrO$_2$	2009	[74]
RF-MS	Zr	Ar, O_2	P: 3.2 Pa P’: Unknown Ar: 40 Sccm O_2: 10 Sccm	Si Wafer, Glass	28-550	HRTEM, AFM, Refractive Index	m-, t-ZrO$_2$	2009	[75]
DCMS	Zr	Ar, O_2	P: 0.4 Pa P_{O2}: 0.04 Pa P’: 140 W	Si, Quartz	Not heated, HT: 600, 800	XRD, FTIR, Electrical properties	Orthor-, m-ZrO$_2$	2012	[76]
DCMS	Zr	Ar, O_2	P: 0.4 Pa P_{O2}: 0.008-0.0 Pa P’: 140 W	Si, Quartz	Not heated	XRD, Optical transmittance	m-ZrO$_2$	2013	[77]
HiPIMS[27]	Zr	Ar, O_2	P: 2 Pa P’: 5-103 Wm^{-2} Ar: 30 Sccm	Si	Not heated	Hardness, Optical properties	m-ZrO$_2$	2013	[78]

Suhail et al. [64] obtained ZrO$_2$ coatings on fused quartz substrates by means of d.c. reactive magnetron sputtering from a metallic Zr target at a different substrate temperature (25-450 °C) in constant deposition pressure (3×10^{-2} Torr), Oxygen partial pressure (3×10^{-5} Torr), and target power (450W). According to authors, a low substrate temperature ($T \leq 150$ °C) created a single-phase coating with a monoclinic structure, whereas increasing the temperature enhanced nucleation of tetragonal phase so that at a temperature above 250°C the intensity of XRD peaks for monoclinic phase decreased and crystalline peaks for tetragonal phase were observed. The substrate temperature also affected the packing density of coatings (ratio of the density of coating to the density of bulk material) and it increased from 0.686 to 0.813 on heating to 450°C.

Gao et al. [65–67] in three different researches investigated the effect of power densities (1.9 W/cm^2 to 3.18 W /cm^2), oxygen concentration (1 to 30%), total gas pressures (0.1 to 1 Pa), and target-substrate distance (60-100 mm) on ZrO$_2$ coatings obtained by RF magnetron sputtering from

---

[26] Gas Flow Sputtering

[27] High Power Impulse Sputtering

a Zr target. According to the authors, a minimum of 2% oxygen concentration in sputtering gas is required to obtain fully oxidized coatings. At higher oxygen concentrations, coatings were composed of dominant monoclinic ZrO_2 phase with a small fraction of the tetragonal phase regardless of oxygen concentration. Nevertheless, increasing the oxygen concentration changed the crystalline orientation of grains from preferred orientation along (200) plane at oxygen concentrations lower than 5% to randomly orientation at higher oxygen concentrations. Increasing the oxygen concentration influenced the quality of coatings as well, so that coatings showed a loosely packed structure with high roughness at high oxygen concentrations. Increasing the deposition pressure like oxygen concentration decreased the density of ZrO_2 coatings with a subtle effect on the phase composition of coatings. The coatings were composed of dominant monoclinic phase with a small fraction of the tetragonal phase. However, high-pressure conditions were more suitable for tetragonal phase nucleation as the XRD peak intensity of the tetragonal phase increased by increasing the deposition pressure. On the other hand, the target power density and target-substrate distance had no effect on crystalline orientation and phase composition of ZrO_2 coatings as grains had a random orientation with a structure composed of dominant monoclinic phase and a small fraction of tetragonal phase. Nevertheless, the target power density and target-substrate distance had some effect on the quality of coatings like roughness and residual stress. The residual stress and roughness of the coatings increased as the substrate-target distance increased.

Huang et al. [68] deposited ZrO_2 coatings onto Si (100) wafer substrates by RF magnetron sputtering from a ZrO_2 target (diameter 50 mm) in Ar atmosphere at a constant substrate temperature (550 °C). They investigated the effect of substrate bias (-300-0 V) on microstructure and interfacial properties between film and Si substrate in their research. According to the authors, all the coatings had an orthorhombic crystal structure regardless of substrate bias. However, the crystallinity of coatings was improved, and grains were highly oriented along (111) plane direction at high substrate bias. Moreover, applying substrate bias suppressed the growth of SiO_x and $ZrSiO_x$ interfacial layers, but at the expense of diminishing of the coating's growth rate.

Ma et al. [69] prepared ZrO_2 coatings by means of RF magnetron sputtering (Zr-Target) with a variation of oxygen partial pressure from 7 to 100% on Si wafer substrates with no intentional substrate heating. Their results indicated that microstructure of coatings is influenced significantly by oxygen partial pressure so that amorphous coatings are produced at oxygen partial pressure lower than 15%, while oxygen partial pressure above 73% induced transformation of a mixture of monoclinic and tetragonal phases microstructure to a single monoclinic structure. According to the authors, this transformation was attributed to a decrease in the oxygen vacancy concentration in the film and an increase in the energetically neutral particles in the plasma caused by increased oxygen partial pressure. The $SiOx$ interfacial layer was also observed for coatings prepared above 51% oxygen partial pressure and increasing the oxygen partial pressure culminated to coatings with high roughness.

Zhao et al.[73] evaluated the effect of coating's thickness on structural properties of RF-magnetron sputtered ZrO_2 coatings. For this purpose, coatings with a thickness in the range of 17-559 nm were deposited on Si wafer and glass substrates at 270 °C. The authors concluded that monoclinic ZrO_2 preferentially grew in the initial stage, whereas the tetragonal ZrO_2 phase starts to appear for coatings thicker than 125 nm and its fraction increased steadily with the increase of coating thickness. According to authors, stabilization of the tetragonal phase in thicker coatings can be attributed to incremental substrate temperature during the deposition and the oxygen deficiency with the film thickness.

Other methods including; Electron beam evaporation [79], pulsed laser ablation[80], pulsed cathodic arc evaporation or high-power impulse sputtering [78,81] have also been used by various researchers for depositing ZrO_2 coatings which their observations are not discussed here.

Up until now, deposition of pure ZrO_2 coatings was described. However, the stabilization of the tetragonal and cubic ZrO_2 phase in coatings is mainly influenced by the addition of e.g. Y_2O_3 [82–86], CeO_2[87], Fe[88], Gd_2O_3 [89] or Al_2O_3 [90–97]. In the bulk material, e.g. Y-TZP a Y_2O_3 content of 7 wt.-% - 8 wt.-% is required [45], whereas a comparable proportion in coatings, depending on the process parameters, results in a phase mixture of monoclinic and cubic phase[86] or a phase mixture of tetragonal phase and a low fraction of the monoclinic phase [84,98].

Boulouz et al. [86] deposited ZrO_2-based coatings using RF high-performance cathode sputtering in an Ar/O_2 atmosphere (O_2 content: 10%) with four different targets (5.1 cm in diameter): a pure Zr target and ZrO_2 targets with a Y_2O_3 content of 8 wt.-%, 15 wt.-%, and 20 wt.-%. The power was constant at 75W and the total gas pressure at 0.2 Pa. The substrate used was polished Pyrex and the substrate temperature varied between room temperature and 600 °C. The coatings deposited by the Zr target show a monoclinic phase with $(\bar{1}11)$ orientation independent of the substrate temperature (max 400 ° C). The coatings deposited from the target with 8 wt.-% Y_2O_3 showed a mixture of monoclinic and cubic phase and a grain size of 19.8 nm. The coatings become single-phase cubic when the proportion of Y_2O_3 in the target is 15% by weight or higher (this is within the stated range of about 13% by weight and higher in Ruh et al. [99]).

Ruddell et al. [100] investigated the effect of oxygen content variation in the working gas (0% to 10%) and the substrate temperature (20 °C to 600 °C) on Y_2O_3 -doped Zr coatings deposited by a high-performance cathode sputtering method. A ZrO_2 target doped with 3 mol% Y_2O_3 and 7.63 cm diameter was used with a constant power 350 W. The substrates used were Si wafers and Al_2O_3 bars. In a non-reactive deposition, depending on the substrate temperature, coatings with an O/Zr ratio of 1.80 to 1.87 are formed. The authors attribute the lower oxygen content in the coatings to recombination of atomic oxygen in the plasma. In these coatings, a phase mixture of monoclinic and tetragonal phase is formed. The tetragonal phase has a volume fraction of over 80%. The authors suggest that the formation of the tetragonal phase is thermodynamically favored due to the higher number of lattice defects in the stoichiometric coatings. At an oxygen content of 5-10% and a substrate temperature of up to 310 °C, the monoclinic phase fraction increases significantly to 53%- 67%. The O/Zr ratio was between 2.09 to 2.14. At a substrate temperature of 600 °C, the O/Zr ratio drops to 1.96-2.01, and the monoclinic phase ratio drops to 28% -36%.

Ji et al. [84] deposited ZrO_2-Y_2O_3 coatings by two Zr targets in DC mode (P = 600 W, diameter 7.6 cm) and a Y target in RF mode (P = 100 W or 300 W, diameter 7.6 cm) in Ar/O_2 atmosphere (O/Ar = 1.6, p = 1.33 Pa). The coatings contained either 2 mol% Y_2O_3 or 4.5 mol% Y_2O_3 due to the different performance on the Y target. The coatings with a 2 mol% Y_2O_3 concentration have a tetragonal phase with strong (111) orientation and a low monoclinic phase fraction. By applying a substrate bias of -400 V, a single-phase coating with a tetragonal structure is deposited. At a 4.5 mol% Y_2O_3 concentration, only the cubic phase is deposited. An amorphous phase is also deposited in addition to the cubic phase due to a substrate bias of -400 V.

Trinh et al. [94] have deposited Al-Zr-O coatings on Si wafers using RF high-performance cathode sputtering and an Al and a Zr target (diameter 5 cm). The power density was between 1 W/cm^2 and 5 W/cm^2 and the substrate temperature at 450 °C and 750 °C. The Ar partial pressure was kept constant at 0.27 GPa while the partial pressure of oxygen was 0.027 Pa or 0.054 Pa. At a substrate temperature of 450 °C and an oxygen partial pressure of 0.027 Pa, a two-phase ZrO_2 coating is formed, which is dominated by the $(\bar{1}11)$ monoclinic phase and a cubic phase fraction. In a pure

Al_2O_3 coatings, the γ phase is formed. At a Zr content of 10 at. %, The coatings were amorphous. Due to a higher substrate temperature of 750 °C and a higher oxygen partial pressure of 0.054 Pa, the cubic phase was stabilized at 27 at. % Zr and the lattice parameter drops to 0.506 nm.

Gilmore et al. [95,96] have deposited Al-Zr-O coatings on Al_2O_3 single crystals and quartz by high-performance cathode sputtering of Al / Zr targets. The targets consist of an Al target on which Zr discs were attached, and vice versa. In order to influence the composition of the coatings, the size of the slices was varied. The total gas pressure was 0.4 Pa. After depositions, all coatings were amorphous. Only at a post heat treatment temperature of 1000 ° C in the air, the coatings were crystallized. The zirconia coating had a monoclinic phase, and alumina coatings were amorphous. At high Al contents (Zr / Al = 52/48) in the ZrO_2 coatings, the tetragonal phase was formed, while at low Al contents (Zr / Al = 76/24) a monoclinic phase was formed. A mixture of monoclinic and tetragonal phase was not observed. Further work by Qadri et al.[101,102] showed that the crystallization of Al-rich coatings requires 48h -72h, while the crystallization of the Zr-rich layers requires only 2h- 6h. The coating thickness was 1 μm to 2 μm, and XRD analysis was used as evidence for the crystallization. As the Al content in target increases above 30%, the Al_2O_3 matrix compresses the volume of the monoclinic ZrO_2-based phase, which approaches the volume of t-ZrO_2 so that the t-phase is formed. For a Zr/Al ratio of 68/32, a c-ZrO_2 phase is formed first, and only after long-term heat post-treatment, the t-ZrO_2 phase is formed.

Musil et al. [97] deposited Al-Zr-O layers from an Al/Zr target by pulsed RF high-performance cathode sputtering. Two different targets were used, consisting of an Al plate (diameter 5 cm) fixed with a Zr ring (inner diameter 2.4 cm and 2 cm). The substrate temperature was kept constant at 500 °C and the total gas pressure was kept constant at 1 Pa. They showed that if the oxygen partial pressure is $P_{O2} \leq 0.01$ Pa, the target is in metallic mode and, according to the authors, a biphasic coating consisting of nanocrystalline Zr and amorphous Al_2O_3 is formed. In the "poisoned" mode ($P_{O2} \geq 0.1$ Pa), Al-Zr-O coatings are formed, which consist of a nanocrystalline t-ZrO_2 phase and an amorphous Al_2O_3 phase. The literature on ZrO_2-based PVD coatings shows that the metastable ZrO_2-based phases can be stabilized either by a substoichiometric oxygen lattice, a small grain size or by the addition of foreign atoms.

2.1.3 Materials in The Ternary Chromium-Zirconium-Oxygen System

Both powder and compact materials in the Cr-Zr-O system are known, which have been investigated for catalytic [103–107], magnetic[108,109] and gas sensor[110] applications. In contrast, limited research exists on coatings in Cr-Zr-O system at the time of writing of this dissertation. A number of recent publications focus on the stabilization and characterization of metastable ZrO_2 particles by the substitution of Zr^{4+} with Cr^{3+} and Cr^{4+} [111–115], respectively.

Figure 2-5, illustrates the quasi-binary phase diagram of ZrO_2-Cr_2O_3 (according to Jerebtsov et al. [116]). According to the authors, both oxides have limited mutual solubility. A r-Cr_2O_3-based solid solution with at least 60% by mass of r-Cr_2O_3 is formed, while the solubility of r-Cr_2O_3 in ZrO_2 is significantly lower. The monoclinic and tetragonal phase of ZrO_2 can dissolve up to 9% by mass of r-Cr_2O_3 and the cubic ZrO_2 phase up to 25% by mass of r-Cr_2O_3. At a temperature of 1950 °C between 25 mass% and 60 mass% r-Cr_2O_3 a two-phase area of solid solutions based on cubic ZrO_2 (with the content of r-Cr_2O_3 of 25 mass%) and r-Cr_2O_3 (with a r-Cr_2O_3 content of 60% by mass) is formed. Below a temperature of 1840 °C between 9% by mass and 60% by mass of r-Cr_2O_3 a two-phase area of solid solutions based on tetragonal ZrO_2 (containing 9% by mass of r-Cr_2O_3) and r-Cr_2O_3 (with a r-Cr_2O_3 content of 60% by mass) is formed. These two transformation temperatures also mean that the stability of the tetragonal and cubic modification of ZrO_2 by solid solution formation can be significantly reduced compared to pure ZrO_2. Below a temperature of 1115°C, the tetragonal phase completely converts to the monoclinic phase, wherein the compositions of the solid solutions are retained. In addition to the single-phase areas, there are also two-phase mixtures based on ZrO_2. The tetragonal and cubic two-phase region consists of a temperature range of 1840 °C and about 2350 °C with a maximum solubility of 25 mass% r-Cr_2O_3. The two-phase region of monoclinic and tetragonal phase exists only in a narrow temperature range (<100 °C) and concentration range 0 mass% to 9 mass% r-Cr_2O_3. Like the binary Zr-O phase diagram, there is also a transformation hysteresis in the quasi-binary ZrO_2-Cr_2O_3 from the tetragonal to the monoclinic phase. The phase transformation in the saturated solid crystal of monoclinic to tetragonal phase takes place at 1115 ° C, however, the reverse transformation at 945 °C instead.

The following section deals with the phase formation of compact and powder materials in the Cr-Zr-O system. First, the results on materials based on ZrO_2 will be presented, followed by research on Cr_2O_3 basis. Ruh and Garrett [117] have investigated the solubility of Cr in a ZrO_2 phase from fired compact material. All samples had a monoclinic ZrO_2 phase structure. According to the authors, metallic Cr could not stabilize high-temperature phases of ZrO_2. The results showed that the maximum solubility of Cr in the ZrO_2 is about 1 at. %, a higher Cr content leads to the formation of a second metallic Cr phase.

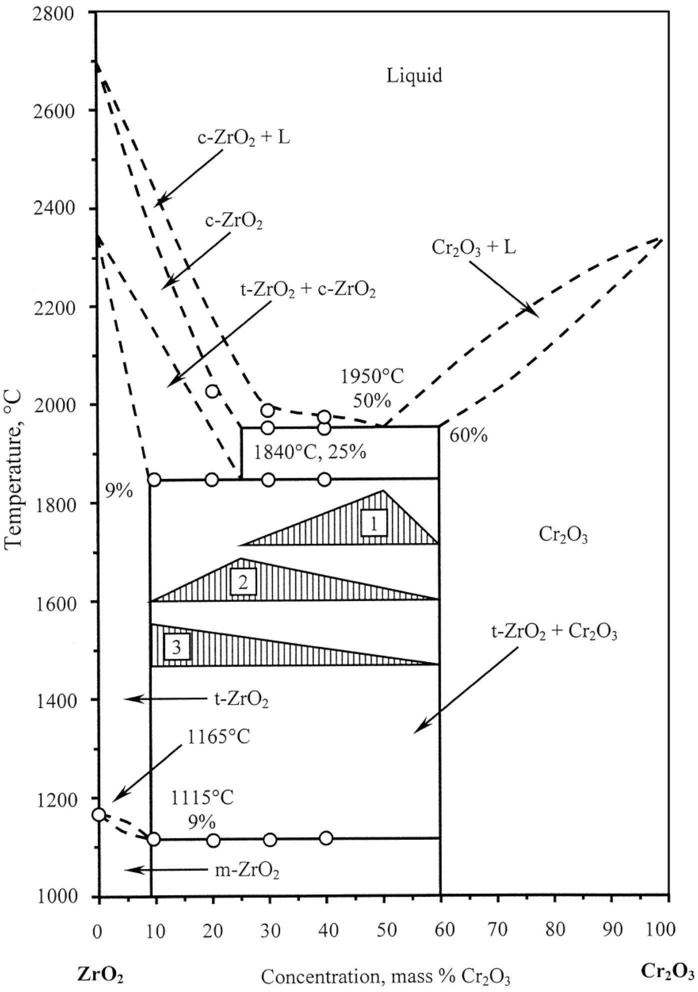

Figure 2-5: Quasi-binary section ZrO_2-Cr_2O_3 phase diagram according to Jerebtsov et al. [116] from 1000 °C to 2700 °C. There are four crystalline phases: m-ZrO_2, t-ZrO_2, c-ZrO_2, and r-Cr_2O_3.

In comparison to the quasi-binary section of ZrO_2-Cr_2O_3 diagram by Jerebtsov et al. [116], Ruh and Garrett showed that the maximum solubility of Cr in ZrO_2 is much lower (compared to a maximum solubility estimate of about 9 mol% Cr_2O_3). Furthermore, instead of a two-phase mixture of ZrO_2 and Cr_2O_3-based microstructure or a single-phase r-Cr_2O_3-based microstructure at higher Cr levels, the microstructure was composed of a monoclinic ZrO_2 phase and a pure Cr phase. In addition to the phases and the solubility limits, the mechanical properties were also investigated in Ruh and Garrett work. The pure m-ZrO_2 had, according to the authors, a microhardness of 505 HV, which is significantly below the literature value of 11.5 GPa [56]. As a result of the formation of a solid solution, the hardness increases to 840 HV and drops to 817 HV for samples with higher Cr contents.

Collins and Ferguson [115] have determined the lattice parameters variation of monoclinic ZrO_2-based structure powder materials as a function of the mole content of additive oxides, e.g. Cr_2O_3. Due to the formation of solid solutions, according to the authors, the volume of the monoclinic unit cell decreases from 0.1415 nm^3 (m-ZrO_2) to 0.1405 nm^3, depending on the composition. If this volume is fallen below 0.1405 nm^3, a two-phase mixture is formed whose phases are based on the monoclinic and tetragonal ZrO_2 structure. The different oxides showed different solubilities in the monoclinic phase. The r-Cr_2O_3 had the highest solubility (with 30 mol% solubility) into monoclinic ZrO_2 among the investigated oxides despite the highest difference in the ionic radius between Cr^{3+} and Zr^{4+}. According to the authors, this can be attributed to the different oxidation states of Cr^{3+} and Zr^{4+}, since the valence of the cation controls the number of oxygen vacancies in the anion lattice and is thus an important factor in solid solution formation in addition to the ionic radius. The high solubility of 30 mol% r-Cr_2O_3 (approximately 35% by mass) into m-ZrO_2 as well as observation of the tetragonal and monoclinic two-phase region with a higher r-Cr_2O_3 content is in contrast to the Jerebtsov et al. [116] phase diagram (described above).

Wu et al. [118] have produced compact material in Cr_2O_3-ZrO_2 system by annealing of powders composed of different Cr and Zr contents. The annealing treatments on the pure ZrO_2 samples at a temperature of 600 °C resulted in the tetragonal phase and a small proportion of monoclinic phase. Samples with a Cr content of 10% of the total metal portion (Cr / (Cr + Zr)), showed only the tetragonal ZrO_2 phase in the microstructure after annealing at 600°C. With a Cr content of 20%, a cubic ZrO_2-based structure in which the Cr is dissolved is formed in the sample. An annealing temperature of above 700 °C on ZrO_2 samples containing up to 20% Cr led to the formation of r-Cr_2O_3 and the conversion of the cubic ZrO_2 phase into the monoclinic phase. Authors showed that depending on the powder production method, however, even at 600 °C, a two-phase mixture of r-Cr_2O_3 and tetragonal ZrO_2 can be achieved without any evidence of solid solution formation between chromium and zirconium oxides.

Ray et al. [111] and Ram [112] have investigated the thermal, structural, and optical properties of ZrO_2 nanoparticles produced by amorphous polymeric precursors. Due to the manufacturing process, according to the authors, the particles contained both Cr^{3+} and Cr^{4+} ions; the total concentration of Cr ions was varied between 0 at. % and 30 at.%. At low Cr contents of up to 4 at. %, almost exclusively phase mixtures of cubic, tetragonal or monoclinic ZrO_2-based structures were observed, with the cubic phase had the largest share. At a Cr content of up to 10 at. %, particles with single-phase cubic structure were obtained. At high calcination temperatures from 900 ° C and over, a monoclinic phase with an increasing volume fraction and a r-Cr_2O_3 phase were observed. For particles with a higher Cr content of up to 30 at. %, the r-Cr_2O_3 phase is formed at much lower temperatures below 600 °C. Particles calcined at the highest temperature of 1050 °C were composed exclusively of mixed structures based on monoclinic ZrO_2 and r-Cr_2O_3.

Stefanic et al. [114] have produced sintered compact material in the pseudobinary ZrO_2-Cr_2O_3 system to investigate the influence of the r-Cr_2O_3 content on the stability of t-ZrO_2. The pure ZrO_2 was only composed of the monoclinic phase. The addition of up to 20 mol% of r-Cr_2O_3 into ZrO_2 produced a phase mixture of m- and t-ZrO_2 as well as r-Cr_2O_3. At a concentration of 50 mol% to 95 mol%, the samples were predominantly composed of r-Cr_2O_3 with portions of the monoclinic and tetragonal phases. The mutual solubility of r-Cr_2O_3 in ZrO_2 and vice versa was negligible according to the authors. They exclude the lower cation radius of Cr^{3+}compared to Zr^{4+} as a possible cause (in comparison with corresponding isostructural systems) and cite poor sinterability as a possible cause for the negligible solubility. The stabilization of the tetragonal phase at room temperature did not occur according to the authors via solid solution formation, but they observed the occupancy of surface sites of these particles with r-Cr_2O_3. In a subsequent work by Stefanic et al [119], the phase formation of amorphous precursors was investigated as a function of the calcination temperature. The amorphous precursors crystallized from a temperature of 435 °C when no Cr was contained in the sample. By adding Cr^{3+} ions up to 50 mol%, the crystallization temperature raised up to 822 °C. In contrast to the previous work of the authors, this method of production produces tetragonal and single-phase solid solutions depending on the calcination temperature and the Cr concentration, in which up to 26 mol% of Cr^{3+} can be dissolved. The O/Zr ratio drops to 1.87 by adding Cr^{3+} ions. The calculated lattice parameters decrease in comparison with t-ZrO_2 so that the volume of the unit cell decreases from 0.067 nm^3 to 0.065 nm^3. The cubic phase also was not observed.

The publications described so far mainly dealt with ZrO_2-based materials. Takano et al. [120] studied the r-Cr_2O_3-rich region of a Cr_2O_3 / ZrO_2 (2.5Y) compact ceramics. The calcined starting powder (1 h at 1000 ° C) consisted of r-Cr_2O_3 particles surrounded by fine t-ZrO_2 particles, with the volume fraction of the tetragonal phase to the monoclinic phase being 94/6 (determined by XRD). The authors attribute the high proportion of the tetragonal phase to the small particle size of these particles, which is below the critical particle size for the phase transformation from tetragonal to monoclinic. By adding up to 50 mol% ZrO_2 (2.5 Y) to r-Cr_2O_3, the sintered ceramic hardness dropped from 23 GPa for r-Cr_2O_3 to less than 19 GPa, with the hardness values following the linear mixing rule, according to the authors.

Chekhomova [121], investigated the abrasive properties of ZrO_2-modified r-Cr_2O_3 powders. A comparison of the determined lattice parameters with those of r-Cr_2O_3 (the lattice parameters were larger) suggested the substitution of Cr^{3+} by larger Zr^{4+} ions. This led to lattice defects and an increase in the volume of the unit cell due to the different charge states and ionic radii. He concluded that the ZrO_2 phases, which are metastable at room temperature, can be stabilized as a solid solution by the substitution of Zr ions with Cr ions. The observed solubilities of Cr in the tetragonal and cubic phases were 26 mol% and 10 at. %, respectively.

Recently, Spitz et.al. and Landälv et.al. [25,122], deposited Cr-Zr-O coatings by magnetron sputtering technique at 500 °C and investigated the microstructure evolution of the deposited films by changing the chemical composition and subsequent annealing treatments. They illustrated that the host structure of hexagonal $(Cr, Zr)_2O_3$ can accommodate up to 12 at. % of zirconium and the maximum hardness reported for their coatings was 19 GPa which was still well below the bulk Cr_2O_3. As mentioned earlier only limited research on coatings in Cr-Zr-O system are yet available which clearly shows the oxide coatings in this ternary system still need to be investigated with the hope to obtain coatings with interesting properties for technical applications.

2.2 Summary of literature review

The literature was reviewed for the binary material systems Cr-O, Zr-O, and the ternary material systems Cr-Zr-O. The focus was on literature results on coatings deposited by a PVD process, in particular, RF-magnetron sputtering. According to the literature, in order to obtain the Cr_2O_3 phase in crystalline form, a substrate temperature of at least 230 °C is required. The Cr_2O_3-ZrO_2 phase diagram shows a limited solubility on both sides. Both the ZrO_2 phases and the Cr_2O_3 phase are present as solid solution phases. There are also two-phase regions of the Cr_2O_3 phase and the respective ZrO_2 phase (depending on the temperature). The incorporation of Zr into Cr_2O_3 phase occurs as Zr^{4+}, with the Zr^{4+} ions presumably substituted for Cr^{3+} ions. The larger ion radius of Zr^{4+} also leads to an increase in the volume of the unit cell. By incorporation of Cr^{3+} ions, the high-temperature phases of ZrO_2 (tetragonal and cubic) can be stabilized at room temperature. At low Cr contents, the monoclinic phase is probably formed, while at high Cr contents the cubic phase is formed. However, the literature showed that the synthesis method has a substantial effect on phase formation and solubility limits in materials produced in the pseudobinary Cr_2O_3-ZrO_2 system.

CHAPTER 3

EXPERIMENTAL METHODS

The coating development not only includes a defined deposition process and a systematic variation of the deposition parameters but also the selection of the substrate material as well as the substrate preparation. In this work, the coating deposition, following the substrate preparation and pretreatment, usually comprises a multi-stage process since depending on the subsequent procedures, a buffer layer might be selected to improve the adhesive strength.

This chapter presents the experimental methods used for the deposition and characterization of coatings in this dissertation. The section 3.1 discusses the selection of the substrates as well as their preparation and then selection of targets and process gases. The process of RF-magnetron sputtering is explained, and the choice of physical process parameters is scientifically justified in section 3.2. The sections 3.3 and 3.4 were dedicated to the methods of coating analysis. The coating analysis comprises the characterization of the coating phase and structure (section 3.3) as well as the coating properties (section 3.4).

3.1 Materials: Substrate, Targets, and Gases

The cutting tool steels (HSS grade M42), commercial cemented carbide inserts (Grade K68, WC-6%Co), and stainless steels (316L) have been used as the substrate material which corresponds to the later industrial application of the coatings in the production technology. In addition, for special analysis, such as coating stress measurements, Si (100) single-crystal substrates were prepared. A brief overview of the substrate materials used, and their geometry can be found in Table 3-1.

The hard metal cutting tool substrates (HSS M42 and K68) and stainless steel (316L) were predominantly used in the geometry 10 mm × 10 mm × 5 mm and 25 mm × 25 mm × 5mm, respectively.

Table 3-1: Overview of the substrate materials used and their geometry.

Substrate	Geometry in (mm)	Hardness (GPa)
Cemented carbide K68	10 mm × 10 mm × 5 mm	20
HSS M42	10 mm × 10 mm × 5 mm	11
SS 316L	25 mm × 25 mm × 5mm	3
Si (100)	20 mm × 2 mm × 0.525 mm	8

For coating deposition purposes, the substrates were mirror-polished manually up to a 3 μm diamond suspension. The mean average roughness Ra of these samples is approximately 1.0 nm. Si (100) single crystal substrates in the geometry 20 mm × 2 mm × 0.525 mm (polished on one side) were used to determine the coating's residual stress.

Before positioning the substrates in the coating chamber, they were cleaned in acetone for 15 minutes in an ultrasonic bath at room temperature, then rinsed with reagent grade acetone and dried with a lint-free cloth.

For this work, pure Cr and Zr target plates (99.95% purity with 3" diameter) were used. The targets with a thickness of 0.25" were attached on Cu-holding backplates, which are cooled during the deposition with water. The Cr and Zr targets are shown in Figure 3-1.

Figure 3-1: Image of Cr and Zr targets with a diameter of 3 inches.

For the coating process, working and reactive gases are introduced into the chamber. The gas flow rates can be controlled by two mass flow controllers. For this work, two separate channels for Ar (Purity 5.0[28]) and O_2 (Purity 4.3) were used. To create a vacuum in the chamber, the pre-vacuum is generated by a mechanical backing pump and a turbomolecular pump creates a high vacuum in the range of 10^{-4} Pa.

3.2 Deposition Technique and Parameters

A SPLD620-FLR PVD coating machine (manufactured by Plasmionique Inc) was used for coating deposition purposes employed a reactive RF magnetron sputtering method. The substrate holder was equipped by a stationary heating etching station for heating and etching purposes during deposition. The configuration of the SPLD620-FLR coating system is illustrated in Figure 3-2. The following sections describe the configuration of the SPLD620-FLR coating system and the experimental set-up.

---

[28] The degree of purity of technical gases is given in the form x.y. The number x stands for the number of "9", which are separated after the second decimal place. The number y gives the last one decimal place. So, a purity of 5.0 corresponds to a purity of 99.9990 vol.%.

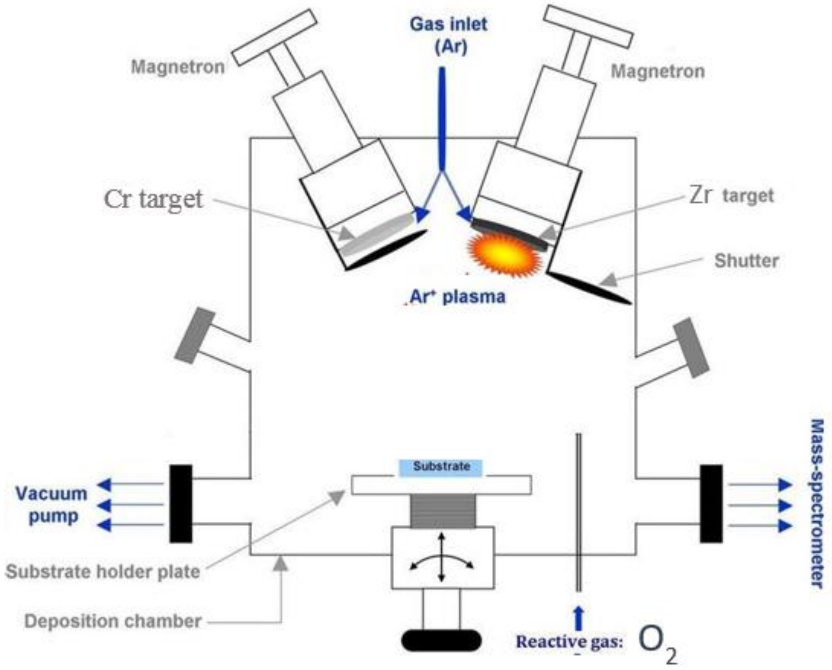

Figure 3-2: The configuration of the SPLD620-FLR coating system. The system employed different match boxes to match the power between power generators and the two RF-powered magnetron sources.

In the coating system, the deposition can only take place in the RF mode (frequency 13.56 MHz). Hence, the deposition of the binary Cr-O and ternary Cr-Zr-O coatings was performed in RF mode. In RF mode, a matching network is needed, consisting of two capacitors and one coil, so that the output impedance of the generators is matched to the input impedance of the magnetron sources and therefore the transfer of power between the generators and the magnetrons is maximized. To generate the alternating voltages, three RF generators (made by Seren, Model R601 and R301), were used. Two RF generators 600 W (13.56 MHz) were available for two magnetron sources and one RF generator 300 W (13.56 MHz) was dedicated to substrate for biasing purposes.

The heating etching station is a substrate heater which to its heating disk a substrate bias can be applied and is stationary in the coating chamber. The samples are positioned on top of it in predefined position to achieve uniform coatings and thus cannot be moved during the individual process steps. The heating element is made of SiC and has a diameter of 10 cm. This SiC element can be heated by resistive heating up to 900°C. The heater conductor is connected to a RF supply which can apply up to 100 W power to create a desired bias during deposition.

Temperature measurement is done using a Type K thermocouple enclosed in an Inconel sheath and positioned close to the substrate. It should be noted that the actual substrate temperature may differ slightly from the measured temperature since the thermocouple is not in direct contact with the substrate.

Two separate sets of experiments were designed for deposition of binary Cr-O and ternary Cr-Zr-O coatings. For all the depositions the chamber was evacuated to a base pressure of better than 10^{-4} Pa. The target–substrate distance was kept to 50 mm. To remove any chemical contaminants on the substrate surface, the substrates were etched at a DC equivalent voltage of -150 V, corresponding to a RF power of about 50 W, for 20 min in a pure Ar plasma at 0.3 Pa pressure. At the same time, the targets were sputtered at 300 W for 20 min to remove impurities at the target surface. The shutters in front of targets were closed during the target cleaning period to prevent any deposition on substrates. Immediately after the substrate bias is turned off and the target cleaning is finished, the substrate grounded, the shutters moved away, and pure Ar replaced by a mixture of Ar and O_2 and the coating process begins. The following explains the experiments designed for each coating system:

a) Binary Cr-O coatings:

In this set of experiments, the effect of deposition parameters including deposition pressure, temperature, Cr-target voltage, and Ar/O_2 ratio on the structure, phase composition, and mechanical properties of chromium oxide coatings was investigated. First, depositions were performed at room temperature (without external substrate heating) using a Cr target voltage of 260 V. The Ar/O_2 ratio was 6, while the deposition pressure varied from 1 to 1.6×10^{-1} Pa. In the second series, the deposition temperature altered between room temperature and 400 °C, with deposition pressure constant at 1.6×10^{-1} Pa. In the third series, Cr target voltage was tuned from 180 V to 300 V, while deposition pressure and deposition temperatures were 1.6×10^{-1} Pa and room temperature, respectively. In the final series, the Ar/O_2 ratio changed between 6 and 3, whereas deposition pressure, Cr target voltage, and temperature remained constant at 1.6×10^{-1} Pa, 260 V, and room temperature, respectively. Detailed deposition parameters are summarized in Table 3-2. This experimental design allows for the investigation of the individual effects of each deposition parameters on the structure and mechanical properties of chromium oxide coatings.

Table 3-2: Detailed deposition parameters for chromium oxide coatings.

Parameter	Cr Voltage (V)	Ar Flow Rate (sccm)	O_2 Flow Rate (sccm)	Temperature (°C)	Pressure (Pa)
Pressure Change	260	30	5	25	1 0.82 0.29 0.16
Temperature Change	260	30	5	25 150 300 400	0.16
Cr Voltage Change	300 260 220 180	30	5	25	0.16
Ar/O_2 Ratio Change	260	30 25 20 15	5	25	0.16

b) Ternary Cr-Zr-O coatings:

In this ternary system, depositions were performed at the optimum parameters determined from the previous step (a) in which chromium oxide coatings with a hardness value close to bulk Cr_2O_3 (H~29 GPa) had been produced, i.e. at working pressure of 0.16 Pa, Cr-target voltage of 260 V, and a mixture of Ar and O_2 with 6/1 ratio, respectively. The influence of the composition and substrate temperature, varied in 150°C steps from 25°C to 850°C, on structure, phase composition, and mechanical properties of Cr-Zr-O coatings were evaluated. Table 3-3 shows a summary of the deposition conditions for the prepared oxide coatings in Cr-Zr-O system.

Table 3-3: Deposition conditions for Cr-Zr-O coatings.

Cr Power (W)	**Zr Power (W)**	**Ar flow rate (sccm)**	**O_2 flow rate (sccm)**	**Temperature (o C)**	**Pressure (Pa)**	**Deposition time (h)**
300	0	30	5	25-850	0.16	24
300	50	30	5	25-850	0.16	24
300	75	30	5	25-850	0.16	24
300	100	30	5	25-850	0.16	24
300	125	30	5	25-850	0.16	24

3.3 Characterization of Coating Structure and Phases

The coatings were examined for chemical composition, morphology, structure, and phases. The chemical composition was determined by Energy Dispersive Spectroscopy (EDS). The coating thickness was determined by means of an optical profilometry and cross-section observation by Scanning Electron Microscope (SEM). The morphology and surface profilometry of coatings were also studied by SEM. X-ray diffraction (XRD) in grazing incident mode and Raman spectroscopy were used to determine the phases in the coatings. The oxidation state of the elemental composition of coatings was determined by X-ray photoelectron spectroscopy (XPS). To determine the elemental composition by means of EDS, a SEM device equipped with a SXFiveFE detector from Hitachi was used. For each sample, at least 10 measurements were taken in the middle of the sample and the mean value was reported. For each measurement, a field of 1 x 1 μm^2 was scanned. For all coatings, the elements Cr, Zr, O were measured. Energy dispersive spectroscopy is a nondestructive method for determining the elemental composition in the surface area of a sample. The penetration depth of the electron beam is approximately 1 µm, which roughly corresponds to the lateral extent of the electron beam on the sample surface. The electron beam penetrates the sample with high kinetic energy (here: 30 kV excitation voltage). If the electron beam hits an electron from an atomic inner shell (such as K, L, M) with sufficient energy, the electron can leave the shell and leave a vacancy (see Fig. 3-3). An electron from a higher shell can go to the void of the lower shell (see Fig. 3-3) resulting in characteristic X-rays emission. The radiation is differentiated, depending on the shell in which the vacancy occurred. Since the transition can be made from different shells, this radiation has several lines. The energy of the lines is characteristic of each element. Standards of known composition can also be measured, and these traces subsequently compared to those of the unknown sample. By comparing the energy and intensities of characteristic X-rays emitted from the unknown sample with those of the standards, the composition of the sample can be calculated [123–125].

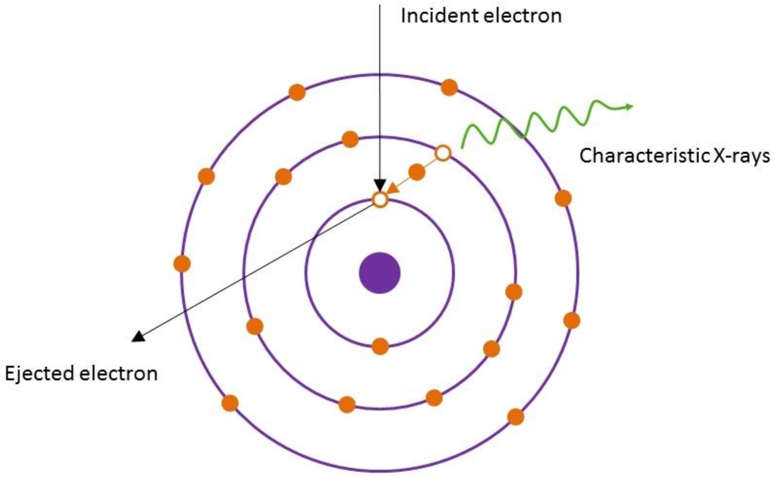

Figure 3-3: Formation of characteristic X-rays (according to [123]). An incident electron triggers an electron out of the K shell to form a vacancy. Then an electron from a higher shell transforms to a lower shell, emitting characteristic X-radiation.

To determine the coating thickness and roughness, an optical profilometry method was employed. A New View 8000 optical profilometer (Figure 3-4), manufactured by Zygo Corporation with a 50X Mirau objective and standard filter type (bandwidth 125 nm and center wavelength 550 nm), was used to measure both the mean roughness (Ra) and thickness of the coatings. The roughness and thickness value of each coating was based on three measurements and an average value was reported.

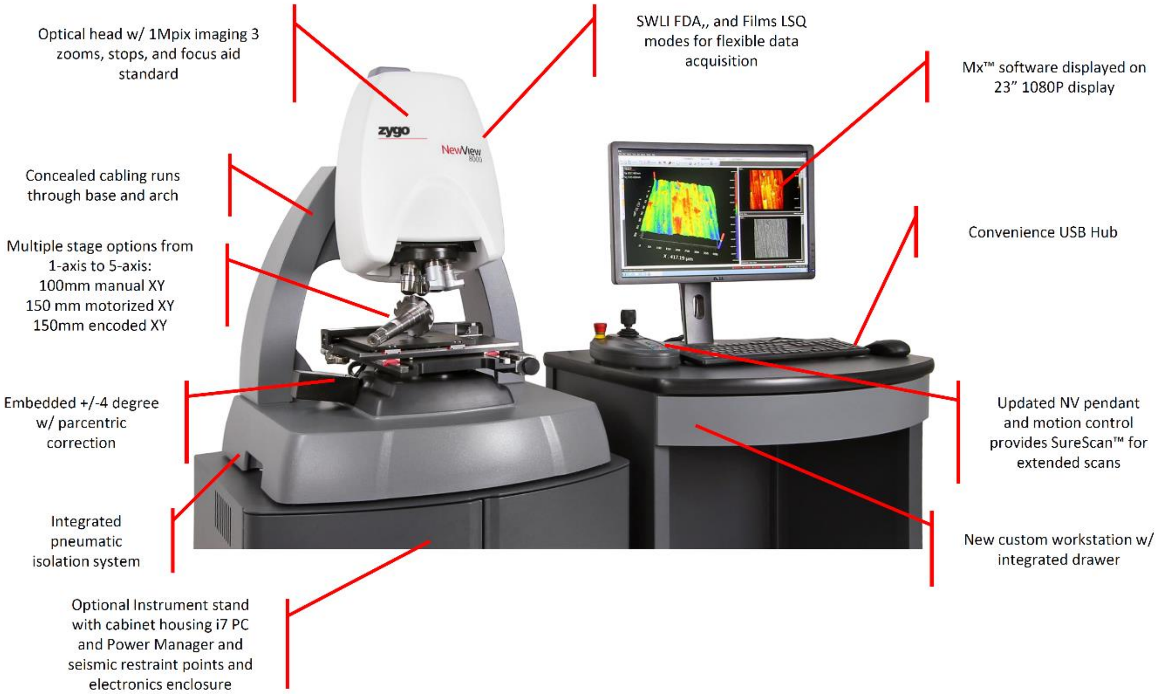

Figure 3-4: Zygo NewView 8000 optical profilometer.

In order to use the optical profilometry method, part of the sample was covered before the coating process so that a step was created after the deposition. Then, the mask was removed so that the height difference between the coating surface and substrate surface could be measured with the optical profilometer.

The optical profilometry is a non-destructive method and employs the coherence scanning interferometry (CSI) method to provide a three-dimensional graphic image associated with a high-resolution numerical analysis of surfaces. The profiler works based on interference between light waves. When the two waves are completely in phase the resultant wave is larger in magnitude than the initial waves. If the waves are out of phase the resultant wave will be zero (see Figure 3-5-a). The intensity of the resulting wave is a function of the phase difference or optical path difference. The light beam generated in the coherent light source is divided by a half-silver mirror, one divided part is reflected from the test surface, and the other half is reflected from a reference surface (see Figure 3-5-b). The optical path difference will determine whether the detector sees a bright or dark spot so that the intensity of the resulting light at any point is a function of the optical path difference. Thus, for points where the optical path difference is the same, the intensity will be the same. Variations in the optical path difference between different parts of the surface will result in light and dark bands (known as interference fringes) at the detector (see Figure 3-5-c). Each pixel on the camera will produce a signal during the vertical scan of the objective. Comparing these signals allows for the formation of a very precise relative height map of the surface (see Figure 3-5-d).

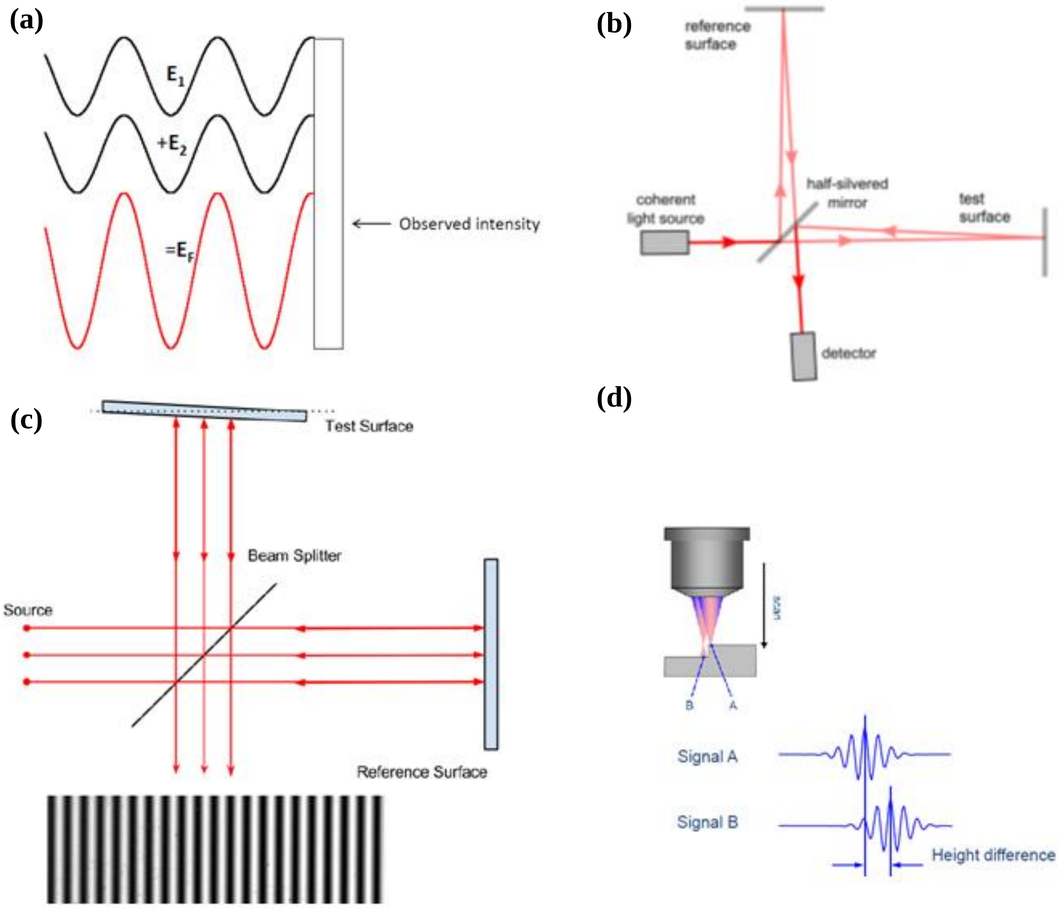

Figure 3-5: (a) Constructive in phase lights, (b) Profiler operation, (c) Interference fringes creation, and (d) three dimensions map creation [126].

By means of scanning electron microscopy, the morphology of the sample surface can be recorded. an FE-SEM-cold field emission scanning electron microscope (Hitachi SU8010) was used to take photos of the coating surface and the cross-section of fracture samples. Based on the illustrations, a qualitative statement about the surface topography or the morphology of the grains can then be derived. In a scanning electron microscope, the sample surface is scanned with an electron beam and an image is generated via the signals generated therewith. The beam path in a scanning electron microscope is shown schematically in Figure 3-6. The electron beam is accelerated to the anode and focused on the sample surface via a lens system (condenser lens and objective lens). By the interaction of the electron beam with the sample arise different signals due to backscattered electrons, secondary electrons, Auger electrons, X-rays (characteristic X-ray and X-ray brake radiation) and cathode luminescence. These signals are used with the desired detectors. The objective lens with a variable working length can be ensured that the signals are detected. The detected signals are then processed into pixels and assembled into a complete image[124,125].

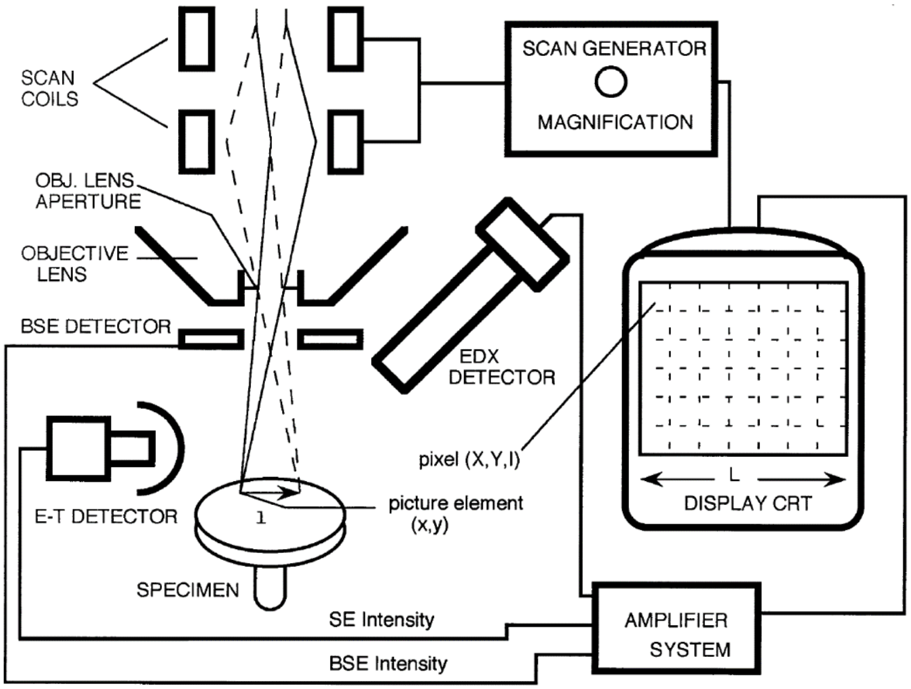

Figure 3-6: Schematic of the electron beam path in a scanning electron microscope (after [124]). The electron beam is focused on the sample surface by a lens system (condenser lens and objective lens). The scanning coils direct the beam across the surface. Detectors pick up the signals generated by X-ray, cathode luminescence, Auger electrons, backscattered electrons, and secondary electrons.

To investigate the phase composition fo coatings, the samples were analyzed by means of X-ray diffraction with parallel beam geometry in grazing incidence mode at θ = 5°. The selected 2-theta range was 20 °-90 ° with a step size of 0.05 °. For this purpose, a 1D D/teX Ultra detector and a

Cu anode (CuKα_1 radiation with a wavelength of 1.5406 nm) were used on a Rigaku Ultima IV X-Ray diffractometer.

The X-ray diffraction is based on the Bragg condition ($n\lambda = 2d\sin\theta$, where d is the spacing between atomic planes in the crystalline phase), where a beam of X-ray is incident on the specimen and is diffracted by the crystalline phases whenever the Bragg's law is met. The X-rays are diffracted at the lattice planes and show constructive interference when the path difference (in Fig. 3-7 path difference between the upper and lower of the wave) corresponds to the integer multiple of the wavelength [124,125].

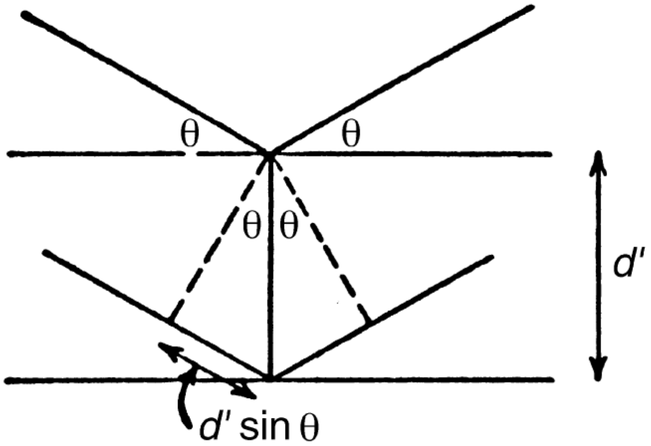

Figure 3-7: Schematic of the Bragg condition in which the X-rays show constructive interference when the path difference corresponds to the integer multiple of the wavelength [124].

The diffracted X-rays with different intensities are recorded with the 1D detector and plotted in the X-ray diffractogram as a function of the double diffraction angle θ. Each material has a characteristic diffractogram, which identifies the material and its phase. For phase identification, the obtained XRD patterns will be compared with the Joint Committee on Powder Diffraction Standards (JCPDS) database called PDFs. Further information can also be derived from the diffractograms. From the diffraction angle and the Miller indices, the lattice parameters, as well as the volume of the unit cell, can be calculated. Deviations from the theoretical unit cell arise e.g. from the shift of a reflex from its theoretical position. A shift of the diffraction reflex to smaller ones in most crystal systems means increasing lattice parameters and thus increasing volume of the unit cell. With the diffraction angle and the half width of a reflex, the grain size can be calculated by Scherrer formula [127]:

$$B = \frac{K\lambda}{L\cos\theta} \tag{3.1}$$

where:

B= Full Width at Half Maximum

K=: Numeric constant (0.93)

λ= Wavelength of X-rays

L= the linear dimension of the grain

θ= Bragg angle

Hence, a high half width means a small grain size. Very fine-grained or amorphous phases cannot be identified by X-ray diffraction.

To obtain more information about the structure and the binding properties of the coatings, Raman spectra were taken from selected samples. For this purpose, a Renishaw Invia Reflex Microscope with an Ar ion laser (wavelength 514.5 nm) was used (Figure 3-8). Raman spectra were recorded in the relevant wavenumber range of 100-900 cm^{-1}. Before the Raman measurements, calibration was done using a silicon reference sample, and the peak positions were determined using Wire.3.3 software. The laser power was set at 5 mW with a measurement duration of 30s. The intensity maxima due to cosmic radiation was removed from the spectra.

Figure 3-8: The Renishaw Invia Reflex Microscope used in this work.

In Raman spectroscopy, the analysis is based on the inelastic scattering of light by matter and it can be used for characterization of both amorphous and crystalline materials. The formation or destruction of a phonon is coupled with a change in polarizability. When the laser photons interact with the lattice atoms, the energy of the photon can be absorbed, and a virtual energy level is created, as shown in Figure 3-9. In elastic scattering, the so-called Rayleigh scattering, the energy of the unscattered and scattered photon is the same.

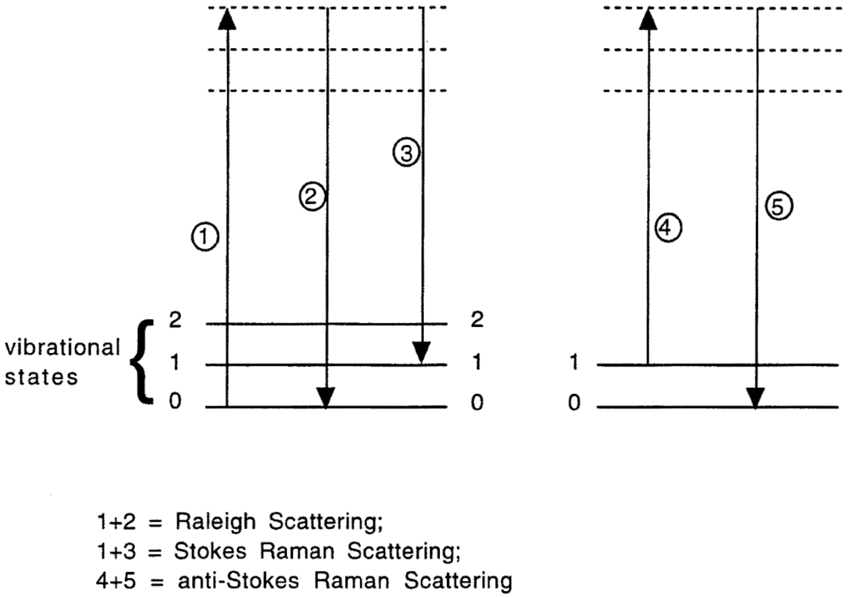

Figure 3-9: Schematic representation of the three types of scattering in Raman spectroscopy: Stokes scattering, anti-Stokes scattering, and Rayleigh radiation (according to [124]).

In inelastic scattering, a photon of lower or higher energy is emitted. These are Stokes and anti-Stokes scattering. In Stokes scattering, excitation into the virtual energy level occurs from an unexcited state. The scattered photon has lower energy and a phonon with the corresponding energy difference is generated. In the case of anti-Stokes scattering, the excitation takes place from an already excited energy state. By destroying a phonon, the scattered photon has higher energy than the unscattered photon. The intensity of the anti-Stokes radiation is lower than that of the Stokes radiation since the initial state must already be excited. Overall, in the crystal, there are 3n-3 (n: number of atoms in the primitive unit cell) optical normal vibrations. Designation of these vibrations takes place according to the possible symmetry operations in the crystal lattice so that if an inversion center is present then the normal mode is Raman active and IR inactive[124].

The chemical state of elemental compositions of coatings was investigated by X-ray photoelectron spectroscopy (XPS). An AIXS SUPRA XPS with aluminum K-alpha (Al-Kα) radiation as the excitation source was used for this purpose. Before XPS measurements, the surface of the coatings was sputter-etched with Ar ions for 20 s to remove surface contaminants. During XPS analysis, due to the insulating properties of oxide materials, a charge correction was also accomplished by monitoring a high-resolution spectrum of adventitious hydrocarbon on the surface of the samples. XPS is a surface sensitive technique which its physical principle is based on the external photoelectric effect. By irradiating the sample surface with X-rays of characteristic energy (wavelength) whose energy (hν) is greater than the work function (WAP) of the sample, electrons are emitted from occupied initial states into the vacuum and an ionized final state is formed (Figure 3-10). The photoelectrons emitted from the material are energy-dispersively detected as a function of their kinetic energy by means of a special spectrometer arrangement.

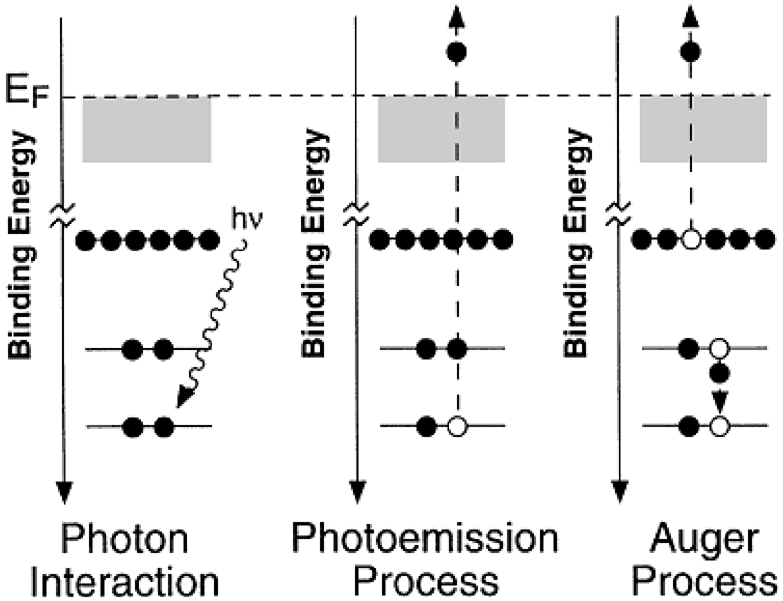

Figure 3-10: Schematics of the excitation process in XPS leading to photoemission of a core electron and the subsequent Auger relaxation process that can occur[124].

According to the total energy balance ($E_k = h\nu - E_B - WAP$), the kinetic energy of the photoelectron (E_k) is determined and the binding energy (E_B) is calculated with known excitation energy and work function WAP of the spectrometer and finally the number of photoelectrons collected in a defined time interval is plotted versus binding energy [124,125,128].

3.4 Characterization of Coating Properties

The deposited coatings were examined for selected mechanical properties. Hardness and Young's modulus measurements were made using a nanoindentation technique with a three-face pyramid Berkovich indenter. From the resulting load-penetration curve, hardness and elastic modulus were determined. The residual stress of coatings was determined from the deflection of a coated substrate compared to the deflection of an uncoated substrate. To evaluate the adhesion properties of coatings qualitatively, Rockwell "C" Indentation technique was employed. The corrosion resistance of the samples was tested by electrochemical potentiodynamic polarization method, and tribological properties of coated substrates were evaluated by a reciprocating wear test machine. An inductively coupled plasma optical emission spectrometer was employed to measure the toxicity level of coatings.

Hardness is the resistance of a material to plastic deformation. For this work, an instrumented indentation tests were performed with a nanoindenter. To determine the hardness of coatings on substrates, a UMT Multi-Specimen Test System from CETR was used. The selection of the measurement parameters was made in accordance with the ISO 14577-1 standard[129]. The depth where the indenter penetrated to the surface was, on one hand 20 times higher than the surface roughness and on the other hand, below 10 % of the coating thickness to minimize the uncertainty of hardness values. This led to an indentation load of 3 mN. The loading and unloading rate (load/ time) was 0.2 mN and the holding time at maximum load was 30 s. This holding time at the maximum load is enough for any time related plastic deformation (creep) to be completed. Subsequently, the Oliver & Pharr method [130] was used to interpret the nanoindentation load-displacement graphs and an average of fifty indentations was reported as the hardness value. Figure 3-11 shows a schematic of the load-displacement curve in nanoindentation. The load curve is recorded when penetrating the indenter into the material. After a holding time of 30s at the maximum of the curve, the indenter is moved out of the material, while the unloading curve is recorded. Based on the unloading curve, certain characteristic values can now be determined. The highest point of the load and unloading curve corresponds to the maximum force (P_{max}). The associated (x) value represents the maximum penetration depth (h_{max}) of the indenter. If you place a tangent on the upper part of the unloading curve (at F_{max}), then the slope (S) corresponds to the contact stiffness at maximum load. The intersection of the unloading curve with the x-axis marks the permanent penetration depth (h_f). The area between the loading and unloading curves represents the plastic part of the penetration work and the area below the unloading curve represents the elastic part of the penetration work. The sum of the plastic deformation work and the elastic recovery results in the applied mechanical work.

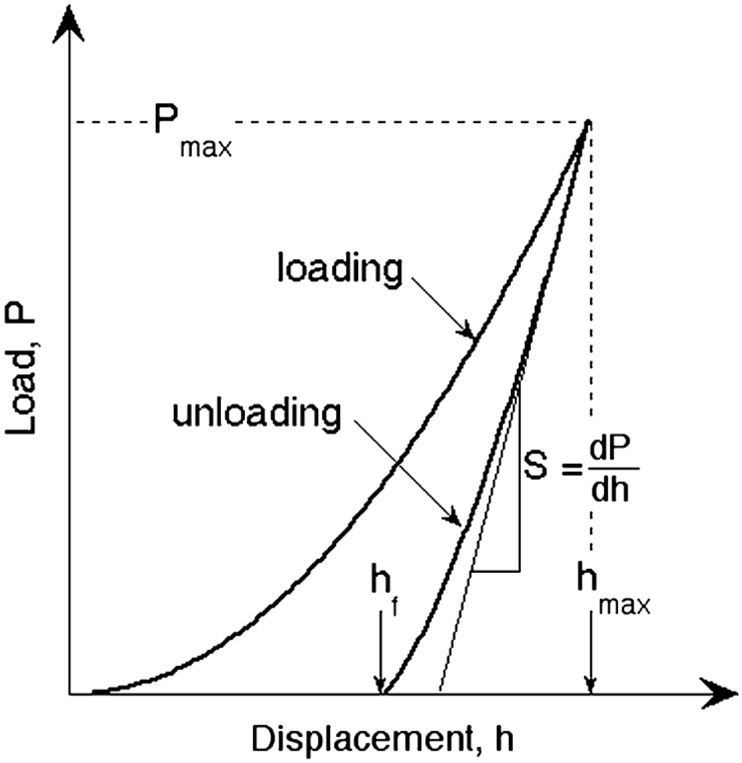

Figure 3-11: Schematic load-displacement curve, which is included in the measurement of the penetration hardness. P_{max} stands for the maximum test force, h_{max} for the maximum penetration depth of the test specimen, h_f for the permanent penetration depth and S the contact stiffness at maximum load (after [130]).

According to Oliver & Pharr [130], The penetration hardness is determined as follows:

$$H = \frac{P_{max}}{A_p} \tag{3.2}$$

where

P_{max}= Maximum test load

A_p= the projected contact area, the value of the indenter area function at the contact depth.

For a modified Berkovich indenter:

$A_p = 24{,}50 \times h_c^2$

where

$h_c = h_{max} - \varepsilon\,(h_{max} - h_r)$

where

h_r= Point of the intersection of the tangent S with the indentation depth-axis.

ε= 0.75 for Berkovich indenter

The indentation modulus (E_{IT}) can be calculated from the slope of the tangent for the calculation of indentation hardness (H) and is comparable with Young's modulus of the material.

$$E_{IT} = \frac{1-(V_s)^2}{\frac{1}{E_r}-\frac{1-(V_i)^2}{E_i}} \qquad (3.3)$$

where;

$$E_r = \frac{\sqrt{\pi}}{2C\sqrt{A_p}} \qquad (3.4)$$

where

ν_s= is the Poisson's ratio of the test piece.

ν_i= is the Poisson's ratio of the indenter (for diamond 0,07).

E_r= is the reduced modulus of the indentation contact.

E_i= is the modulus of the indenter (for diamond $1{,}14 \times 10^6$ N/mm^2).

C= is the compliance of the contact, i.e. dh/dF of the test force removal curve evaluated at maximum test force (reciprocal of the contact stiffness).

A_p is the projected contact area, value of the indenter area function at the contact depth.

The coating internal stresses can cause a significant bending of the surface, as shown in Figure 3-12. A separate Si substrate with a dimension of 2 mm × 20 mm × 0.5 mm was prepared according to ISO 1071-11 standard [131] for residual stress analysis.

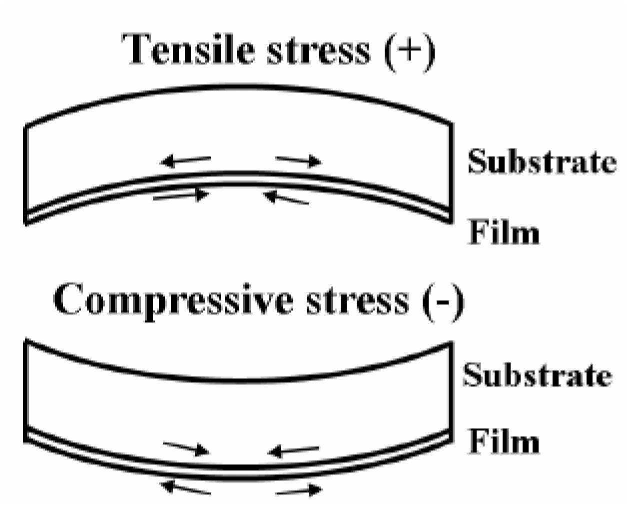

Figure 3-12: Scheme of a surface profile under both tensile and compressive stress due to coating residual stress.

The curvature of substrates was determined using a New View 8000 surface optical profilometer. Subsequently, the internal stress in the coating is deduced from the measured radius of curvature, through the application of the Stoney formula:

$$\sigma_0 = -\frac{1}{6}\frac{E_s}{1-\upsilon_s}\frac{{h_s}^2}{h_f}\left(\frac{1}{R_f}-\frac{1}{R_0}\right) \qquad (3.5)$$

where h_f and h_s denote the thickness of the coating and substrate respectively, and where E_s and υ_s denote Young's modulus and Poisson's ratio of the substrate respectively. The radius of curvature of the substrate before (R_0) and after the coating (R_f) are obtained from the profile of the sample by an optical profilometer.

The quotient $(\frac{E_s}{1-\upsilon_s})$ is the elastic constant of the substrate. For the calculation of the residual stress of coatings on Si (100) substrates, a value of 1.80×10^{11} Pa for the elastic constant of the substrate is used in the mathematical calculations.

The corrosion resistance of the substrates was tested by electrochemical Potentiodynamic polarization method exposing a surface area of 1 cm^2 of substrates into open to air physiological saline solution (0.9% NaCl). All electrochemical Potentiodynamic polarization measurements were carried out according to ASME G5 standard [132] at 298 K with a sweep rate of 0.6 V h^{-1} on a GAMRY reference 600 electrochemical analyzer. A three-electrode cell, using a saturated calomel as the reference electrode and graphite as the counter electrode, was set up for this purpose (Figure 3-13). The test started after about an hour immersing the specimen in the electrolyte to reach a steady state condition for the open circuit potential. The anodic and cathodic portion of obtained Potentiodynamic polarization curves were Fitted by a customized python module [133] resulted in the Tafel plots and corrosion data.

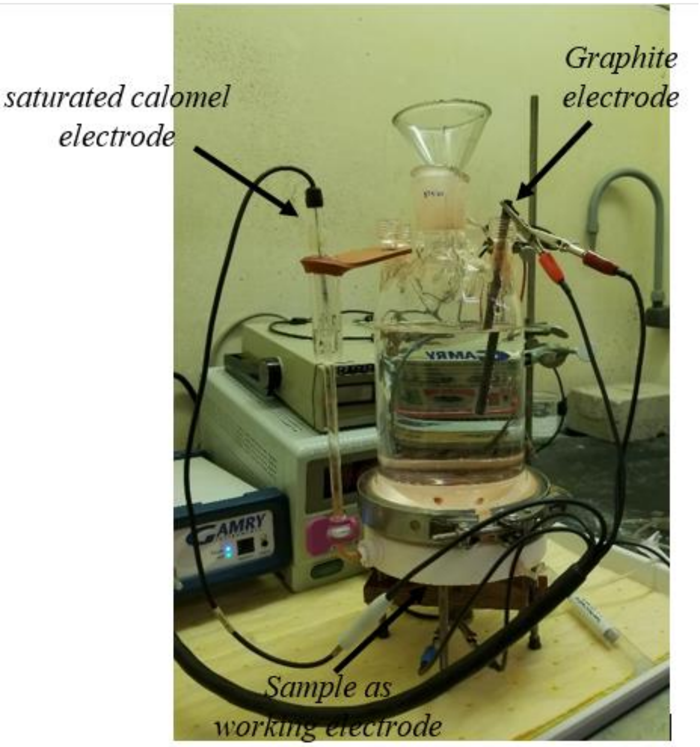

Figure 3-13: The three-electrode cell setup in electrochemical Potentiodynamic polarization method used in this work.

Friction and wear tests were performed according to BS EN 1071-12 standard [134] using a wear test machine with ball-on-disk configuration (UTM with a 440-C martensitic steel ball, 10 N load). The test started after the samples were immersed in saline solution at room temperature. 10,000 cycles with a displacement length of 2.5 mm were set in linear reciprocating motion for all the samples. The actual applied load, friction force, and Coefficient of Friction (COF), which is the ratio of the frictional force to the loading force on the disk were provided by UMT software. The wear rate of the substrates is measured using the follow equation:

$$W = \frac{V}{2LSN} \tag{3.6}$$

where;

W= is the wear rate.

V= is the volume lost from the plate.
L= is the applied load.
S= is the stroke length.
N= is the total number of reciprocations.

The volume lost of each substrate was measured by 3D surface profile investigations mapped by optical profilometer after each test.

Rockwell “C” Indentation testing is a well-known method to qualitatively evaluate adhesion strength in a coating and substrate system. It is a fast, easy, and low-cost method compared to other techniques which exist in evaluating the coating adhesion. Hence, to evaluate the adhesion properties of coatings qualitatively, Rockwell “C” Indentation tester (Instron Wolpert GmbH Rockwell C hardness tester) with a load of 981 N (100 kgf) was performed on three different areas of coatings according to ISO 26443 standard[135]. During the testing, an impression is created by the Rockwell C diamond indenter pressed into the coating. Depend upon the coating adhesion quality a cracking and delamination might occur and extend at the area surrounding the indentation. Subsequently, The imprints will be observed using an optical microscope and compared to ISO 26443 standard guideline [135]. A coating with good adhesion shows no spallation and cracks around the indentation imprint comparing to the unacceptable failure images, as shown in Figure 3-14.

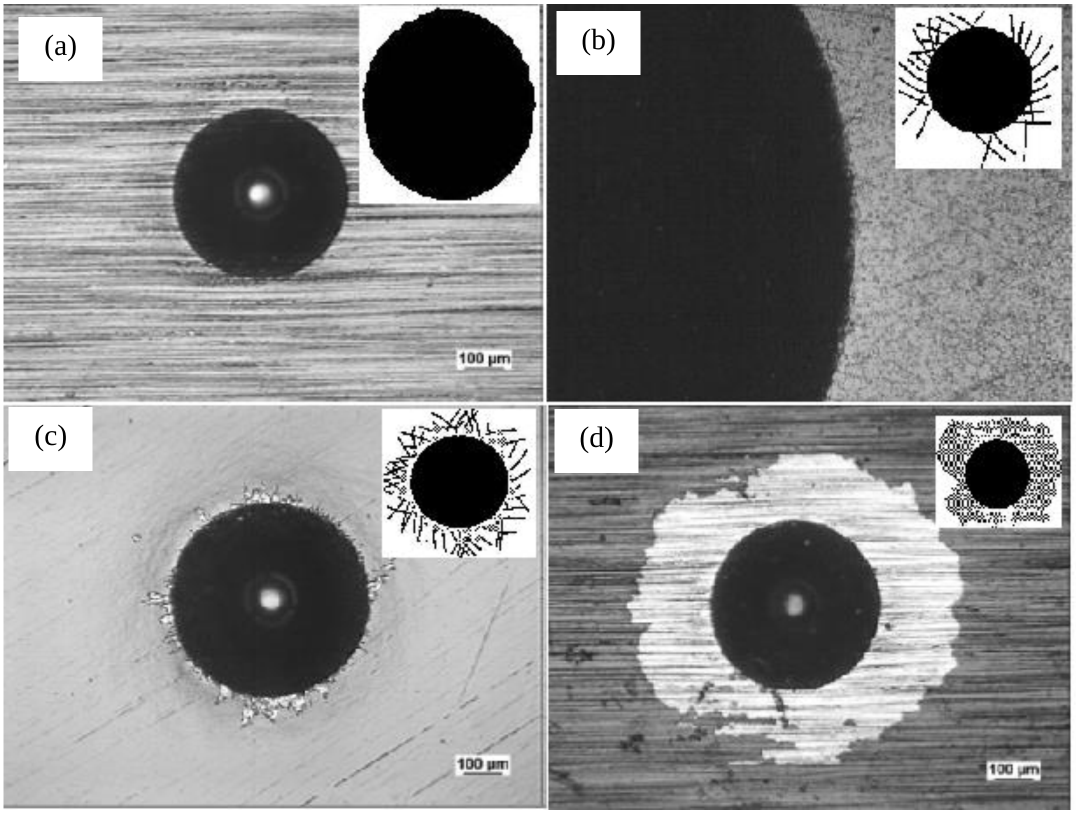

Figure 3-14: guideline representations and sample photographs for classification of adhesion results by Rockwell C indentations; a and b) Acceptable adhesion, c and d) Unacceptable adhesion.

An inductively coupled plasma optical emission spectrometer (ICP-OES, iCAP™ 7400 made by ThermoFisher Scientific, Massachusetts, USA) was employed to analyze the toxicity level of the samples. For this purpose, both coated and uncoated SS316L substrates were immersed in the physiological saline solution for 5 months. The saline solution then was probed by ICP-OES analyzer and the amount of toxic Cr ions released into the solution was detected.

In ICP-OES analyzer atoms are excited by passing through a plasma source. The energy then is released in the form of photon whenever the excited atoms move to their initial ground state due to the relaxation process. The wavelength of the emitted photons is detected that is characteristic of their respective elements [136]. The excitation process of an atom by a plasma source in ICP-OES analyzer is shown in Figure 3-15.

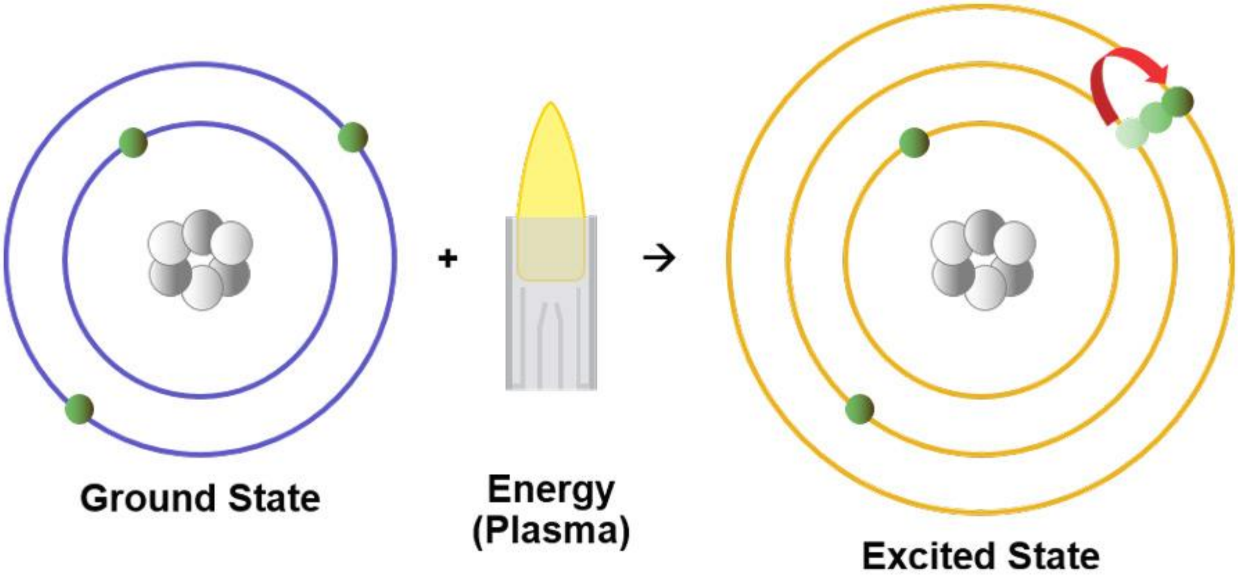

Figure 3-15: Excitation of an atom by a plasma source in ICP-OES[136].

CHAPTER 4

SYNTHESIS AND CHARACTERIZATION OF Cr-O COATINGS

In this chapter, a reactive RF magnetron sputtering technique was used to deposit chromium oxide coatings, considering the effects of principal deposition parameters, including deposition pressure, temperature, Cr-target voltage, and Ar/O_2 ratio, and the correlation between structure, phase composition, and hardness of the chromium oxide coatings was established. Finally, the principal factors which were responsible for observing the high hardness in magnetron sputtered chromium oxide coatings were pointed out. This results serve as a basis for later comparison with the coatings of the ternary Cr-Zr-O system (Chapter 7).

This Chapter has been published in the journal “coatings” as follows:

The Effect of Deposition Parameters on the Structure and Mechanical Properties of Chromium Oxide Coatings Deposited by Reactive Magnetron Sputtering, Masoud Mohammadtaheri, Qiaoqin Yang *, Yuanshi Li and Jesus Corona-Gomez, Coatings 2018, 8, 111.

My contributions to this paper were: conceived and designed the experiments, performed the experiments, interpretation of experimental results, and preparing the manuscripts under the supervision of Professor Qiaoqin Yang. The manuscript was reviewed and revised by my supervisor before submission to the journal for publication. The present manuscript is a modified version of the published paper. Copyright permission has been obtained and provided in the Appendix B.

Abstract: Appropriate conditions for depositing hard Cr_2O_3 coatings by reactive sputtering techniques have yet to be defined. To fill this gap, the effect of principal deposition parameters, including deposition pressure, temperature, Cr-target voltage, and Ar/O_2 ratio, on both the structure and mechanical properties of chromium oxide coatings were investigated. A relationship between processing, structure, and the mechanical properties of chromium oxide coatings was established. Scanning electron microscopy (SEM), X-ray diffraction (XRD), Raman spectroscopy, and X-ray photoelectron spectroscopy (XPS) were used to characterize the

morphology, structure, and chemical compositions of the coatings that were prepared. An optical profilometer was employed to measure both the roughness and thickness of the coatings. The hardness and Young's modulus of the coatings both as-deposited and after annealing conditions were measured by nanoindentation. The results showed that depositing hard Cr_2O_3 coatings is a highly critical task, requiring special deposition conditions. Cr_2O_3 coatings with a high hardness of approximately 25 GPa could be achieved at room temperature, at a low pressure of 1.6×10^{-1} Pa, where Cr-target voltage and oxygen content were 260 V and between 15–25 vol % of total gas, respectively. A dense Cr_2O_3 structure was found to be responsible for the high hardness observed for chromium oxide coating deposited by this method.

4.1. Introduction

Bulk Cr_2O_3 is one of the hardest oxides, with a hardness of 29.5 GPa [9–12], and can be deposited as a protective coating for many purposes, due to its high wear resistance, low coefficient of friction, and excellent corrosion resistance [16,48,137]. Many methods, including plasma-spray [1–3], sputtering [4,5], chemical vapor deposition (CVD) [6], and pulsed laser deposition [7], have been used to produce Cr_2O_3 coatings. However, among them, only sputtering techniques have so far been successful in producing Cr_2O_3 coatings with a hardness value close to that of bulk Cr_2O_3 [5,11,38,47]. Nevertheless, chromium oxide coatings deposited by sputtering methods can also show weak mechanical properties if appropriate deposition parameters are not selected during the deposition process. Chromium oxides exist in various forms (phases), including CrO_3, $CrO_{2.906}Cr_8O_{21}$, Cr_5O_{12}, CrO_2, Cr_2O_3, Cr_3O_4, CrO, and Cr_3O, due to the different valance states of metallic chromium [9,38,49]. Thus, the various forms of chromium oxides, with different microstructures and chemical compositions, could be the main reason for the wide range of mechanical properties observed in chromium oxide coatings deposited under nonequilibrium sputtering conditions at low temperatures and pressure. In this context, Hones et al. [11] investigated the effect of deposition temperature and oxygen partial pressure on the hardness of chromium oxide coatings deposited by a reactive magnetron sputtering technique. They showed that Cr_2O_3 coatings with good adhesion and a hardness value up to 32 GPa can be obtained for 1–2 µm thick films when substrate temperatures exceeded 500 K and oxygen partial pressure is between 15% and 25%. Moreover, Luo et al. [5,47] used the same method to evaluate the effect of oxygen flow rate and radio frequency (RF) powers on the microstructure and hardness of chromium oxide coatings. They illustrated that chromium oxide coatings with high hardness can be obtained at a high oxygen flow rate and a low RF power. We tried to deposit hard Cr_2O_3 coatings using the same deposition parameters reported by those researchers, who successfully obtained hard Cr_2O_3 coatings using the reactive magnetron sputtering technique [5,11,16,38,47], but unfortunately, the hardness of our coatings was as low as 4 GPa. This repeatability problem could be associated with the lack of comprehensive research on the relationships between the processing, structure, and mechanical properties of chromium oxide coatings deposited by reactive magnetron sputtering. Furthermore, the hardness value reported in the majority of the literature seems to have high uncertainty due to the lack of using international standards. According to the authors' knowledge, no previous research exists considering all principal deposition parameters together to show the importance of each deposition parameter in achieving chromium oxide coatings with a hardness value close to the bulk counterpart. Therefore, in the current research, reactive RF magnetron sputtering was used to deposit chromium oxide coatings, considering the effects of principal deposition parameters, including deposition pressure, temperature, Cr-target voltage, and Ar/O_2 ratio, and the correlation between structure, phase composition, and hardness of the chromium oxide coatings was established. A microstructural and phase compositional analysis confirmed that the dense Cr_2O_3 structure is responsible for the high hardness of chromium oxide coatings obtained in a specific deposition condition.

4.2. Materials and Methods

All the chromium oxide coatings were deposited for 10 h on silicon (100) wafers using a RF-magnetron sputtering system (SPLD620-FLR made by Plasmionique Inc., Rimouski, QC, Canada added by us, pls confirm) from a 76.2 mm-diameter Cr target (99.95% pure) in plasma of Ar + O_2. The chamber was evacuated to a vacuum of 2.6×10^{-5} Pa before deposition. The target–substrate distance was kept to 50 mm and the substrates were rotating at a speed of 5 rpm. Depositions were performed at room temperature (without external substrate heating) using a Cr target voltage of 260 V. The Ar/O_2 ratio was 6, while the deposition pressure varied from 1 to 1.6×10^{-1} Pa. In the second series, the deposition temperature altered between room temperature and 400 °C, with deposition pressure constant at 1.6×10^{-1} Pa. In the third series, Cr target voltage was tuned from 180 V to 300 V, while deposition pressure and deposition temperatures were 1.6×10^{-1} Pa and room temperature, respectively. In the final series, the Ar/O_2 ratio changed between 6 and 3, whereas deposition pressure, Cr target voltage, and temperature remained constant at 1.6 × 10^{-1} Pa, 260 V, and room temperature, respectively. The detailed deposition parameters are summarized in Table 4-1. This experimental design allows for the investigation of the individual effects of each deposition parameter on the structure and mechanical properties of chromium oxide coatings. An optical profilometer (New View 8000), manufactured by Zygo Corporation, with a 50X Mirau objective and standard filter type (bandwidth 125 nm and center wavelength 550 nm), was used to measure both the mean roughness (R_a) and thickness of the coatings. The roughness and thickness value of each coating was based on three measurements and an average value was reported. The phase composition of the coatings was investigated by XRD (Rigaku XRD Ultima IV) using CuKα radiation at grazing incidence ($\theta = 7°$). The obtained XRD patterns were matched with the Joint Committee on Powder Diffraction Standards (JCPDS) database, using X'Pert HighScore Plus software to identify the chromium oxide peaks. Raman spectroscopy was also performed on the coatings using a Renishaw 2000 spectroscope with an Argon ($\lambda = 514$ nm, $P = 0.5$ mW) laser source to support the XRD patterns and identify the different oxide states. Before the Raman analysis, the Raman spectroscope was calibrated by identifying the position of the main Raman peak of the silicon reference sample, and the peak positions were adjusted accordingly using Wire.3.3 software. A X-ray photoelectron spectroscopy (XPS) with Al Kα radiation was used to characterize the chemical states of the coatings. Before XPS measurements, the surface of the coatings was sputter-etched with Ar ions for 20s to remove surface contaminants. Due to the insulating properties of oxide materials, during XPS analysis a charge correction was also accomplished by monitoring a high-resolution spectrum of adventitious hydrocarbon on the surface of the samples. Scanning electron microscopy (SEM) was employed to observe the surface morphology of the coatings. The mechanical properties of the coatings (hardness and Young's modulus) were measured according to ISO standard 14577-1 [129] using a nanoindentation technique with a three-face pyramid Berkovich indenter. The load-displacement graphs obtained during nanoindentation were interpreted using the Oliver−Pharr method [130], and the hardness values reported were an average value based on fifty indentations at 3 mN load.

Table 4-1: Detailed deposition parameters for the deposition of chromium oxide coatings.

Parameter	**Cr Voltage (V)**	**Ar Flow Rate (sccm)**	**O_2 Flow Rate (sccm)**	**Temperature (°C)**	**Pressure (Pa)**
Pressure Change	260	30	5	25	1 0.82 0.29 0.16
Temperature Change	260	30	5	25 150 300 400	0.16
Cr Voltage Change	300 260 220 180	30	5	25	0.16
Ar/O_2 Ratio Change	260	30 25 20 15	5	25	0.16

During the measurements, the indentation depth was kept 20 times larger than the surface roughness and lower than 10% of the coating thickness, in order to avoid the effect of surface roughness and substrate hardness on the measured hardness values. The thermal stability of the coatings was also evaluated by a 3 h annealing procedure in the air in a tube furnace at temperatures in the range of 400–700 °C, with a 10 °C/min heating and cooling rate. The hardness of the coatings was measured after the annealing treatments using the nanoindentation method.

4.3. Results and Discussion

4.3.1. Roughness and Thickness of Coatings

Figure 4-1, shows the effects of deposition parameters on the thickness and roughness of chromium oxide coatings. The thickness of the coatings (the deposition rate) was strongly related to the deposition pressure. The coating thickness increased consistently with increasing deposition pressure and reached a maximum at 0.82 Pa (Figure 4-1-a). This trend was expected since the Argon ions (Ar^+), responsible for sputtering of Cr-target, increased as the deposition pressure increased. At deposition pressures higher than 0.82 Pa, the deposition rate decreased again, which could be attributed to the collisions occurring between the sputtered atoms and gas molecules when the average free path of gas molecules (λ) decreased at higher pressures [138].

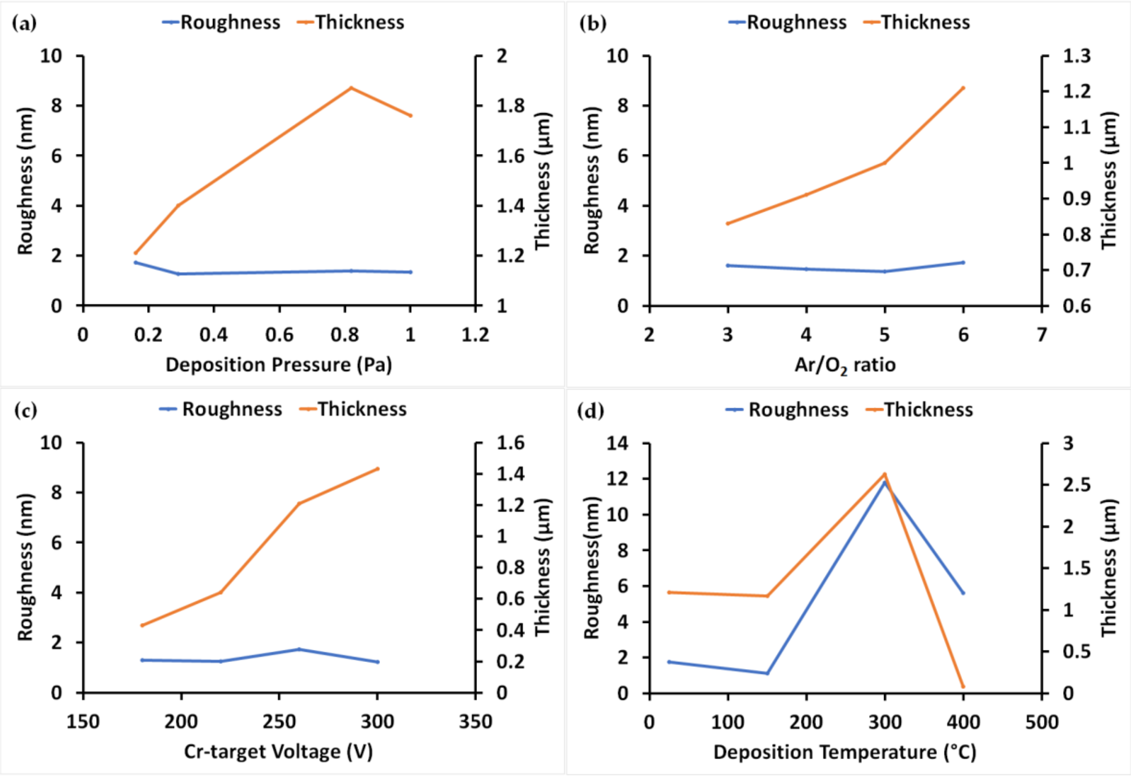

Figure 4-1: The effect of deposition parameters on the roughness (R_a) and thickness of chromium oxide coatings: (a) Pressure; (b) Ar/O_2 ratio; (c) Cr-target voltage; and (d) Temperature. Standard deviations are too small to be seen in the graphs.

Thickness also increased with the increasing Ar/O_2 ratio and sputtering voltage (Figure 4-1-b, c). Argon ions are responsible for the sputtering of the Cr target, so as the Ar/O_2 ratio increases at a constant oxygen flow rate, the sputtering rate rises. The increment in the energy and quantity of plasma ions as the sputtering voltage increases is responsible for the increase in the deposition rate. Thickness analysis of the chromium oxide coatings deposited under various deposition temperatures is illustrated in Figure 4-1-d. The thickness of coatings substantially increased at 300 °C. Since the sputtering rate of the Cr-target was not related to the substrate temperature, the increasing coating thickness with the increasing temperature may be correlated with other factors. Figure 4-2 shows the SEM cross-section and surface morphology of coatings deposited at room temperature and 300 °C. The coatings deposited at 300 °C showed a spongy structure (Figure 4-2-a) compared to the dense structure of the coatings deposited at room temperature (Figure 4-2-c). A flake-like surface morphology was observed for the coatings deposited at 300 °C (Figure 4-2-b), which can be attributed to the crystallization of coatings at high temperatures; whereas, a nanocrystalline morphology was observed for the coatings deposited at room temperature (Figure 22d). According to structural analysis by SEM (Figure 4-2- a, c), the porous structure of the coatings due to the volatilization of Cr_2O_3 at high temperatures, which prevents the coatings forming a dense and compact structure, is thought to be the reason for the high thickness for coatings deposited at 300 °C. The volatilization of Cr_2O_3 at high temperatures has already been confirmed in ceramics composed of Cr_2O_3 phase sintered at high temperatures, and it has been shown in Cr-O phase diagrams [13,139]. Under-dense chromium oxide coatings were also observed by Pedersen et al. [140] for coatings deposited at 300 °C by reactive inductively coupled plasma magnetron sputtering. They assumed the shadowing effect was responsible for the low density of the coatings deposited at high temperatures, which is not understandable to the present authors. At 400 °C, the coatings completely lost their adhesion and integration so that the coatings were indeed particles which could be easily wiped out by a tissue paper. The excessive volatilization of Cr_2O_3 at high temperatures and low pressures could also be responsible for the very low thickness (80 nm) of coatings deposited at 400 °C.

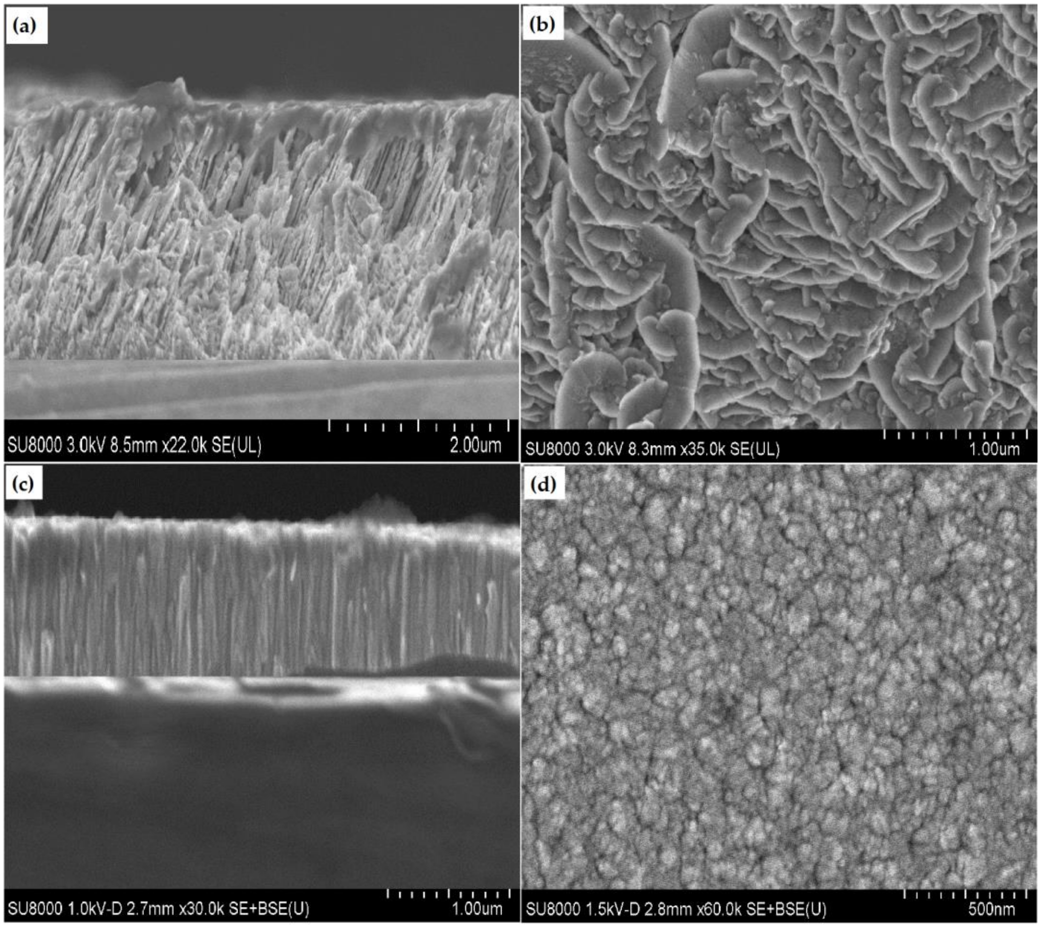

Figure 4-2: SEM cross-section and surface micrographs of chromium oxide coatings deposited at 300 °C (a,b) and room temperature (c,d), respectively.

Among all the deposition parameters, only substrate temperature had a substantial effect on the surface roughness of the coatings (Figure 4-1-d). All the coatings deposited at room temperature showed very smooth surfaces, in the range of 1–2 nm, indicating that the coatings had a nanocrystalline or amorphous structure. The SEM results were consistent with the optical profilometer data, showing that a porous structure and well-crystallized morphology are responsible for increasing both the thickness and roughness of coatings deposited 300 °C, respectively.

4.3.2. Structure and Phase Composition of Coatings

The structural analysis conducted by XRD (not shown here) on chromium oxide coatings deposited at different deposition pressures showed that the coatings had an amorphous structure, regardless of the deposition pressure, as they showed only a broad peak centered at the beginning of the patterns. However, the presence of crystalline phases was not completely excluded, since crystalline phases cannot be detected if their fraction falls below the XRD detection limit or the crystalline size is very small. The amorphous structure of coatings can be attributed to low substrate temperatures. Since Raman spectroscopy is a well-known method for the characterization of both amorphous and crystalline materials [141], this method was employed to complement the XRD results and the results are shown in Figure 4-3. Raman shifts at 648 cm^{-1}, 607 cm^{-1}, 548 cm^{-1}, 348 cm^{-1}, and 303 cm^{-1} can be assigned to the Raman modes of Cr_2O_3 [28,30,142]; whereas, the broad peaks at 691 cm^{-1} and 800–900 cm^{-1} can be assigned to amorphous CrO_2 and either CrO_3 or Cr_8O_{21}, respectively [7,142–144].

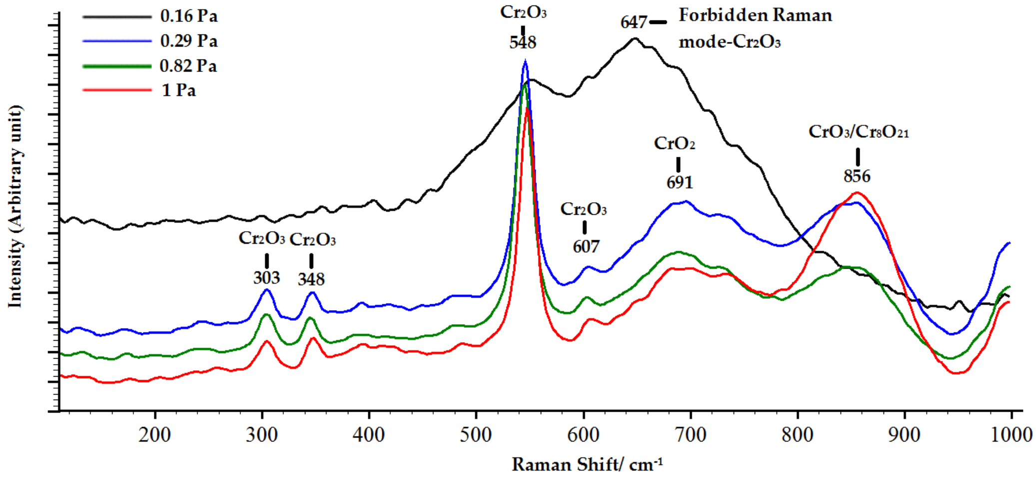

Figure 4-3: Raman spectra of chromium oxide coatings deposited at different pressures.

With a decrease in deposition pressure from 1 to 0.16 Pa, the Raman peaks related to CrO_2 and CrO_3/Cr_8O_{21} phases disappeared and the intensity of Cr_2O_3 Raman shifts decreased significantly, indicating that the coatings transformed from a multi-phase structure to a single-phase, amorphous Cr_2O_3 structure. Thus, increasing the deposition pressure induced the formation of amorphous chromium oxide phases with a higher oxidation state. This was likely related to the elevated oxygen level in the deposition atmosphere when the deposition pressure increased. The high-resolution Cr 2p XPS analysis performed on the chromium oxide deposited at 0.16 Pa (Figure 4-4) confirmed that Cr_2O_3 was the only phase that existed in the coatings. According to the XPS data, the Cr $2p_{3/2}$ spectrum binding energy was 576.6, and the difference between the Cr $2p_{3/2}$ and Cr $2p_{1/2}$ binding energies was 9.7, which corresponded to Cr_2O_3 [128]. Therefore, the Raman peak observed at 647 cm^{-1} for the chromium oxide deposited at 0.16 Pa can be attributed to the forbidden Raman modes of Cr_2O_3 activated in amorphous materials [49,145].

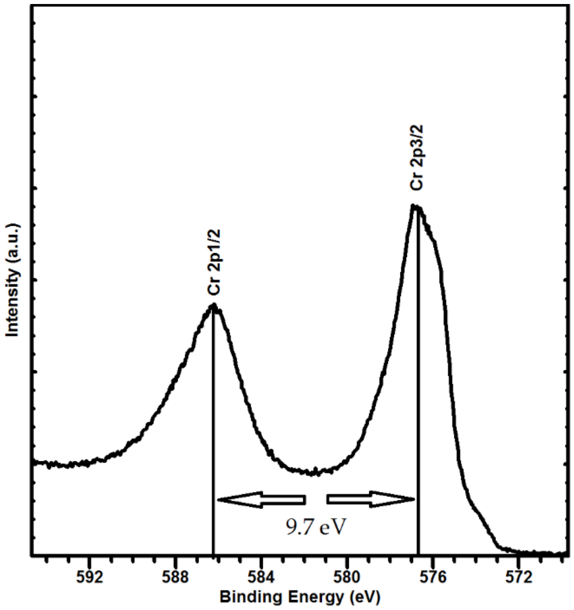

Figure 4-4: The high-resolution Cr 2p XPS spectrum of coatings deposited at 0.16 Pa pressure.

The XRD patterns of the coatings, deposited at different temperatures, are shown in Figure 4-5a. All the crystalline peaks belonged to the hexagonal Cr_2O_3 structure, according to (PDF-98-009-7850) databases. The XRD results showed that the crystallization developed throughout the coatings at a temperature of 150 °C. One more crystalline Cr_2O_3 peak was observed for the coatings deposited at 300 °C, however, the peak intensity at 300 °C looks lower than at 150 °C, which might be due to the special texture formed in the coatings deposited at this temperature as spectra were obtained from grazing incidence X-ray. The Raman spectra of the coatings deposited at a temperature higher than room temperature showed single-phase crystalline Cr_2O_3 peaks (Figure 4-5-b). The Raman results were in agreement with the XRD data and were also consistent with the thermodynamic data since they previously showed that all types of chromium oxide phases transformed to a stable Cr_2O_3 phase with increasing temperature [139,146,147].

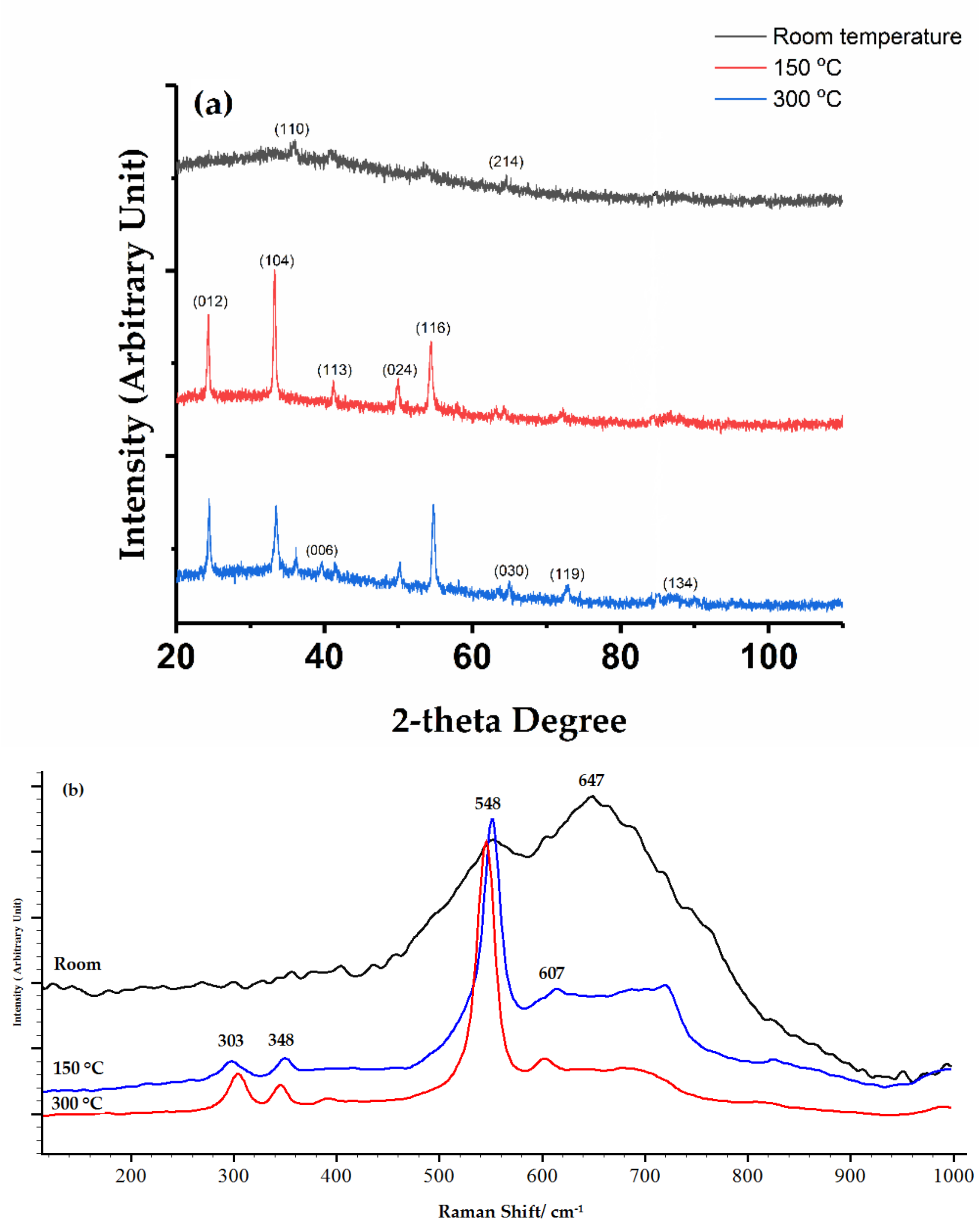

Figure 4-5: (a) XRD patterns and (b) Raman spectra of chromium oxide coatings deposited at different temperatures.

The chromium oxide coatings also showed a major amorphous structure, regardless of the Cr-target voltage, as long as they were deposited at room temperature (Figure 4-6-a). According to the Raman spectra of the coatings deposited at 180 and 220 V (Figure 4-6-b), they were mostly composed of the amorphous CrO_3 phase, as broad Raman peaks can be seen at 800–900 cm^{-1}. They also showed main Cr_2O_3 Raman shifts at 548 cm^{-1}. The amount of the Cr_2O_3 phase is believed to be negligible, according to the low intensity of the Cr_2O_3 peak. The Si substrate Raman peak at 520 cm^{-1} was also observed in the Raman spectrum of coatings deposited at 180 V due to the very low thickness of the coatings. Nevertheless, the coatings deposited at 260 and 300 V showed only an amorphous Cr_2O_3 peak in both Raman (548 cm^{-1}) and XRD analysis.

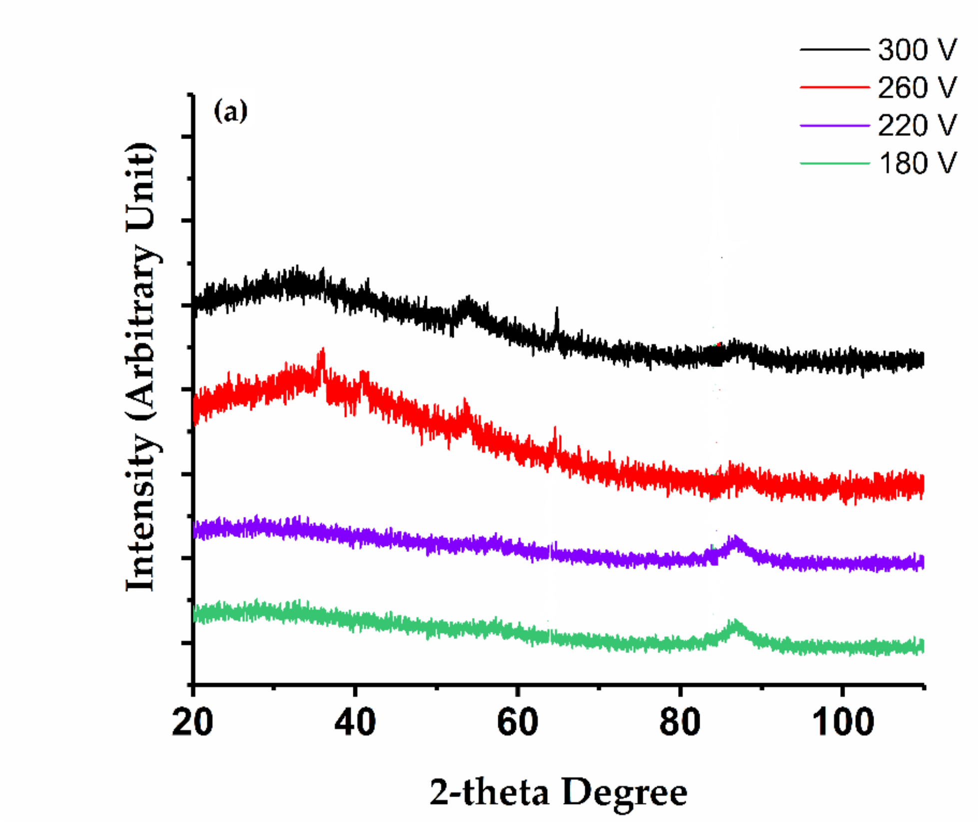

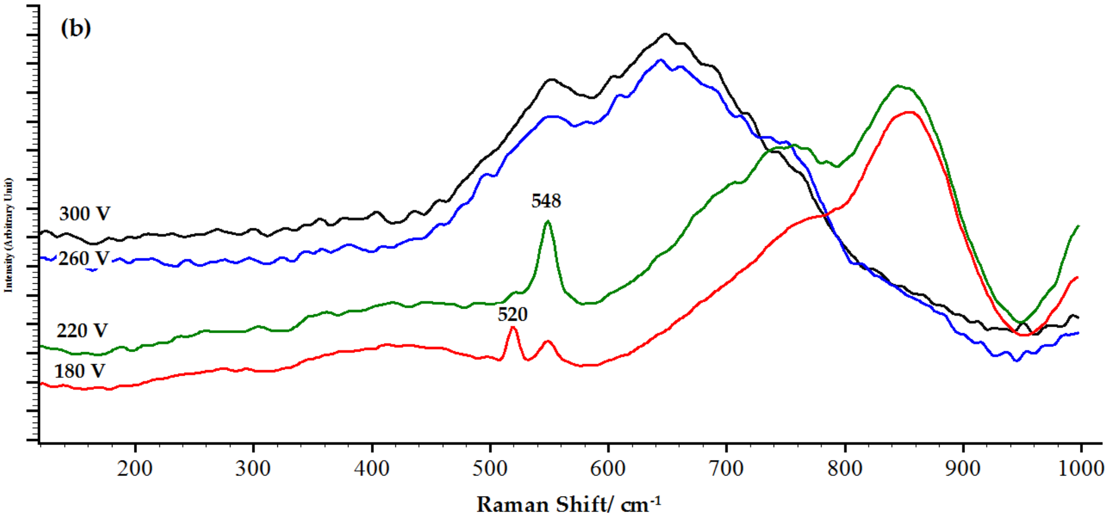

Figure 4-6: (a) XRD patterns and (b) Raman spectra of chromium oxide coatings deposited at different voltages.

Figure 4-7 illustrates the high-resolution Cr2p XPS spectra of coatings deposited at 300 V. This revealed the existence of metallic Cr in the coatings. According to XPS data, the Cr $2p_{3/2}$ spectrum could be curve fitted with two separate peak components at binding energies of 574.1 and 576.6, and the difference between the Cr $2p_{3/2}$ and Cr $2p_{1/2}$ binding energies was 9.3 and 9.7, corresponding to metallic Cr and Cr_2O_3, respectively [128]. From the XPS results, it can be inferred that a small fraction of metallic chromium existed in the structure of the coatings deposited at 300 V, which cannot be detected by XRD and Raman spectroscopy. A deficiency in the oxygen needed to oxidize the excessive amount of sputtered metallic chromium at higher voltages is believed to be the reason for observation of the metallic chromium in the coatings.

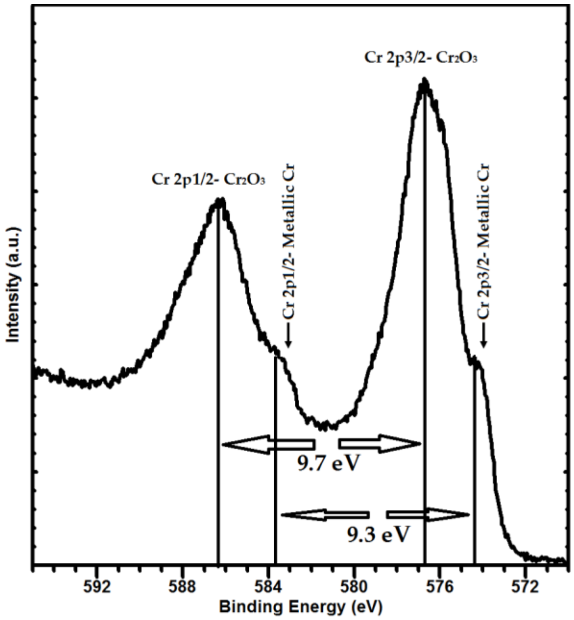

Figure 4-7: The high-resolution Cr 2p XPS spectrum of coatings deposited at 300 Cr-target voltages.

Contrary to other deposition parameters, changing the Ar/O_2 ratio from 6 to 3 did not have a considerable effect on both the phase composition and crystal structure of coatings, according to the XRD and Raman spectroscopy results illustrated in Figure 4-8. All the coatings showed a mainly amorphous structure and the small diffraction lines detected at 2θ = 35.95°, 40.92°, 53.69°, 64.53°, and 87.20° belonged to the nano-Cr_2O_3 structure. The broad Raman shift observed at 548 cm^{-1} was assigned to the strongest Raman mode of Cr_2O_3, which supports the XRD results.

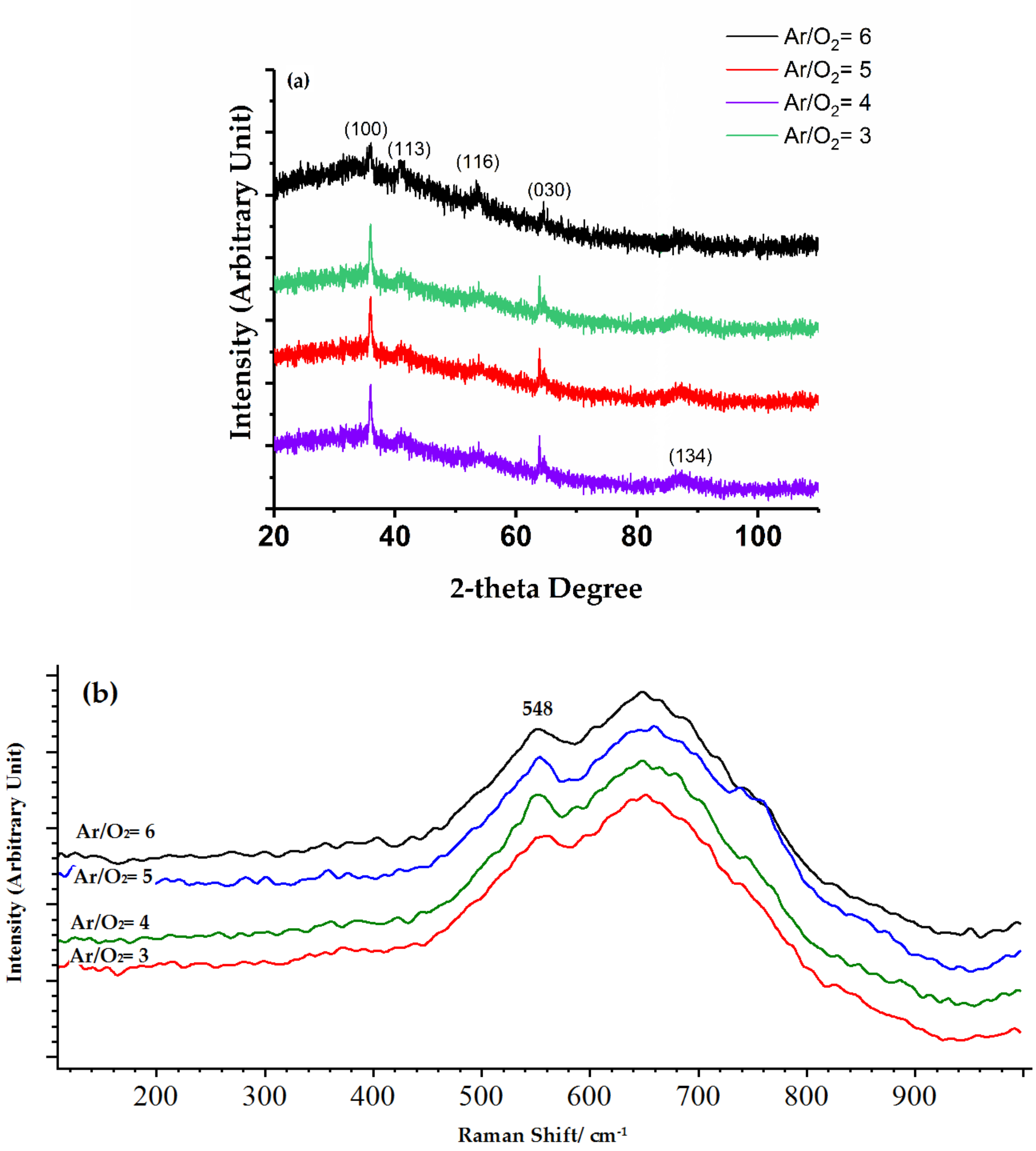

Figure 4-8: (a) XRD patterns and (b) Raman spectra of chromium oxide coatings deposited at different Ar/O_2 ratios.

4.3.3. Mechanical Properties of Coatings

In Figure 4-9-a, variation in hardness and Young's modulus as a function of deposition pressure is displayed. When the deposition pressure was in the range of 1–0.29 Pa, the chromium oxide coatings had an average hardness and Young's modulus value of about 5 and 80 GPa, respectively. This result is consistent with Figure 6 in Kao's [12] research, in which chromium oxide coatings showed a low hardness value of 8 GPa when deposited at a process pressure between 0.5–2.5 Pa. Decreasing the operation pressure to 0.16 Pa, the hardness and Young's modulus of the coatings increased significantly and reached an average hardness and Young's modulus value of about 25 and 289 GPa, respectively, which is near the bulk Cr_2O_3 values reported in previous literature [9–12,148].

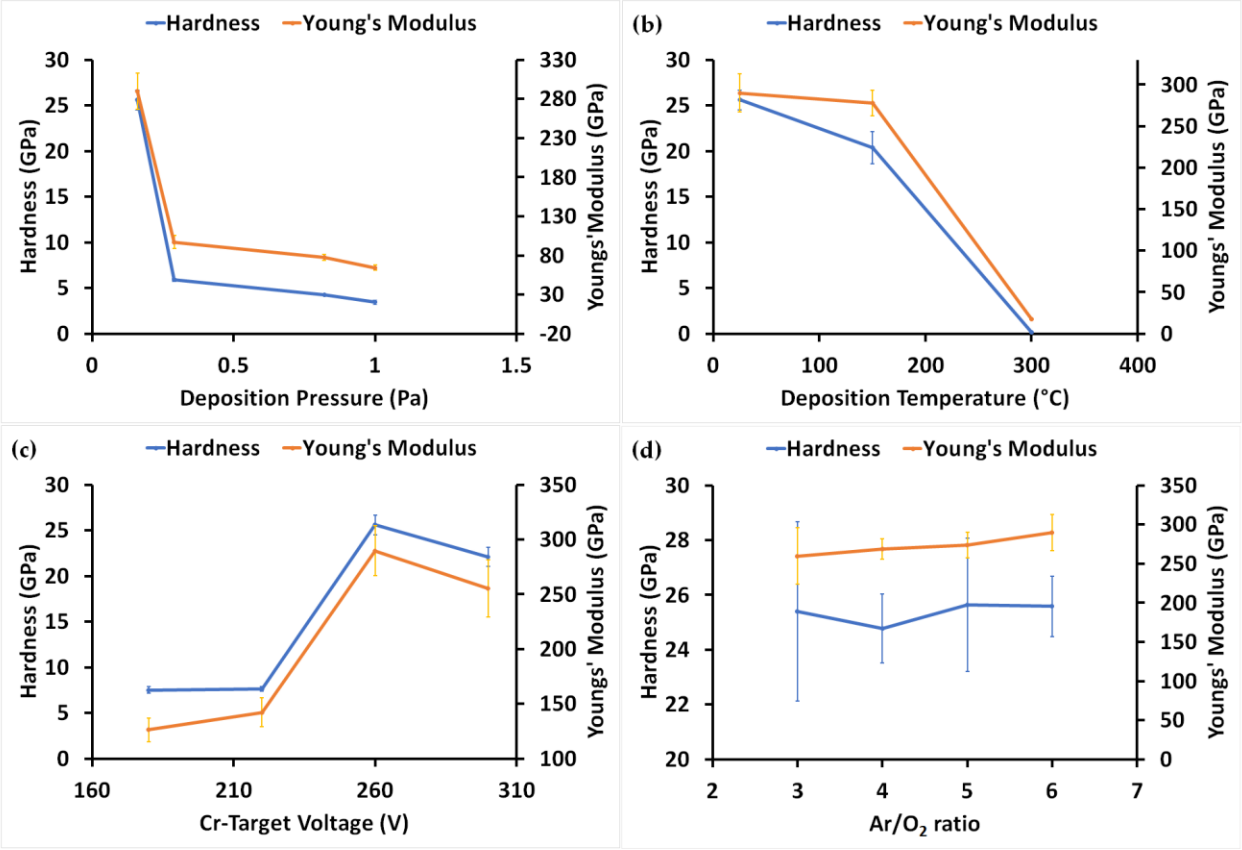

Figure 4-9: Effect of (a) deposition pressure, (b) deposition temperature, (c) Cr-target voltage, and (d) Ar/O_2 ratio on the hardness and Young's modulus of the coatings. Some of the Standard deviations are too small to be seen in the graphs.

According to structural analysis results, it can be inferred that the low hardness of the chromium oxide coatings deposited at higher pressures was due to the formation of mixed chromium oxide phases. It is noteworthy that the coatings that showed mechanical properties near the bulk Cr_2O_3 values at 0.16 Pa consisted of a dense single Cr_2O_3 phase with a nanocrystalline and amorphous structure.

With respect to the substrate temperature, the hardness of the coatings decreased significantly as the deposition temperature increased (Figure 4-9-b). The coatings showed a minimum hardness and Young's modulus of 0.16 and 17 GPa, respectively, when the deposition was performed at 300 °C. Structural analysis showed that the coatings prepared at 300 °C had a porous structure, thus a low density, which is thought to be the main reason for the very low mechanical properties. The coatings deposited at 150 °C had a single-phase crystalline Cr_2O_3 structure with a hardness of 20 GPa, which shows that the hardness of crystalline Cr_2O_3 coatings can also reach the bulk Cr_2O_3 hardness if they are prepared with a dense structure.

There was significant variation in the hardness and Young's modulus of coatings as a function of Cr-target voltage (Figure 4-9-c). A low hardness and Young's modulus of about 7 and 130 GPa, respectively, was measured for the coatings deposited at low voltages (180 and 220 V). Notably, these coatings were composed of various chromium oxide phases in their structure. The reason for dropping the hardness of the coatings deposited at 300 V is related to the presence of metallic Cr in the structure of the coatings, as the increasing voltage enhanced the amount of metallic chromium sputtered in the chamber so there was not enough oxygen to oxidize all the metallic chromium during the deposition.

Figure 4-9-d shows the influence of the Ar/O_2 ratio on the hardness and Young's modulus of the chromium oxide coatings. The mechanical properties of the coatings remained almost constant, regardless of the Ar/O_2 ratio. This can be attributed to the similar structure and phase composition of coatings obtained under various Ar/O_2 ratios.

4.3.4. Thermal Stability of Chromium Oxide Coatings

Many applications need coatings which can preserve their mechanical properties at high temperatures. Therefore, the thermal stability and mechanical properties of Cr_2O_3 coatings were investigated while keeping them at elevated temperatures. For this purpose, Cr_2O_3 coatings with an average hardness of 25 GPa were selected for the thermal stability studies performed in the air. The coatings had been deposited at room temperature with a Cr-target voltage of 260 V, deposition pressure of 0.16 Pa, and Ar/O_2 ratio of 6. No delamination was observed for the coatings after heat treatment up to 700 °C, indicating that coatings had good adhesion on Si substrates. Figure 4-10 shows the hardness variation of Cr_2O_3 coatings with annealing temperatures. The hardness of coatings continuously dropped with an increase in annealing temperature and reached 16 GPa at

700 °C. Several factors were responsible for the hardness reductions, namely transferring from an amorphous to a crystalline structure, stress relaxation, and increasing crystallite size. It is a well-known phenomenon that the crystallite size of materials increases with an increase in annealing temperature due to the diffusion and mobility of grain boundaries at elevated temperatures. The structural changes and increase in crystallite size with annealing temperature in chromium oxide coatings were confirmed by the Raman data (Figure 4-11). According to the Raman results, the amorphous structure of the coatings did not change at 300 °C but transferred to a well crystallized one at 700 °C. Moreover, different research [11,12] has shown that chromium oxide coatings deposited by PVD techniques possess high compressive stress. This stress can add to the hardness of coatings, which is relieved with the annealing procedure, thus decreasing the hardness of coatings.

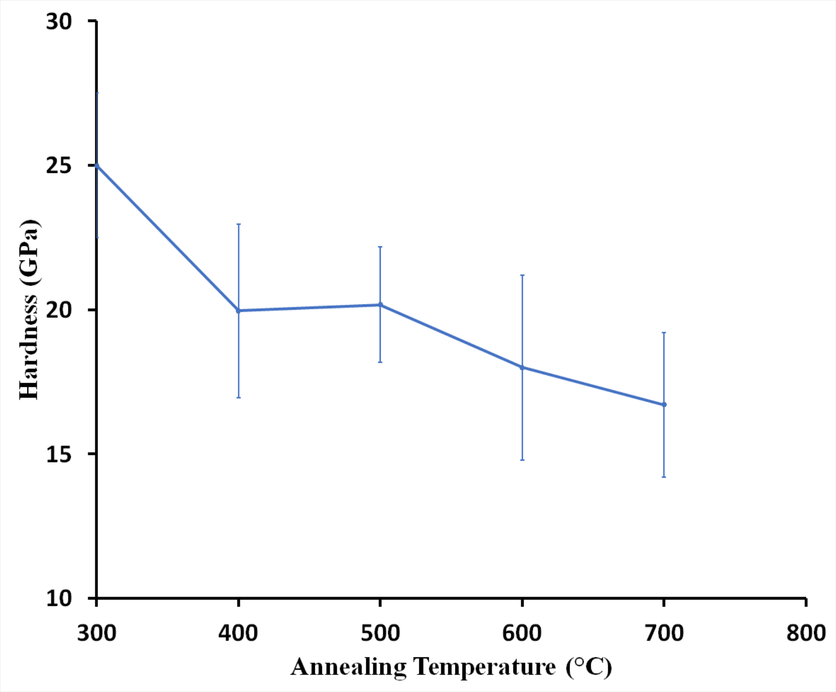

Figure 4-10: The effect of annealing temperature on the average hardness of Cr_2O_3 coatings.

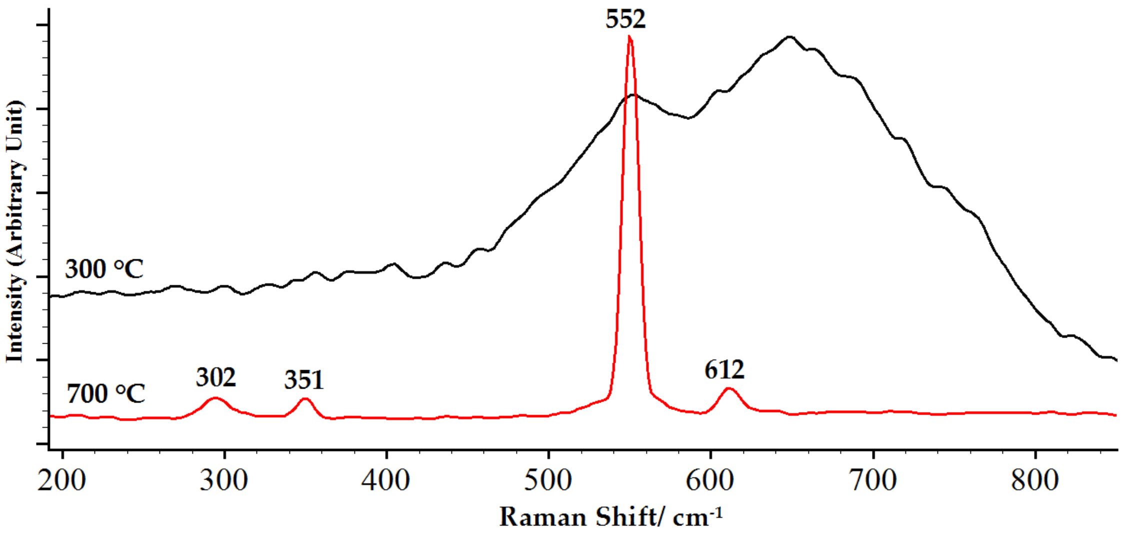

Figure 4-11: The effect of annealing temperatures on the crystal structure of hard chromium oxide coatings.

4.4. Conclusions

A thorough investigation was conducted to explore the appropriate conditions for depositing hard chromium oxide coatings using a reactive magnetron sputtering technique. A correlation between deposition parameters and the microstructure, phase composition, and mechanical properties of chromium oxide coatings was established. The results showed that Cr_2O_3 coatings with a high hardness of approximately 25 GPa could be achieved at room temperature, at a low pressure of 1.6×10^{-1} Pa, where Cr-target voltage and oxygen content were 260 V and between 15–20 vol % of total gas, respectively. A dense Cr_2O_3 structure was responsible for the high hardness observed. The structure and mechanical properties of the coatings did not show any sensitivity to the amount of oxygen when it changed between 15–25 vol % of total gas. However, other deposition parameters, namely temperature, pressure, and Cr-target voltage had a huge impact on the final structure, and thus, the mechanical properties of the coatings. The hard Cr_2O_3 coatings exhibited poor thermal stability at high temperatures and their hardness dropped to 16 GPa after annealing at 700 °C.

CHAPTER 5

ADHESIVE, TRIBOLOGICAL, AND CORROSIVE PROPERTIES OF Cr-O COATINGS

In this chapter, the previous research is continued to present one of the potential applications of the reactively sputtered hard Cr_2O_3 coatings. In the current section, 316L SS substrates were coated by hard Cr_2O_3 coatings and their tribological, corrosion, adhesion, and toxic ion release rate of the samples were tested in physiological saline solution according to the international standards. This chapter has been published in the journal "Environmental science and pollution research" as follows:

Hard Cr_2O_3 coatings on SS316L substrates prepared by reactive magnetron sputtering technique: A potential candidate for orthopedic implants, Mohammadtaheri, M., Li, Y. & Yang, Q. Environ Sci Pollut Res (2019).

My contributions to this paper were: conceived and designed the experiments, performed the experiments, interpretation of test results, and preparing the manuscripts under the supervision of Professor Qiaoqin Yang. The manuscript was reviewed and revised by my supervisor before submission to the journal for publication. The present manuscript is a modified version of the published paper. Copyright permission has been obtained and provided in the Appendix B.

Abstract:

316L stainless steel (SS) implants suffer from tribological and biocompatibility problems which limit their service lifetime. In order to improve the surface properties of 316L SS for orthopedic implant applications, hard chromium oxide coatings were applied on 316L SS substrates using a reactive magnetron sputtering technique. The morphological, structural, and phase compositional analysis were conducted on the deposited coatings by Scanning electron microscopy, X-ray diffraction, Raman spectroscopy, and X-ray photoelectron spectroscopy. The Rockwell C indentation tests were performed on the coated substrates to qualitatively evaluate the adhesion of coatings on the steel substrates. The surface characteristics of coatings were measured by using an optical profilometer. The mechanical properties of coatings were reported by measuring the Hardness and Young's modulus. The corrosion resistance of coated and uncoated SS substrates was compared using potentiodynamic polarization tests. An inductively coupled plasma optical emission spectrometry (ICP-OES) was employed to analyze the biocompatibility of the samples by measuring the amount of toxic Cr ions released after the immersion test. The results show that the coatings are adherent and composed of a single Cr_2O_3 phase with a hardness of 25 to 29 GPa. The corrosion resistance of the SS has been improved by applying a chromium oxide coating. The coated SS samples have also demonstrated better wear resistance and lower friction coefficient compared to bare SS samples under a reciprocating sliding condition in saline solution. The toxic level of the SS has been decreased by the Cr_2O_3 coating as much fewer Cr ions were released after immersion tests. These results indicate that the hard Cr_2O_3 coatings can be considered as a candidate for extending the lifetime of SS implants.

5.1. Introduction

316L SS has been widely used for orthopedic implants due to the comprehensive characters of low cost, high toughness, high corrosion resistance, and superior mechanical properties. However, 316L steel possesses a low hardness and it readily suffers from early degradation under corrosion and wear interactions[20,149]. Therefore, hard non-toxic corrosion resistant coatings which also adhere very well to substrates are required to solve the tribo-corrosion problems for orthopedic implant applications. This is due to the fact that tribological and corrosion processes substantially influence the biocompatibility of materials. For instance, pains, pseudotumor formation and inflammation in patients are the direct effects of wear debris and toxic ions released by Fe, Cr, and Ni chemical elements presented in 316L SS which, however, can be prevented by applying a wear, corrosion and biocompatible protective coating material on the implant surface [150]. In this context, various ceramic coatings have been employed by different researchers for biomedical applications. Among them, diamond-like carbon (DLC), chromium nitride (CrN), hydroxyapatite (HA), titanium nitride (TiN) and titanium niobium nitride (TiNbN) have been extensively investigated [150–157]. TiN and TiNbN coatings have been commercially used in hip and knee prostheses, while other coating systems are still under the different stage of investigation [150,156,157]. DLC coatings show poor adhesion on the substrates due to a high level of internal stress generated during the coating process, and severe delamination of DLC coatings usually occurs during in vivo tests which is still the main drawback for practical application[158,159]. HA coatings, due to their poor toughness and high brittleness, are not desired in applications where the material is subjected to various loading regimes, despite their excellent biomaterial properties [150,160]. Recently, researchers reveal that bulk Cr_2O_3 can reach a hardness value of up to 29.5 GPa[9–12,161]. It also possesses interesting properties such as a low coefficient of friction, high wear, and corrosion resistance, which makes it a potential protective coating for many applications [16,48,137]. To obtain Cr_2O_3 coatings, different techniques such as plasma-spray [1–3], sputtering [4,5], chemical vapor deposition (CVD) [6], and pulsed laser deposition [7], have already been used. However, high-quality Cr_2O_3 coatings with hardness as high as bulk Cr_2O_3 have only obtained by sputtering techniques so far [5,11,38,47,161]. Metallic chromium, due to its different valance state, can form various chromium oxide compounds, including CrO_3, Cr_8O_{21}, Cr_5O_{12}, $CrO_{2.906}$, CrO_2, Cr_3O_4, Cr_2O_3, CrO, and Cr_3O [9,38,49]. It has been confirmed that depending on the preparation method and deposition conditions, chromium oxides with different oxidation states, microstructure, chemical composition, and mechanical properties can be formed. For instance, single-phase Cr_2O_3 coatings with a hardness value of over 25 GPa can only be produced in a specific deposition condition. Cr_2O_3 coatings have already been used for various applications, such as advanced heat engines[15], digital magnetic recording units[16], gas bearing applications[17], electronics[18], and optics[19,20]. However, to the best of authors' knowledge, comprehensive investigations on the application of chromium oxide coatings for biomedical implants have not been performed yet. We have recently established a correlation between phase composition, microstructure, and mechanical properties of chromium oxide coatings and the deposition parameters in a reactive magnetron sputtering technique [161]. Now, in this research, authors are determined to continue the previous research and conduct a detailed study on the potential application of such hard chromium oxide coatings for biomedical applications. In the current research, tribological properties, corrosion, adhesion, and toxicity behavior of reactively sputtered chromium oxide coatings prepared on 316L SS are tested in physiological saline solution according to the international standards.

5.2. Materials and Methods

A RF-magnetron coater (SPLD620-FLR made by Plasmionique Inc., Rimouski, QC, Canada) was used to deposit chromium coatings on mirror-polished AISI 316L SS substrates with the dimension of 25 mm×25mm×5 mm. A 76.2 mm-diameter Cr target plate (99.95% pure) was installed in the system to produce chromium oxide coatings in the simultaneous presence of argon and oxygen plasma. The deposition parameters (Table 5-1) were the optimum ones determined from our previous research [161] in which chromium oxide coatings with a hardness value as high as bulk Cr_2O_3 (H~29 GPa) have been produced.

Table 5-1: Deposition parameters for hard Cr_2O_3 coating.

Cr-target power (W)	Cr-target voltage (V)	Ar flow rate (sccm)	O_2 flow rate (sccm)	Temperature (ºC)	Pressure (Pa)
360	260	30	5	150	0.16

The mean roughness (R_a) and wear volume of coatings were measured with the aid of an optical profilometer (New View 8000, manufactured by Zygo Corporation, Middlefield, CT, USA). The system was equipped with a 50X Mirau objective and using a standard filter type (bandwidth 125 nm for the light with λ=550 nm) for surface characterization measurements. Grazing incidence XRD (Rigaku XRD Ultima IV, CuK_α radiation) technique at an incidence angle of θ=7° was used to investigate the phase composition of the coatings. X'Pert HighScore Plus software was employed to compare the obtained XRD patterns with the standard databases (known as PDF files) to identify the chromium oxide peaks. Raman spectroscopy (Renishaw 2000 spectroscope, argon laser source λ= 514 nm, P= 0.5 mW) was used to identify different oxide states and support the XRD patterns. A silicon reference sample was used to calibrate the Raman spectroscope and the peak positions were fitted with the aid of Wire.3.3 software. The oxidation state of metallic chromium in the coatings was determined by X-ray Photoelectron Spectroscopy (XPS). The spectrometer used in this method was a Kratos Axis Ultra model with a monochromatic Al Kα radiation made by Kratos Analytical Ltd, Manchester, UK. Before XPS measurements, the surface contaminants were removed by sputtering the surface of coatings with Ar ions for 20 seconds. To compensate the charge effects during XPS analysis of insulating oxide coatings, the high-resolution spectrum of adventitious hydrocarbon was also monitored. The morphological characteristics of the coatings were observed by Scanning Electron Microscope (SEM). To evaluate the adhesion properties of coatings qualitatively, Rockwell “C” Indentation with a load of 981 N (100 kgf) was performed on three different areas of coatings according to ISO 26443 standard[135]. The imprints were then observed subsequently using an optical microscope. The hardness and Young's modulus of coatings were measured by nanoindentation technique (UMT with a Berkovich indenter at 3 mN load) according to ISO standard 14577-1 [129]. The Oliver & Pharr method [130] was used to interpret the nanoindentation load-displacement graphs and an average of fifty indentations was reported as the hardness value. The depth where the indenter penetrated to the surface was on one hand 20 times higher than the surface roughness and on the other hand, below 10 % of the coating thickness to minimize the uncertainty of hardness values. The corrosion resistance of the substrates was tested by electrochemical potentiodynamic polarization method exposing a surface area of 1 cm^2 of substrates into open to air physiological saline solution (0.9% NaCl). All electrochemical Potentiodynamic polarization measurements were carried out according to ASME standard G5 [132] at 298 K with a sweep rate of 0.6 V h^{-1} on a GAMRY electrochemical analyzer (Warminster, United States of America). A three-electrode cell, using a saturated calomel as the reference electrode and graphite as the counter electrode, was set up for this purpose. The test started after about an hour immersing the specimen in the electrolyte to reach a steady state condition for the open circuit potential.

Friction and wear tests were performed according to BS EN 1071-12 standard [134] using a wear test machine with ball-on-disk configuration (UTM with a 440-C martensitic steel ball, 10 N load). The test started after the samples were immersed in saline solution at room temperature. 10,000 cycles with a displacement length of 2.5 mm were set in linear reciprocating motion for all the samples. An inductively coupled plasma optical emission spectrometer (iCAP™ 7400 made by ThermoFisher Scientific, Massachusetts, USA) was employed to analyze the toxic level of the samples by probing the amount of toxic Cr ions released into the solution after 5 months immersion tests.

5.3. Results and Discussion

Figure 5-1(a and b) shows the SEM images from cross-section and surface morphology of chromium oxide coatings, while Fig.5-1 c and d compare the roughness of coatings and substrates, respectively. The coatings show dense nanocrystalline morphology with a very low roughness in the range of 1-2 nm. This smoothness of coatings can be an indication of coatings imitation from the bare substrate roughness during the film growth and nanocrystalline structure of coatings.

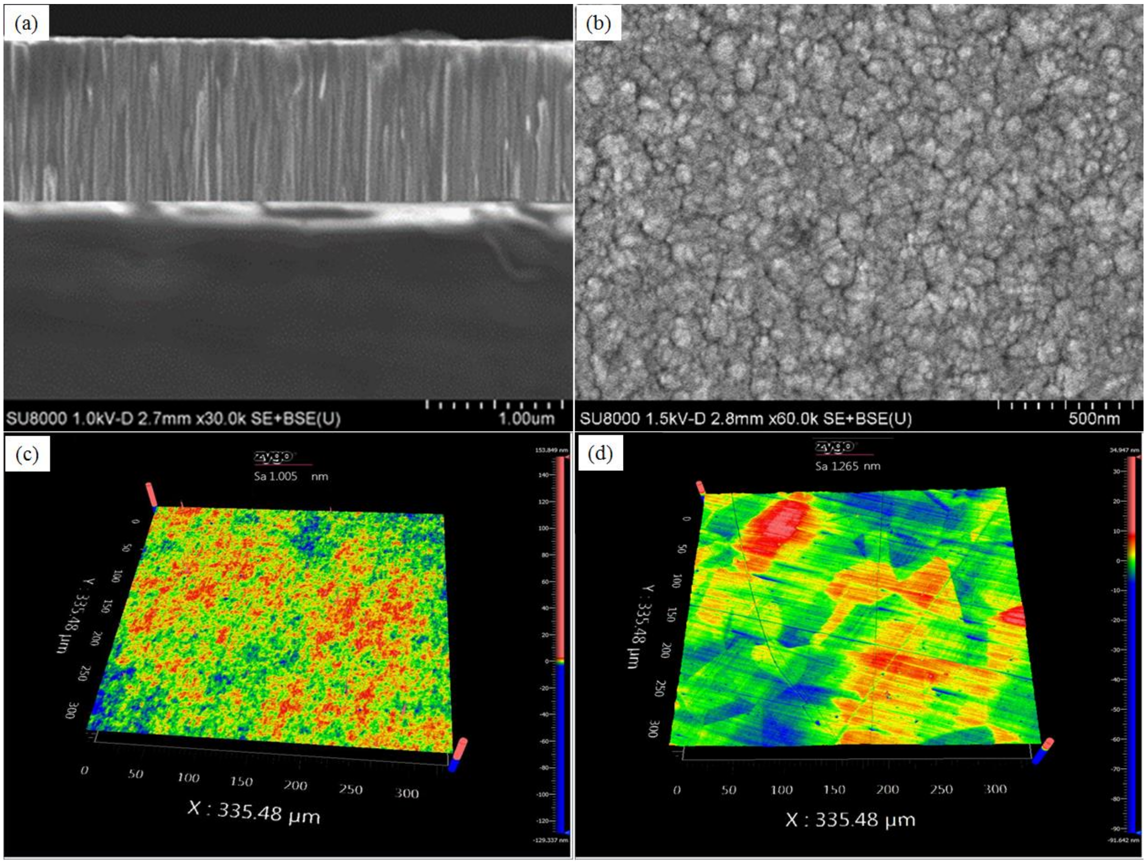

Figure 5-1: a) SEM cross-section, b) Surface micrograph, c) Surface roughness of chromium oxide coatings, and d) Surface roughness of bare 316L substrates

The structural analysis conducted by XRD (Figure 5-2-a) on chromium oxide coatings showed that the coatings were only composed of Cr_2O_3 phase as the positions of the peaks were all matched with the corundum Cr_2O_3 peak positions according to (PDF-98-009-7850) databases. Raman spectroscopy was also employed to backup XRD data since it is a recognized technique to analyze both amorphous and crystalline oxide materials [141]. In Figure 5-2-b, Raman shifts observed at 305 cm^{-1}, 345 cm^{-1}, 547 cm^{-1}, and 606 cm^{-1} are well-match with the Raman modes of crystalline Cr_2O_3 mentioned in literature [28,30,142]. Moreover, the existence of single Cr_2O_3 phase in the coatings was confirmed by the high-resolution Cr 2p XPS analysis (Figure 5-2-c). The Cr 2p high-resolution spectrum was composed of Cr $2p_{3/2}$ and Cr $2p_{1/2}$ splits with Cr $2p_{3/2}$ binding energy at 576.6 eV and the energy gap between the splits was 9.7 eV, which is consistent with Cr_2O_3 [128]. Therefore, both the Raman and XPS results agreed well with the XRD data and confirmed that the coatings were composed of one Cr_2O_3 crystalline phase.

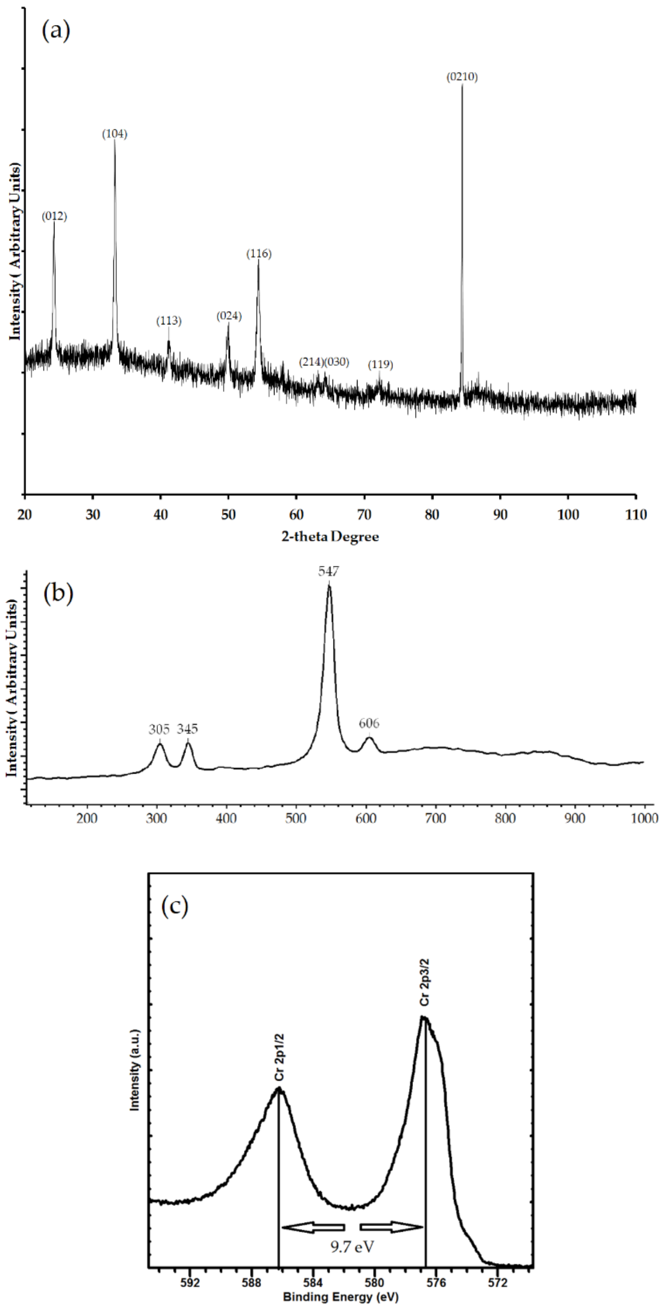

Figure 5-2: a) XRD patterns, b) Raman spectra and c) the high-resolution Cr 2p XPS spectrum of deposited oxide coatings

The adhesion quality of chromium oxide coatings was evaluated with Rockwell-C indentation tests, where the imprints were observed by an optical microscope for a sign of any failure or delamination. The results showed that the coatings conformed well to the indentation, indicating that they have an acceptable adhesion without any adhesive delamination (Figure 5-3).

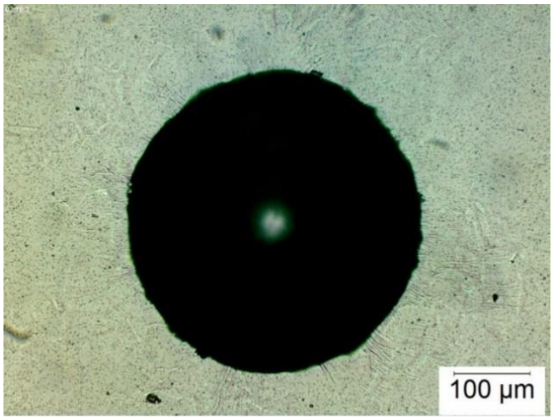

Figure 5-3: Adhesion quality of chromium oxide coatings on SS316L substrates performed by Rockwell-C tester

Figure 5-4 indicates the hardness and Young's modulus of bare 316L SS substrates and chromium oxide coated substrates. The average hardness and Young's modulus values of chromium oxide coated substrates are about 29.76 and 304.9 GPa, respectively, which is in agreement with the reported values for the bulk Cr_2O_3 in literature [9–12,148]. The bare 316L substrates have a hardness value significantly lower than chromium oxide coatings and in agreement with the literature reported values [162].

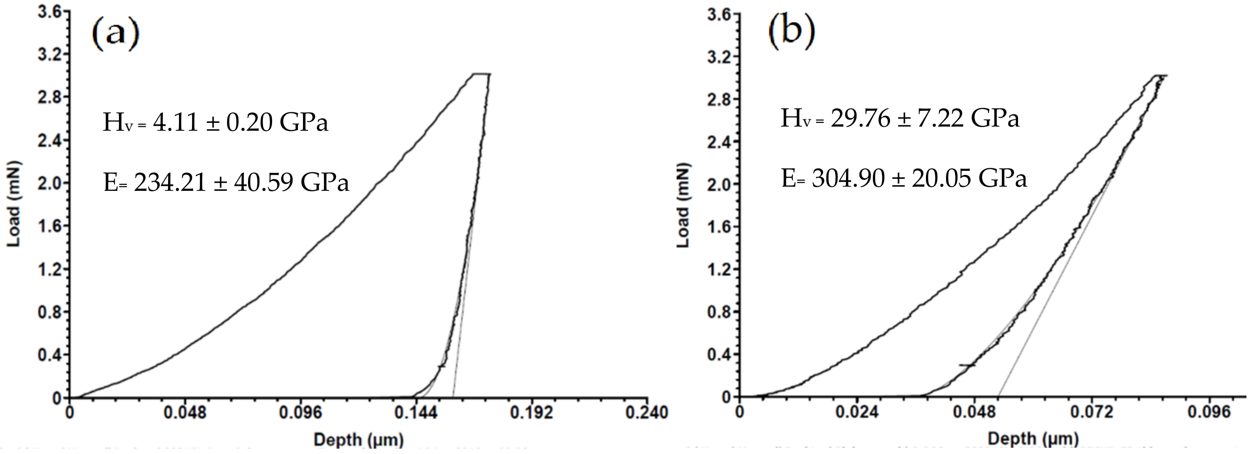

Figure 5-4: a) indentation curve measured on bare SS316L and b) Indentation curve measured on a 1.5 µm thick chromium oxide coating. H_V means the plastic Vickers hardness and E the elastic modulus corrected for deformation of the diamond.

Figure 5-5 shows the Potentiodynamic polarization curves of the 316L SS and Cr_2O_3 coated substrates obtained in a motionless open to air physiological saline solution at room temperature. Fitting the anodic and cathodic portion of polarization curves by a customized python module [133] resulted in the Tafel plots and corrosion data. Table 5-2 compares the obtained corrosion data (corrosion potentials (Ecorr), corrosion current densities (icorr) and polarization resistance (R_p)) for both the 316L SS and Cr_2O_3 coated substrates. Figure 5-5 shows that the samples obviously have a passivation region regardless of sample type and the corrosion resistance of the substrates is enhanced when they were coated by chromium oxide coatings.

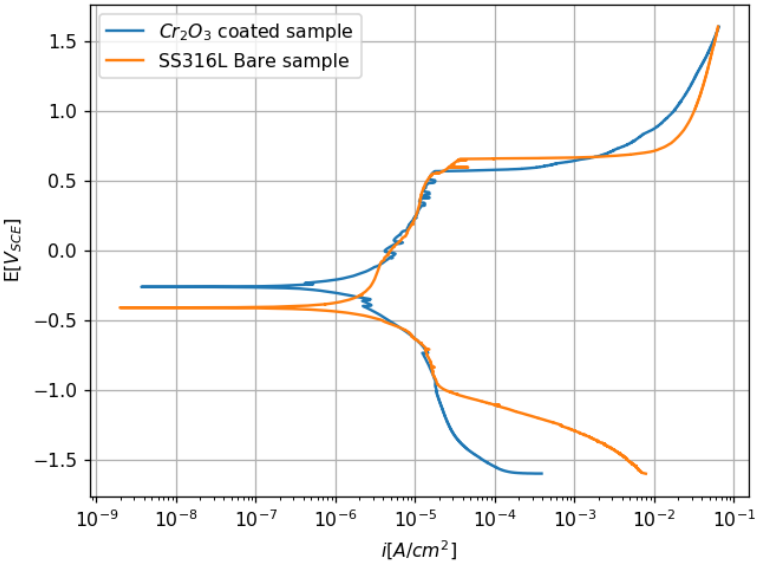

Figure 5-5: Polarization curves for 316L stainless steel and Cr_2O_3 coated substrates.

Table 5-2 shows that the corrosion potential (Ecorr) increases after applying chromium oxide coatings, with an Ecorr of −0.41 V for bare 316L SS substrates and −0.19 V for the sample with the chromium oxide coatings. Furthermore, the corrosion rates can be evaluated by comparing the corrosion current densities. This is due to the proportional relationship between the corrosion current densities and the kinetics of corrosion reactions. The corrosion current density of bare SS316L substrates is about 3 $\mu A/cm^2$ which decreases to 1 $\mu A/cm^2$ with applied chromium oxide coatings. The decrease in icorr is a confirmation for the corrosion resistance improvement of Cr_2O_3 coated samples when they are compared with the bare substrates. The R_p term is a definition for the charge transfer resistance in the solution–metal interface, which can be used as a parameter in anticipating the corrosion protection properties of coatings on metal surfaces [20]. Based on the polarization resistance data, the chromium oxide coatings have improved the R_p from 30.662 to 40.156 KΩ, so they can be an effective protective coating for 316L SS substrates in the physiological saline solutions.

Table 5-2: Electrochemical parameters obtained from polarization curves in Fig. 40

Samples	**Ecorr(v)**	**Icorr (μA/cm^2)**	**Rp (KΩ)**
Bare SS316L	-0.41	3	30.662
Cr_2O_3-Coated	-0.19	1	40.156

Figure 5-6 shows the effect of chromium oxide coatings on the wear behavior and friction coefficient of bare SS316L substrates. After applying hard chromium oxide coatings, both the wear rate and friction coefficient decreased significantly (Figure 5-6-c and d).

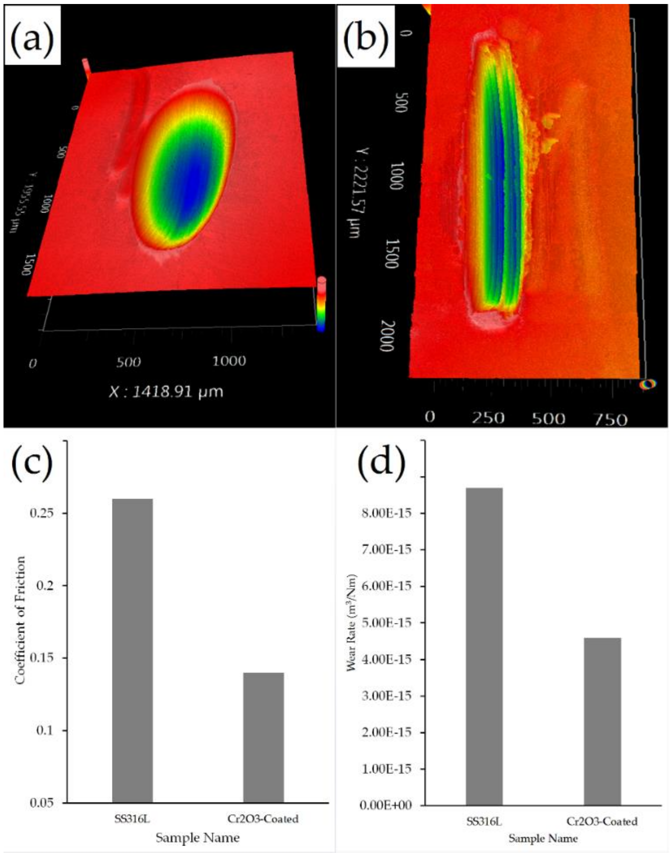

Figure 5-6: Effect of hard chromium oxide coatings on tribological properties of SS316L substrates. a) wear volume of the bare substrate, b) wear volume of the coated substrate, c) coefficient of friction and d) wear rate of both bare and coated substrates.

The wear rate of substrates can be calculated using the following formula [134]:

$$W = \frac{\mathrm{V}}{2\mathrm{LSN}} \tag{5.1}$$

Where V is the volume lost from substrates (m^3); L is the applied load (N); S is the stroke length (m); N is the total number of reciprocations.

As shown in Figure 5-6, the wear rate is about 50% lower for coated substrates compared to bare 316L SS. The friction coefficients, hardness, and film adhesion can influence the wear life of protective coatings [44]. Cr_2O_3 coatings act as solid lubricants and tend to reduce the friction coefficient [163]. The adhesion measurements (Figure 5-3) confirm that chromium oxide coatings have good adhesion on SS316L substrates. Hence, the enhancement observed in the wear resistance can be attributed to the high hardness and low friction coefficient of chromium oxide coatings which also have good adhesion on 316L substrates.

Figure 5-7 illustrates the amount of toxic chromium ions released from substrates by probing saline solution used in the immersion tests. The optical emission spectroscopy results indicate that the chromium oxide coated samples released negligible chromium ions of about 0.01 ppm compared to 0.09 ppm for the bare substrates.

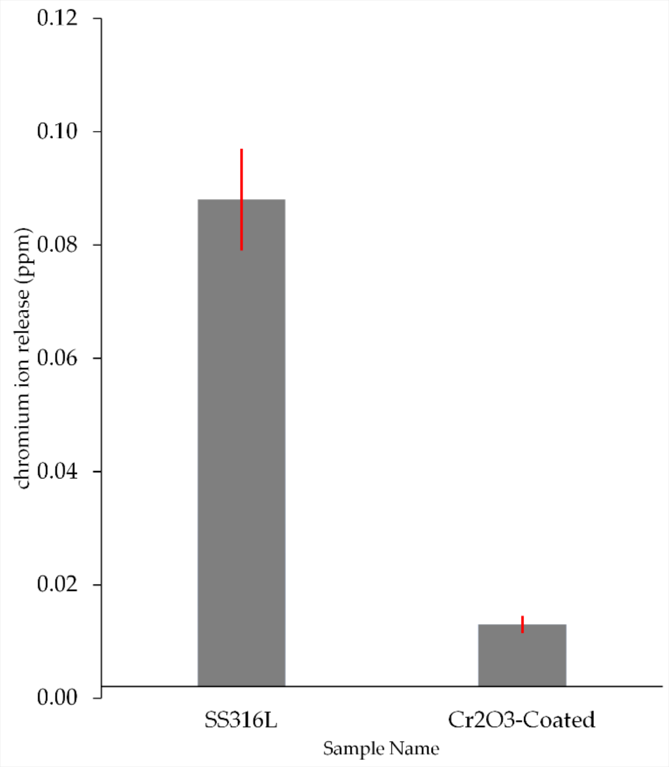

Figure 5-7: Chromium ion released from substrates exposed to Saline solution at 37°C.

Decreasing chromium and nickel ions released from 316L steel in artificial body fluid media at 37 °C have been investigated by previous researchers, however, no significant success has been reported. In this regard, Diaz et al [164,165] investigated the effect of passivation layer thickness on the amount of chromium and nickel ions released from 316L SS used as prosthetic implant materials in simulated body fluids. In their research, the passivation layer thickness was changed by an anodization process and the metal ion release was measured using atomic absorption spectroscopy after 1, 6, 11 and 15 days, respectively. They showed that the amount of nickel and chromium ions detected in body fluids were proportional to the passivation layer and increased from 2 to 10 times as the passivation layer increased. Moreover, two other researchers, Kocadereliet et al [166] and Agaoglu et al [167], investigated the amount of nickel and chromium ions released from SS orthodontic fixtures in the patients' salivary samples. They showed that considerable amounts of chromium and nickel are detected in the salivary samples. Therefore, our research implies that Cr_2O_3 coatings are suitable for redcuing toxic ion release from SS implants in biological environments.

5.4. Conclusions

The compatibility of hard chromium oxide coatings prepared by reactive magnetron sputtering on SS316L substrates has been investigated for biomedical applications at room temperature in Saline solution. According to structural and phase compositional analysis, dense Cr_2O_3 coatings were successfully prepared on the steel substrate at appropriate deposition parameters. The coatings have a high hardness and good adhesion on SS316L substrates. The corrosion results based on potentiodynamic polarization measurements showed an enhancement in corrosion resistance for chromium oxide coated stainless steel samples compared to the bare SS substrate. The corrosion current density for chromium oxide-coated stainless steel is three times lower than uncoated stainless steel, suggesting the presence of a higher resistant passive film on the coatings. Tribological test results exhibited that Cr_2O_3 coated substrates possessed better wear resistance under sliding wear test conditions in saline solution. This can be related to the properties such as high hardness, low coefficient of friction, and good adhesion of chromium oxide coatings.

The ion release results from the ICP-OES measurements indicate that there were negligible chromium ions (at the parts per billion (ppb) level) released from the chromium oxide-coated samples into saline solution after 5 months immersion under testing conditions. These results indicated that hard Cr_2O_3 coatings can be a good candidate for extending the lifetime of biomedical stainless-steel implants, however, more researches are required to pave the way for orthopedic and other possible medical implant applications of chromium oxide coatings.

CHAPTER 6

Cr_2O_3-Cr AS AN INTERLAYER FOR DIAMOND NUCLEATION

In this chapter, the reactively sputtered Cr_2O_3 interlayers are introduced as a potential candidate to enhance the diamond nucleation on WC-Co inserts. This is due to the fact that Cr_2O_3 possesses a demonstrated diffusion barrier property and close thermal expansion coefficient to diamond. This chapter has been published in the journal “Surface and Coatings Technology” as follows:

Diamond nucleation and growth on WC-Co inserts with Cr_2O_3-Cr interlayer, Fan Ye, Masoud Mohammadtaheri, Yuanshi Li, Sheida Shiri, Qiaoqin Yang, Ning Chen, Surface & Coatings Technology 340 (2018) 190–198.

My contributions, as a co-author, to this paper, were: deposited the coatings on the substrates, cooperated in analyzing and interpretation of test results. The present manuscript is a modified version of the published paper. Copyright permission has been obtained and provided in the Appendix B.

Abstract:

Cr_2O_3-Cr interlayer was prepared by magnetron sputtering to restrict graphite formation on WC-Co before diamond nucleation. Continuous diamond coatings containing little graphite phase were successfully deposited on single Cr_2O_3 interlayered WC-Co substrates. For Cr_2O_3/Cr duplex interlayer, a low nucleation density was observed at a low CH_4 concentration, but a continuous diamond coating was readily obtained with an increased CH_4 concentration during the nucleation stage. X-ray diffraction and X-ray absorption analysis reveals that the Cr top

layer was carburized to Cr_3C_2 and Cr_7C_3 after diamond deposition while the Cr_2O_3 layer remained unchanged. In addition, the indentation test shows that the diamond coating has poor adhesion to the substrate with a single Cr_2O_3 interlayer, while the adhesion was significantly enhanced with the Cr_2O_3/Cr duplex interlayer combined with a high CH_4 concentration for nucleation.

6.1. Introduction

Cemented carbide cutting tools are widely used in the machining industry due to their high modulus of elasticity, high thermal conductivity, and wide temperature range for operation. However, they are subject to high wear rate when cutting aluminum alloys, green ceramics, and abrasive composites. The fast development of new materials appeals for the research of new cutting tools. Diamond has unique properties such as high hardness, corrosion resistance and chemical inertness [168]. As a result, it is considered as one of the most promising coating materials to improve both the lifetime and cutting productivity of cemented carbide cutting tools. The poor adhesion between diamond coatings and cemented carbide cutting tools restricts their wider application. This is caused by several factors. The major factor is the Co, a binder phase inside cemented carbide, diffuses to the surface during diamond deposition to catalyze the formation of graphite before diamond nucleation [169]. The presence of graphite in the interface between diamond and carbide substrate results in deteriorated adhesion. Additionally, the mismatch of thermal expansion coefficient between diamond and carbide substrate would lead to large thermal compressive stress inside diamond coating once the coating is cooled down from high deposition temperature [170], even though the existence of compressive stress may improve the wear resistance of the diamond coatings by suppressing the crack propagation under load [171]. Various methods have been applied to solve the problems. One way is to use chemicals including acid and Murakami's solution to remove the Co from the near surface of WC-Co substrate [172–174]. However, the lack of Co on the surface may affect the toughness of the inserts [175]. Another way is to apply interlayers to suppress the diffusion of Co. Many interlayers have been tried so far, including CrN, Cr, Ti, Al, W, SiC [176–182]. Our group's previous research has discovered Al as an efficient interlayer material to block the diffusion of Co due to the formation of an aluminum oxide [183,184]. However, Al is soft and easily damaged during diamond seeding pre-treatment in an ultrasonic bath. In this work, Cr_2O_3 is chosen as an interlayer candidate considering its high hardness and demonstrated diffusion barrier property. To compare the efficiency of Cr_2O_3 in suppressing the diffusion of Co, Cr_2O_3 was deposited on as-polished and Murakimi's solution and Caro's acid etched bare WC-Co substrates, respectively. Meanwhile, Cr_2O_3/Cr interlayer is designed to illustrate the mechanism of nucleation and growth of diamond coating on Cr_2O_3 and Cr.

6.2. Experiment Methods

Commercial cemented carbide inserts (Grade K68, WC-6%Co) purchased from Kennametal were chosen as the substrates. They were firstly polished by sandpaper and diamond suspension into the mirror-like surface and then cleaned by ethanol. One group of substrates were pre-etched by Murakami's solution (10 g $K_3[Fe\ (CN)_6]$ +10 g KOH+100 mL H_2O) for 10 min and followed by Caro's acid (3 mL H_2SO_4 (96%) +88 mL H_2O_2 (30%)) for 10s to remove Co from the surface. The interlayers were deposited by magnetron sputtering system manufactured by Plasmionique with RF power of 300 W. The Cr_2O_3 layer was deposited at the temperature of 150 °C by sputtering 99.95% Cr target in the plasma of O_2 and Ar. The flow rates of the O_2 and Ar were 5 sccm and 30 sccm, respectively and the deposition pressure was 0.76 mTorr. Prior to the deposition of Cr_2O_3, a thin layer of Cr was deposited for 5 min to enhance the adhesion. The thickness of Cr_2O_3 after 3 h deposition is around 250–300 nm measured by Zygo Newview 8000 optical profilometer. Cr layer was deposited by directly sputtering Cr target in an Ar plasma. The deposition pressure was also kept at 0.76 mTorr. The thickness of the top Cr layer was around 70–75 nm after 15 min deposition. The diamond coating was deposited by a microwave plasma enhanced chemical vapor deposition (MPCVD) manufactured by Plasmionique in the gas mixture of H_2 and CH_4. The pressure was 23 Torr and the methane concentration was 1 vol%. The microwave power was kept at 800 W. The substrate temperature measured by the thermocouple at the back of the substrate was around 670 °C. The thickness of the diamond coating after 7 h deposition was around 1.2 µm. To increase the nucleation, the nano-diamond powders with a diameter of 3–4 nm were applied to scratch the surface of all the samples in an ultrasonic bath prior to the diamond deposition. Renishaw 2000 Raman Microscopy with Ar+ laser (wavelength of 514.5 nm) was used to characterize the bonding state of Cr_2O_3 interlayer and diamond coatings. Rigaku Ultima IV Grazing Incident X-ray Diffraction (GIXRD) with Cu Kα radiation was employed to identify the phases of as-deposited interlayers.

The incident angle was 7°. JEOL JSM-6010 LV SEM was used to observe the morphology and microstructure of deposited diamond coatings. X-ray diffraction (XRD) with Co Kα radiation was used to identify the phase composition of the samples after diamond deposition. Cr K edge X-ray Absorption Near Edge Structure (XANES) Microscopy with fluorescence mode was employed to observe the chemical state change of interlayers after diamond deposition. The X-ray absorption spectra were measured in Hard X-ray MicroAnalysis (HXMA) beamline of Canadian Light Source. Rockwell C indentation tester manufactured by Instron Wolpert with a load of 1471 N was used to compare the adhesion strength of diamond coatings on the WC-Co inserts. The AXIS SUPRA photoelectron spectrometer manufactured by Kratos Analytical was employed to measure the X-ray photoelectron spectra (XPS) of the imprint areas of the diamond coatings after adhesion testing. The photoelectrons were collected from a circular area with 27 μm diameter. Monochromatic Al Kα excitation was used with the tube voltage set as 15 kV and the emission current set as 25 mA.

6.3. Results and Discussion

6.3.1. Characterization of Interlayers

Figure. 6-1(a) shows the Raman spectrum of the as-deposited Cr_2O_3. For Cr_2O_3, only two A_{1g} and five E_g vibrational modes are Raman active. The detailed reference table can be found in Mougin and Shim's work [30,32]. In the Raman spectrum of the deposited Cr_2O_3 layer, it is obvious to see one A_{1g} vibration at the peak of 550 cm^{-1} and four E_g vibrations at the peaks of 294 cm^{-1}, 350 cm^{-1}, 526 cm^{-1} and 611 cm^{-1}, respectively. The slight shift of the peaks may be affected by the stress inside the coating. The Grazing Incident XRD patterns of the sputtered Cr_2O_3 interlayer and Cr_2O_3/Cr interlayer are shown in Figure. 6-1(b), confirming that the Cr_2O_3 interlayer is mainly composed of crystalline Cr_2O_3, as all the visible XRD peaks match well with Cr_2O_3 (PDF#38-1479). In the Cr_2O_3/Cr interlayer, the existence of Cr (110) and Cr (200) peaks (PDF#06-0694) confirms the presence of the Cr sublayer, but two small Cr_2O_3 peaks of (006) and (119) disappear due to the cover of a Cr top layer. The SEM surface images of Cr_2O_3 and Cr_2O_3/Cr interlayers before and after seeding are shown in Fig. 6-2. It can be seen that a lot of scratches were created after diamond seeding for 5 min on both interlayers (Fig. 6-2-c and d). Compared with single Cr_2O_3 interlayer, more defects were created on Cr_2O_3/Cr interlayer (see

Fig. 6-2-e and f) and more diamond agglomerates were embedded onto Cr sublayer since Cr is much softer than Cr_2O_3.

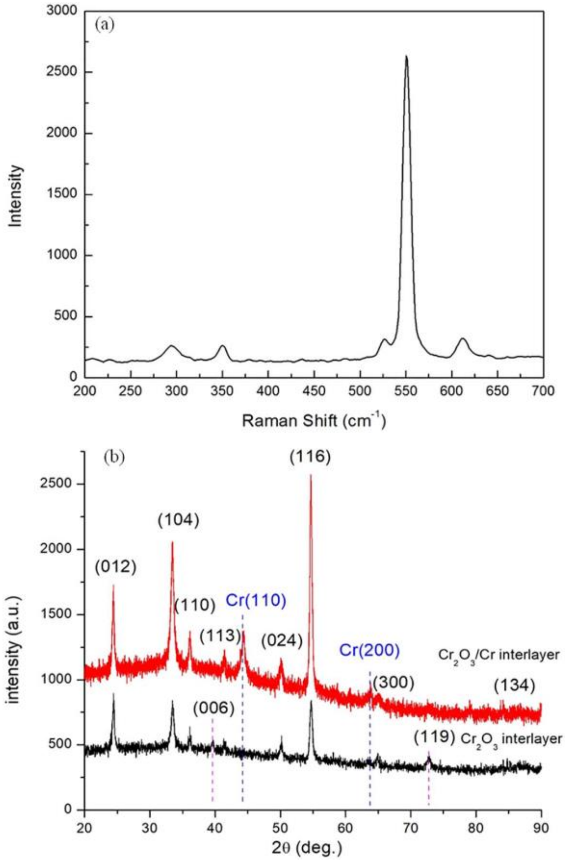

Figure 6-1: (a) Raman Spectrum and (b) Grazing Incident XRD patterns of Cr_2O_3 interlayer and Cr_2O_3/Cr interlayer.

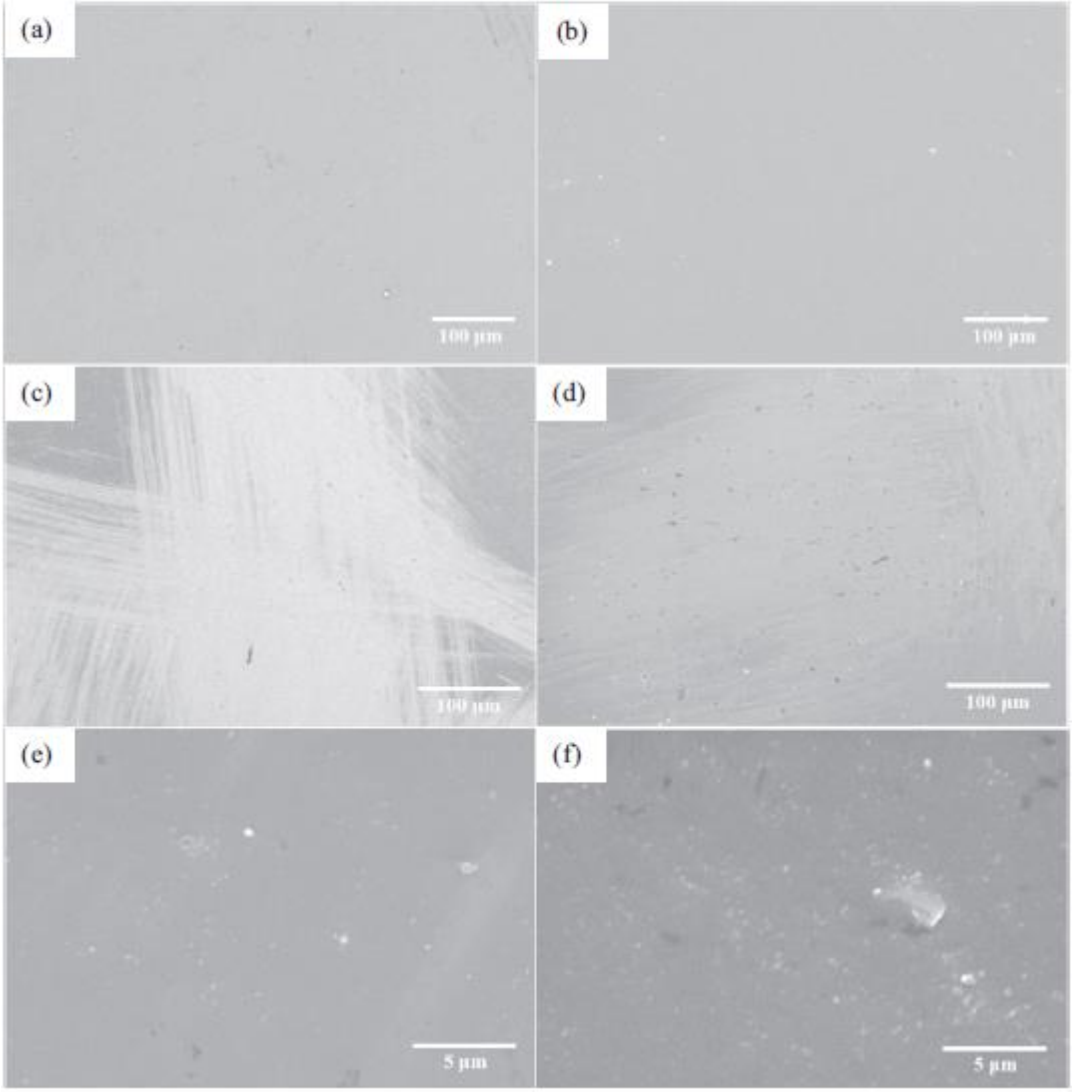

Figure 6-2: SEM surface images of as-deposited interlayer (a,b), after diamond seeding showing scratches (c,d) and diamond seeds embedded (e,f) of Cr_2O_3 interlayer (a,c,e) and $C_{r2}O_3$/Cr interlayer (b,d,f), respectively.

6.3.2. Characterization of Diamond Coatings

Raman spectra of diamond coatings are shown in Fig. 6-3. The diamond peak of 1337 cm^{-1} can be observed in the samples with Cr_2O_3 interlayer and etched surface with Cr_2O_3 interlayer. A broad peak around 1500 cm^{-1} is found in the pre-etched sample with Cr_2O_3 interlayer, which is usually ascribed to the sp^2 amorphous carbon inside the coating [185]. In the sample with a single Cr_2O_3 interlayer, another broad peak located around 1600 cm^{-1} appears, which is attributed to the graphite phase [186]. Considering the Raman sensitivity (for Ar+ laser with a wavelength of 514.5 nm) of the π-bonded amorphous carbon and graphite phase, which is 50 times higher than sp^3 bonded diamond phase, the diamond phase dominates the coating [187]. On the sample with Cr_2O_3/ Cr duplex interlayer, the Raman peaks are more complicated, indicating various carbon phases are mixed inside the diamond coating. Besides the diamond peak located at 1334 cm^{-1} and the microcrystalline graphite peak at 1574 cm^{-1} [188], some other peaks can be observed as well. The origin of the peak at approximately 1240 cm^{-1} could be attributed to the peak in the phonon density of states (PDOS) of diamond or transpolyacetylene [189]. The shoulder around 1300 cm^{-1} could be ascribed to the sp^3 bonded amorphous carbon [190]. The small broad peaks from 1400 to 1470 cm^{-1} might be due to the existence of transpolyacetylene [189]. The shoulder at around 1615 cm^{-1} is attributed to the D band of microcrystalline graphite or disordered carbon [188].

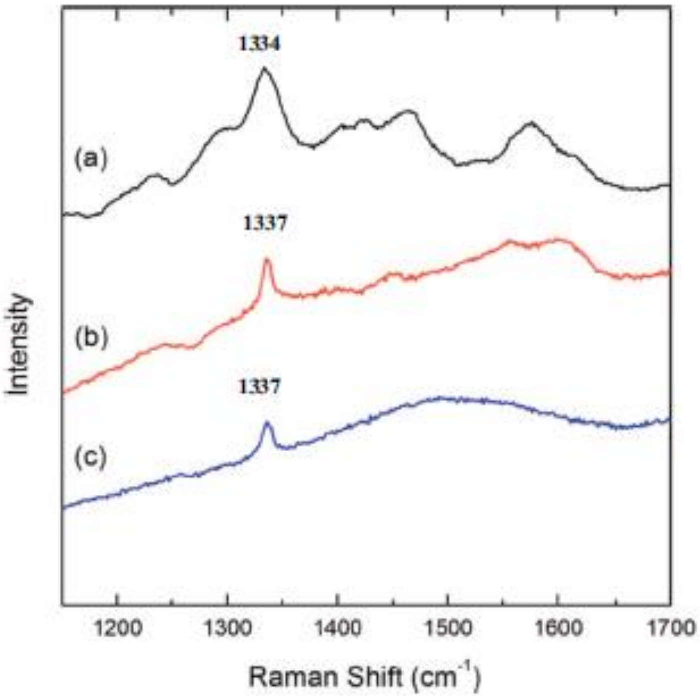

Figure 6-3: Raman spectra of diamond coatings grown on (a) Cr_2O_3/Cr interlayered, (b) Cr_2O_3 interlayered, (c) pre-etch/Cr_2O_3 interlayered WC-Co substrates.

It should be noted that the Raman peak of natural diamond is located at 1332 cm^{-1}, while the peak of diamond coating grown on Cr_2O_3 interlayer is shifted upward to 1337 cm^{-1}, and the peak of diamond grown on Cr_2O_3/Cr layer is shifted to 1334 cm^{-1}. This upward shift of the diamond peak can be explained as a result of compressive stress inside the coating. Fig. 6-4 demonstrates the microstructure of diamond crystals grown on different interlayers. Most of the diamond crystals grown on the pre-etched WC-Co substrate with Cr_2O_3 interlayer show {111} octahedral face as shown in Fig. 6-4 (a). On the Cr_2O_3 interlayered sample without pre-etching, the diamond crystals demonstrate {111} face along with some other faces, as shown in Fig. 6-4(b). CVD deposited diamond crystals usually consist of both {111} and {100} faces. The diamond crystal shape depends on the ratio of growth rate in ⟨100⟩ and ⟨111⟩ direction [191]. Low temperature and low hydrocarbon concentration favor the growth in ⟨111⟩ direction, while high temperature and high hydrocarbon concentration facilitate the growth in ⟨100⟩ direction [192]. Considering the diamond grown on single Cr_2O_3 interlayered sample includes microcrystalline graphite phase inside it, as revealed from its Raman spectrum shown in Fig. 6-3 (b), we can attribute the various shapes of diamond grains to the presence of graphite, which might change the hydrocarbon concentration on the surface. The grain size of the diamond on a single Cr_2O_3 interlayered sample is also smaller than the diamond grown on the pre-etched sample. Nevertheless, continuous coatings have been deposited on both single Cr_2O_3 interlayered samples whereas the diamond grown on Cr_2O_3/Cr interlayered sample is dispersed particles with localized clusters (see Fig. 6-4(c)), showing lower nucleation density. As shown in Fig. 6-4(c), the diamond prefers to nucleate and grow at the scratch area with high surface defect density. In the magnified image, shown in Fig. 6-4(d), we can see that only diamond clusters, instead of continuous diamond coatings, have been obtained even at the scratch area and each diamond cluster consists of large {111} faceted diamond crystals surrounded by nano-diamond grains or amorphous carbon. So that it would be more reasonable to attribute the broad Raman peaks shown in Fig. 6-3(a) to the amorphous carbon or transpolyacetylene in the grain boundaries. However previous findings [180,181] have shown that diamond fragments were embedded into softer Cr layer during the seeding or fluidized bed pinning to provide nuclei for diamond growth, and thus continuous diamond coating could be grown on Cr layer. The possible reasons that no continuous diamond coating formed on Cr_2O_3/Cr interlayered samples in the present work will be discussed in the following sections.

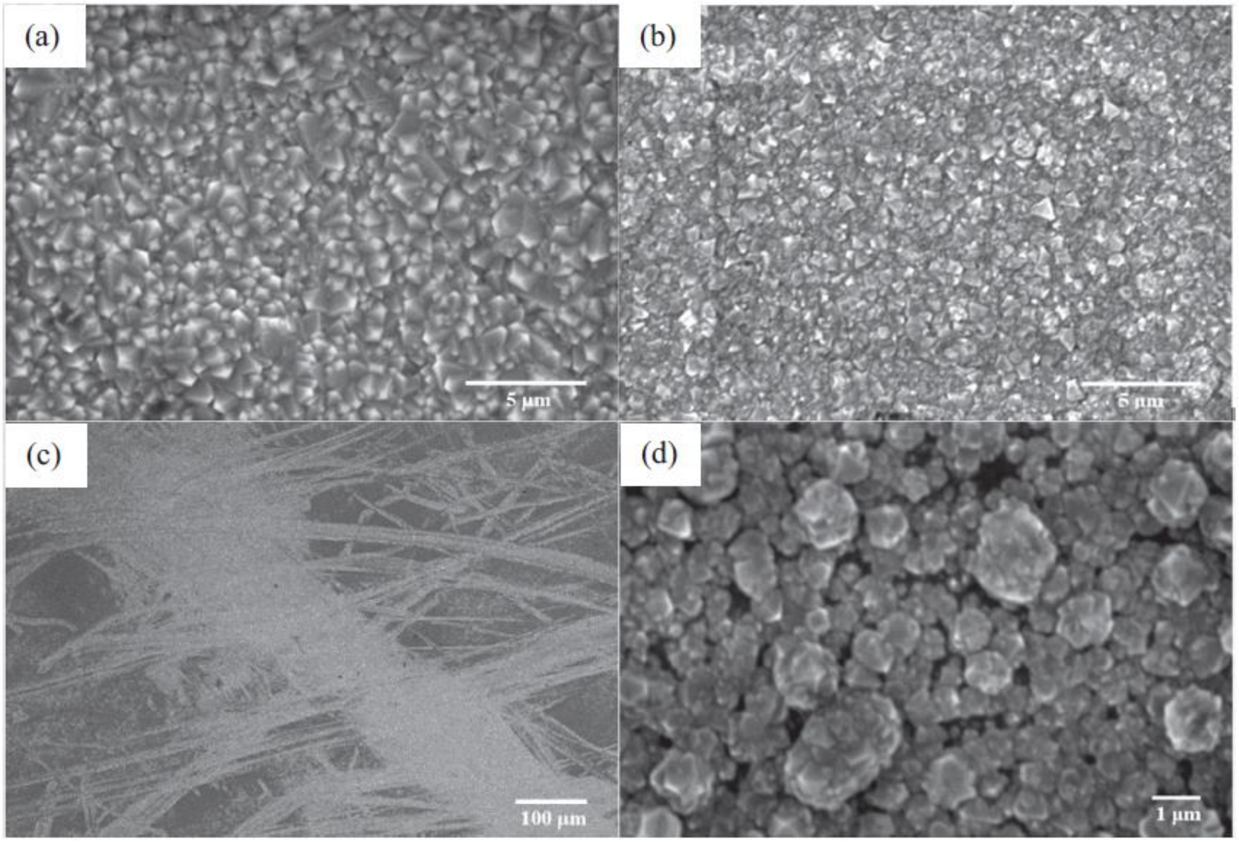

Figure 6-4: Microstructures of diamond coating deposited on (a) pre-etch/Cr_2O_3 interlayered, (b) Cr_2O_3 interlayered, (c) Cr_2O_3/Cr interlayered (low magnification) and (d) $C_{r2}O_3$/Cr interlayered (high magnification) WC-Co substrates.

6.3.3. Phase Change of Interlayers after Diamond Deposition

The XRD patterns of various samples after diamond deposition are shown in Fig. 6-5. Diamond (111) peak at 52° (PDF#06–0675) is clearly seen for all the samples. This is in agreement with the SEM images shown in Fig. 6-4. Additionally, Cr_2O_3 peaks (PDF#38-1479) appear in all the samples and there are no other peaks in the Cr_2O_3 interlayered samples, while the XRD pattern of Cr_2O_3/Cr interlayered samples shows Cr_3C_2 (111) peak at 41.1° (PDF#65-0897) and Cr_7C_3 (600) peak at 52.4° (PDF#11-0550) in addition to the Cr_2O_3 peaks. The Cr_7C_3 (421) peak (PDF#11-0550) is overlapped with the diamond (111) peak. These results indicate that the Cr_2O_3 interlayer was not carburized during diamond deposition, but the Cr layer was carburized to various carbides. This result is in agreement with previous findings from other researchers [193,194].

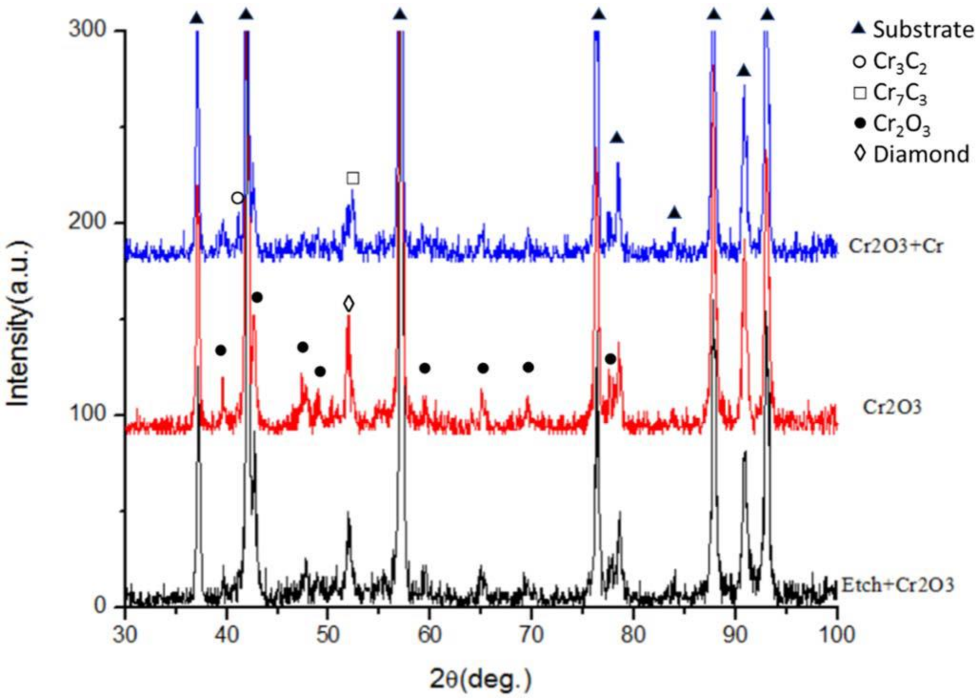

Figure 6-5: XRD patterns of various interlayered samples after diamond deposition.

XANES was further conducted to illustrate the chemical state of the interlayers after diamond deposition. Fig. 6-6 shows the XANES spectra of all the samples. In general, each Cr XANES spectrum has three components [195]: (1) the pre-edge region where the energy is lower than major absorption energy, (2) the near-edge region, where the energy is within 30 eV around the absorption energy, and (3) the post-edge region, where the energy is 30 eV or higher than the absorption energy.

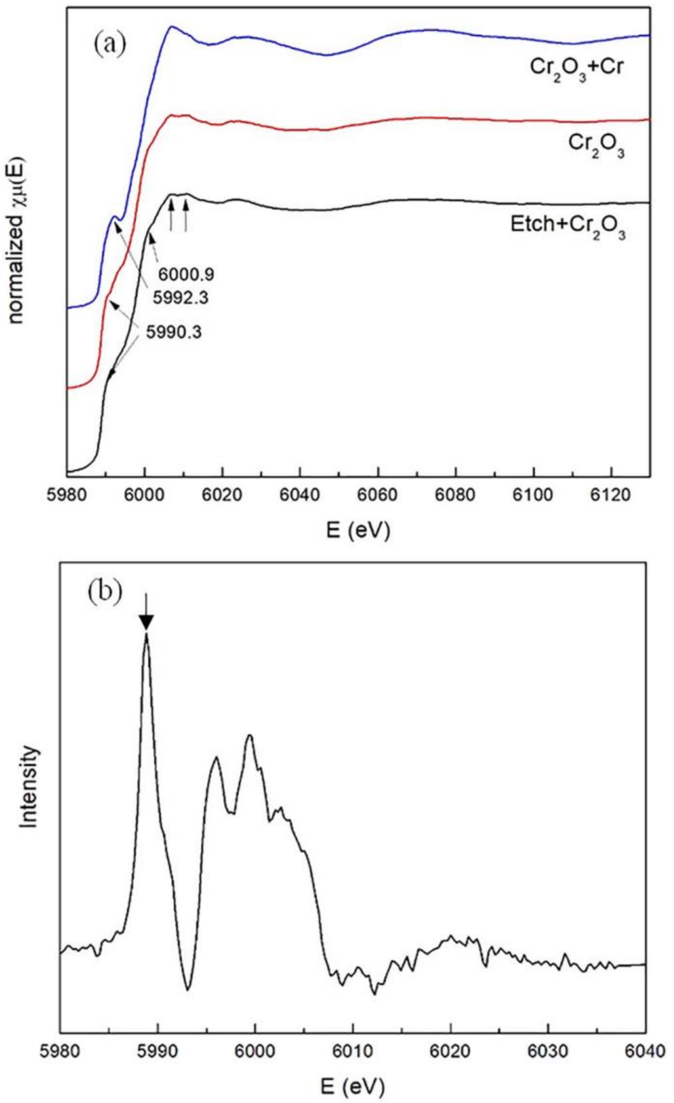

Figure 6-6: (a) Cr K edge X-ray absorption spectra for all the samples and (b) first derivative of XANES spectrum of Cr_2O_3/Cr interlayered sample.

From Fig. 6-6(a), it is noticeable that the Cr K edge XANES spectra of Cr_2O_3 deposited on bare WC-Co substrate and pre-etched substrate are almost the same. As reported in other literature [195–198], the feature of Cr_2O_3 spectrum is the double peaks in the near-edge region and the shoulder at approximately 6000 eV. Combining the XANES spectra of Cr_2O_3 with the XRD pattern shown in Fig. 6-5, it is reasonable to conclude that the Cr_2O_3 interlayer keeps the same chemical state after diamond deposition. The XANES spectra of Cr and CrC_x look very similar. They both have a pre-edge peak. However, the energy of the pre-edge peak of Cr is higher than chromium carbide. Additionally, Cr has more peaks in the post-edge region [195–197]. After comparing with the reference spectra, we confirmed that the XANES spectrum of Cr_2O_3/Cr interlayered sample is from chromium carbide, indicating the Cr layer has been carburized. Fig. 6-6(b) is the first derivative of the XANES spectrum of Cr_2O_3/Cr interlayered sample. The first peak of the derivative curve is located at 5988.8 eV, which is called edge energy E_0. The position of the pre-edge peak depends on the chemical state of the absorbing element. In the case of chromium carbide, the pre-edge peak is caused by the transition of an electron from 1s to 3d and admixed with carbon's p orbital to form hybridized Cr_3d-C_2p states [198,199]. From the result reported by Olovsson, the edge energy E_0 increases with the carbon concentration inside the chromium carbide [198]. The upward shift of E_0 means the higher ionization of the chemical state of the absorbing Cr atoms when carbon fraction increases [198]. From Olovsson's result [198], E_0 is 5988.7 eV when C concentration is 42–47% and increases to 5989.1 eV when C concentration is 67%. So that the carbon concentration in our carburized Cr interlayer is estimated around 50–65%.

6.3.4. The Influence of Interlayer on Diamond Nucleation

The appearance of graphite peak at 1600 cm^{-1} in the Raman spectrum in Fig. 6-3(b) implies that the Cr_2O_3 interlayer itself with a thickness of 250–300 nm could not efficiently suppress the formation of graphite. This might be caused by the defects such as pinholes or microcracks formed inside the interlayer during Cr_2O_3 deposition or diamond deposition because of the relatively low deposition temperature (150 °C) of Cr_2O_3 interlayer. These defects inside the interlayer provide a diffusion path for Co from the substrate to the surface of Cr_2O_3 to catalyze the formation of the graphite phase. From the SEM images shown in Fig. 6-4, it can be seen that continuous diamond coating has been successfully deposited on Cr_2O_3 interlayered WC-Co insert no matter whether the substrate is pre-etched or not, despite some graphite phases are mixed in the diamond coating on the sample without pre-etching. However, the diamond on Cr_2O_3/Cr interlayered WC-Co inserts has relatively low nucleation density, which is different from what other researchers reported [180,181,194]. Previous research showed that diamond nucleation density on carbide forming substrate is usually one or two orders of magnitude higher than non-carbide forming substrate [200]. One possible explanation is the difficulty to achieve supersaturation of carbon on the surface of the Cr_2O_3/Cr interlayer. Basically, diamond nucleation requires two preconditions during the incubation time. One is the suppression of graphite formation by atomic hydrogen etching and the other one is high supersaturation of carbon on the surface [191]. In the case of Cr_2O_3/Cr interlayer, on one hand, the formation of Cr carbides may facilitate the nucleation of diamond and benefit the adhesion of diamond on the substrate; on the other hand, the depletion of carbon atoms on the interlayer surface may prevent supersaturation of carbon on the surface for diamond nucleation, especially when the composition of carbon gas precursors is low during the deposition. It has been reported that the formation of chromium carbide between carbon and chromium is diffusion controlled, and the activation energy for diffusion and reaction was approximately 38 kJ/mol [201]. In the Cr_2O_3 interlayered samples, the reaction between carbon and Cr_2O_3 is also diffusion controlled. But the activation energy for diffusion and reaction was approximately 89 kcal/mol (372 kJ/mol) based on the calculation by Tagawa [202]. Therefore, it is difficult to form carbide on Cr_2O_3 interlayer during diamond deposition and in this case, the carbon precursors reaching the surface are mainly used for diamond nucleation. On the contrary, the carbon would react with Cr to form chromium carbides (Cr_7C_3 and Cr_3C_2) as revealed by XRD pattern shown in Fig. 6-5. Cr_3C_2 is reported to be a more stable phase than Cr_7C_3 because of its lower Gibbs free energy [203]. Therefore, there is potential for Cr_7C_3 to react with more diffused carbon atoms to form Cr_3C_2. The continuous consumption of carbon atoms for chromium carbide formation decreases the carbon concentration on the surface and thus reduces the diamond nucleation density. This is in agreement with Polini's previous research [204] that the diamond nucleation is a competition between the carburization reaction and the formation of stable nuclei. Additionally, the diamond growth on the scratches in Fig. 6-2(c) could be explained by the formation of scratches on the interlayer surface during diamond seeding, as shown in Fig. 6-2(c) and (d). As diamond growth was observed mainly on the scratches but the embedded diamond particles were scattered across the whole surface of Cr interlayer, it is reasonable to assume that the diamond growth on Cr layer is mainly due to heterogeneous nucleation on surface defect sites. This should also be the prevailing way for diamond nucleation on Cr_2O_3 interlayer since even fewer diamond particles were embedded onto the Cr_2O_3 interlayer (Fig. 6-2-e). To achieve continuous diamond coating, new samples with Cr_2O_3/Cr interlayer were prepared and the diamond coating was then deposited with 6.5% CH_4 in the CH_4/H_2 gas mixture for the first hour to provide sufficient carbon for nucleation. After this nucleation stage, CH_4 concentration was turned back to 1% for diamond growth. The SEM image (Fig. 6-7a) of this sample reveals that continuous diamond coating can be obtained when more carbon precursors are provided for nucleation. The XRD patterns of the samples shown in Fig. 6-7(b) demonstrate the appearance of another Cr_3C_2 (130) peak (PDF#65-0897) besides the previously observed Cr_3C_2 and Cr_7C_3 peaks after diamond deposition, indicating Cr_7C_3 in the interlayer might be further carburized. As a result, more carbon atoms remaining on the surface to achieve supersaturation for diamond nucleation. Consequently, diamond nucleation density increases and continuous diamond coatings have been deposited on Cr_2O_3/Cr interlayered WC-Co inserts. The Raman spectrum of diamond coating deposited by two stages is illustrated in Fig. 6-7(c). It is noticeable that the diamond peak becomes weak and broadened, indicating smaller diamond grain size or the existence of other amorphous carbon phases [205], which is also supported by the small broad peak at around 1500 cm^{-1} [185,205]. The appearance of more amorphous carbon phases might be caused by the higher CH_4 concentration at the early stage of diamond nucleation as high methane concentration (> 3%) facilitates the formation of amorphous carbon phase [206]. The substrate temperature lower than 800°C also favors the formation of amorphous phase [207]. In addition, there are broad peaks at around 1240–1280 cm^{-1} and around 1440 cm^{-1} in the spectrum, which might be attributed to the transpolyacetylene at grain boundaries [189]. It should be also noted that the diamond peak is around 1335 cm^{-1}, less upshift than that of single Cr_2O_3 interlayered samples, implying lower compressive stress inside the diamond coating.

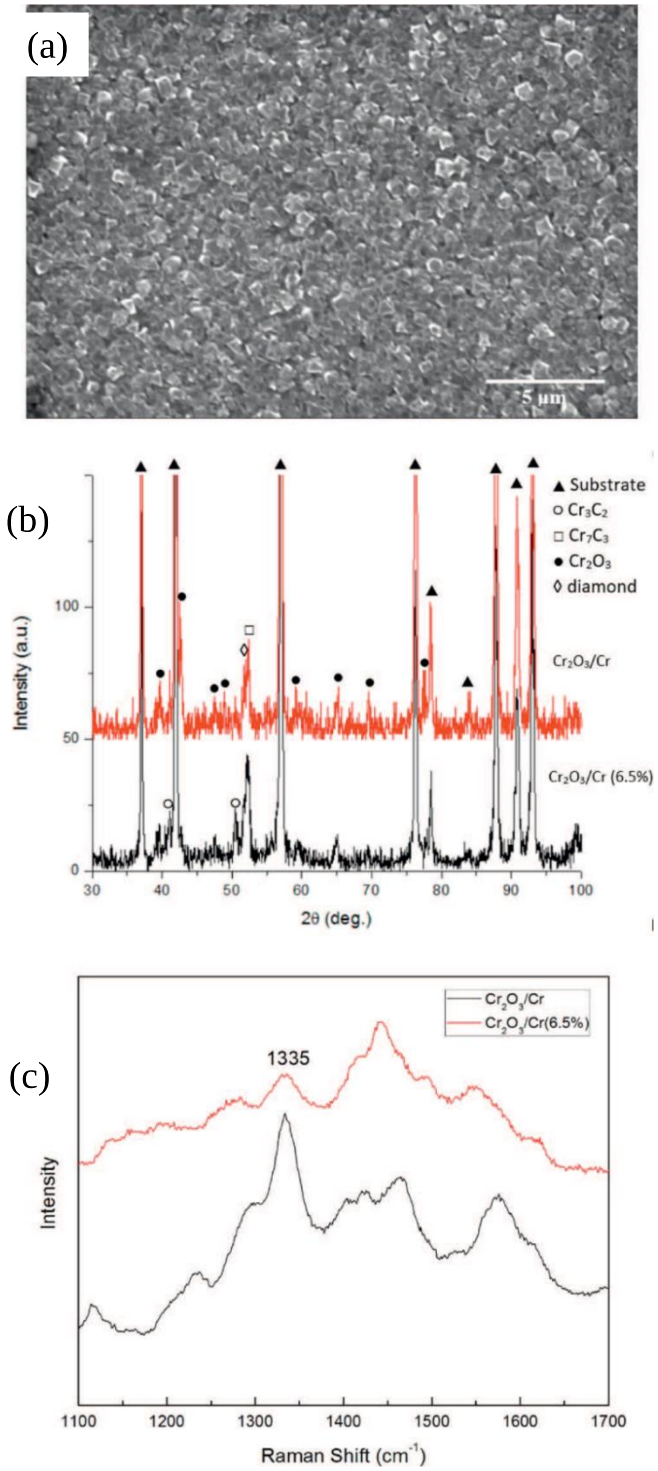

Figure 6-7: (a) Microstructure of diamond deposited on Cr_2O_3/Cr interlayered sample with 6.5% CH_4 for nucleation; (b) XRD patterns and (c) Raman spectra of Cr_2O_3/Cr interlayered. samples after diamond deposition with different CH_4 concentration for nucleation, top: 6.5%; bottom: 1%.

6.3.5. Adhesion Testing of Diamond Coatings on iInterlayered Substrates

Fig. 6-8 shows the SEM images of diamond coatings on Cr_2O_3 and Cr_2O_3/Cr interlayered samples after indentation testing. The imprint area reveals that there is less delamination of the diamond coating on Cr_2O_3 interlayered sample than on the pre-etch/ Cr_2O_3 interlayered sample, indicating higher adhesion for the one without pre-etching.

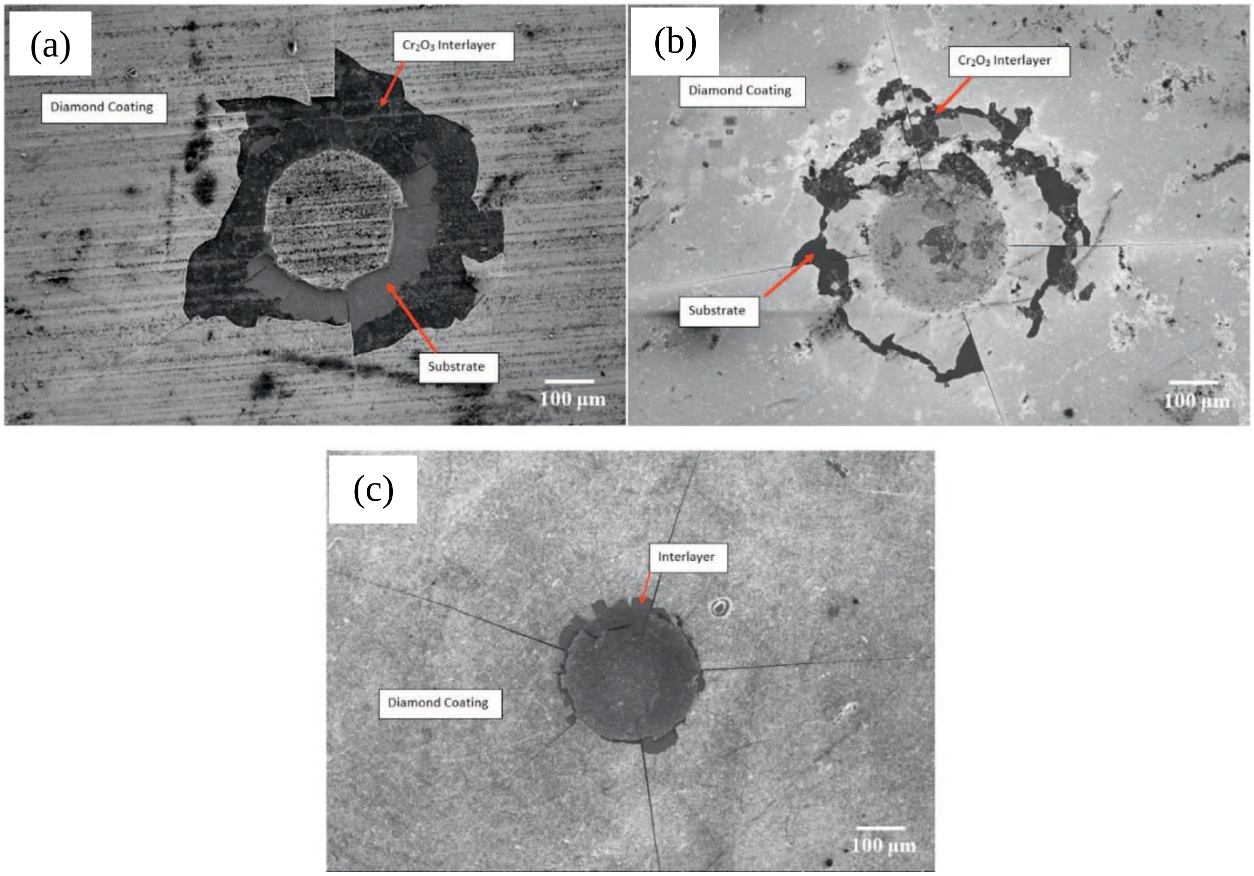

Figure 6-8: Surface morphology of diamond coating deposited on (a) pre-etch/Cr_2O_3 interlayered and (b) Cr_2O_3 interlayered and (c) Cr_2O_3/Cr (6.5% CH_4) interlayered samples after Rockwell C indentation.

The XPS spectra, as illustrated in Fig. 6-9(a) and (b), demonstrate the delamination occurred at both interfaces of diamond/ Cr_2O_3 and Cr_2O_3/WC-Co no matter whether or not the substrate is pre-etched. Comparing the imprint areas of these two samples in Fig. 6-8(a) and (b), however, it is noticeable to find that more Cr_2O_3 interlayer was delaminated in the sample with pre-etching treatment than the one without pre-etching. This might be caused by the removal of Co near the surface through pre-etching, as Co from the substrate is able to form metallic bond with Cr at the interface via interdiffusion during high temperature diamond deposition to enhance the adhesion. Nevertheless, the adhesion of the diamond coating is poor for both Cr_2O_3 interlayered samples. In contrast, the diamond coating deposited on Cr_2O_3/Cr interlayered sample demonstrates a relatively better adhesion, as shown in Fig. 6-8(c). There is only localized small part of diamond coating delaminated after 1471 N Rockwell C indentation. The delaminated area of the diamond coating is much smaller than the samples without Cr interlayer. The appearance of W peaks in the XPS spectrum of the delaminated area (Fig. 6-9c) indicates the failure of substrate/interlayer interface. The Cr peaks may come from the thin Cr layer underneath the Cr_2O_3 sublayer. Given the smaller Raman diamond peak shift in Cr_2O_3/Cr interlayered sample, the improved adhesion of diamond may be attributed to the low stress inside the coating. Additionally, the formation of chromium carbides due to the reaction between carbon and chromium enhances the adhesion strength of the diamond coating to the interlayer. This result is consistent with the previous finding that the formation of chromium carbide during CVD process could improve the adhesion of diamond coatings on Cr based interlayers [208]. On the whole, the adhesion of diamond is still not as good as that deposited on Al/AlN interlayer in our previous research [184], where only some cracks observed after Rockwell C indentation with the load of 1471 N. One probable reason is that the oxidized Al layer in Al/AlN interlayer could efficiently suppress the diffusion of Co and restrict the formation of graphitic carbon. Al also could easily diffuse into the substrate at diamond CVD temperature forming stronger metallic bond with the substrate. We are working on depositing a denser and flawless Cr_2O_3/Cr interlayer to further improve the adhesion of the diamond coating.

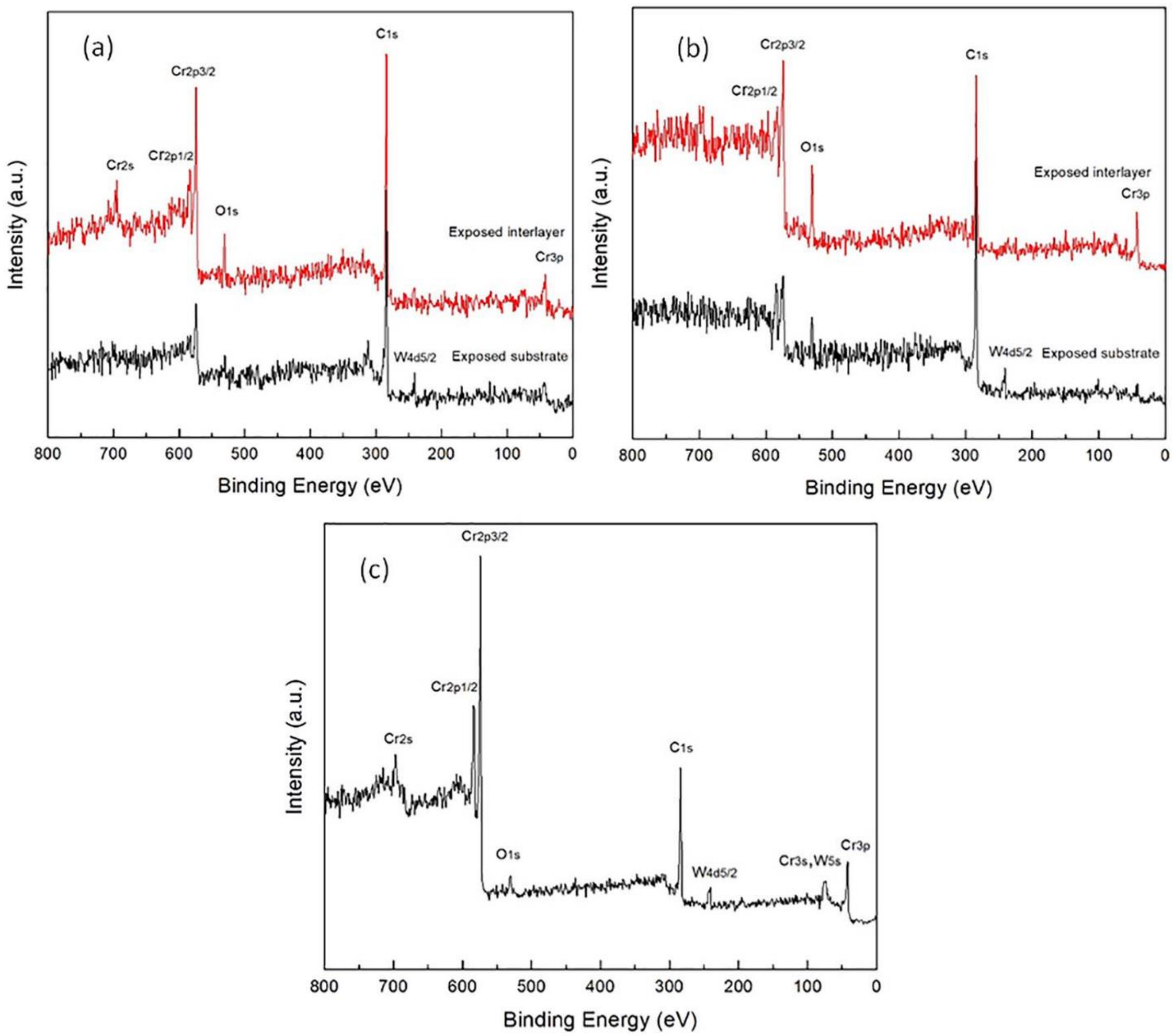

Figure 6-9: XPS spectra of the imprint area after indentation testing on (a) pre-etch/Cr_2O_3 interlayered and (b) Cr_2O_3 interlayered and (c) Cr_2O_3/Cr (6.5% CH_4) interlayered samples.

6.4. Conclusions

Cr_2O_3 has been demonstrated to be an effective interlayer to suppress the formation of graphite at the diamond coating/WC-Co interface by suppressing the diffusion of Co. As a result, the continuous diamond coating can be successfully deposited on Cr_2O_3 interlayered WC-Co substrate no matter whether the substrate is pre-etched or not. The pre-etching of WC-Co substrate combined with Cr_2O_3 interlayer showed better efficiency than the sample without pre-etching in suppressing the formation of graphite. Nevertheless, the adhesion of the diamond coating on Cr_2O_3 interlayer is relatively low due to lack of strong chemical bonding at the interface. A top Cr layer on Cr_2O_3 enhanced the adhesion of diamond due to the formation of carbides, and higher CH_4 concentrations are especially beneficial in enhancing nucleation and the following formation of the continuous diamond coating. Therefore, methane concentration should be carefully designed to ensure sufficient carbon on the surface during the diamond nucleation stage when carbide forming materials are used as the interlayer.

CHAPTER 7

Cr-Zr-O COATINGS

In this chapter, systematic research will be conducted on Cr-Zr-O coatings. First, screening tests are conducted to investigate the influence of the chemical composition on the phase formation and the properties of Cr-Zr-O coatings deposited at a constant substrate's temperature (150 °C). The variation in composition was achieved by tuning the RF power of the Zr target. Subsequently, the effect of deposition temperature on the phase formations in the coatings with Zr concentrations up to 18 at.% is investigated by depositing of coatings in various temperature in the range of 25- 850 °C. Finally, the structural stability of coatings is evaluated by post-annealing treatments and the results are compared with those of the coatings of the binary Cr-O system.

This chapter has been published in the journal "Surface and Coatings technology" as follows: An Investigation on Synthesis and Characterization of Superhard Cr-Zr-O Coatings, M. Mohammadtaheri, Y. Li, J. Corona-Gomez, Q. Yang, Surface and Coatings technology, Volume 375, 15 October 2019, Pages 694-700.

My contributions to this paper were: conceived and designed the experiments, performed the experiments, interpretation of experimental results, and preparing the manuscripts under the supervision of Professor Qiaoqin Yang. The manuscript was reviewed and revised by my supervisor before submission to the journal for publication. The present manuscript is a modified version of the published paper. Copyright permission has been obtained and provided in the Appendix B.

Abstract

Coatings with superior hardness, high temperature thermal stability, and oxidation resistance are required to protect cutting tools in machining applications. Hence, the synthesis of such coatings was investigated in a ternary Cr–Zr–O system by reactive radio-frequency magnetron sputtering technique. For this purpose, the Cr–Zr–O coatings with various chemical compositions were deposited at different temperatures on HSS M42 and Si (100) substrates. The coatings were then characterized by energy dispersive spectroscopy, X-ray diffraction, Raman spectroscopy, and Nanoindentation and a correlation between their chemical composition, crystal structure, phase composition, and mechanical properties was established. The structural stability of the coatings was also investigated after annealing treatments at 300°C, 700°C, 800°C, and 1000 °C. The results indicated that adding zirconium to Cr_2O_3 coatings shifted the onset of crystallization for the coatings to higher temperatures. The hardness measurements showed that Cr-Zr-O coatings with a hardness value over 40 GPa were only obtained in specific conditions. According to the chemical and phase compositional analysis by EDS, XRD and Raman spectroscopy on superhard coatings, it was assumed that a nanocomposite structure formation was the responsible mechanism for observed superhardness. Annealing treatments at the elevated temperatures showed that the thermal stability of the superhard Cr-Zr-O coatings was higher than pure Cr_2O_3 coatings. Moreover, the coatings in Cr-Zr-O system showed an interesting composite formation toward t-ZrO_2 + m-ZrO_2 + h-Cr_2O_3 structure at elevated temperatures, indicating that Zr has low solubility in Cr_2O_3 in an equilibrium condition.

Keywords: Coatings; Cr-Zr-O; Characterization; Hardness; XRD; Raman.

7.1. Introduction

Hard coatings are being applied on more than 40% of cutting tools to reduce operating costs, energy consumption, and environmental degradation. According to the market's statistics, this trend is still surging fast so that the attention has been drawn to this field of research [209]. According to the hardness value (H), coatings can be categorized to hard ($H < 40$ GPa), superhard ($40 \leq H \leq 80$ GPa), and ultrahard ($H > 80$ GPa) [210]. Currently developing oxide-based superhard coatings for cutting tools applications drawing large attention. This is due to the fact that oxide-based coatings with high hardness, good temperature thermal stability, and high temperature oxidation resistance can fulfill the increasing demand for advanced tools with high performance [25,122,211]. Nowadays researchers plan to improve the properties of oxide materials by adding the alloying elements. In this regard, pseudobinary oxide coatings in Al-Cr-O and Al-Zr-O systems have been extensively investigated [35,90,212–214]. Klostermann et al. [91] reported that the hardness of Al_2O_3 coatings can be enhanced by adding Zr element in a ternary Al-Zr-O system. The coatings were obtained by reactively sputtering of the Aluminum (Al) and Zirconium (Zr) targets in presence of oxygen and at temperature in the range of 500-700 °C. The hardness of Al_2O_3 coatings was enhanced to 30 GPa at about 8 at. % Zr. According to the authors, the hardness enhancement was attributed to formation of a nanocomposite structure. Moreover, different researchers [35,212] have stabilized the corundum phase of alumina, α-Al_2O_3, at room temperature by incorporation of chromium into the crystal structure of alumina in a Al-Cr-O system. It is believed that α-Al_2O_3 is the hardest phase of alumina with hardness about 21 GPa [215]. However, these coatings are not hard enough yet to compete with commercially available superhard coatings like Cubic Boron Nitride (c-BN), Ti-Si-N and diamond. Recently, researchers revealed that bulk Cr_2O_3 can have a hardness value up to 29.5 GPa [10–12,216]. However, in most of the literature, their efforts to obtain Cr_2O_3 coatings with high quality have been unsuccessful and the coatings illustrated a hardness well below the bulk value [5,6,12,43,48,49,215]. According to the author's expectations, the mechanical properties of Cr_2O_3 coatings can be tailored and improved if they are mixed or/doped with appropriate elements in a well-designed coating process. Therefore, obtaining an oxide-based superhard coating is not farfetched if the properties of the hard Cr_2O_3 coatings are enhanced by a solid-solution or nanocomposite mechanism. Among all the elements, zirconium (Zr) has shown minimal solubility in Chromium (Cr) confirmed by the equilibrium phase diagram of Cr-Zr [22]. Moreover, a close look at the binary phase diagram of ZrO_2-Cr_2O_3, reveals a miscibility gap between these oxides [116,217]. It has also been approved by RUH et.al [117] and Rafaja et.al [218] that Cr has less than 1 at. % solubility in ZrO_2 and metastable hexagonal $(Cr, Zr)_2O_3$ is able to accommodate just up to ~3 at. % Zr, respectively. Therefore, zirconium seems to be an appropriate doping element for Cr_2O_3 coatings to improve their hardness by the nanocomposite mechanism. The hardness enhancement by nanocomposite mechanism has been extensively studied in ternary Ti-Si-N coatings resulted in the new generation of superhard materials [209,219–223]. Nevertheless, ceramists previously paid little attention to the Cr_2O_3-ZrO_2 system due to poor densification properties of these mixtures in the sintering process. This is due to the fact that volatilization of Cr_2O_3 at high temperature results in the materials with low density which have poor mechanical properties [13,224,225]. However, J.H. Ouyang et.al [226] used the low-pressure plasma sprayed technique to evaluate the mechanical properties of Cr_2O_3 ceramic coatings doped with ZrO_2 additives. They illustrated that ZrO_2 additives have destructive effect on properties of chromium oxide coatings so that the hardness of Cr_2O_3 coatings significantly dropped by ZrO_2 additives [226]. Nowadays various type of coatings can be deposited at room temperature by employing physical vapor deposition (PVD) techniques [227]. Hence, these techniques provide new ways for the researchers to produce the temperature sensitive compounds at low temperature. To the present authors' knowledge, limited research exists investigating the mechanical properties of Cr-Zr-O coatings synthesized by vapor deposition techniques. Recently, Spitz and et.al [25,122], deposited Cr-Zr-O thin films by magnetron sputtering technique at 500 °C and investigated the microstructure evolution of the deposited films by changing chemical composition and post-annealing treatments. They illustrated that the host structure of hexagonal $(Cr, Zr)_2O_3$ can accommodate up to 12 at. % of zirconium and the maximum hardness reported for their coatings was 19 GPa which is still well below the bulk Cr_2O_3. Therefore, in the current research, the Cr-Zr-O coatings were deposited by reactive RF magnetron sputtering technique under appropriate coating process parameters obtained by the author's previous research [161]. This work addresses issues such as potential of the ternary Cr-Zr-O system for creation of novel oxide-based superhard coatings under new coating process parameters. Furthermore, the structural stability of coatings is evaluated through post-annealing processes. The coatings are then characterized by energy dispersive spectroscopy, X-ray diffraction, Raman spectroscopy, and Nanoindentation and a correlation between their chemical composition, crystal structure, phase composition, and mechanical properties is established.

7.2. Experimental Details

7.2.1. Coating Deposition

A reactive dual radio-frequency (RF) magnetron sputtering coater (made by Plasmionique Inc) was used to synthesize the oxide coatings in the Cr-Zr-O system. Two separate Cr and Zr plates with a diameter of 76.2 mm and 99.95% purity were selected as the sputtering targets. The chemical composition of coatings was altered by tuning the RF power of Zr target. Before the deposition, the chamber was evacuated to a vacuum of 2.5× 10^{-5} Pa. The coatings were deposited on HSS M42 and silicon (100) substrates. The substrates were cleaned with acetone before putting in the vacuum chamber. The target-substrate distance was kept 50 mm, and the substrates were rotating at a speed of 5 rpm. In the first run of depositions the Cr-Zr-O coatings with wide range of chemical compositions from Cr-rich to Zr-rich were produced at 150° C substrate temperature where the Cr target power and deposition pressure were 160 W and 10^{-1} Pa, and a mixture of Ar and O_2 (purity of 99.99%), with an oxygen content of 25 % Vol, were used as the sputtering and reactive gases, respectively. This process conditions was the optimum ones determined from our previous research [161] in which crystalline chromium oxide coatings with a hardness value close to bulk Cr_2O_3 (H~29 GPa) had been produced. In the second series, Cr-rich coatings (i.e. coatings with Zr concentrations up to 18 at. %) were deposited in various substrate temperature and the effect of deposition temperature on phase, structure, and chemical composition of coatings was investigated. The pure Cr_2O_3 coatings were also deposited in various temperature to be compared with Zr doped coatings. The substrate temperature was increased from room temperature to 850°C with 150°C increments in each deposition round, while the other deposition parameters were kept the same. For the second series of experiments, the coatings were deposited 24 hours to ensure they have enough thickness to minimize the influence of the substrate hardness on the nanoindentation measurements. Table 7-1 and 7-2 show a summary of the deposition conditions for the prepared oxide coatings.

Table 7-1: Deposition conditions for Cr-Zr-O coatings.

Sample No.	Cr target Power (W)	Zr target Power (W)	Cr target bias (V)	Zr target bias (V)	Deposition pressure (Pa)	Deposition temperature (°C)	Ar flow rate (sccm)	O_2 flow rate (Sccm)	Deposition Time (h)
1	160	0	260	0	0.1	150	15	5	10
2	160	5	260	50	0.1	150	15	5	10
3	160	10	260	100	0.1	150	15	5	10
4	160	50	260	100	0.1	150	15	5	10
5	160	75	260	130	0.1	150	15	5	10
6	160	100	260	160	0.1	150	15	5	10
7	160	125	260	191	0.1	150	15	5	10
8	160	150	260	200	0.1	150	15	5	10
9	160	175	260	231	0.1	150	15	5	10
10	160	200	260	257	0.1	150	15	5	10
11	160	225	260	267	0.1	150	15	5	10
12	0	300	0	370	0.1	150	15	5	10

Table 7-2: Deposition conditions for Cr-rich oxide coatings.

Cr target Power (W)	Zr target Power (W)	Cr target bias (V)	Zr target bias (V)	Deposition pressure (Pa)	Substrate Temperature (°C) with 150 °C increments	Ar flow rate (sccm)	O2 flow rate (Sccm)	Deposition Time (h)
160	0	260	0	0.1	25-850	15	5	24
160	50	260	100	0.1	25-850	15	5	24
160	75	260	130	0.1	25-850	15	5	24
160	100	260	160	0.1	25-850	15	5	24

7.2.2. Coating Characterization and Analysis

Right after the deposition, an optical profilometer (New View 8000) manufactured by Zygo Corporation and JEOL JSM 6010 Scanning Electron Microscopy (SEM) were employed to measure the thickness of coatings. The curvature radii of the samples was also realized by the optical profilometer with 50X Mirau objective and converted to residual stress of coatings using Stoney equation. The chemical composition of the coatings was evaluated by Energy Dispersive Spectroscopy (EDS) and their phase composition was investigated by X-ray diffraction (XRD) technique with parallel beam geometry in grazing incidence mode at $\theta = 5°$. The selected 2-theta range was 20 °-90 ° with a step size of 0.05 °. For this purpose, a 1D D/teX Ultra detector and a Cu anode ($CuK\alpha_1$ radiation with a wavelength of 1.5406 nm) were used on a Rigaku Ultima IV X-Ray diffractometer. The obtained XRD patterns were matched, after their baselines were corrected, with the Joint Committee on Powder Diffraction Standards (JCPDS) database susing X'Pert HighScore Plus software provided by PANalytical. Raman spectroscopy (Renishaw 2000) was also performed on coatings to supporting XRD results. All the measurements in Raman spectroscopy were carried out at room temperature with a 514.5-nm laser source and 0.5mW laser power. The calibration was done using silicon reference sample and the peak positions were determined using Wire.3.3 software. The Hardness measurements were accomplished according to ISO standard 14577-1 [129] using a nanoindentation technique fitted with a three-face pyramid Berkovich indenter. The load-displacement graphs obtained by nanoindentation techniques were interpreted by Oliver & Pharr method [130] and an average of fifty indentations at 3 mN load were calculated to report the hardness values.

7.2.3- Heat-Treatment Procedures

The thermal stability of coatings was evaluated by annealing treatments under flowing of Ar gas in separate runs. The samples were placed in a tube furnace and heated (heating rate 9°C/min) to four different annealing temperatures, 300 °C, 700 °C, 800 °C, 1000 °C. The samples were kept 3 hours at the respective peak temperature and then cooled down (cooling rate 4.5°C/min) to room temperature. A sample heat-treatment cycle designed for coatings is illustrated in Figure 7-1.

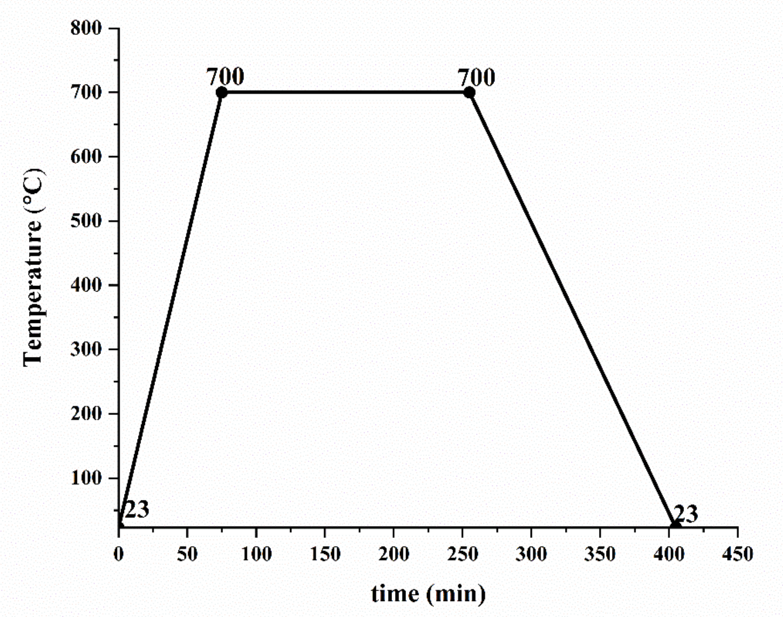

Figure 7-1: A sample heat-treatment cycle performed at 700 °C on Cr-Zr-O coatings.

7.3. Results and Discussion

7.3.1. Effect of Elemental Composition on Phases and Characteristics

The deposition rate was calculated based on the determined coating thickness (measured by optical profilometer) and the duration of the coating process. For the single-phase Cr_2O_3 coatings, the deposition rate was about 25 nm/hr. By applying RF power to the Zr target, to co-sputter both Cr and Zr targets in the same deposition atmosphere, the deposition rate continuously increased and reached to 131 nm/hr for coatings deposited with 225 W Zr target power. Figure 7-2 shows the measured thickness of deposited coatings. A RF power lower than 50 W for Zr target has a subtle effect on deposition rate, however, there is a noticeable change in deposition rate for the coatings deposited with Zr target power higher than 50 W.

The chemical composition of all the deposited coatings, performed by EDS, is indicated in table 7-3. EDS is not a suitable technique for quantifying light elements, however, its relative analysis on heavy elements like Cr and Zr can be trusted. Hence, in addition to the elemental composition, (Zr/Cr+Zr) ratios were indicated in the table. With increasing Zr target's power the concentration of zirconium in the coatings increased, while the concentration of chromium decreased as expected.

The coatings deposited with a 100 W Zr target power (sample No.6) have a Zr / (Cr + Zr) ratio of about 0.5. The Cr content is 22.20 at. % and the Zr content is 17.75 at.%. It means by increasing the Zr target power more than 100 W, the coatings' chemical composition moves from Cr-rich to Zr-rich region of ternary Cr-Zr-O system. For the binary Zr-O coatings deposited by 300W Zr and 0W Cr targets power (sample No.12), the oxygen and Zr concentrations increased up to 66.6 and 33.40 at. %, respectively, which are about the same as the pure zirconia.

Figure 7-3 shows the XRD patterns of all the coatings sputtered with different zirconium RF target power. The coatings deposited with 0 W Zr power, indicated a crystalline r-Cr_2O_3 structure, as they showed the main crystalline r-Cr_2O_3 peak centered at $2\theta=36°$ according to (PDF-038-1479) database. The low-intensity crystalline peaks observed in the XRD patterns of these coatings can be attributed to their low thickness. The XRD patterns related to coatings deposited with 5 and 10 W Zr target power are close to the position of r-Cr_2O_3 structure with a small shift toward lower diffraction angle. However, their grain size decreased as their peaks are broadening compared to coatings with 0 at. % Zr.

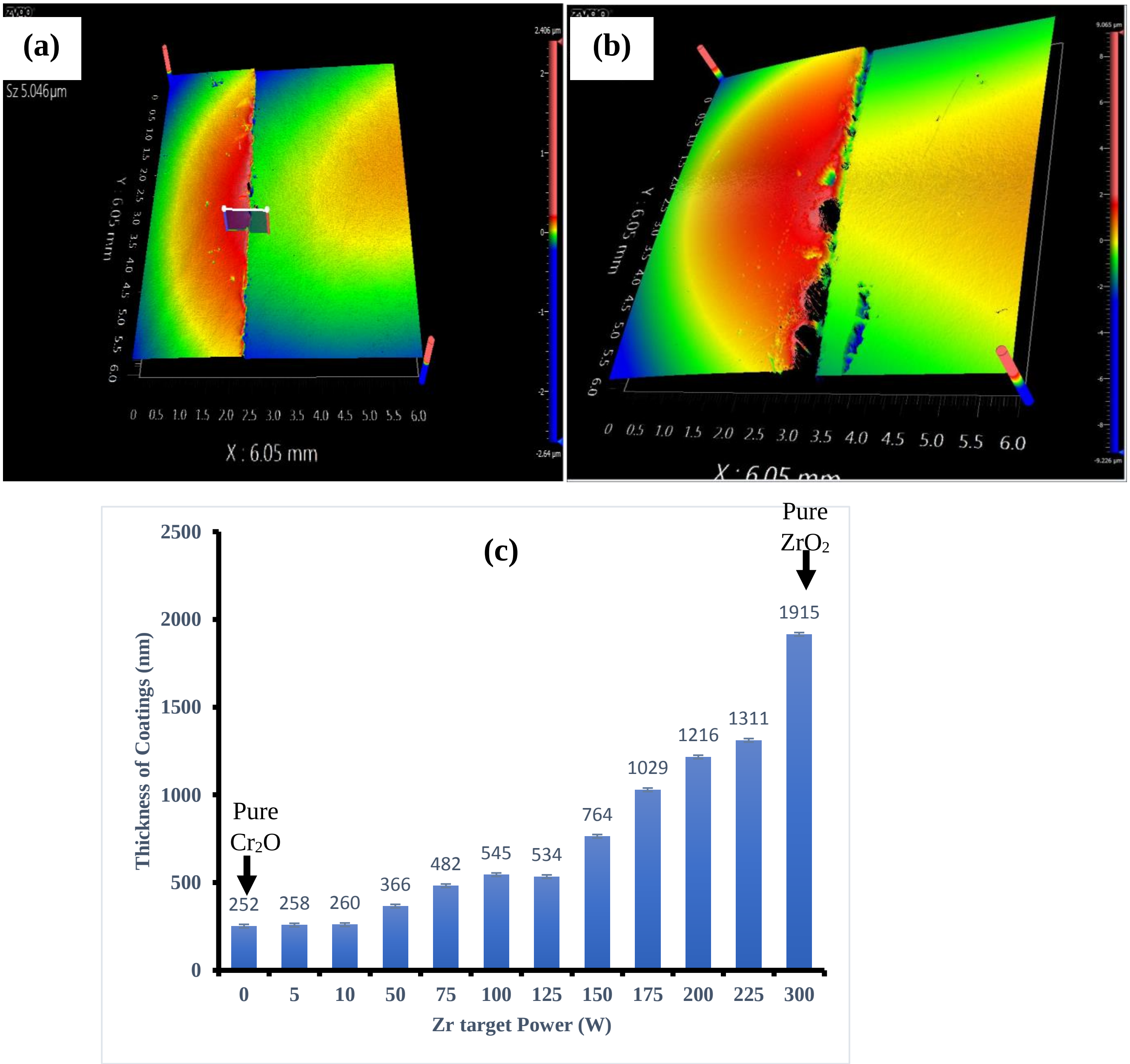

Figure 7-2: a and b) typical thickness measurements by optical profilometer for pure Cr_2O_3 and ZrO_2 coatings, respectively and c) the calculated average thickness after three measurements for Cr-Zr-O coatings deposited with the different Zr target power.

Table 7-3: Composition and calculated Zr / (Cr + Zr) ratios of Cr-Zr-O coatings.

Sample	at. % Cr	at. % Zr	at. % O	(Zr / Cr+Zr) %
1	40.25	0	59.75	0
2	40.10	0.20	59.70	0.5
3	40.00	0.35	59.65	0.87
4	30.20	9.50	60.30	23.93
5	26.40	13.40	60.20	33.67
6	22.20	17.75	60.05	44.43
7	16.50	21.85	61.65	56.98
8	10.08	25.12	64.08	71.36
9	5.72	29.08	65.20	83.56
10	3.23	31.45	65.32	90.68
11	1.76	32.34	65.90	94.83
12	0	33.40	66.60	100

This shift can be attributed to the bigger zirconium ions dissolved in the r-Cr_2O_3 structure. For the coatings sputtered with 50-100 W Zr target power, a completely amorphous structure was obtained as no peaks were observed in their XRD patterns. This can be attributed to the higher crystallization temperature of Cr-Zr-O coatings compared to pure Cr_2O_3 coatings. Increasing the crystallization temperature of zirconium-doped Cr_2O_3 materials have already been reported by various researchers who synthesized the compact and powder material in the Cr_2O_3-ZrO_2 system [25,119,218,228–230]. Thus, a deposition temperature of 150°C is not high enough to crystallize the coatings. The coatings again start to crystallize by increasing the Zr target power to 125 W, but this time with monoclinic ZrO_2 structure as the main crystalline peak of m-ZrO_2 was observed around $2\theta=30°$. This diffraction angle is higher than pure m-ZrO_2 which can be attributed to the high amount of smaller Cr^{3+} ions dissolved in the m-ZrO_2 structure. Further increasing the Zr target power to 225 W, facilitate the formation of crystalline coatings with m-

ZrO_2 structure, since the XRD peaks were sharper with higher intensity. The coatings deposited with 300 W Zr and 0 W Cr targets power, showed well crystalline monoclinic ZrO_2 structure according to (PDF-98-002-7987). The XRD results are in agreement with EDS analysis, illustrated that by increasing the Zr target power more than 100 W, the coatings move from Cr-rich region to Zr-rich region of Cr-Zr-O system. Moreover, the r-Cr_2O_3 structure was preserved for the coatings deposited with 0-50W Zr target power, indicating that the sputtering rate of Zr target is very low at RF target powers lower than 50W.

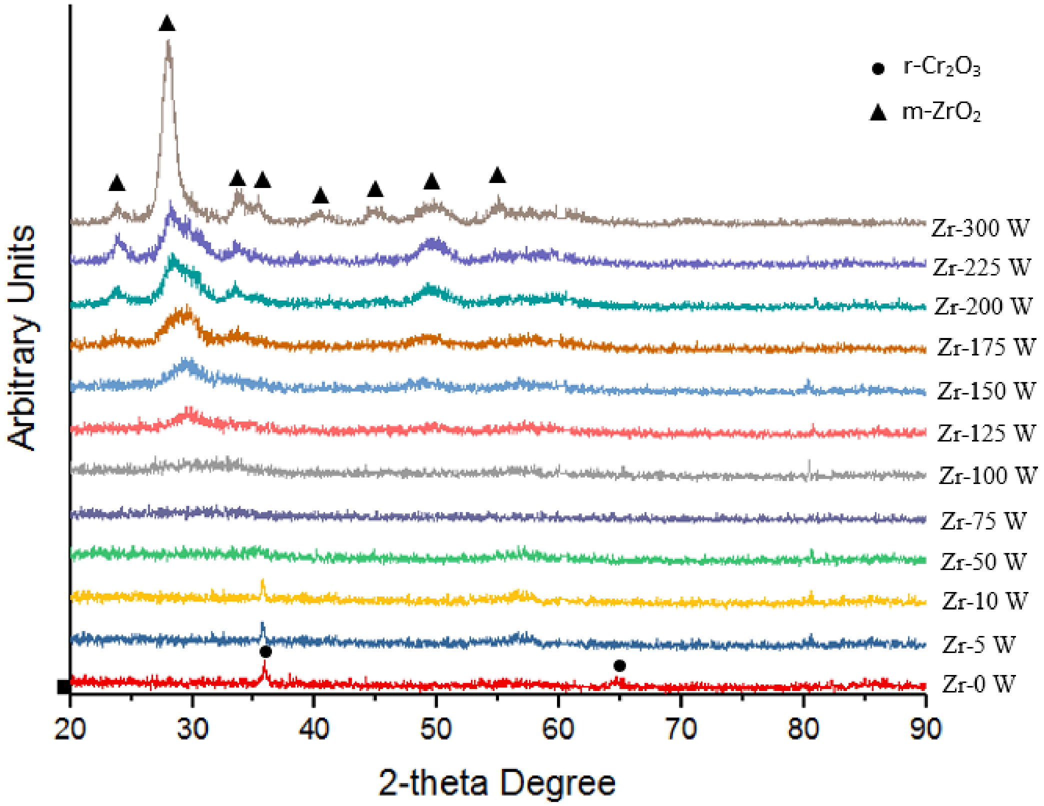

Figure 7-3: XRD patterns of deposited Cr-Zr-O coatings at 150 °C.

The coatings' residual stress was determined for all the deposited coatings and plotted in Figure 7-4-c. The pure r-Cr_2O_3 coatings showed the highest compressive stress (≈ 2.2 GPa). The compressive residual stress for the coatings decreased steadily by increasing the Zr concentration and dropped to about 0.07 GPa for pure ZrO_2 coatings.

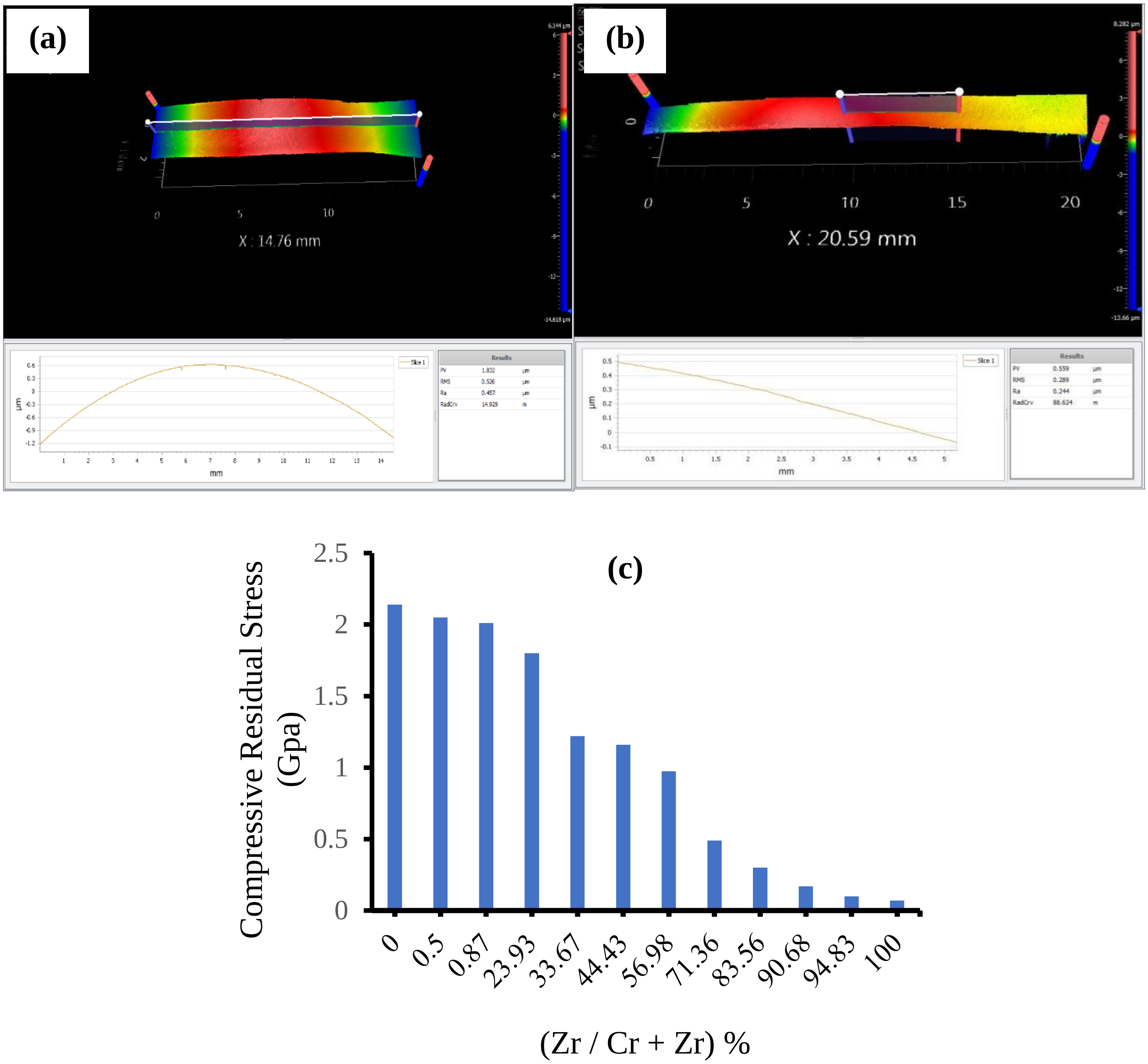

Figure 7-4: a and b) typical curvature radii measurement by optical profilometer for pure Cr_2O_3 and ZrO_2 coatings, respectively and c) the calculated residual stress measurements for Cr-Zr-O coatings deposited with the different Zr concentrations.

The hardness values of the deposited coatings with respect to the zirconium concentration is illustrated in Figure 7-5. The average hardness of the pure r-Cr_2O_3 coatings was around 22 GPa. The hardness for the coatings with (Zr / Cr + Zr) % up to 1% was close to pure r-Cr_2O_3 coatings and the difference in hardness value was in the range of the measurement error. However, the hardness of coatings was enhanced from 22 GPa to about 25 GPa when (Zr / Cr + Zr) % reached 24 %. Further increasing the zirconium content was associated with a decrease in the hardness so that the hardness steadily dropped and reached 15.5 GPa for Zr-rich coatings. The hardness of coatings with a high content of zirconium was close to the bulk hardness of ZrO_2 materials (12 GPa) reported in various literature [10,56].

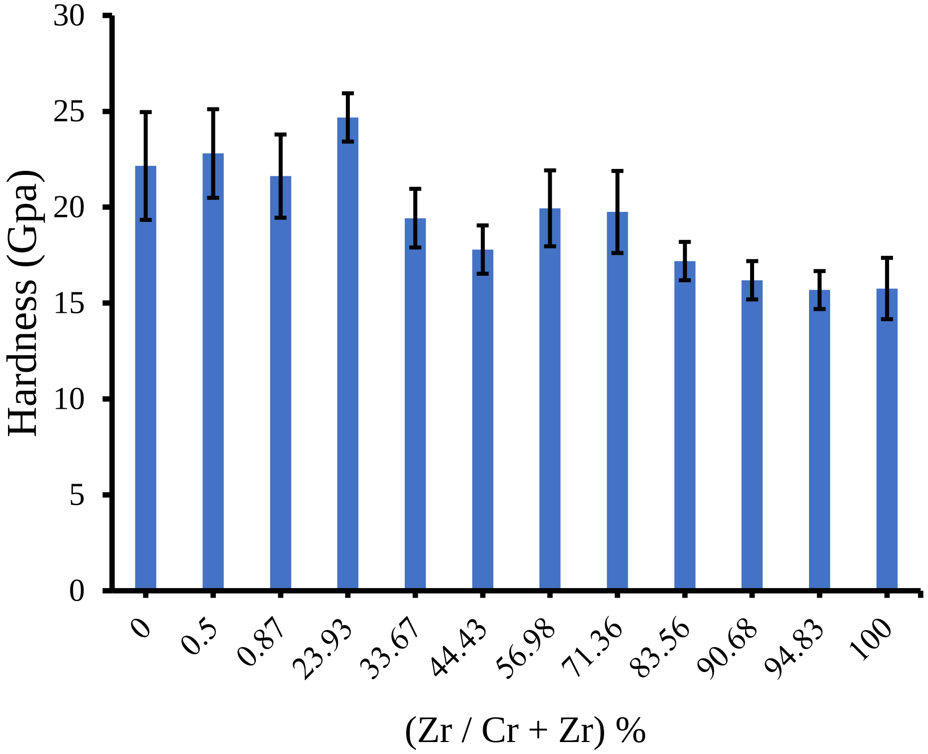

Figure 7-5: The penetration hardness results for the deposited coatings as a function of the Zirconium concentration.

The hardness results match with the XRD results, showed that at very low Zr concentration, where the coatings still have rhombohedral Cr_2O_3 structure, the hardness values were close to r-Cr_2O_3 coatings. For the Zr-rich coatings also the hardness values were close to monoclinic ZrO_2 since they all have monoclinic ZrO_2-based structure. The hardness enhancement at 24% (Zr / Cr + Zr) can be attributed to the amorphous structure of coatings as the amorphous coatings usually possess higher hardness than crystalline materials. Nevertheless, the hardness enhancement mechanism for coatings composed of 9.5 at. % Zr still needs to be investigated.

7.3.2. Influence of Substrate Temperature on Phases and Characteristics

To investigate the effect of deposition temperature on structure and properties of Cr-Zr-O coatings, the Cr-rich coatings were deposited at various temperature. The coatings with high concentrations of Cr were selected as it is expected that the mechanical properties of Cr_2O_3 coatings to be tailored and improved by a nanocomposite or solid solution hardening mechanism. Therefore, the creation of superhard coatings is more probable if the coatings have a higher percentage of hard Cr_2O_3 phase in their structure.

The obtained diffractograms of the coatings with various Zr concentration deposited in different substrate temperature are plotted in Figures 7-6 to 7-9. Pure Cr_2O_3 coatings cannot be deposited at temperatures higher than 300°C confirmed by our previous research[37], thus, XRD patterns are not available for Cr_2O_3 coatings deposited at high temperatures. In the first instance, by comparing XRD patterns of coatings in figures 7-6 to 7-9, it is seen that by the increasing amount of Zr the onset of crystallization of coatings is shifted to higher temperature i.e. from 25°C for pure Cr_2O_3 to 300°C and 600°C for coatings with 9.5 at. % and more than 13.5 at. % Zr, respectively. According to XRD patterns for the deposited Cr-Zr-O coatings with Zr concentrations higher than 13.5 at. % (Figures 7-8 and 7-9), the crystallization developed throughout the coatings at a temperature of 600 °C. The crystallized phase was assumed to be a metastable $(Cr, Zr)_2O_3$. The presence of a metastable $(Cr, Zr)_2O_3$ phase was concluded as the XRD pattern of this phase has shifted towards the lower diffraction angle compared to the hexagonal Cr_2O_3 phase. This can be related to the solubility of the bigger zirconium ions into the hexagonal Cr_2O_3 crystal structure under the nonequilibrium deposition condition. At 850°C, the formation of t-ZrO_2 phase was confirmed by the presence of the small diffraction lines detected at $2\theta = 30.22°$ according to (PDF-98-002-7987). The formation of zirconium oxide phases at 850 °C is assumed to be originated by the segregation of zirconium oxide from the metastable $(Cr, Zr)_2O_3$ phase, as the hexagonal Cr_2O_3 peaks were observed at their original peak positions at this temperature. An increasing amount of zirconium facilitates the formation of t-ZrO_2 phase as in the XRD pattern of Cr-17.5% Zr-O coatings (Fig. 7-9) the crystallized t-ZrO_2 phase was observed at 600°C, whereas, this phase was only observed at 850°C for Cr-9.5% Zr-O coatings.

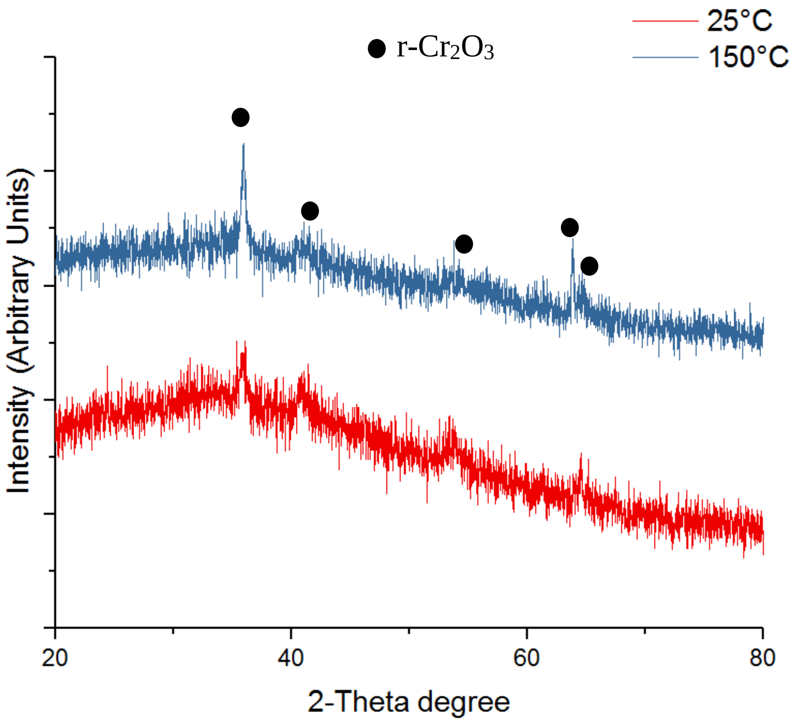

Figure 7-6: XRD patterns of pure Cr_2O_3 coatings deposited at different substrate temperatures.

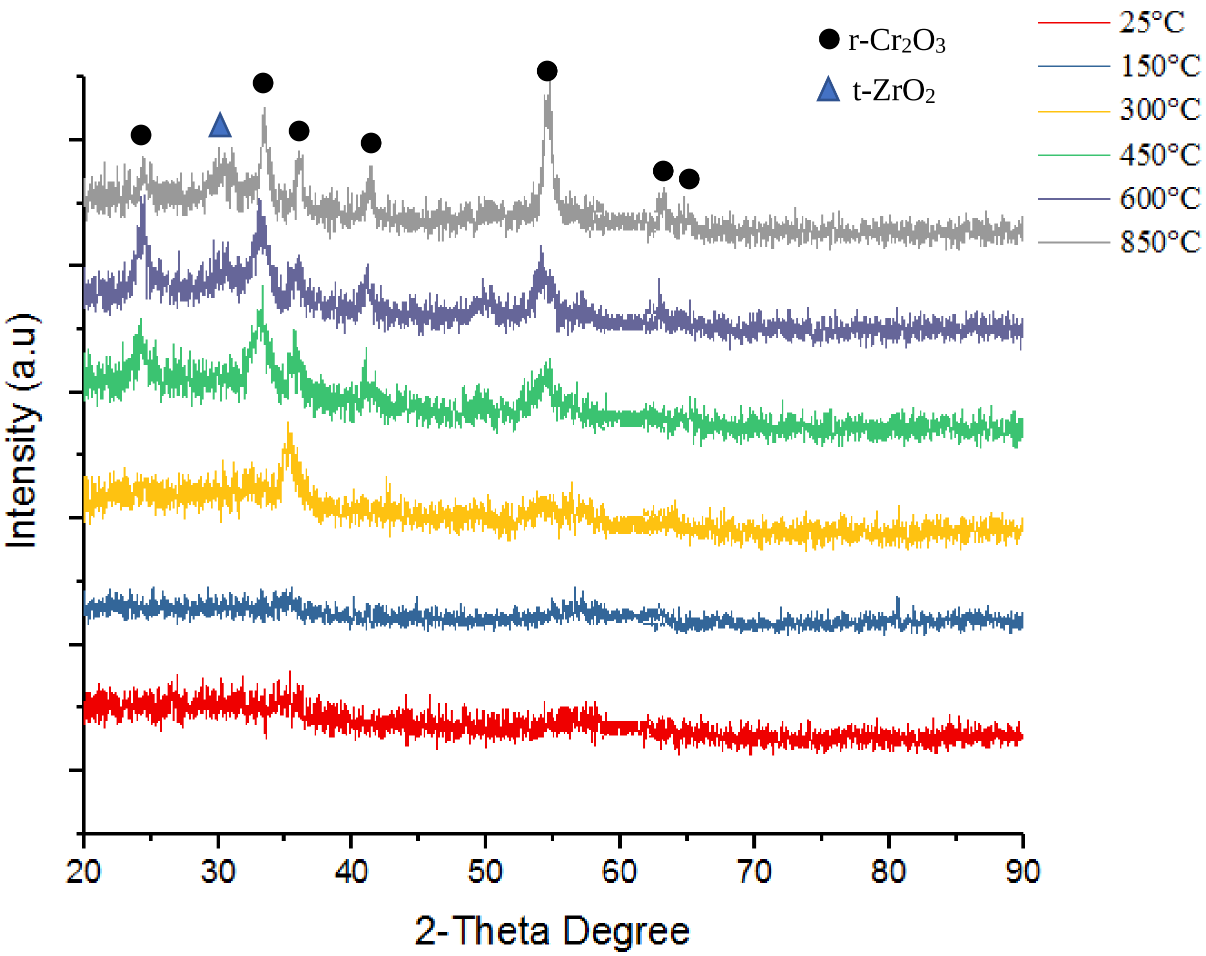

Figure 7-7: XRD patterns of Cr-9.5% Zr-O coatings deposited at different substrate temperatures.

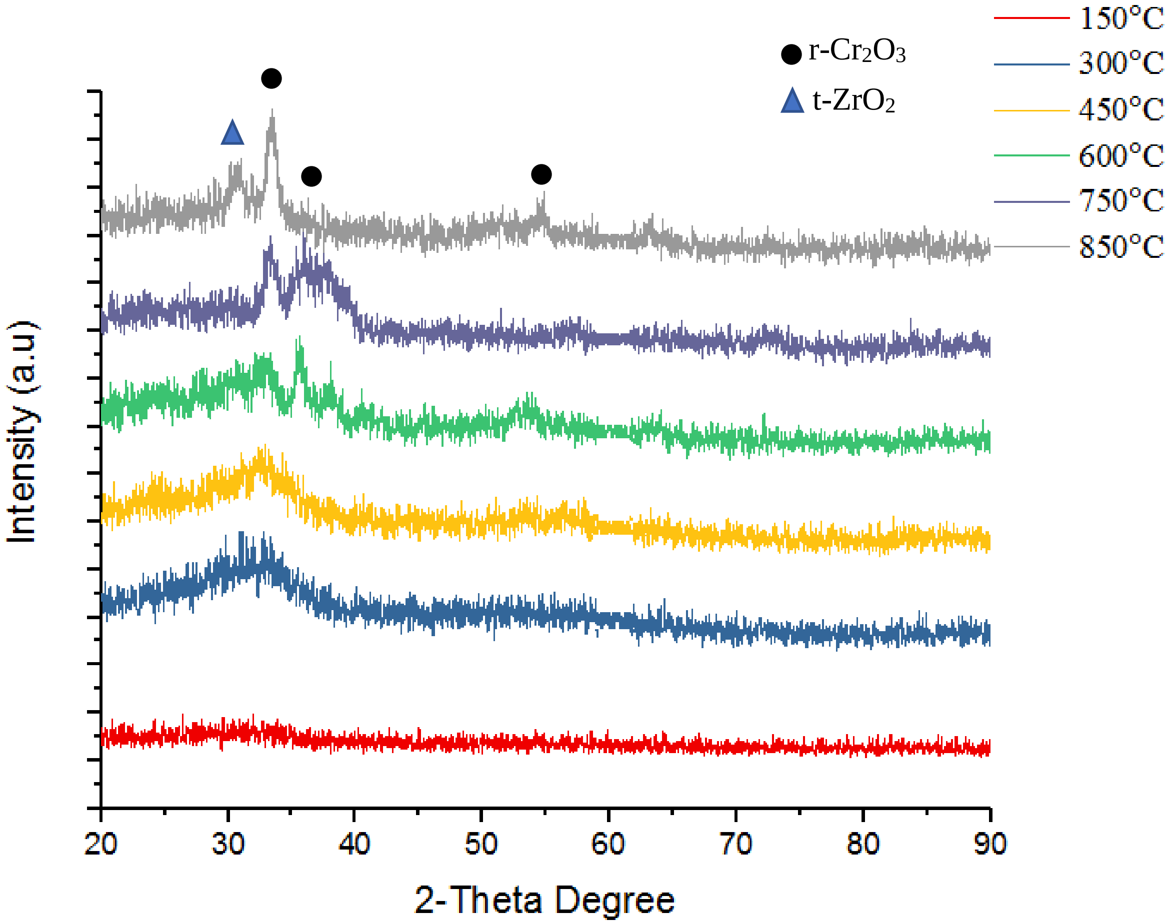

Figure 7-8: XRD patterns of Cr-13.5% Zr-O coatings deposited at different substrate temperatures.

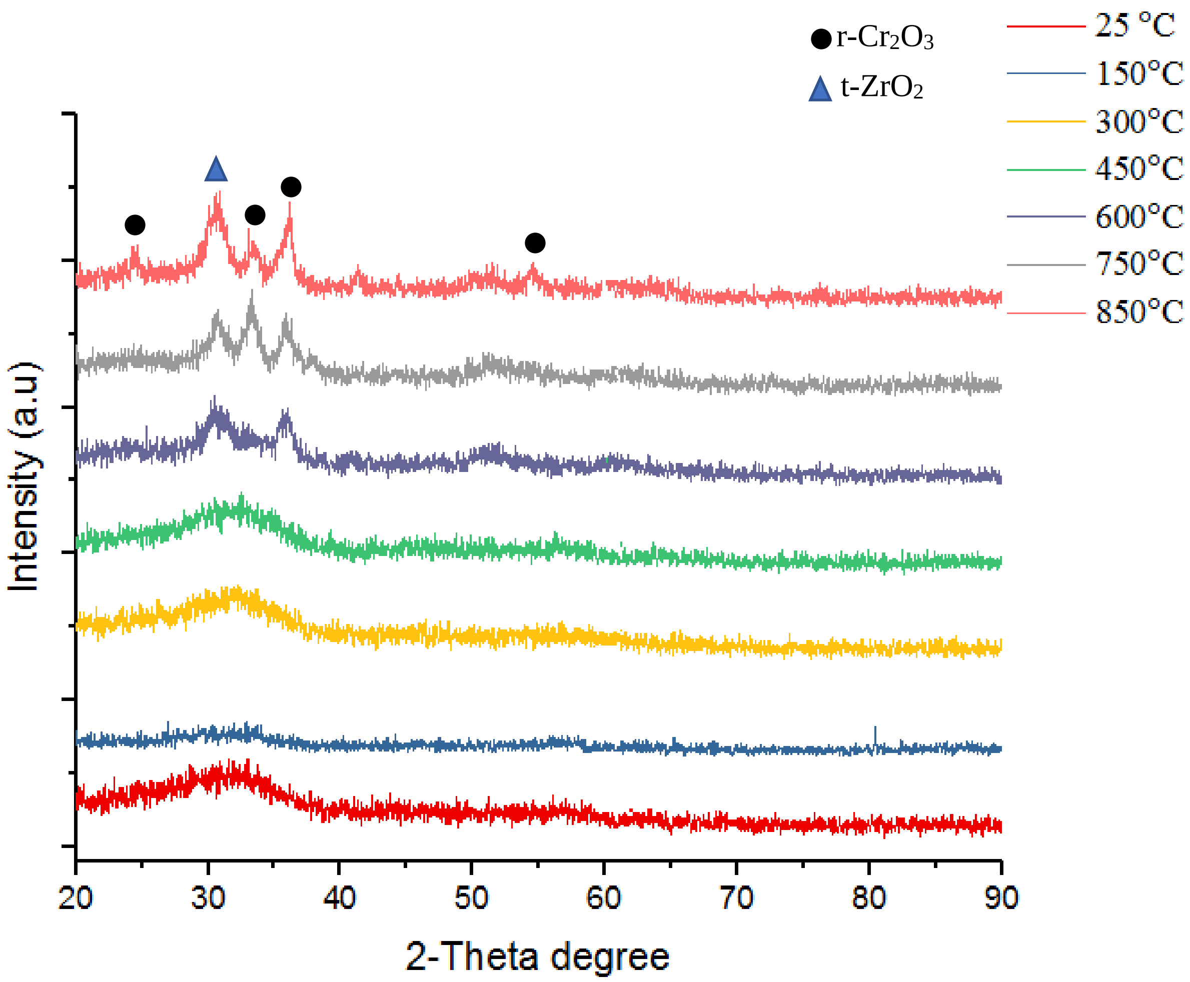

Figure 7-9: XRD patterns of Cr-17.5% Zr-O coatings deposited at different substrate temperatures.

The EDS analysis was performed on the coatings deposited in different substrate temperature to realize the effect of deposition temperature on the chemical composition of coatings. For instance, the chemical composition of the coatings deposited with 50W and 100W Zr-target power at two substrate temperature of 25°C and 850°C are compared in table 7-4. According to the EDS analysis, the variation of the chemical composition for the deposited coatings at extreme different substrate temperatures is very small and it is within the error of the measurements so that they can be considered to have a similar composition. Hence, the effect of substrate temperature on the chemical composition of coatings can be neglected.

Table 7-4: Chemical composition of coatings deposited at different temperatures.

Sample	at. % Cr	at. % Zr	at. % O
Cr-Zr-O-50W-25°C	30.20	9.50	60.30
Cr-Zr-O-50W-850°C	31.90	9.50	58.6
Cr-Zr-O-100W-25°C	22.20	17.75	60.05
Cr-Zr-O-100W-850°C	21.50	17.45	61.05

The values of the penetration hardness of the deposited coatings as a function of the substrate temperature and Zr concentration are given in Table 7-5. For the pure Cr_2O_3 coatings (i.e. 0 at. % Zr), the hardness of the coatings decreased significantly as the deposition temperature increased. The structural analysis in our previous research [37] showed that the density of Cr_2O_3 coatings decreased by increasing the deposition temperature, which results in coatings with low mechanical properties. Further increasing the deposition temperature to 300°C, the Cr_2O_3 coatings completely lost their integration which easily wiped off by a tissue paper. Thus, the mechanical properties of chromium oxide coatings deposited at high temperatures could not be measured. Nevertheless, adding Zr into chromium oxide coatings stabilized Cr-rich oxide coatings at high temperatures. The coatings with 9.5 at. % Zr deposited at room temperature have hardness values close to pure Cr_2O_3 counterparts deposited in same deposition temperature. However, compared to the chromium oxide coatings, they have an amorphous structure (See Fig.7-3). By increasing the substrate temperature to 300°C for coatings with 9.5 at. % Zr, the hardness increased substantially and reached to a superhardness value of 42.60 GPa. According to XRD results, this temperature matches with the onset of crystallization for Cr-9.5%Zr-O coatings. Since the residual stress measurements (Fig.7-4) and EDS analysis (table 7-4) confirmed that with increasing the Zr content the compressive residual stress decreases and the substrate temperature does not have any effect on the chemical composition of coatings, therefore, this hardness enhancement can only be attributed to microstructural changes occurred at this temperature which needs more investigations. Nevertheless, at substrate temperature over 450°C, the hardness of the Cr-9.5% Zr-O coatings dropped to about 5 GPa. RUH et.al [117] and Rafaja et.al [218] previously showed that Cr has less than 1 at. % solubility in ZrO_2 and metastable hexagonal $(Cr, Zr)_2O_3$ is able to accommodate just up to ~3 at. % Zr. Therefore, it is assumed that at these elevated temperatures the Zr is completely segregated from metastable (Cr, Zr)$_2$O$_3$ phase. Hence, formation of dense and compact coatings is prevented, due to the excessive volatilization of remained Cr_2O_3 phase at high temperatures [13,139], which results in coatings with low mechanical properties. In contrast, at room deposition temperature, increasing the Zr content to 13.5 and 17.5 at. %, the hardness of coatings decreased to about 19 and 17 GPa, respectively. This is expected since the hardness of the ZrO_2 phase is much lower than Cr_2O_3 and by increasing the Zr content the hardness of coatings approaches toward ZrO_2 hardness. However, the hardness for these coatings steadily increased by increasing the deposition temperature and reached to about 28 GPa at 850°C which is close to pure Cr_2O_3 coatings when deposited at room temperature. This hardness enhancement at a high temperature can be related to the creation of nanocomposite structure in the Cr-Zr-O coatings as the XRD patterns (Fig. 7-8 and 7-9) showed that at these elevated temperatures both t-ZrO_2 and Cr_2O_3 phases are present. This result is consistent with Landalv et.al [122] research, in which hardness of as-deposited (Cr, Zr)$_2$O$_3$ coatings with 10 at. %Zr increased from 9.5 GPa to 16.5 GPa when they were annealed at 750°C in a vacuum atmosphere.

Table 7-5: Hardness of Cr-Zr-O coatings as a function of deposition temperature and chemical composition

	Zr at. %			
	0	9.5	13.5	17.5
Temperature (°C)				
25	27.57±1.64	28.99±2.76	19.15±1.24	16.97±0.87
150	22.16±2.8	24.68±1.26	19.43±1.53	17.79±1.26
300	1.45± 0.85	42.60±3.52	21.75±1.35	21.45±1.39
450	NC	3.88±0.94	22.41±1.58	20.23±1.29
600	NC	5.85±2.56	22.29±4.34	16.96±1.77
750	NC	5.71±4.78	28.02±2.81	24.99±1.91
850	NC	5.71±4.78	28.08±2.90	26.58±2.44

NC: stands for no coating

7.3.3. Effect of Annealing Treatments on The Structure and Properties of Superhard Cr-Zr-O Coatings.

The structural and phase stability of the superhard coatings were evaluated after high temperature experiments by XRD and Raman spectroscopy, illustrated in figures 7-10 and 7-11 respectively. According to XRD analysis (Figure 7-10), at a temperature of 700 °C, the crystallization developed throughout the coatings. The crystallized phase was assumed to be a metastable $(Cr, Zr)_2O_3$ which its growth continued up to 800 °C. The presence of a metastable $(Cr, Zr)_2O_3$ phase was concluded as the XRD pattern of this phase has shifted towards the lower diffraction angle compared to the hexagonal Cr_2O_3 phase. This can be related to the solubility of the bigger zirconium ions into the hexagonal Cr_2O_3 crystal structure under the nonequilibrium deposition condition. Further increasing the temperature to 1000 °C, the formation of both Tetragonal and monoclinic ZrO_2 phases was confirmed by the presence of the small diffraction lines detected at $2\theta = 50.4°$ and $91.7°$ for tetragonal ZrO_2 and $2\theta = 32.4°$ and $108.6°$ belong to monoclinic ZrO_2 according to (PDF-98-002-7987) and (PDF-98-000-5298) databases respectively. The formation of zirconium oxide phases at 1000 °C is assumed to be originated by the segregation of zirconium oxide from the metastable $(Cr, Zr)_2O_3$ phase, as the hexagonal Cr_2O_3 peaks were observed at their original peak positions after the 1000 °C treatments. This confirms the extremely low solubility of ZrO_2 in the hexagonal Cr_2O_3 noted by various researchers [117,218,231] who previously considered the Cr_2O_3-ZrO_2 system under the equilibrium condition.

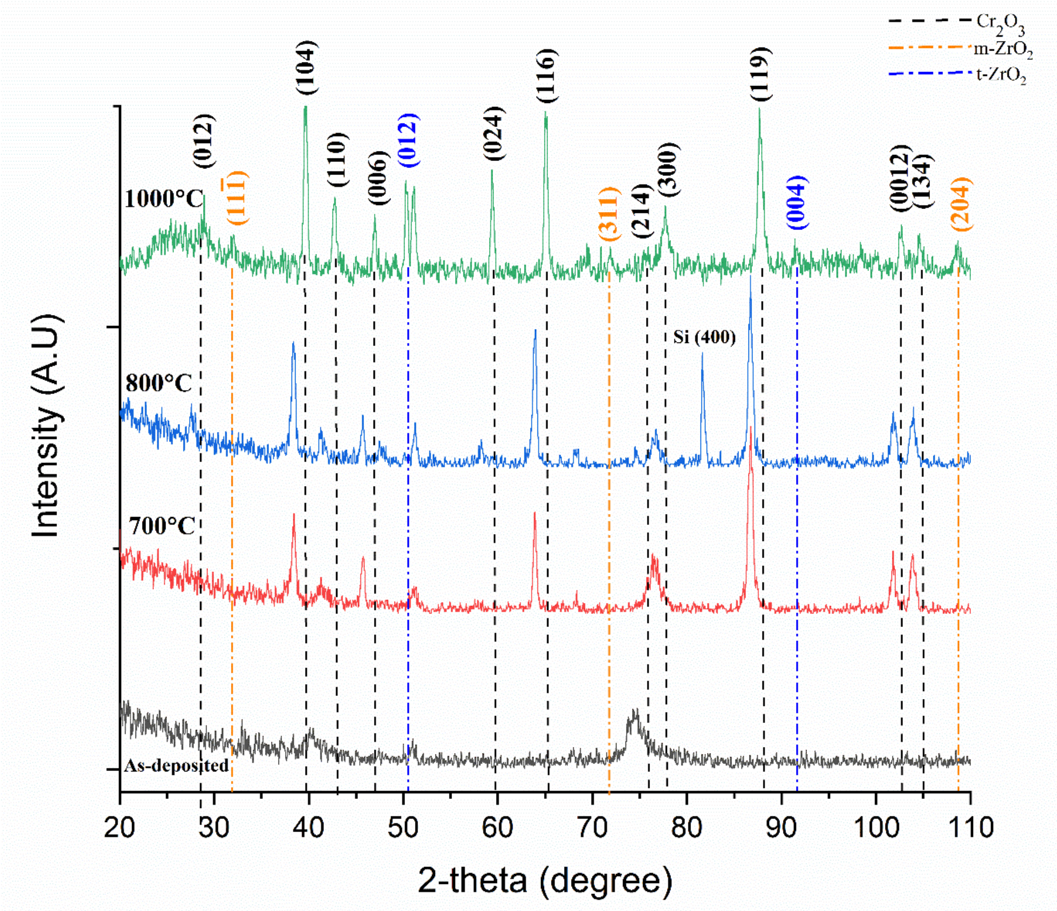

Figure 7-10: XRD patterns of the superhard coatings after heat treatments at indicated temperatures.

The Raman spectroscopy was also employed to supplement the XRD analysis data. Raman spectra of the superhard coatings before and after the heat treatments are shown in Figure 7-11. The Raman spectra of the coatings treated at 300 °C are similar to the as-deposited one which indicates this temperature is not high enough to induce any structural changes. The broad peaks at 552 cm^{-1} and the other one in the range of 600-700 cm^{-1} can be assigned to the Raman mode of nanocrystalline Cr_2O_3 and the defect lines, originating from the intergranular region and strongly defected crystals, respectively [7]. The heat treatments at temperatures 700 and 800 °C resulted in a well-growth crystallized microstructure with peaks at 551 cm^{-1}, 302 cm^{-1}, 350 cm^{-1}, and 611 cm^{-1}, which can be assigned to the hexagonal Cr_2O_3 [27,30,142,232,233]. According to this result, the solubility of zirconium (about 9.5 at. %) into the crystal structure of the hexagonal Cr_2O_3 has a subtle effect on the position of Cr_2O_3 Raman modes, which is lower than the resolution of the Raman spectroscopy to be detected. Two other peaks at 369 cm^{-1} and 411 cm^{-1} were observed along with characteristic hexagonal Cr_2O_3 peaks on the Raman spectrum of the heat treated coating at 1000 °C. These peaks can be assigned to the monoclinic and tetragonal ZrO_2 phases [58] segregated at high temperature from the metastable $(Cr, Zr)_2O_3$ phase. The Raman spectroscopy results are consistent with XRD results showing that the heat treatment at a temperature above 700 °C could transform the nanocrystalline/amorphous coatings into the well-crystallized one. Moreover, the heat treatment at 1000 °C is sufficient to induce the segregation of ZrO_2 phases from the metastable $(Cr, Zr)_2O_3$ phase.

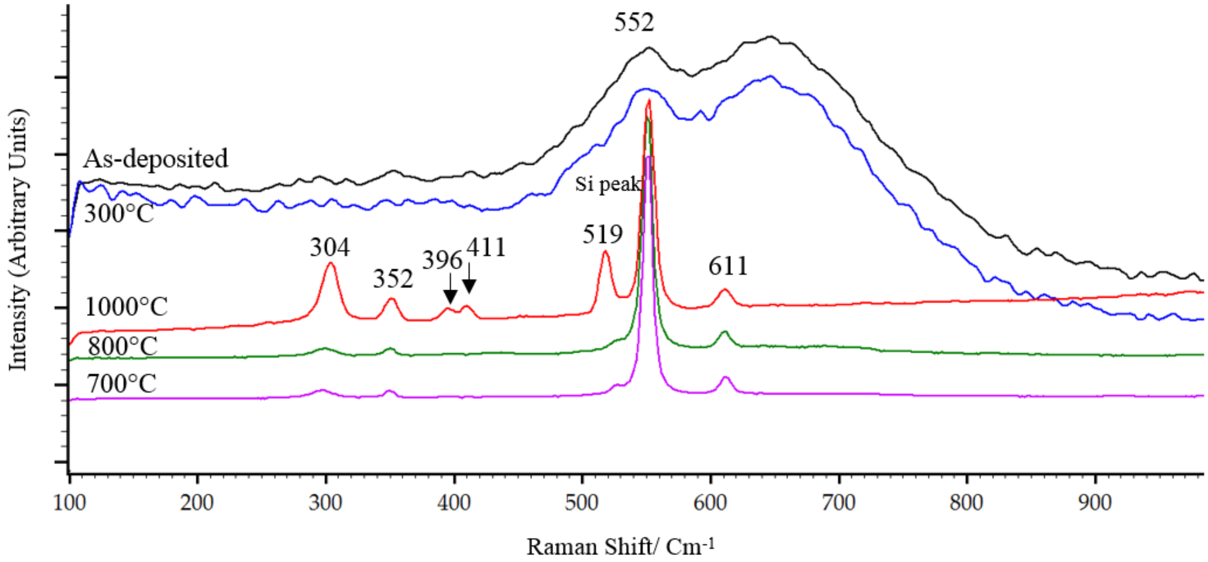

Figure 7-11: Raman Spectra of the as-deposited superhard coatings and after heat treatments at indicated temperatures.

The effect of heat treatment procedures on the hardness of as-deposited superhard coatings is depicted in figure 7-12. The results are also compared with those of the hard Cr_2O_3 coatings. The hardness of superhard coatings did not change up to 500°C as the structure of coatings was intact. By exposing the coating to a temperature above 700 °C, the hardness dropped from 40 GPa to about 30 GPa which can be related to the grain size of coatings grown at high temperature. Unfortunately, further increasing the temperature to 1000 °C caused the coatings to be delaminated from the substrate and it was impractical to measure their hardness. It is predicted that the hardness could have increased again when a composite structure is obtained by the heat treatment at 1000 °C. In contrast, the hardness of hard Cr_2O_3 coatings decreased steadily by increasing the annealing temperature.

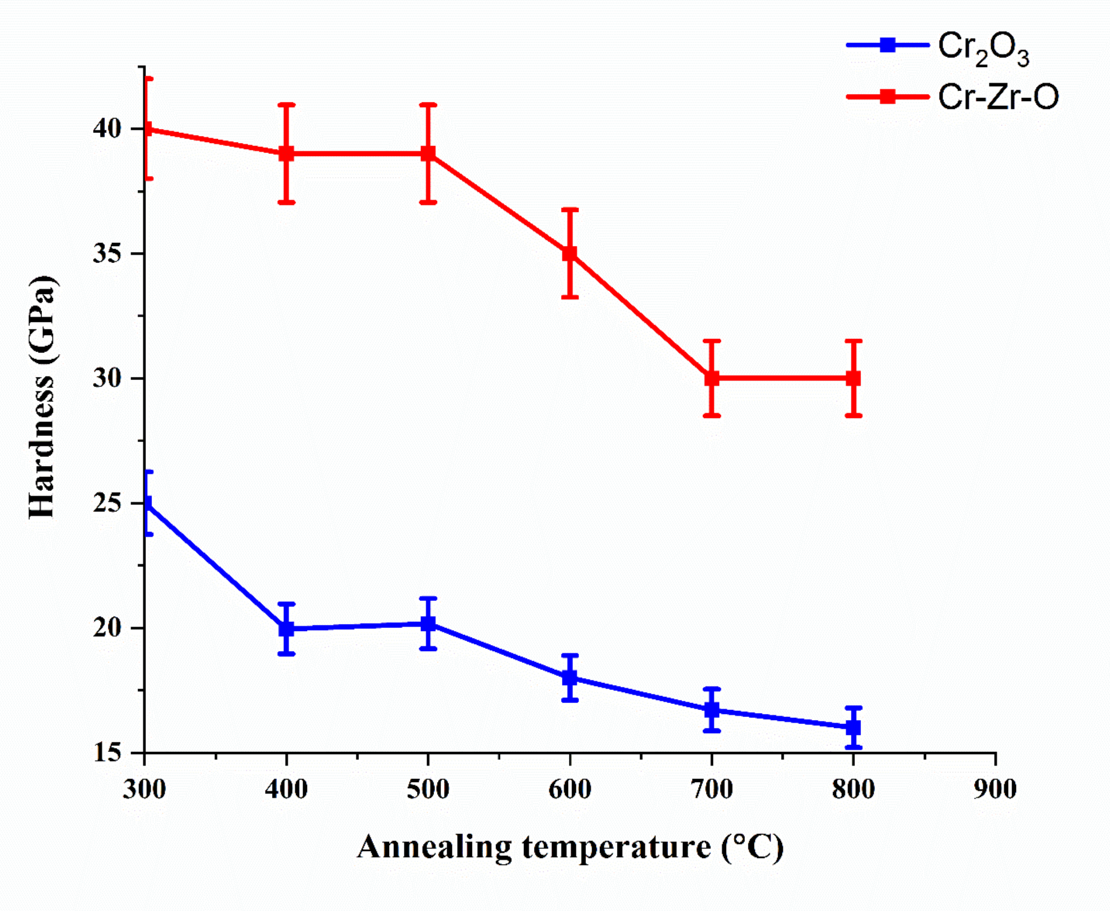

Figure 7-12: The effect of the post-heat treatment temperature on the hardness of the superhard coatings.

7.4. Conclusion

Reactive dual radio-frequency (RF) magnetron sputtering technique was used to deposit ternary Cr-Zr-O coatings on HSS M42 and silicon wafer substrates. The potential of Cr-Zr-O system for producing new superhardness (Hardness ≥ 40 GPa) nanocomposite coatings was investigated in a well-design coating process. The results indicated that with adding Zr into Cr_2O_3 coatings, the compressive residual stress decreases and the crystallization temperature for Cr-rich coatings increases. The superhardness in Cr-Zr-O coatings can only be achieved in narrow chemical composition and deposition temperature range i.e. when the zirconium concentration was 9.5 at.% and substrate temperature was 300°C.

Moreover, the solubility of ZrO_2 into Cr_2O_3 structure is considerable if they are prepared under a nonequilibrium deposition conditions such as magnetron sputtering. However, Crystalline ZrO_2 phases were observed in XRD patterns of Cr-Zr-O coatings deposited at a temperature higher than 600°C resulted in a significant hardness enhancement related to formation of a nanocomposite structure in Cr-Zr-O coatings. A heat treatment at temperature higher than 1000 °C induced the segregation of ZrO_2 phases and removed the zirconium from the host hexagonal Cr_2O_3 crystal structure, indicating that Zr has low solubility in Cr_2O_3 in an equilibrium condition. Annealing treatments at elevated temperatures showed that the thermal stability of superhard (Cr-Zr-O) coatings is much higher than single phase Cr_2O_3 coatings as they could preserve their high hardness up to 500°C. The coatings in Cr-Zr-O system showed an interesting composite formation toward t-ZrO_2 + m-ZrO_2 + h-Cr_2O_3 structure at elevated temperatures which can be interesting for coating microstructure design and motivate more investigation on this ternary oxide systems.

CHAPTER 8

SUMMARY, CONCLUSIONS, AND RECOMMENDATIONS FOR FUTURE WORK

8.1. Summary and Conclusions

In this Ph.D. dissertation, a thorough investigation was conducted to explore the appropriate conditions for deposition of hard r-Cr_2O_3 coatings using a reactive magnetron sputtering technique. In this work also new potential applications of magnetron sputtered hard r-Cr_2O_3 coatings were illustrated. Moreover, to tailor and improve the properties of hard Cr_2O_3 coatings by a nanocomposite mechanism the pseudobinary Cr-Zr-O system was systematically investigated.

In this dissertation the following significant results have been achieved and published in international scientific journals:

- In a reactive magnetron sputtering technique, the Cr_2O_3 coatings with a hardness value close to that of bulk Cr_2O_3 (29 GPa) could be achieved at room temperature, at a low pressure of 1.6×10^{-1} Pa, where Cr-target voltage and oxygen content were 260 V and between 15–20 vol % of total gas, respectively.
- The structure and mechanical properties of the Cr_2O_3 coatings did not show any sensitivity to the amount of oxygen when it changed between 15–25 vol % of total gas. However, other deposition parameters, namely temperature, pressure, and Cr-target voltage had a huge impact on the final structure, and thus, the mechanical properties of the coatings.

- A dense Cr_2O_3 structure was responsible for the observed high hardness.
- The lifetime of biomedical stainless-steel implants could be extended by applying hard Cr_2O_3 coatings. This is due to the fact that hard Cr_2O_3 coatings have good adhesion on SS316L substrates which enhance the corrosion and wear resistance and decrease the toxic ions released from biomedical stainless-steel implants.
- Cr_2O_3 was illustrated to be an effective interlayer to suppress the formation of graphite at the diamond coating/WC-Co interface. As a result, the continuous diamond coating can be successfully deposited on Cr_2O_3 interlayered WC-Co substrate no matter whether the substrate is pre-etched or not.
- By adding Zr into Cr_2O_3 coatings, the compressive residual stress decreases and the crystallization temperature for Cr-rich coatings increases.
- in the Cr-Zr-O system, the results indicated that the superhardness can be achieved in a narrow chemical composition and deposition temperature range i.e. when the zirconium concentration was 9.5 at.% and substrate temperature was 300°C.
- Crystalline ZrO_2 phases were observed in XRD patterns of Cr-Zr-O coatings deposited at a temperature higher than 600°C.
- By formation of an oxide composite structure (i.e. presence of both ZrO_2 and Cr_2O_3 phases) for coatings up to 50 % (Zr/Zr+Cr), a significant increase of hardness was observed. The nanocomposite mechanism was assumed to be responsible for the hardness enhancement.
- Annealing treatments at elevated temperatures showed that the thermal stability of superhard (Cr-Zr-O) coatings is much higher than single phase Cr_2O_3 coatings as they could preserve their high hardness up to 500°C.

8.2. Recommendations for Future Work

The coatings produced in Cr-Zr-O system showed an interesting hardness enhancement when deposited at high temperature. Such hardness enhancement at elevated temperatures is notable for applications as wear protective coatings on cutting tools. Thus, research on the performance of cutting tools coated with superhard Cr-Zr-O coatings in a simulated machining process is reccomended. In addition to the hardness, these coatings may possess high toughness as t-ZrO_2 phase martensitic transformation can be activated to increase the toughness of coatings.

Moreover, binary materials based on ZrO_2 offer high transparency, and there are differences in the electrical conductivities between Cr_2O_3 and ZrO_2. Therefore, depending on the composition, these coatings may even show electro-optical properties. Hence, the detailed investigation on ternary Cr-Zr-O coatings to establish a correlation between their structure, atomic structure, and the optical properties could be an interesting topic for further development of these coating.

REFERENCES

[1] S. Dong, B. Song, B. Hansz, H. Liao, C. Coddet, Microstructure and properties of Cr2O3 coating deposited by plasma spraying and dry-ice blasting, Surf. Coatings Technol. 225 (2013) 58–65. doi:10.1016/j.surfcoat.2013.03.016.

[2] V.P. Singh, A. Sil, R. Jayaganthan, Wear of plasma sprayed conventional and nanostructured Al2O3and Cr2O3, based coatings, Trans. Indian Inst. Met. 65 (2012) 1–12. doi:10.1007/s12666-011-0070-0.

[3] P.S. Babu, D. Sen, A. Jyothirmayi, L.R. Krishna, D.S. Rao, Influence of microstructure on the wear and corrosion behavior of detonation sprayed Cr 2 O 3 -Al 2 O 3 and plasma sprayed Cr 2 O 3 coatings, Ceram. Int. 44 (2018) 2351–2357. doi:10.1016/j.ceramint.2017.10.203.

[4] G. Contoux, F. Cosset, A. Célérier, J. Machet, Deposition process study of chromium oxide thin filmsobtained by d.c. magnetron sputtering, Thin Solid Films. 292 (1997) 75–84. doi:10.1016/S0040-6090(96)08941-9.

[5] F. Luo, K. Gao, X. Pang, H. Yang, L. Qiao, Y. Wang, Characterization of the mechanical properties and failure modes of hard coatings deposited by RF magnetron sputtering, Surf. Coatings Technol. 202 (2008) 3354–3359. doi:10.1016/j.surfcoat.2007.12.020.

[6] G. Carta, M. Natali, G. Rossetto, P. Zanella, G. Salmaso, S. Restello, V. Rigato, S. Kaciulis, A. Mezzi, A comparative study of Cr2O3 thin films obtained by MOCVD using three different precursors, Chem. Vap. Depos. 11 (2005) 375–380. doi:10.1002/cvde.200406360.

[7] O. Monnereau, L. Tortet, C.E.A. Grigorescu, D. Savastru, C.R. Iordanescu, F. Guinneton, R. Notonier, A. Tonetto, T. Zhang, I.N. Mihailescu, D. Stanoi, H.J. Trodahl, Chromium oxides mixtures in PLD films investigated by Raman spectroscopy, J. Optoelectron. Adv. Mater. 12 (2010) 1752–1757.

[8] J.W. Mellor, A comprehensive treatise on inorganic and theoretical chemistry Vol. 11,

Longmans, Green, 1946.

[9] I.S. Kainarskii, E. V. Degtyareva, Chromic oxide as refractory material, Refractories. 18 (1977) 42–47. doi:10.1007/BF01319646.

[10] G. V. Samsonov, THE OXIDE HANDBOOK, IFI/Plenum press, 1973. doi:10.1007/978-1-4615-9597-7.

[11] P. Hones, M. Diserens, F. Lévy, Characterization of sputter-deposited chromium oxide thin films, Surf. Coatings Technol. 120–121 (1999) 277–283. doi:10.1016/S0257-8972(99)00384-9.

[12] A.S. Kao, M.F. Doerner, V.J. Novotny, Processing effects on the tribological characteristics of reactively sputtered chromium oxide (Cr2O3) overcoat films, J. Appl. Phys. 66 (1989) 5315–5321. doi:10.1063/1.343722.

[13] Z. Ding, R. Oberacher, F. Thummler, Cr2O3 particulted Reinforced YTZ ceramics with high fracture toughness and strength, in: S.P.S. Badwal, M.J. Bannister, R.H.J. Hannink (Eds.), Sci. Technol. Zirconia 5, Technomic Publishing Co, 1993: pp. 421–431.

[14] A. Cellard, V. Garnier, G. Fantozzi, G. Baret, P. Fort, Wear resistance of chromium oxide nanostructured coatings, Ceram. Int. 35 (2009) 913–916. doi:10.1016/j.ceramint.2008.02.022.

[15] W.J. LACKEY, D.P. STINTON, G.A. CERNY, A.C. SCHAFFHAUSER, L.L. FEHRENBACHER, Ceramic Coatings for Advanced Heat Engines???A Review and Projection, Adv. Ceram. Mater. 2 (1987) 24–30. doi:10.1111/j.1551-2916.1987.tb00048.x.

[16] B. Bhushan, G.S.A.M. Theunissen, X.D. Li, Tribological studies of chromium oxide films for magnetic recording applications, Thin Solid Films. 311 (1997) 67–80. doi:Doi 10.1016/S0040-6090(97)00453-7.

[17] B. Bhushan, Structural and Compositional Characterization of Rf Sputter-Deposited Ni-Cr+Cr2o3 Films, J. Lubr. Technol. Asme. 103 (1981) 211–217.

[18] E. Sourty, J.L. Sullivan, M.D. Bijker, Chromium oxide coatings applied to magnetic tape heads for improved wear resistance, Tribol. Int. 36 (2003) 389–396. doi:10.1016/S0301-679X(02)00214-1.

[19] J. Trube, Low stress and optically transparent chromium oxide layer for x-ray mask making, J. Vac. Sci. Technol. B Microelectron. Nanom. Struct. 11 (1993) 2990. doi:10.1116/1.586574.

[20] H. Liu, J. Tao, J. Xu, Z. Chen, Q. Gao, Corrosion and tribological behaviors of chromium oxide coatings prepared by the glow-discharge plasma technique, Surf. Coatings Technol. 204 (2009) 28–36. doi:10.1016/j.surfcoat.2009.06.020.

[21] H. Okamoto, Cr-O (Chromium-Oxygen), J. Phase Equilibria. 18 (1997). doi:https://doi.org/10.1007/s11669-997-0072-0.

[22] H.E. Kottcamp, ASM METALS HANDBOOK VOLUME 3 Alloy Phase Diagrams, 1992.

[23] and H.Y. Nobuyuki Iwata, Takeshi Asada, Shunpei Ootsuki, Growth and Evaluation of Magnetoelectric Cr2O3 Single Crystal Thin Films, Mater. Res. Soc. Symp. Proc. 1034 (2008) 1–6.

[24] P.M.F.D. Sousa, Chromium Dioxide – Low Temperature Thin Film Growth , Structural and AND PHYSICAL PROPERTIES, UNIVERSITY OF LISBON, 2008.

[25] S. Spitz, M. Stueber, H. Leiste, S. Ulrich, H.J. Seifert, Microstructure evolution of radio-frequency magnetron sputtered oxide thin films in the Cr-Zr-O system, Thin Solid Films. 548 (2013) 143–149. doi:10.1016/j.tsf.2013.09.038.

[26] R.W.G. Wyckoff, Crystal Structures, 2nd ed., Wiley, 1963.

[27] J. Mougin, T. Le Bihan, G. Lucazeau, High-pressure study of Cr 2 O 3 obtained by high-temperature oxidation by X-ray diffraction and Raman spectroscopy, J. Phys. Chem. Solids. 62 (2001) 553–563.

[28] D.A. Brown, D. Cunningham, W.K. Glass, The infrared and Raman spectra of chromium

(III) oxide, Spectrochim. Acta Part A Mol. Spectrosc. 24 (1968) 965–968. doi:10.1016/0584-8539(68)80115-1.

[29] R.L. Farrow, A.S. Nagelberg, Raman spectroscopy of surface oxides at elevated temperatures, Appl. Phys. Lett. 36 (1980) 945–947. doi:10.1063/1.91659.

[30] S.-H. Shim, T.S. Duffy, R. Jeanloz, C.-S. Yoo, V. Iota, Raman spectroscopy and x-ray diffraction of phase transitions in Cr2O3 to 61 GPa, Phys. Rev. B. 69 (2004) 144107. doi:10.1103/PhysRevB.69.144107.

[31] Y-T. Qian, R. Kershaw, K. Dwight, A. Wold, ON Preparation AND CHARACTERIZATION OF CHROMIUM(III) OXIDE FILMS BY A NOVEL SPRAY PYROLYSIS METHOD, 1990.

[32] J. Mougin, T. Le Bihan, G. Lucazeau, High-pressure study of Cr2O3 obtained by high-temperature oxidation by X-ray diffraction and Raman spectroscopy, J. Phys. Chem. Solids. 62 (2001) 553–563. doi:10.1016/S0022-3697(00)00215-8.

[33] M.A. Vuurman, D.J. Stufkens, A. Oskam, J.A. Moulijn, F. Kapteijn, Raman Spectra of Chromium Oxide Species in CrO3/A12O3 Catalysts, J. Mol. Catal. 60 (1990) 83–98.

[34] B. Bhushan, Friction and Wear Results From Sputter-Deposited Chrome Oxide With and Without If chrome Metallic Binders and Interlayers, J. Lubr. Technol. Asme. 103 (1981) 218–227.

[35] A. Khatibi, J. Lu, J. Jensen, P. Eklund, L. Hultman, Phase transformations in face centered cubic (Al0.32Cr0.68)2O3 thin films, Surf. Coatings Technol. 206 (2012) 3216–3222. doi:10.1016/j.surfcoat.2012.01.008.

[36] M. Witthaut, R. Cremer, K. Reichert, D. Neuschtz, Preparation of Cr 2 O 3 -Al 2 O 3 Solid Solutions by Reactive Magnetron Sputtering, Microchim. Acta. 133 (2000) 191–196. doi:10.1007/s006040070092.

[37] M. Mohammadtaheri, Q. Yang, Y. Li, J. Corona-Gomez, The Effect of Deposition Parameters on the Structure and Mechanical Properties of Chromium Oxide Coatings

Deposited by Reactive Magnetron Sputtering, Coatings. (2018). doi:10.3390/coatings8030111.

[38] J. Lin, W.D. Sproul, Structure and properties of Cr2O3 coatings deposited using DCMS, PDCMS, and DOMS, Surf. Coatings Technol. 276 (2015) 70–76. doi:10.1016/j.surfcoat.2015.06.044.

[39] B. Bhushan, development of r.f. Sputtered chromium oxide coating for wear application, thin solid films. 64 (1979) 231–241.

[40] B. Bhushant, characterization of r . f . -sputter-deposited chromium oxide films, Thin Solid Films. 73 (1980) 255–265.

[41] A.S. Kao, M.F. Doerner, V.J. Novotny, Processing effects on the tribological characteristics of reactively sputtered chromium oxide (Cr_2O_3) overcoat films, J. Appl. Phys. 66 (1989) 5315–5321. doi:10.1063/1.343722.

[42] U. Rothhaar, H. Oechsner, R.f. magnetron sputter deposition of Cr2O3 layers on ceramic Al_2O_3 substrates, Surf. Coatings Technol. 59 (1993) 183–186. doi:10.1016/0257-8972(93)90080-8.

[43] D.-Y. Wang, J.-H. Lin, W.-Y. Ho, Study on chromium oxide synthesized by unbalanced magnetron sputtering, Thin Solid Films. 332 (1998) 295–299. doi:10.1016/S0040-6090(98)01266-8.

[44] M.-C.C. Da-Yung Wang, Characterization of Cr2O3/CrN duplex coatings for injection molding applications, Surf. Coat. Technol. 137 (2001) 164–169. doi:10.1016/j.jmmm.2003.12.245.

[45] B.X. Pang, K. Gao, H. Yang, L. Qiao, Y. Wang, A.A. Volinsky, Interfacial Microstructure of Chromium Oxide Coatings **, Adv. Eng. Mater. 9 (2007) 594–599. doi:10.1002/adem.200700057.

[46] X. Pang, K. Gao, A.A. Volinsky, Microstructure and mechanical properties of chromium oxide coatings, J. Mater. Res. 22 (2007) 3531–3537. doi:10.1557/JMR.2007.0445.

[47] F. Luo, X. Pang, K. Gao, H. Yang, Y. Wang, Role of deposition parameters on microstructure and mechanical properties of chromium oxide coatings, Surf. Coatings Technol. 202 (2007) 58–62. doi:10.1016/j.surfcoat.2007.04.066.

[48] X. Pang, K. Gao, F. Luo, H. Yang, L. Qiao, Y. Wang, A.A. Volinsky, Annealing effects on microstructure and mechanical properties of chromium oxide coatings, Thin Solid Films. 516 (2008) 4685–4689. doi:10.1016/j.tsf.2007.08.083.

[49] H.C. Barshilia, K.S. Rajam, Growth and characterization of chromium oxide coatings prepared by pulsed-direct current reactive unbalanced magnetron sputtering, Appl. Surf. Sci. 255 (2008) 2925–2931. doi:10.1016/j.apsusc.2008.08.057.

[50] A.M. and A.L. M Audronis, Pulsed-bias magnetron sputtering of non-conductive crystalline chromia films at low substrate temperature, J. Phys. D. Appl. Phys. 41 (2008). doi:10.1088/0022-3727/41/3/035309.

[51] S.Y. Jeong, J.B. Lee, H. Na, T.Y. Seong, Epitaxial growth of Cr2O3 thin film on Al 2O3 (0001) substrate by radio frequency magnetron sputtering combined with rapid-thermal annealing, Thin Solid Films. 518 (2010) 4813–4816. doi:10.1016/j.tsf.2010.01.046.

[52] K. Pedersen, J. Bottiger, M. Sridharan, M. Sillassen, P. Eklund, Texture and microstructure of Cr2O3 and (Cr,Al)2O3 thin films deposited by reactive inductively coupled plasma magnetron sputtering, Thin Solid Films. 518 (2010) 4294–4298. doi:10.1016/j.tsf.2010.01.008.

[53] M.M.G. Editor, Technology of Zirconium Ferroalloys, in: Handb. Ferroalloys, Theory Technol., 2013: p. 435. doi:https://doi.org/10.1016/B978-0-08-097753-9.00016-2.

[54] R. Riedel, I. Chen, Ceramics Science and Technology, Wiley-VCH, 2010.

[55] J. Zhang, A.R. Oganov, X. Li, H. Dong, Q. Zeng, Novel compounds in the Zr-O system, their crystal structures and mechanical properties, Phys. Chem. Chem. Phys. 17 (2015) 17301–17310. doi:10.1039/c5cp02252e.

[56] J.F. Shackelford, Y.-H. Han, S. Kim, S.-H. Kwon, CRC MATERIALS SCIENCE AND

ENGINEERING HANDBOOK, 4th ed., CRC Press Taylor & Francis Group, 2016.

[57] K.G. Haragopal S, Sreeramulu B, Shalini K, Sudha Madhuri D, ZIRCONIA : A CREDITABLE RESTORATIVE MATERIAL – A REVIEW, Ann. Essences Dent. 4 (2012) 63–65.

[58] Vassilis G. Keramidas, W.B. White, Raman Scattering Study of the Crystallization and Phase Transformations of ZrO2, J. Am. Ceram. Soc. 57 (1974) 22–24.

[59] T. Hirata, E. Asari, M.Kitajima, Infrared and Raman spectroscopic Studies of ZrO2 polymorphes dopped with Y2O3, J. Solid State Chem. 110 (1994) 201–207.

[60] E. Fernández López, V. Sánchez Escribano, M. Panizza, M.M. Carnasciali, G. Busca, Vibrational and electronic spectroscopic properties of zirconia powders, J. Mater. Chem. 11 (2001) 1891–1897. doi:10.1039/b100909p.

[61] D.P.C. Thackeray, The Raman spectrum of zirconium dioxide, Spectrochim. Acta Part A Mol. Spectrosc. 30 (1974) 549–550. doi:10.1016/0584-8539(74)80096-6.

[62] K.S. Phillippi, C.M., Mazdyasni, Infrared and Raman Spectra of Zirconia Polymorphs, J. Am. Ceram. Soc. 54 (1971) 254–258. doi:10.1063/1.1712198.

[63] P. Barberis, T. Merle-Méjean, P. Quintard, On Raman spectroscopy of zirconium oxide films, J. Nucl. Mater. 246 (1997) 232–243. doi:10.1016/S0022-3115(97)00038-X.

[64] M.H. Suhail, G. Mohan Rao, S. Mohan, Effect of substrate temperature on the properties of ZrO2 films prepared by d.c. reactive magnetron sputtering, Mater. Sci. Eng. B. 12 (1992) 247–251. doi:10.1016/0921-5107(92)90295-K.

[65] P. Gao, L.J. Meng, M.P. Dos Santos, V. Teixeira, M. Andritschky, Characterisation of ZrO2 films prepared by rf reactive sputtering at different O2 concentrations in the sputtering gases, Vacuum. 56 (2000) 143–148.

[66] P. Gao, L.J. Meng, M.P. Santos, V. Teixeira, M. Andritschky, Influence of sputtering power and the substrate - target distance on the properties of ZrO 2 films prepared by RF

reactive sputtering, Thin Solid Films. 377–378 (2000) 557–561. doi:10.1016/S0040-6090(00)01291-8.

[67] P. Gao, L.J. Meng, M.P. Santos, V. Teixeira, M. Andritschky, Influence of sputtering pressure on the structure and properties of ZrO 2 films prepared by rf reactive sputtering, Appl. Surf. Sci. 173 (2001) 84–90. doi:10.1016/S0169-4332(00)00888-6.

[68] A.P. Huang, P.K. Chu, Microstructural improvement of sputtered ZrO2 thin films by substrate biasing, Mater. Sci. Eng. B Solid-State Mater. Adv. Technol. 121 (2005) 244–247. doi:10.1016/j.mseb.2005.04.002.

[69] C.Y. Ma, F. Lapostolle, P. Briois, Q.Y. Zhang, Effect of O2 gas partial pressure on structures and dielectric characteristics of rf sputtered ZrO2 thin films, Appl. Surf. Sci. 253 (2007) 8718–8724. doi:10.1016/j.apsusc.2007.04.054.

[70] H. Sohn, The Effect of the RF-Sputtering Condition on the ZrO 2 Thin Film ' s Characteristics, 51 (2007) 1038–1041. doi:10.3938/jkps.51.1038.

[71] S. Zhao, F. Ma, K.W. Xu, H.F. Liang, Optical properties and structural characterization of bias sputtered ZrO2 films, J. Alloys Compd. 453 (2008) 453–457. doi:10.1016/j.jallcom.2006.11.134.

[72] K. Prabakar, A. Park, N. Cho, W.I. Lee, C.K. Hwangbo, J.G. Lee, C. Lee, rf-Magnetron sputter deposited ZrO2 dielectrics for metal-insulator-semiconductor capacitors, Vacuum. 82 (2008) 1367–1370. doi:10.1016/j.vacuum.2008.03.039.

[73] S. Zhao, F. Ma, Z. Song, K. Xu, Thickness-dependent structural and optical properties of sputter deposited ZrO2 films, Opt. Mater. (Amst). 30 (2008) 910–915. doi:10.1016/j.optmat.2007.04.001.

[74] S. Iwatsubo, K. Ishii, Structure and mechanical properties of ZrO2 films deposited by gas flow sputtering, Vacuum. 83 (2008) 579–581. doi:10.1016/j.vacuum.2008.04.056.

[75] H.H. Zhang, C.Y. Ma, Q.Y. Zhang, Scaling behavior and structure transition of ZrO2 films deposited by RF magnetron sputtering, Vacuum. 83 (2009) 1311–1316.

doi:10.1016/j.vacuum.2009.04.041.

[76] P. Kondaiah, G.M. Rao, S. Uthanna, Preparation of magnetron sputtered ZrO 2 films on Si for gate dielectric application, J. Phys. Conf. Ser. 390 (2012) 012031. doi:10.1088/1742-6596/390/1/012031.

[77] P. Kondaiah, V. Madhavi, S. Uthanna, Oxygen partial pressure influenced structural and optical properties of DC magnetron sputtered ZrO[sub 2] films, 756 (2013) 756–757. doi:10.1063/1.4791258.

[78] J. Vlček, J. Rezek, J. Houška, R. Čerstvý, R. Bugyi, Process stabilization and a significant enhancement of the deposition rate in reactive high-power impulse magnetron sputtering of ZrO2 and Ta2O5 films, Surf. Coatings Technol. 236 (2013) 550–556. doi:10.1016/j.surfcoat.2013.10.052.

[79] Y. Shen, S. Shao, H. Yu, Z. Fan, H. He, J. Shao, Influences of oxygen partial pressure on structure and related properties of ZrO2 thin films prepared by electron beam evaporation deposition, Appl. Surf. Sci. 254 (2007) 552–556. doi:10.1016/J.APSUSC.2007.06.029.

[80] J. Gottmann, E.W. Kreutz, Pulsed laser deposition of alumina and zirconia thin films on polymers and glass as optical and protective coatings, Surf. Coatings Technol. 116–119 (1999) 1189–1194. doi:10.1016/S0257-8972(99)00191-7.

[81] J. Vlček, J. Rezek, J. Houška, T. Kozák, J. Kohout, Benefits of the controlled reactive high-power impulse magnetron sputtering of stoichiometric ZrO2 films, Vacuum. 114 (2015) 131–141. doi:10.1016/j.vacuum.2014.12.004.

[82] S. Sønderby, kemi och biologi. Linköpings universitet. Institutionen för fysik, Physical Vapor Deposition of Yttria-Stabilized Zirconia and Gadolinia-Doped Ceria Thin Films for Fuel Cell Applications, Department of Physics, Chemistry and Biology (IFM), Linköping University, 2012.

[83] S. Sprio, S. Guicciardi, A. Bellosi, G. Pezzotti, Yttria-stabilized zirconia films grown by radiofrequency magnetron sputtering: Structure, properties and residual stresses, Surf. Coatings Technol. 200 (2006) 4579–4585. doi:10.1016/j.surfcoat.2005.04.003.

[84] Z. Ji, J.A. Haynes, E. Voelkl, J.M. Rigsbee, Phase Formation and Stability in Reactively Sputter Deposited Yttria-Stabilized Zirconia Coatings, J. Am. Ceram. Soc. 84 (2001) 929–936. doi:10.1111/j.1151-2916.2001.tb00770.x.

[85] H. Tomaszewski, J. Haemers, J. Denul, N. De Roo, R. De Gryse, Yttria-stabilized zirconia thin films grown by reactive r.f. magnetron sputtering, Thin Solid Films. 287 (1996) 104–109. doi:10.1016/S0040-6090(96)08743-3.

[86] M. Boulouz, A. Boulouz, A. Giani, A. Boyer, Influence of substrate temperature and target composition on the properties of yttria-stabilized zirconia thin films grown by r.f. reactive magnetron sputtering, Thin Solid Films. 323 (1998) 85–92. doi:10.1016/S0040-6090(97)01053-5.

[87] T. Hirai, K. Teramoto, H. Koike, K. Nagashima, Y. Tarui, Initial Stage and Growth Process of Ceria, Yttria-Stabilized-Zirconia and Ceria-Zirconia Mixture Thin Films on Si(100) Surfaces, Jpn. J. Appl. Phys. 36 (1997) 5253–5258. doi:10.1143/JJAP.36.5253.

[88] A. Lamperti, E. Cianci, R. Ciprian, D. Sangalli, A. Debernardi, Stabilization of tetragonal/cubic phase in Fe doped zirconia grown by atomic layer deposition, Thin Solid Films. 533 (2013) 83–87. doi:10.1016/J.TSF.2012.11.127.

[89] A. Portinha, V. Teixeira, J. Carneiro, M.F. Costa, N.P. Barradas, A.D. Sequeira, Stabilization of ZrO_2 PVD coatings with Gd_2O_3, Surf. Coatings Technol. 188–189 (2004) 107–115. doi:10.1016/J.SURFCOAT.2004.08.016.

[90] D.H. Trinh, M. Ottosson, M. Collin, I. Reineck, L. Hultman, H. Högberg, Nanocomposite Al2O3-ZrO2 thin films grown by reactive dual radio-frequency magnetron sputtering, Thin Solid Films. 516 (2008) 4977–4982. doi:10.1016/j.tsf.2007.10.001.

[91] H. Klostermann, B. Bocher, F. Fietzke, T. Modes, O. Zywitzki, Nanocomposite oxide and nitride hard coatings produced by pulse magnetron sputtering, Surf. Coatings Technol. 200 (2005) 760–764. doi:10.1016/j.surfcoat.2005.02.120.

[92] S. Bruns, M. Vergöhl, O. Werner, T. Wallendorf, High rate deposition of mixed oxides by controlled reactive magnetron-sputtering from metallic targets, Thin Solid Films. 520

(2012) 4122–4126. doi:10.1016/j.tsf.2011.07.014.

[93] J. Musil, P. Baroch, High-rate pulsed reactive magnetron sputtering of oxide nanocomposite coatings, Vacuum. 87 (2013) 96–102. doi:10.1016/j.vacuum.2012.02.023.

[94] D.H. Trinh, H. Högberg, J.M. Andersson, M. Collin, I. Reineck, U. Helmersson, L. Hultman, Radio frequency dual magnetron sputtering deposition and characterization of nanocomposite Al2O3–ZrO2 thin films, J. Vac. Sci. Technol. A Vacuum, Surfaces, Film. 24 (2006) 309–316. doi:10.1116/1.2171709.

[95] C.M. Gilmore, C. Quinn, E.F. Skelton, C.R. Gossett, S.B. Qadri, Stabilized zirconia–alumina thin films, J. Vac. Sci. Technol. A Vacuum, Surfaces, Film. 4 (1986) 2598–2600. doi:10.1116/1.573733.

[96] C.M. Gilmore, C. Quinn, S.B. Qadri, C.R. Gossett, E.F. Skelton, Stabilization of tetragonal ZrO_2 with Al_2O_3 in reactive magnetron sputtered thin films, J. Vac. Sci. Technol. A Vacuum, Surfaces, Film. 5 (1987) 2085–2087. doi:10.1116/1.574925.

[97] J. Musil, J. Sklenka, R. Cerstvy, Transparent Zr–Al–O oxide coatings with enhanced resistance to cracking, Surf. Coatings Technol. 206 (2012) 2105–2109. doi:10.1016/J.SURFCOAT.2011.09.035.

[98] D.E. Ruddell, B.R. Stoner, J.Y. Thompson, Effect of deposition interruption and substrate bias on the structure of sputter-deposited yttria-stabilized zirconia thin films, J. Vac. Sci. Technol. A Vacuum, Surfaces, Film. 20 (2002) 1744–1748. doi:10.1116/1.1501573.

[99] R. RUH, K.S. MAZDIYASNI, P.G. VALENTINE, H.O. BIELSTEIN, Phase Relations in the System ZrO_2- Y_2O_3 at Low Y_2O_3 Contents, J. Am. Ceram. Soc. 67 (1984) C-190-C-192. doi:10.1111/j.1151-2916.1984.tb19618.x.

[100] D.E. Ruddell, B.R. Stoner, J.Y. Thompson, The effect of deposition parameters on the properties of yttria-stabilized zirconia thin films, Thin Solid Films. 445 (2003) 14–19. doi:10.1016/j.tsf.2003.07.009.

[101] S.B. Qadri, C.M. Gilmore, C. Quinn, E.F. Skelton, C.R. Gossett, Phase stability of ZrO

2 − Al 2 O 3 thin films deposited by magnetron sputtering, Phys. Rev. B. 39 (1989) 6234–6237. doi:10.1103/PhysRevB.39.6234.

[102] S.B. Qadri, C.M. Gilmore, C. Quinn, E.F. Skelton, C.R. Gossett, Structural stability of ZrO_2–Al_2O_3 thin films deposited by magnetron sputtering, J. Vac. Sci. Technol. A Vacuum, Surfaces, Film. 7 (1989) 1220–1224. doi:10.1116/1.576258.

[103] J.R. Sohn, S.G. Ryu, H.W. Kim, Acidic property and catalytic behavior of chromium oxide-zirconia catalyst, J. Mol. Catal. A Chem. 135 (1998) 99–106. doi:10.1016/S1381-1169(97)00295-1.

[104] S. Deng, H. Li, S. Li, Y. Zhang, Activity and characterization of modified Cr2O3/ZrO2 nano-composite catalysts for oxidative dehydrogenation of ethane to ethylene with CO2, J. Mol. Catal. A Chem. 268 (2007) 169–175. doi:10.1016/j.molcata.2006.12.033.

[105] L.Y. Jin, R.H. Ma, J.J. Lin, L. Meng, Y.J. Wang, M.F. Luo, Bifunctional Pd/Cr2O3-ZrO2 catalyst for the oxidation of volatile organic compounds, Ind. Eng. Chem. Res. 50 (2011) 10878–10882. doi:10.1021/ie200599v.

[106] K.. Wang S.a Murata, Cr2O3/ZrO2 catalysts for CO2 dehydrogenation of ethane to ethylene, Stud. Surf. Sci. Catal. 147 (2004) 691–696. http://www.scopus.com/inward/record.url?eid=2-s2.0-9444271601&partnerID=40&md5=a45f09ced21b3b7b2d9135c9f5a95513.

[107] R. Wu, P. Xie, Y. Cheng, Y. Yue, S. Gu, W. Yang, C. Miao, W. Hua, Z. Gao, Hydrothermally prepared Cr2O3-ZrO2 as a novel efficient catalyst for dehydrogenation of propane with CO2, Catal. Commun. 39 (2013) 20–23. doi:10.1016/j.catcom.2013.05.002 Short Communication.

[108] S.S. MANIKPRAGE JAYARATNA, MASAHIRO YOSHIMURA, Electrical conductivity of Cr203-doped Y2O3-stabilized ZrO2, J. Mater. Sci. 22 (2016) 2011–2016.

[109] A. Sengupta, S. Misra, S. Ram, Magnetism in a Spintronic Compound Zr<sub>0.8</sub>Cr<sub>0.2</sub>O<sub>2</sub> of Small Crystallites, J. Nano Res. 28 (2014) 101–108.

doi:10.4028/www.scientific.net/JNanoR.28.101.

[110] Sudhakar B. Deshmukh, Ganesh E. Patil, Ramesh H. Bari, Gotan H. Jain, Ammonia gas sensing properties of Cr2O3 activated ZrO2 thick film resistors, in: 2012 Sixth Int. Conf. Sens. Technol., 2012: pp. 517–526.

[111] J.C. Ray, P. Pramanik, S. Ram, Formation of Cr3+ stabilized ZrO2 nanocrystals in a single cubic metastable phase by a novel chemical route with a sucrose-polyvinyl alcohol polymer matrix, Mater. Lett. 48 (2001) 281–291. doi:10.1016/S0167-577X(00)00316-5.

[112] S. Ram, Synthesis and structural and optical properties of metastable ZrO 2 nanoparticles with intergranular Cr 3 + / Cr 4 + doping and grain surface modification, 8 (2003) 643–655.

[113] J.C. Ray, C.R. Saha, P. Pramanik, Stabilized nanoparticles of metastable ZrO 2 with Cr 3 + / Cr 4 + cations : preparation from a polymer precursor and the study of the thermal and structural properties, J. Eur. Ceram. Soc. 22 (2002) 851–862.

[114] S.M. G. Stefanic , S. Popovic, Influence of Cr2O3 on the stability of low temperature t-ZrO2, Mater. Lett. 36 (1998) 240–244.

[115] J. F. Collins, F. Ferguson, Lattice Parameter Variations in Mixed Oxides with the Monoclinic Zirconia Structure : the Systems ZrO2-Fe2O3, ZrO2-SnO2, and ZrO2-Cr2O3 By, J. Chem. Soc. (1968) 4–5.

[116] D.A. Jerebtsov, G.G. Mikhailov, S. V Sverdina, Phase diagram of the system : Cr 2 O 3 - ZrO 2, Cermaics Int. 27 (2001) 247–250.

[117] R. RUH, H.J. GARRETT, Reactions of Zirconia and Chromium, J. Am. Ceram. Soc. 47 (1964) 627–629.

[118] P. Wu, R. Kershaw, K. Dwight, A. Wold, Preparation and characterization of members of the chromium-zirconium oxide system, J. Mater. Sci. Lett. 6 (1987) 753–755.

[119] G. Štefanić, S. Musić, A. Gajović, Thermal behavior of the amorphous precursors in the

ZrO2–CrO1.5 system, J. Mol. Struct. 744–747 (2005) 541–549. doi:10.1016/j.molstruc.2004.10.076.

[120] Y. Takano, T. Komeda, M. Yoshinaka, K. Hirota, O. Yamaguchi, Fabrication, Microstructure, and Mechanical Properties of Cr2O3/ZrO2(2.5Y) Composite Ceramics in the Cr2O3-Rich Region, J. Am. Ceram. Soc. 81 (1998) 2497–2500.

[121] L.F. Chekhomova, Abrasive Properties of Modified Chromia, Inorg. Mater. 37 (2001) 342–348.

[122] L. Landälv, J. Lu, S. Spitz, H. Leiste, S. Ulrich, M.P. Johansson-Jõesaar, M. Ahlgren, E. Göthelid, B. Alling, L. Hultman, M. Stüber, P. Eklund, Structural evolution in reactive RF magnetron sputtered (Cr,Zr) 2 O 3 coatings during annealing, Acta Mater. 131 (2017) 543–552. doi:10.1016/j.actamat.2017.03.063.

[123] Ruth E. Whan, ASM Handbook- Materials Characterization, 1992.

[124] Elton N. Kaufmann, Characterization of Materials, John Wiley & Sons, Inc, 2003.

[125] W.S. Richard Brundle. C, Evans. Charles A, Encyclopedia of materials characterization, 1992.

[126] Zygo, Zygo New view 8000- operation manual, (2012).

[127] M. Suryanarayana, C and Grant Norton, X-Ray Diffraction- A Practical Approach, Springer Science+Business Media, 1998. doi:10.1007/978-1-4899-0148-4.

[128] J.F. Moulder, W.F. Stickle, P.E. Sobol, K.D. Bomben, Handbook of X-ray Photoelectron Spectroscopy, (1992) 261. doi:10.1002/sia.740030412.

[129] ISO 14577-1, Metallic Materials-Instrumented indentation test for hardness and materials parameters-test method, (2015).

[130] W.C. Oliver, G.M. Pharr, An improved technique for determining hardness and elastic modulus using load and displacement sensing indentation experiments, Mater. Res. Soc. 7 (1992) 1564–1583.

[131] ISO 1071-11-Advanced technical ceramics — Methods of test for ceramic coatings- Part 11: Determination of internal stress by the Stoney formula, (2005).

[132] ASTM G5, Standard Reference Test Method for Making Potentiodynamic Anodic Polarization MEasurements, (2015) 1–9. doi:10.1520/G0005-14.2.

[133] A.D.S. Li, Gang; Evitts, Richard; Boulfiza, Moh; Li, A customized Python module for interactive curve fitting on potentiodynamic scan data, (2018). https://zenodo.org/record/1343975#.W6FZvc5KjIU.

[134] BS EN1071-12, Advanced technical ceramics. Methods of test for ceramic coatings. Reciprocating wear test, (2010).

[135] ISO 26443, Fine ceramics (advanced ceramics, advanced technical ceramics) — Rockwell indentation test for evaluation of adhesion of ceramic coatings, (2002).

[136] Inductively Coupled Plasma Optical Emission Spectroscopy (ICP-OES) Information, (n.d.). https://www.thermofisher.com.

[137] a. . Ji, W. Wang, G.. Song, Q.. Wang, C. Sun, L.. Wen, Microstructures and mechanical properties of chromium oxide films by arc ion plating, Mater. Lett. 58 (2004) 1993–1998. doi:10.1016/j.matlet.2003.12.029.

[138] S. Wu, H. Chen, X. Du, Z. Liu, Effect of deposition power and pressure on rate deposition and resistivity of titanium thin films grown by DC magnetron sputtering, Spectrosc. Lett. 49 (2016) 514–519. doi:10.1080/00387010.2016.1212244.

[139] O. FUKUNAGA, S. SAITO, Phase Equilibrium in the System CrO 2 -Cr 2 O 3, J. Am. Ceram. Soc. 51 (1968) 362–363. doi:10.1111/j.1151-2916.1968.tb11893.x.

[140] K. Pedersen, J. B??ttiger, M. Sridharan, M. Sillassen, P. Eklund, Texture and microstructure of Cr2O3 and (Cr,Al)2O3 thin films deposited by reactive inductively coupled plasma magnetron sputtering, Thin Solid Films. 518 (2010) 4294–4298. doi:10.1016/j.tsf.2010.01.008.

[141] Elton N. Kaufmann, Raman Spectroscopy of Solids, in: Charact. Mater., John Wiley & Sons, Inc, 2003: pp. 698–700.

[142] S. Kikuchi, K. Kawauchi, M. Kurosawa, H. Honjho, T. Yagishita, Non-destructive Rapid Analysis Discriminating between Chromium(VI) and Chromium(III) Oxides in Electrical and Electronic Equipment Using Raman Spectroscopy, Anal. Sci. 21 (2005) 197–198. doi:10.2116/analsci.21.197.

[143] M. Iliev, A. Litvinchuk, H.-G. Lee, C. Chu, A. Barry, J. Coey, Raman spectroscopy of ferromagnetic CrO_2, Phys. Rev. B. 60 (1999) 33–36. doi:10.1103/PhysRevB.60.33.

[144] D. Stanoi, G. Socol, C. Grigorescu, F. Guinneton, O. Monnereau, L. Tortet, T. Zhang, I.N. Mihailescu, Chromium oxides thin films prepared and coated in situ with gold by pulsed laser deposition, Mater. Sci. Eng. B Solid-State Mater. Adv. Technol. 118 (2005) 74–78. doi:10.1016/j.mseb.2004.12.016.

[145] R.S. Berg, P.Y. Yu, E.R. Weber, Raman spectroscopy of intrinsic defects in electron and neutron irradiated GaAs, Appl. Phys. Lett. 47 (1985) 515–517. doi:10.1063/1.96111.

[146] G. Yasumasa, K. Toshio, On at the Phase Diagram of the Cr-O System at High Pressure of Oxygen and some properties of the Compound CrO2 + x, J. Japan Soc. Powder Powder Metellurgy. 9 (1962) 109–113. doi:http://doi.org/10.2497/jjspm.9.109.

[147] H.F. Levin, E.M., Robbins, C.R., McMurdie, Phase diagrams for ceramists, The American Ceramic Society, 1964.

[148] I. Saeki, T. Ohno, D. Seto, O. Sakai, Y. Sugiyama, T. Sato, A. Yamauchi, K. Kurokawa, M. Takeda, T. Onishi, Measurement of Young's modulus of oxides at high temperature related to the oxidation study, Mater. High Temp. 28 (2011) 264–268. doi:10.3184/096034011X13182685579795.

[149] S. Ningshen, U. Kamachi Mudali, G. Amarendra, P. Gopalan, R.K. Dayal, H.S. Khatak, Hydrogen effects on the passive film formation and pitting susceptibility of nitrogen containing type 316L stainless steels, Corros. Sci. 48 (2006) 1106–1121. doi:10.1016/j.corsci.2005.05.003.

[150] A.M. Oje, A.A. Ogwu, Chromium oxide coatings with the potential for eliminating the risk of chromium ion release in orthopaedic implants Subject Category :, R. Soc. Open Sci. 4 (2017) 170218. doi:10.1098/rsos.170218.

[151] C.A. Love, R.B. Cook, T.J. Harvey, P.A. Dearnley, R.J.K. Wood, Diamond like carbon coatings for potential application in biological implants—a review, Tribol. Int. 63 (2013) 141–150. doi:10.1016/J.TRIBOINT.2012.09.006.

[152] R.K. Roy, K.-R. Lee, Biomedical applications of diamond-like carbon coatings: A review, J. Biomed. Mater. Res. Part B Appl. Biomater. 83B (2007) 72–84. doi:10.1002/jbm.b.30768.

[153] J. Fisher, X.Q. Hu, T.D. Stewart, S. Williams, J.L. Tipper, E. Ingham, M.H. Stone, C. Davies, P. Hatto, J. Bolton, M. Riley, C. Hardaker, G.H. Isaac, G. BERRY, Wear of surface engineered metal-on-metal hip prostheses, J. Mater. Sci. Mater. Med. 15 (2004) 225–235. doi:10.1023/B:JMSM.0000015482.24542.76.

[154] J. Fisher, X.Q. Hu, J.L. Tipper, T.D. Stewart, S. Williams, M.H. Stone, C. Davies, P. Hatto, J. Bolton, M. Riley, C. Hardaker, G.H. Isaac, G. Berry, E. Ingham, An *in vitro* study of the reduction in wear of metal-on-metal hip prostheses using surface-engineered femoral heads, Proc. Inst. Mech. Eng. Part H J. Eng. Med. 216 (2002) 219–230. doi:10.1243/09544110260138709.

[155] R.P. van Hove, I.N. Sierevelt, B.J. van Royen, P.A. Nolte, Titanium-Nitride Coating of Orthopaedic Implants: A Review of the Literature, Biomed Res. Int. 2015 (2015) 1–9. doi:10.1155/2015/485975.

[156] I. Gotman, E.Y. Gutmanas, Titanium nitride-based coatings on implantable medical devices, Adv. Biomater. Devices Med. 1 (2014) 53–73.

[157] A.P. Serro, C. Completo, R. Colaço, F. dos Santos, C.L. da Silva, J.M.S. Cabral, H. Araújo, E. Pires, B. Saramago, A comparative study of titanium nitrides, TiN, TiNbN and TiCN, as coatings for biomedical applications, Surf. Coatings Technol. 203 (2009) 3701–3707. doi:10.1016/J.SURFCOAT.2009.06.010.

[158] K.Y. Anttila A, Lappalainen R, Heinonen H, Santavirta S, Superiority of diamondlike carbon coating on articulating surfaces of artificial hip joints, New Diam. Front Carbon Technol. 9 (1999) 283–288.

[159] G. Taeger, L.E. Podleska, B. Schmidt, M. Ziegler, D. Nast-Kolb, Comparison of Diamond-Like-Carbon and Alumina-Oxide articulating with Polyethylene in Total Hip Arthroplasty, Materwiss. Werksttech. 34 (2003) 1094–1100. doi:10.1002/mawe.200300717.

[160] C.P. Charalambous, Calcium Phosphate Ceramics as Hard Tissue Prosthetics, in: Class. Pap. Orthop., Springer London, London, 2014: pp. 419–421. doi:10.1007/978-1-4471-5451-8_106.

[161] M. Mohammadtaheri, Q. Yang, Y. Li, J. Corona-Gomez, The Effect of Deposition Parameters on the Structure and Mechanical Properties of Chromium Oxide Coatings Deposited by Reactive Magnetron Sputtering, Coatings. 8 (2018) 111. doi:10.3390/coatings8030111.

[162] C. Tromas, J.C. Stinville, C. Templier, P. Villechaise, Hardness and elastic modulus gradients in plasma-nitrided 316L polycrystalline stainless steel investigated by nanoindentation tomography, Acta Mater. 60 (2012) 1965–1973. doi:10.1016/J.ACTAMAT.2011.12.012.

[163] X.Q. and W.H. Jianjun, Wei, Friction and wear of Cr203 coating in inorganic salt solutions, Wear. 152 (1992) 161–170.

[164] M. Díaz, P. Sevilla, A.M. Galán, G. Escolar, E. Engel, F.J. Gil, Evaluation of ion release, cytotoxicity, and platelet adhesion of electrochemical anodized 316 L stainless steel cardiovascular stents, J. Biomed. Mater. Res. Part B Appl. Biomater. 87B (2008) 555–561. doi:10.1002/jbm.b.31144.

[165] T. Santonen, H. Stockmann, A. ZITTING, Review on toxicity of stainless steel, 2010.

[166] L. Kocadereli, P.A. Ataç, P.S. Kale, D. Ozer, Salivary nickel and chromium in patients with fixed orthodontic appliances., Angle Orthod. 70 (2000) 431–4. doi:10.1043/0003-

3219(2000)070<0431:SNACIP>2.0.CO;2.

[167] G. Ağaoğlu, T. Arun, B. Izgi, A. Yarat, B. Izgü, Nickel and chromium levels in the saliva and serum of patients with fixed orthodontic appliances., Angle Orthod. 71 (2001) 375–9. doi:10.1043/0003-3219(2001)071<0375:NACLIT>2.0.CO;2.

[168] P.W. May, CVD diamond: a new technology for the future?, Endeavour. 19 (1995) 101–106. doi:10.1016/0160-9327(95)97494-S.

[169] M. Schwander, K. Partes, A review of diamond synthesis by CVD processes, Diam. Relat. Mater. 20 (2011) 1287–1301. doi:10.1016/J.DIAMOND.2011.08.005.

[170] G. Knuyt, K. Vandierendonck, C. Quaeyhaegens, M. Van Stappen, L.M. Stals, Study of the delamination of diamond coatings under thermal stress, 1997. https://ac.els-cdn.com/S0040609096094977/1-s2.0-S0040609096094977-main.pdf?_tid=c7b2819e-89a9-41e9-b571-342697497fb5&acdnat=1549044332_dedb5348d4cba0bf04812a6785b04337 (accessed February 1, 2019).

[171] A.I. M.A. Taher, W.F. Schmidt, A.P. Malshe, E.J. Oles, The state-of-the-art in adhesion of CVD diamond to carbide cutting inserts, in: Adhes. Asp. Thin Film. Vol.1, K.L. Mittal (Ed.), 2001: pp. 79–139.

[172] A.K. Mehlmann, A. Fayer, S.F. Dirnfeld, Y. Avigal, R. Porath, A. Kochman, Nucleation and growth of diamond on cemented carbides by hot-filament chemical vapor deposition, Diam. Relat. Mater. 2 (1993) 317–322. doi:10.1016/0925-9635(93)90074-C.

[173] F. Deuerler, H. van den Berg, R. Tabersky, A. Freundlieb, M. Pies, V. Buck, Pretreatment of substrate surface for improved adhesion of diamond films on hard metal cutting tools, Diam. Relat. Mater. 5 (1996) 1478–1489. doi:10.1016/S0925-9635(96)00569-9.

[174] M.G. Peters, R.H.Cummings, Methods for Coating Adherent Diamond Films on Cemented Tungsten Carbide Substrates, US5236740, (1993)., n.d.

[175] R. Polini, Chemically vapour deposited diamond coatings on cemented tungsten carbides:

Substrate pretreatments, adhesion and cutting performance, Thin Solid Films. 515 (2006) 4–13. doi:10.1016/J.TSF.2005.12.042.

[176] T. Isozaki, Y. Saito, A. Masuda, K. Fukumoto, M. Chosa, T. Ito, E.J. Oles, A. Inspector, C.E. Bauer, Improvement on adhesion strength of diamond film on cemented carbide by heated intermediate layer, Diam. Relat. Mater. 2 (1993) 1156–1159. doi:10.1016/0925-9635(93)90161-T.

[177] W.C. Lai, Y.-S. Wu, H.-C. Chang, Y.-H. Lee, Enhancing the adhesion of diamond films on cobalt-cemented tungsten carbide substrate using tungsten particles via MPCVD system, J. Alloys Compd. 509 (2011) 4433–4438. doi:10.1016/J.JALLCOM.2011.01.149.

[178] F. Xu, J.H. Xu, M.F. Yuen, L. Zheng, W.Z. Lu, D.W. Zuo, Adhesion improvement of diamond coatings on cemented carbide with high cobalt content using PVD interlayer, Diam. Relat. Mater. 34 (2013) 70–75. doi:10.1016/J.DIAMOND.2013.01.012.

[179] A. Poulon-Quintin, C. Faure, L. Teulé-Gay, J.P. Manaud, A multilayer innovative solution to improve the adhesion of nanocrystalline diamond coatings, Appl. Surf. Sci. 331 (2015) 27–34. doi:10.1016/J.APSUSC.2015.01.050.

[180] R. Polini, M. Barletta, G. Cristofanilli, Wear resistance of nano- and micro-crystalline diamond coatings onto WC–Co with Cr/CrN interlayers, Thin Solid Films. 519 (2010) 1629–1635. doi:10.1016/J.TSF.2010.07.128.

[181] R. Polini, M. Barletta, On the use of CrN/Cr and CrN interlayers in hot filament chemical vapour deposition (HF-CVD) of diamond films onto WC-Co substrates, Diam. Relat. Mater. 17 (2008) 325–335. doi:10.1016/J.DIAMOND.2007.12.059.

[182] G. Cabral, J. Gäbler, J. Lindner, J. Grácio, R. Polini, A study of diamond film deposition on WC–Co inserts for graphite machining: Effectiveness of SiC interlayers prepared by HFCVD, Diam. Relat. Mater. 17 (2008) 1008–1014. doi:10.1016/J.DIAMOND.2008.03.017.

[183] Y. Tang, Y.S. Li, Q. Yang, A. Hirose, Deposition and characterization of diamond coatings on WC-Co cutting tools with W/Al interlayer, Diam. Relat. Mater. 19 (2010)

496–499. doi:10.1016/J.DIAMOND.2009.12.019.

[184] F. Ye, Y. Li, X. Sun, Q. Yang, C.-Y. Kim, A.G. Odeshi, CVD diamond coating on WC-Co substrate with Al-based interlayer, Surf. Coatings Technol. 308 (2016) 121–127. doi:10.1016/J.SURFCOAT.2016.06.088.

[185] R.E. Shroder, R.J. Nemanich, J.T. Glass, Analysis of the composite structures in diamond thin films by Raman spectroscopy, Phys. Rev. B. 41 (1990) 3738–3745. doi:10.1103/PhysRevB.41.3738.

[186] A.C. Ferrari, J. Robertson, Resonant Raman spectroscopy of disordered, amorphous, and diamondlike carbon, Phys. Rev. B. 64 (2001) 075414. doi:10.1103/PhysRevB.64.075414.

[187] H.W. Xin, Z.M. Zhang, X. Ling, Z.L. Xi, H.S. Shen, Y.B. Dai, Y.Z. Wan, Composite diamond films with smooth surface and the structural influence on dielectric properties, Diam. Relat. Mater. 11 (2002) 228–233. doi:10.1016/S0925-9635(01)00651-3.

[188] K. Nakamura, M. Fujitsuka, M. Kitajima, Disorder-induced line broadening in first-order Raman scattering from graphite, Phys. Rev. B. 41 (1990) 12260–12263. doi:10.1103/PhysRevB.41.12260.

[189] S. Prawer, R.J. Nemanich, Raman spectroscopy of diamond and doped diamond, Philos. Trans. R. Soc. London. Ser. A Math. Phys. Eng. Sci. 362 (2004) 2537–2565. doi:10.1098/rsta.2004.1451.

[190] J. Wagner, M. Ramsteiner, C. Wild, P. Koidl, Resonant Raman scattering of amorphous carbon and polycrystalline diamond films, Phys. Rev. B. 40 (1989) 1817–1824. doi:10.1103/PhysRevB.40.1817.

[191] B.V. Spitsyn, L.L. Bouilov, B.V. Derjaguin, Vapor growth of diamond on diamond and other surfaces, J. Cryst. Growth. 52 (1981) 219–226. doi:10.1016/0022-0248(81)90197-4.

[192] J.C. Angus, C.C. Hayman, Low-pressure, metastable growth of diamond and "diamondlike" phases., Science. 241 (1988) 913–21. doi:10.1126/science.241.4868.913.

[193] A. Fayer, O. Glozman, A. Hoffman, Deposition of continuous and well adhering diamond films on steel, Appl. Phys. Lett. 67 (1995) 2299–2301. doi:10.1063/1.115132.

[194] Z. Xu, L. Lev, M. Lukitsch, A. Kumar, Effects of surface pretreatments on the deposition of adherent diamond coatings on cemented tungsten carbide substrates, Diam. Relat. Mater. 16 (2007) 461–466. doi:10.1016/J.DIAMOND.2006.08.034.

[195] † Michelle L. Werner, ‡ Peter S. Nico, § and Matthew A. Marcus, † Cort Anastasio*, Use of Micro-XANES to Speciate Chromium in Airborne Fine Particles in the Sacramento Valley, (2007). doi:10.1021/ES070430Q.

[196] H.C. Wells, K.H. Sizeland, R.L. Edmonds, W. Aitkenhead, P. Kappen, C. Glover, B. Johannessen, R.G. Haverkamp, Stabilizing Chromium from Leather Waste in Biochar, ACS Sustain. Chem. Eng. 2 (2014) 1864–1870. doi:10.1021/sc500212r.

[197] V. Singh, V. Palshin, R.C. Tittsworth, E.I. Meletis, Local structure of composite Cr-containing diamond-like carbon thin films, Carbon N. Y. 44 (2006) 1280–1286. doi:10.1016/J.CARBON.2005.10.048.

[198] W. Olovsson, B. Alling, M. Magnuson, Structure and Bonding in Amorphous $Cr_{1-x}C_x$ Nanocomposite Thin Films: X-ray Absorption Spectra and First-Principles Calculations, J. Phys. Chem. C. 120 (2016) 12890–12899. doi:10.1021/acs.jpcc.6b03608.

[199] A. Pantelouris, H. Modrow, M. Pantelouris, J. Hormes, D. Reinen, The influence of coordination geometry and valency on the K-edge absorption near edge spectra of selected chromium compounds, Chem. Phys. 300 (2004) 13–22. doi:10.1016/J.CHEMPHYS.2003.12.017.

[200] H. Liu, D.S. Dandy, H. Liu, D.S. Dandy, Effects of Surface Conditions on Diamond Nucleation, Diam. Chem. Vap. Depos. (1995) 92–130. doi:10.1016/B978-081551380-3.50007-4.

[201] Y. Zhu, L. Wang, W. Yao, L. Cao, The interface diffusion and reaction between Cr layer and diamond particle during metallization, Appl. Surf. Sci. 171 (2001) 143–150. doi:10.1016/S0169-4332(00)00555-9.

[202] H. Tagawa, H. Nakajima, Mechanism of the Carbonization of Chromium(III) Oxide, Bull. Chem. Soc. Jpn. 35 (1962) 1239–1241. doi:10.1246/bcsj.35.1239.

[203] Y.A. Chang, D. Naujock, The relative stabilities of Cr23C6/ Cr7C3/ and Cr3C2 and the phase relationships in ternary Cr-Mo-C system, Metall. Mater. Trans. B. 3 (1972) 1693–1698. doi:10.1007/BF02642548.

[204] R. Polini, D. Gazzoli, E. Molinari, V. Sessa, M.L. Terranova, P. Ascarelli, S. Fontana, Diamond crystallites nucleation on sintered tungsten: temperature and thermal treatment effects, Diam. Relat. Mater. 1 (1992) 205–210. doi:10.1016/0925-9635(92)90026-K.

[205] R.J. Nemanich, J.T. Glass, G. Lucovsky, R.E. Shroder, Raman scattering characterization of carbon bonding in diamond and diamondlike thin films, J. Vac. Sci. Technol. A Vacuum, Surfaces, Film. 6 (1988) 1783–1787. doi:10.1116/1.575297.

[206] M.A. TAHER, W.F. SCHMIDT, H.A. NASEEM, W.D. BROWN, A.P. MALSHE, S. NASRAZADANI, Effect of methane concentration on physical properties of diamond-coated cemented carbide tool inserts obtained by hot-filament chemical vapour deposition, J. Mater. Sci. 33 (1998) 173–182. doi:10.1023/A:1004366217800.

[207] H. Liu, D.S. Dandy, H. Liu, D.S. Dandy, Diamond CVD Techniques, Diam. Chem. Vap. Depos. (1995) 14–45. doi:10.1016/B978-081551380-3.50004-9.

[208] R. Polini, F.P. Mantini, M. Barletta, R. Valle, F. Casadei, Hot filament chemical vapour deposition and wear resistance of diamond films on WC-Co substrates coated using PVD-arc deposition technique, Diam. Relat. Mater. 15 (2006) 1284–1291. doi:10.1016/J.DIAMOND.2005.09.045.

[209] S. Vepřek, The search for novel, superhard materials, J. Vac. Sci. Technol. A Vacuum, Surfaces, Film. 17 (1999) 2401–2420. doi:10.1116/1.581977.

[210] J. Musil, P. Zeman, P. Baroch, 4.13 – Hard Nanocomposite Coatings, in: Compr. Mater. Process., Elsevier Ltd, 2014: pp. 325–353. doi:10.1016/B978-0-08-096532-1.00416-7.

[211] S. Veprek, Recent search for new superhard materials: Go nano!, J. Vac. Sci. Technol. A

Vacuum, Surfaces, Film. 31 (2013) 050822. doi:10.1116/1.4818590.

[212] M. Witthaut, R. Cremer, K. Reichert, D. Neuschutz, Preparation of Cr 2 O 3 -Al 2 O 3 Solid Solutions by Reactive Magnetron Sputtering, Microchim. Acta. 133 (2000) 191–196. doi:10.1007/s006040070092.

[213] H. Najafi, A. Karimi, P. Dessarzin, M. Morstein, Formation of cubic structured (Al1-xCrx)2+??O3 and its dynamic transition to corundum phase during cathodic arc evaporation, Surf. Coatings Technol. 214 (2013) 46–52. doi:10.1016/j.surfcoat.2012.10.062.

[214] S.H. Sheng, R.F. Zhang, S. Veprek, Study of spinodal decomposition and formation of nc-Al2O3/ZrO2 nanocomposites by combined ab initio density functional theory and thermodynamic modeling, Acta Mater. 59 (2011) 3498–3509. doi:10.1016/j.actamat.2011.02.023.

[215] B. Bhushan, B.K. Gupta, Handbook of Tribology: Materials, Coatings and Surface Treatments, McGraw-Hill, 1991.

[216] V.M. Gropyanov, Chromic oxide as refractory material, Ogneupory. 1 (1969) 46–52.

[217] Lopato, reaction of zirconium oxide with chromic oxide, Neorg. Mater. 13 (1977) 1822–1824.

[218] D. Rafaja, C. Wüstefeld, G. Abrasonis, S. Braeunig, C. Baehtz, F. Hanzig, M. Dopita, M. Krause, S. Gemming, Thermally induced formation of metastable nanocomposites in amorphous Cr-Zr-O thin films deposited using reactive ion beam sputtering, Thin Solid Films. 612 (2016) 430–436. doi:10.1016/j.tsf.2016.06.038.

[219] S. Vepřek, M. Haussmann, S. Reiprich, L. Shizhi, J. Dian, Novel thermodynamically stable and oxidation resistant superhard coating materials, Surf. Coatings Technol. 86–87 (1996) 394–401. doi:10.1016/S0257-8972(96)02988-X.

[220] S. Vepřek, S. Reiprich, A concept for the design of novel superhard coatings, Thin Solid Films. 268 (1995) 64–71. doi:10.1016/0040-6090(95)06695-0.

[221] S. Veprek, M.G.J. Veprek-Heijman, Limits to the preparation of superhard nanocomposites: Impurities, deposition and annealing temperature, Thin Solid Films. 522 (2012) 274–282. doi:10.1016/j.tsf.2012.08.048.

[222] S. Veprek, M.G.J. Veprek-Heijman, P. Karvankova, J. Prochazka, Different approaches to superhard coatings and nanocomposites, Thin Solid Films. 476 (2005) 1–29. doi:10.1016/j.tsf.2004.10.053.

[223] S. Veprek, P. Nesladek, A. Niederhofer, F. Glatz, Search for superhard materials: Nanocrystalline composites with hardness exceeding 50 GPa, Nanostructured Mater. 10 (1998) 679–689. doi:10.1016/S0965-9773(98)00106-8.

[224] A. Yamaguchi, Densification Of Cr2O3-ZrO2 Ceramics by Sintering, Commun. Am. Ceram. Soc. 52 (1981) 1981.

[225] M. Jayaratna, M. Yoshimura, Hot pressing of Y203-stabilized Zr02 with Cr203 additions, 21 (1986) 591–596.

[226] J.H. Ouyang, S. Sasaki, Effects of different additives on microstructure and high-temperature tribological properties of plasma-sprayed Cr2O3 ceramic coatings, Wear. 249 (2001) 56–67. doi:10.1016/S0043-1648(01)00530-0.

[227] D.M. Mattox, HANDBOOK OF PHYSICAL VAPOR DEPOSITION (PVD): Film Formation , Adhesion , Surface preparation and contamination control, 1998. doi:10.1080/10426919908907566.

[228] J.R. Sohn, S.G. Ryu, M.Y. Park, Y. Il Pae, Preparation and characterization of chromium oxide supported on zirconia, J. Mater. Sci. 28 (1993) 4651–4659. doi:10.1007/BF00414254.

[229] H.R. Mahmoud, Highly dispersed Cr2O3-ZrO2 binary oxide nanomaterials as novel catalysts for ethanol conversion, J. Mol. Catal. A Chem. 392 (2014) 216–222. doi:10.1016/j.molcata.2014.05.021.

[230] J.R. Sohn, S.G. Ryu, Surface characterization of chromium oxide-zirconia catalyst,

Langmuir. 9 (1993) 126–131. doi:10.1021/la00025a029.

[231] S.W. Rhee, M. Hoch, The Zr-Cr-O System, Trans. Met. Soc. AIME. 230 (1964) 1687–1690.

[232] E. McCafferty, Oxide Networks, Graph Theory, and the Passivity of Cr-Mo, Cr-Zr, and Mo-Ti Binary Alloys, J. Electrochem. Soc. 149 (2002) B333. doi:10.1149/1.1481526.

[233] I.R. Beattie, T.R. Gilson, The single-crystal Raman spectra of nearly opaque materials. Iron(III) oxide and chromium(III) oxide, J. Chem. Soc. A Inorganic, Phys. Theor. 0 (1970) 980. doi:10.1039/j19700000980.

APPENDIX A

List of Publications

1- The Effect of Deposition Parameters on the Structure and Mechanical Properties of Chromium Oxide Coatings Deposited by Reactive Magnetron Sputtering, Masoud Mohammadtaheri, Qiaoqin Yang, Yuanshi Li and Jesus Corona-Gomez, Coatings 2018, 8, 111; doi:10.3390/coatings8030111

2- Hard Cr_2O_3 coatings on SS316L substrates prepared by reactive magnetron sputtering technique: A potential candidate for orthopedic implants, Mohammadtaheri, M., Li, Y. & Yang, Q. Environ Sci Pollut Res (2019). https://doi.org/10.1007/s11356-019-05006-3

3- Diamond nucleation and growth on WC-Co inserts with Cr_2O_3-Cr interlayer, Fan Ye, Masoud Mohammadtaheri, Yuanshi Li, Sheida Shiri, Qiaoqin Yang, Ning Chen, Surface & Coatings Technology 340 (2018) 190–198. https://doi.org/10.1016/j.surfcoat.2018.02.056

4- An Investigation on Synthesis and Characterization of Superhard Cr-Zr-O Coatings, M. Mohammadtaheri, Y. Li, J. Corona-Gomez, Q. Yang, Surface & Coatings Technology (2019)-Accepted.

APPENDIX B

COPYRIGHT PERMISSION

Chapter 4 to 7, have been published in four pre-reviewed international journals by MDPI, Elsevier and Springer, respectively. For articles published by Elsevier and Springer, the authors retain the right to include their article in a thesis or dissertation without the need to obtain written permission. Moreover, for all articles published in MDPI journals, copyright is retained by the authors. The copyright permissions for each journal can be found in below:

- The permission for including the paper “The Effect of Deposition Parameters on the Structure and Mechanical Properties of Chromium Oxide Coatings Deposited by Reactive Magnetron Sputtering” in chapter 4.

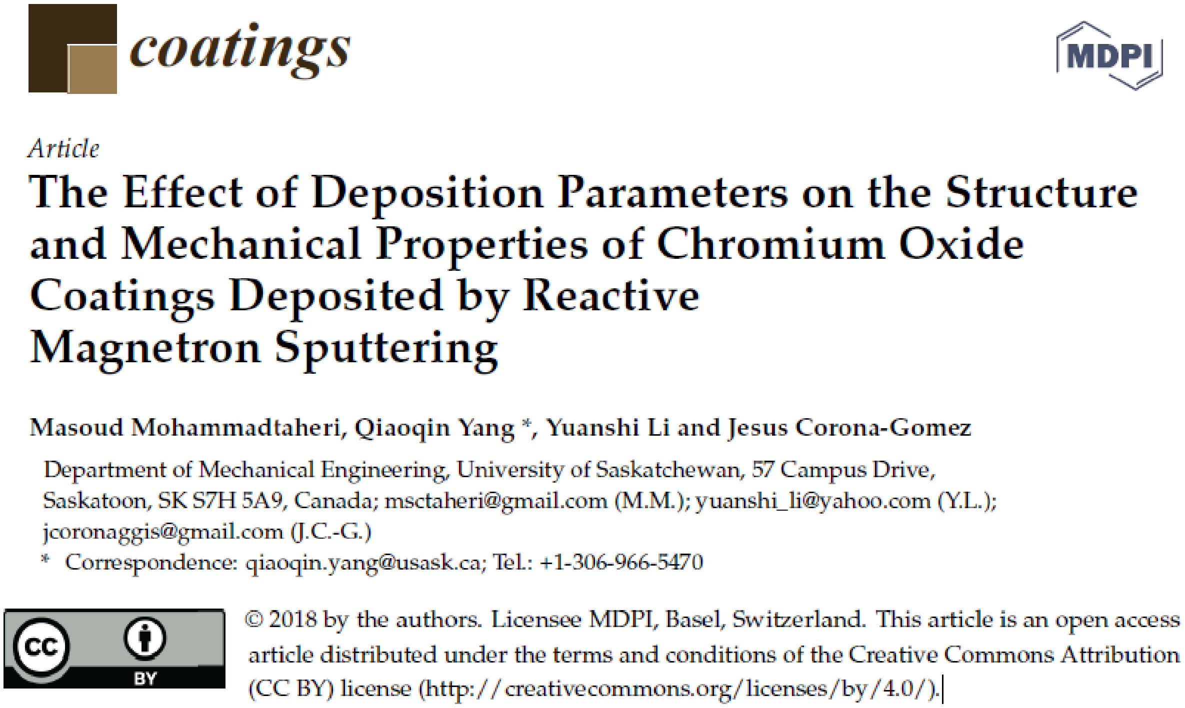

coatings

MDPI

Article

The Effect of Deposition Parameters on the Structure and Mechanical Properties of Chromium Oxide Coatings Deposited by Reactive Magnetron Sputtering

Masoud Mohammadtaheri, Qiaoqin Yang *, Yuanshi Li and Jesus Corona-Gomez

Department of Mechanical Engineering, University of Saskatchewan, 57 Campus Drive,
Saskatoon, SK S7H 5A9, Canada; msctaheri@gmail.com (M.M.); yuanshi_li@yahoo.com (Y.L.);
jcoronaggis@gmail.com (J.C.-G.)
* Correspondence: qiaoqin.yang@usask.ca; Tel.: +1-306-966-5470

© 2018 by the authors. Licensee MDPI, Basel, Switzerland. This article is an open access article distributed under the terms and conditions of the Creative Commons Attribution (CC BY) license (http://creativecommons.org/licenses/by/4.0/).

- The permission for including the paper “Hard Cr_2O_3 coatings on SS316L substrates prepared by reactive magnetron sputtering technique: A potential candidate for orthopedic implants” in chapter 5

SPRINGER NATURE LICENSE

TERMS AND CONDITIONS

May 24, 2019

This Agreement between Masoud mohammadtaheri ("You") and Springer Nature ("Springer Nature") consists of your license details and the terms and conditions provided by Springer Nature and Copyright Clearance Center.

License Number	4573220104984
License date	Apr 20, 2019
Licensed Content Publisher	Springer Nature
Licensed Content Publication	Environmental Science and Pollution Research
Licensed Content Title	Hard Cr2O3 coatings on SS316L substrates prepared by reactive magnetron sputtering technique: a potential candidate for orthopedic implants
Licensed Content Author	Masoud Mohammadtaheri, Yuanshi Li, Qiaoqin Yang
Licensed Content Date	Jan 1,2019
Type of Use	Thesis/Dissertation
Requestor type	academic/university or research institute
Format	electronic
Portion	full article/chapter
Will you be translating?	no
Circulation/distribution	<501
Author of this Springer Nature content	yes
Title	Thesis
Institution name	University of Saskatchewan
Expected presentation date	Aug 2019
Requestor Location	Masoud mohammadtaheri 802-107 Cumberland Ave S Saskatoon, SK S7N2R6 Canada

Terms and Conditions

Springer Nature Terms and Conditions for RightsLink Permissions Springer Nature Customer Service Centre GmbH (the Licensor) hereby grants you a non-exclusive, world-wide licence to reproduce the material and for the purpose and requirements specified in the attached copy of your order form, and for no other use, subject to the conditions below:

1. The Licensor warrants that it has, to the best of its knowledge, the rights to license reuse of this material.

However, you should ensure that the material you are requesting is original to the Licensor and does not carry the copyright of another entity (as credited in the published version).

If the credit line on any part of the material you have requested indicates that it was reprinted or adapted with permission from another source, then you should also seek permission from that source to reuse the material.

2. Where **print only** permission has been granted for a fee, separate permission must be obtained for any additional electronic reuse.

3. Permission granted **free of charge** for material in print is also usually granted for any electronic version of that work, provided that the material is incidental to your work as a whole and that the electronic version is essentially equivalent to, or substitutes for, the print version.

4. A licence for 'post on a website' is valid for 12 months from the licence date. This licence does not cover use of full text articles on websites.
5. Where **'reuse in a dissertation/thesis'** has been selected the following terms apply: Print rights of the final author's accepted manuscript (for clarity, NOT the published version) for up to 100 copies, electronic rights for use only on a personal website or institutional repository as defined by the Sherpa guideline (www.sherpa.ac.uk/romeo/).

6. Permission granted for books and journals is granted for the lifetime of the first edition and does not apply to second and subsequent editions (except where the first edition permission was granted free of charge or for signatories to the STM Permissions Guidelines http://www.stm-assoc.org/copyright-legal-affairs/permissions/permissions-guidelines/), and does not apply for editions in other languages unless additional translation rights have been granted separately in the licence.

7. Rights for additional components such as custom editions and derivatives require additional permission and may be subject to an additional fee. Please apply to Journalpermissions@springernature.com/bookpermissions@springernature.com for these rights.

8. The Licensor's permission must be acknowledged next to the licensed material in print. In electronic form, this acknowledgement must be visible at the same time as the figures/tables/illustrations or abstract, and must be hyperlinked to the journal/book's homepage. Our required acknowledgement format is in the Appendix below.

9. Use of the material for incidental promotional use, minor editing privileges (this does not include cropping, adapting, omitting material or any other changes that affect the meaning, intention or moral rights of the author) and copies for the disabled are permitted under this licence.

10. Minor adaptations of single figures (changes of format, colour and style) do not require the Licensor's approval. However, the adaptation should be credited as shown in Appendix below.

- The permission for including the paper “Diamond nucleation and growth on WC-Co inserts with Cr_2O_3-Cr interlayer” in chapter 6.

Title: Diamond nucleation and growth on WC-Co inserts with Cr2O3-Cr interlayer

Author: Fan Ye,Masoud Mohammadtaheri,Yuanshi Li,Sheida Shiri,Qiaoqin Yang,Ning Chen

Publication: Surface and Coatings Technology

Publisher: Elsevier

Date: 25 April 2018

© 2018 Elsevier B.V. All rights reserved.

If you're a copyright.com user, you can login to RightsLink using your copyright.com credentials.

Already **a RightsLink user** or want to learn more?

Please note that, as the author of this Elsevier article, you retain the right to include it in a thesis or dissertation, provided it is not published commercially. Permission is not required, but please ensure that you reference the journal as the original source. For more information on this and on your other retained rights, please visit: https://www.elsevier.com/about/our-business/policies/copyright#Author-rights

Copyright © 2019 Copyright Clearance Center, Inc. All Rights Reserved. Privacy statement. Terms and Conditions.
Comments? We would like to hear from you. E-mail us at customercare@copyright.com

- The permission for including the paper “An Investigation on Synthesis and Characterization of Superhard Cr-Zr-O Coatings” in chapter 7.

Title: An investigation on synthesis and characterization of superhard Cr-Zr-O coatings

Author: M. Mohammadtaheri,Y. Li,J. Corona-Gomez,Q. Yang

Publication: Surface and Coatings Technology

Publisher: Elsevier

Date: 15 October 2019

© 2019 Elsevier B.V. All rights reserved.

If you're a copyright.com user, you can login to RightsLink using your copyright.com credentials.

Already **a RightsLink user** or want to learn more?

Please note that, as the author of this Elsevier article, you retain the right to include it in a thesis or dissertation, provided it is not published commercially. Permission is not required, but please ensure that you reference the journal as the original source. For more information on this and on your other retained rights, please visit: https://www.elsevier.com/about/our-business/policies/copyright#Author-rights